Development of Advanced Internal Cooling Technologies for Gas Turbine Airfoils under Stationary and Rotating Conditions

Prashant Singh

Dissertation submitted to the faculty of the Virginia Polytechnic Institute and State University in partial fulfillment of the requirements for the degree of

Doctor of Philosophy
In
Mechanical Engineering

Srinath V. Ekkad, Chair
Wing F. Ng
Danesh K. Tafti
Rui Qiao
Kevin T. Lowe

May 23rd, 2017
Blacksburg, VA, USA

Keywords: Gas turbine; Rib turbulators; Jet impingement; Coriolis force

Development of Advanced Internal Cooling Technologies for Gas Turbine Airfoils under Stationary and Rotating Conditions

Prashant Singh

ABSTRACT (academic)

Higher turbine inlet temperatures (TIT) are required for higher overall efficiency of gas turbine engines. Due to the constant push towards achieving high TIT, the heat load on high pressure turbine components has been increasing with time. Gas turbine airfoils are equipped with several sophisticated cooling technologies which protect them from harsh external environment and increase their operating life and reduce the maintenance cost. The turbine airfoils are coated with thermal barrier coatings (TBCs) and the external surface is protected by film cooling. The internals of gas turbine blades are cooled by relatively colder air bled off from the compressor discharge. Gas turbine internals can be divided into three broad segments – (1) Leading edge section, (2) mid-chord section and (3) trailing edge section. The leading edge of the airfoil is subjected to extreme heat loads due to hot main gas stagnation and high turbulence intensity of the combustor exit gases. The leading edge is typically cooled by jet impingement which cross-over the rib turbulators in the feed chamber. The mid-chord section of the turbine airfoils have serpentine passages connected via. 180° bends, and they feature turbulence promotors which enhance the heat exchange rates between the coolant and the internal walls of the airfoil. The trailing edge section is typically cooled by array of pin fins. On one hand, the coolant routed through the internal passages of turbine airfoil help maintain the airfoil temperatures within safe limits of operation, the cooled air comes at a cost of loss of high pressure air from the compressor section. The aim of this study is to develop internal cooling concepts which have high thermal hydraulic performance, i.e. to gain high levels heat transfer enhancement due to cooling concepts at lower pumping power requirements. Experimental and numerical studies have been carried out and new rib turbulator designs such as Criss-Cross pattern, compound channels featuring uniquely organized ribs and dimples, novel jet impingement hole shapes have been developed which have high thermal-hydraulic performance.

Further, gas turbine blades rotate at high rotational speeds. The internal flow routed thought the serpentine passages are subjected to Coriolis and centrifugal buoyancy forces. The combined effects of these forces results in enhancement and reduction in heat transfer on the

pressure side and suction side internal walls. This leads to non-uniformity in the heat transfer enhancement which leads to non-uniform cooling and increase in the sites of high and low internal wall temperatures. Development of cooling concepts which have high thermal hydraulic performance under non-rotating conditions is important, however, under rotation, the heat transfer characteristics of the internal passages is significantly different in an unfavorable way. So the aim of the turbine cooling research is to have concepts which provide highly efficient and uniform cooling. The negative effects of rotation has been addressed in this study and new orientation of two-pass cooling channels has been presented which utilizes the rotational energy in favor of heat transfer enhancement on both pressure and suction side internal walls.

Present study has led to several new cooling concepts which are efficient under both stationary and rotating conditions.

Keywords: Gas turbine, heat transfer, rotation

Development of Advanced Internal Cooling Technologies for Gas Turbine Airfoils under Stationary and Rotating Conditions

Prashant Singh

GENERAL AUDIENCE ABSTRACT

Higher turbine inlet temperatures lead to higher overall efficiency of gas turbines. Hence, the high pressure stages of turbine sections, which are downstream of the combustor section, have significant thermal load. The turbine inlet temperatures can be as high as 1700°C and turbine airfoil material melting point temperature is around 1000°C. In order to protect the blade for the harsh environment, relatively colder air (~700°C) bled off from the compressor discharge is routed through the internal cooling passages of turbine airfoils. The coolant bled from the compressor section contributes the reduction in the performance of the engine. Hence, the aim of the turbine cooling research is to achieve high rates of heat transfer at relatively lower pumping power requirements. In order to enhance the heat transfer rates from between the hot internal walls of airfoil and the coolant, turbulence promotors are typically installed in the mid-section of the airfoil which features serpentine passages interconnected by 180° bends. Present study is focused on development of highly efficient concepts for internal flows in turbine airfoils.

The other aspect of internal cooling research is focused on characterization of heat transfer under rotating conditions. Coriolis force and centrifugal buoyancy forces lead to non-uniform cooling and the heat transfer rates are significantly different under rotating conditions compared to non-rotating conditions. Present study utilizes detailed measurements of heat transfer coefficients under rotating conditions for the development of cooling designs for two-pass ribbed channels where rotational effects can be used in favor of heat transfer enhancement, leading to enhanced and more uniform cooling of internal walls.

Dedicated

To my parents

ACKNOWLEDGEMENTS

I would like to thank Dr. Srinath Ekkad (doctoral advisor) for supporting my research and giving me the freedom of exploring novel ideas. My discussions with him led to the development of several new cooling concepts catered towards gas turbine engines. I am thankful to him for always finding time for discussions, advising on research and much more. I couldn't have found a better doctoral advisor!

I would also like to thank Dr. Wing Ng, Dr. Danesh Tafti, Dr. Rui Qiao and Dr. Todd Lowe for being part of my Ph.D. committee. Support of all the past and present lab members is sincerely acknowledged. In particular, I would like to thank Mr. Yongbin Ji (Shanghai Jiao Tong University), Mr. Weihong Li (Tsinghua University) and Mr. Bharath Viswanath Ravi for carrying out the numerical studies on wide range of cooling designs which I tested experimentally. I am also thankful to Jaideep and David, for having countless discussions on heat transfer with me. Thanks to Diana Israel in particular – the most efficient person I have ever worked with. Without the support of the efficient team I was part of, this work wouldn't have been possible.

TABLE OF CONTENTS

ABSTRACT (academic) ii

ABSTRACT (public) iv

ACKOWLEDGEMENTS vi

LIST OF FIGURES xv

LIST OF TABLES xxiv

PREFACE xxv

BACKGROUND xxvi

CHAPTER 1 1

Experimental and Numerical Study of Heat Transfer due to Developing Flow in a Two-pass Rib Roughened Square Duct

Abstract 1

Introduction 1

Experimental Setup 3

Description of test configuration 4

Computational Methodology, Grid Independence Study and Flow data visualization 4

Boundary conditions 4

Heat transfer coefficient measurement theory and procedure 6

Uncertainty analysis 9

Validation of Numerical Prediction of heat transfer coefficient with experiments 10

Results and discussions 11

Bend heat transfer and fluid flow 16

Bulk fluid distribution (1^{st} pass, 3^{rd} pitch) 16

Area averaged Nusselt number 18

Globally averaged Nusselt number 19

Comparison between experimental measurements and numerical predictions of globally averaged Nusselt number enhancement (Nu/Nus) 20

Friction factor and thermal hydraulic performance (THP) 21

Conclusions 23

Nomenclature 24

References 25

CHAPTER 2 29

Characterization of heat transfer enhancement and frictional losses in a two-pass square duct featuring unique combinations of rib turbulators and cylindrical dimples

ABSTRACT 29

Introduction 29

Experimental setup 35

Description of test configurations, experimental conditions and terminology 39

Heat transfer coefficient calculation methodology 39

Uncertainty analysis 43

Results and discussion 44

Heat transfer characteristics of smooth two-pass duct 45

Basic heat transfer augmentation phenomena due to ribs and dimples 46

Detailed Nusselt number contours for different configurations studied 48

Regionally averaged Nusselt numbers 52

Globally averaged Nusselt number variation with Reynolds number 63

Comparison of globally averaged Nusselt numbers for different types of configurations 64

Friction losses and thermal hydraulic performance of two-pass channel 65

Heat transfer correlations 70

Conclusions and Recommendations 72

Nomenclature 74

References 75

CHAPTER 3 78

Experimental and numerical investigation of heat and fluid flow in a square duct featuring Criss-Cross rib patterns

ABSTRACT 78

Introduction 79

Experimental setup 81

Description of test configuration 83

Experimental conditions 85

Computational details 85

Inlet conditions 85

Selection of turbulence model 85

Computational grid details, mesh independence studies 86

Nusselt number calculations 88

Heat transfer coefficient calculation methodology in experiments 89

Determination of Tw 90

Uncertainty analysis 93

Results and Discussion 93

Smooth channel heat transfer, effects of inlet conditions on heat transfer 93

Detailed measurements of Nusselt number ratio for Inline and Staggered configurations 94

Numerically predicted flow field in planes orthogonal and parallel to bulk flow direction 97

Spanwise averaged, regionally averaged and globally averaged Nusselt number enhancement 99

Comparison with established correlation of Han and Park [3.45] 101

Centerline static pressure (numerical), normalized friction factor (experimental) and thermal hydraulic-performance (experimental) 103

Conclusions and recommendations 105

Nomenclature 105

References 107

CHAPTER 4 113

Effects of spent air removal scheme on internal-side heat transfer in an impingement-effusion system at low jet-to-target plate spacing

ABSTRACT 113

Introduction 114

Details of experimental setup 116

Description of test configurations and experimental conditions 119

Data reduction procedure 120

Heat transfer coefficient calculation 121

Discharge coefficient, jet exit Mach number and pumping power calculations 125

Uncertainty analysis 127

Validation of experimental data with correlations 128

Results and discussion 129

Detailed heat transfer coefficient contours 130

Region-wise averaged Nusselt number distribution 134

Globally averaged Nusselt number and corresponding pumping power 136

Conclusions 140

Nomenclature 140

References 142

CHAPTER 5 144

Experimental Investigation of heat transfer augmentation by different jet impingement hole shapes under maximum crossflow

ABSTRACT 144

Introduction 144

Experimental setup and operating procedure 147

Description of test section and experimental conditions 148

Data reduction procedure 149

Nusselt number calculation procedure 149

Discharge coefficient (CD) and abd jet exit Mach number (M) calculations 153

Uncertainty analysis 155

Results and discussion 157

Detailed heat transfer coefficient contours 157

Spanwise and streamwise averaged Nusselt number 158

Streamwise variation of area averaged Nusselt numbers 162

Globally averaged Nusselt numbers 163

Conclusions 165

Acknowledgements 165

Nomenclature 165

References 167

CHAPTER 6 169

Experimental and numerical investigation of heat transfer inside two-pass rib roughened duct (AR 1:2) under rotating and stationary conditions

ABSTRACT 169

Introduction 170

Experimental setup for transient liquid crystal thermography under rotation 173

Description of the test section 173

Computational methodology, grid independence study and flow data validation 174

Boundary conditions for computations 174

Validation of numerically predicted total pressure drop with experiments 174

Data reduction procedure for TLCT under rotation 177

Uncertainty analysis 179

Results and discussion 179

Detailed heat transfer measurements under rotation 181

Blade tip underside heat transfer and fluid dynamics in bend region – numerical predictions 187

Regionally averaged heat transfer under stationary conditions 190

Smooth and ribbed configurations under stationary conditions – experiments 190

(Nu/Nus) and (Nu/Nu0,RPM) : comparison between experiments and numerical predictions 193

Regionally averaged Nusselt number enhancement (Nu/Nu0) under rotating conditions: experiments 194

Conclusions 196

Nomenclature 197

References 198

CHAPTER 7 201

Experimental investigation of rotating rib roughened two-pass square duct with two different channel orientations

ABSTRACT 201

Introduction 202

Experimental setup 204

Description of test configurations 208

Experimental conditions 209

Data reduction procedure 210

Determination of Tw 212

Uncertainty analysis 213

Results and discussion 214

Detailed Nusselt number enhancement (Nu/Nu0) contours: Model A 214

Detailed Nusselt number enhancement (Nu/Nu0) contours : Model B 219

Regionally averaged Nusselt number enhancement: Model A and Model B 222

Regionally averaged Nusselt number enhancement : Model A and Model B comparisons 229

Globally averaged Nusselt number enhancement and imposed pumping power requirements 231

Conclusions and recommendations 235

Nomenclature 237

References 238

CHAPTER 8 243

Conclusions and recommendations for future work

LIST OF FIGURES

Figure 1.1 Schematic of experimental setup 4

Figure 1.2 Four rib configurations studied (45°, V, W, and M), also indicated are the region #s in M rib (smooth channel was the baseline case, which is not shown here) 5

Figure 1.3 (a) Overview of mesh, (b) zoomed-in view of the cut section near ribs 6

Figure 1.4 (a) Comparison of numerically predicted normalized static pressure with experiments, (b) summary of grid independence study (for 45˚ ribs) 7

Figure 1.5 History of mainstream temperatures measured at inlet, bend and outlet of two-pass channel, normalized wall temperature (α) measured at the inlet plotted with time, green region indicating $0.3 < \alpha < 0.7$. 8

Figure 1.6 (a) Typical Hue versus Wall Temperature relationship observed during experiments, (b) Hue (H), Saturation (S) and (V) time history 9

Figure 1.7 (a) Smooth plate spanwise averaged Normalized Nusselt number (Nu/Nu0) variation in first pass, x/dh = 0 corresponds to start of Region 1 and x/dh = 6 corresponds to end of region 3; (b) region-wise averaged normalized Nusselt number (Nu/Nus) for 45˚ angled rib for Reynolds number of 52000 11

Figure 1.8 Normalized Nusselt number contour plots for four rib configurations, and the baseline smooth channel (Re 35500); left contour: CFD and right contour: experiments, direction of flow specified in Fig. 2 14

Figure 1.9 Streamtraces plotted at a plane located at z/dh = 0.04 from the bottom wall (3rd rib pitch in 1st pass) 15

Figure 1.10 Velocity vectors superimposed by normalized turbulent kinetic energy at a plane located at z/dh = 0.04 above the bottom wall, and normalized heat transfer enhancement in the bend region (mean of region # 4 and 5) 15

Figure 1.11 Streamtraces superimposed with normalized bulk fluid temperature at a plane just downstream of the 3rd rib in the first pass (shown plane is normal to the direction of bulk flow) 17

Figure 1.12 Area averaged Heat transfer enhancement, Nu/Nu0 and Nu/Nus for four rib configurations 18

Figure 1.13 Globally averaged heat transfer enhancement, Nu/Nu0 and Nu/Nus for four rib configurations 20
Figure 1.14 Globally averaged Nusselt number enhancement: Experiment versus CFD 21
Figure 1.15 Normalized friction factor 22
Figure 1.16 Thermal Hydraulic Performances 22
Figure 2.1 (a) Schematic of Experimental setup, (b) description of coolant flow prior to entering the test section, location of mainstream temperature measurement 35
Figure 2.2 (a) Different rib, dimple and rib-dimple compound channel studied, (b) dimensions of rib and dimple relative to each other in terms of rib height 38
Figure 2.3 Two pass channel nomenclature 39
Figure 2.4 History of wall temperature and static temperature measured in plenum chamber, green region indicating $0.3 < \alpha < 0.7$. 40
Figure 2.5 (a) Hue versus wall temperature, (b) Time evolution of Hue, Saturation and Value 41
Figure 2.6 (a) Detailed Nusselt number contour (Nu/Nu_0) at Re = 52000, (b) Spanwise averaged Nusselt number (1^{st} pass) plotted in streamwise direction (x/d_h = 0 corresponds to start of second rib pitch in the first pass, x/d_h = 6 corresponding to end of last rib in the first pass) 45
Figure 2.7 Detailed Nusselt number enhancement contours for all the configurations studied (Re = 35500) (first pass and second pass orientation as shown in Fig. 2) 47
Figure 2.8 Regionally averaged normalized Nusselt number for compound channels 52
Figure 2.9 Regionally averaged normalized Nusselt number for ribbed channels 54
Figure 2.10 Regionally averaged normalized Nusselt number for dimpled channels 56
Figure 2.11 Globally averaged Nusselt number variation with Reynolds number, (a) 45° configuration, (b) configuration V, (c) configuration W, (d) configuration M 60
Figure 2.12 Globally averaged normalized Nusselt number variation with Reynolds number, (a) Rib-dimpled Compound, (b) Rib alone, (c) Dimple alone configurations 62
Figure 2.13 Normalized Friction factors, (a) 45° configuration, (b) configuration V, (c) configuration W, (d) configuration M 66

Figure 2.14 Thermal Hydraulic Performance, (a) 45° configuration, (b) configuration V, (c) configuration W, (d) configuration M 68
Figure 2.15 Comparison of globally averaged Nusselt number obtained from correlation shown in Eq. 10 with experiments 71
Figure 2.16 Comparison of heat transfer enhancement obtained from correlation shown in Eq. 11 with experiments 71
Figure 3.1 Schematic of experimental setup 82
Figure 3.2 Coolant inlet and exit conditions, bulk temperature measurement locations, static pressure measurement locations 82
Figure 3.3 Dimensions of the test section, rib turbulator, and orientation with respect to coolant flow 83
Figure 3.4 (a) Inline configuration (a sample region # has been shown); (b) staggered configuration 84
Figure 3.5 Model validation with experimentally obtained normalized Nusselt number Nu/Nu_s 86
Figure 3.6 Different views of structured grid employed for computations 87
Figure 3.7 Mainstream temperature evolution with time, wall temperature measured at inlet, normalized wall temperature (at inlet) versus time 91
Figure 3.8 Calibration of wall temperature with Hue [LC part # R10C5W] 92
Figure 3.9 Spanwise averaged Nusselt number ratio(Nu/Nu_0) plotted with normalized streamwise distance 94
Figure 3.10 Detailed Nusselt number ratio (Nu/Nu_0) contour for the Inline configuration for all Reynolds numbers - experiment versus CFD 96
Figure 3.11 Detailed Nusselt number ratio (Nu/Nu_0) contours for the Staggered configuration for all Reynolds numbers – experiment versus CFD 96
Figure 3.12 Velocity vectors superimposed with normalized turbulent kinetic energy for two different orthogonal planes for inline and staggered configurations (Re = 30000): coolant flow is into the plane 97
Figure 3.13 Streamlines superimposed with normalized turbulent kinetic energy at a plane parallel to bulk flow and at a normal distance of 0.5e from the endwall featuring rib turbulators, (a) Inline, (b) staggered. 98

Figure 3.14 Region-wise averaged Nusselt number enhancement plotted in streamwise direction – Inline and Staggered configurations 99
Figure 3.15 Experimentally obtained globally averaged Nusselt number enhancement versus Reynolds number – Inline and Staggered configuration 100
Figure 3.16 Comparison of globally averaged normalized Nusselt number $\left(\overline{\overline{Nu}}/Nu_s\right)$ between experiments and CFD 101
Figure 3.17 Heat transfer roughness function (G) versus Roughness Reynolds number (e+) – correlation from present study and its proximity to Han and Park [45] 102
Figure 3.18 Static pressures at the endwall centerline predicted by numerical Calculations 103
Figure 3.19 Normalized friction factor (f/f_0) and thermal hydraulic performance (THP_0) 104
Figure 4.1 (a) Schematic of the experimental setup, (b) Details of test section, camera location, plenum chamber length, liquid crystal location (not drawn to scale) 118
Figure 4.2 (a) Relative arrangement of impingement and effusion holes (top view), also indicated is the region size for area averaged Nusselt number, (b) different crossflow schemes studied (side view). 121
Figure 4.3 Time history of typical plenum temperatures measured at location 1 and location 2, the transient test started at t = 0 seconds, TC measurements shown for maximum crossflow condition 123
Figure 4.4 Calibration of Hue with measured wall temperature, also shown is the saturation and intensity variation with wall temperature 125
Figure 4.5 Variation of discharge coefficient and jet exit Mach number with plenum pressure ratio 126
Figure 4.6 Pumping power versus jet Reynolds number for all configurations for full range of jet Reynolds number investigated in heat transfer experiments (measurements were also carried out at intermediate jet Reynolds numbers in order to obtain high regression coefficient) (Note: Q is the total pumping power required for maintaining an average jet Reynolds number of Re_j across N jets) 128

Figure 4.7 Left figure: Comparison of Nusselt number with correlation prescribed by Florschuetz et al. [18]; Right figure: comparison of heat transfer data with similar past studies 129

Figure 4.8 (a) Detailed heat transfer coefficient contours for all the configurations at $Re_j = 3500$, (b) Detailed heat transfer coefficient contours for all the configurations at $Re_j = 6000$, (c) Detailed heat transfer coefficient contours for all the configurations at $Re_j = 9000$ 131

Figure 4.9 (a) Region-wise averaged Nusselt number for maximum crossflow condition, region 1 (blocked end), crossflow direction – region 1 through 8., (b) (a) Region-wise averaged Nusselt number for intermediate crossflow condition, region 1 (blocked end), crossflow direction – region 1 through 8., (c) (a) Region-wise averaged Nusselt number for minimum crossflow condition, region 1 (blocked end), crossflow direction – region 1 through 8., (d) (a) Region-wise averaged Nusselt number for zero crossflow condition, region 1 (blocked end), crossflow direction – region 1 through 8. 134

Figure 4.10 Globally averaged Nusselt number variation with jet Reynolds number 138

Figure 4.11 Globally averaged Nusselt number with pumping power requirements for full range of Reynolds number investigated in the present study (Note: Q is the total pumping power required for N jets) 139

Figure 5.1 Description of experimental setup 146

Figure 5.2 (a) Isometric view of impingement test section, (b) top view of the jet plate with jet nomenclature and region number, (c) side view of plenum feed chamber, spacer and spent flow direction 148

Figure 5.3 Jet hole shape designs and their orientation with respect to coolant flow in plenum 149

Figure 5.4 History of wall temperature and static temperature measured in plenum chamber, green region indicating $0.3 < \alpha < 0.7$ 150

Figure 5.5 Time evolution of H, S, and V in the calibration region 151

Figure 5.6 Typical Hue versus wall temperature relationship 152

Figure 5.7 Variation of discharge coefficient of different hole shapes with plenum pressure ratio 154

Figure 5.8 Jet exit Mach number variation for different jet hole shapes with plenum pressure ratio 155

Figure 5.9 Validation of present experiment with established literature 156

Figure 5.10 Detailed heat transfer coefficient (W/m^2K) plots for three hole shapes Studied 157

Figure 5.11 Spanwise averaged Nusselt number plotted in streamwise direction for (a) round, (b) racetrack, and (c) V jet hole shapes, respectively 160

Figure 5.12 Streamwise averaged Nusselt number plotted in spanwise direction for (a) round, (b) racetrack, and (c) V jet hole shapes, respectively 162

Figure 5.13 Streamwise variation of area averaged Nusselt number for different hole shapes 163

Figure 5.14 Globally averaged Nusselt numbers for racetrack and V hole shapes, normalized with round holes 163

Figure 5.15 Normalized flow resistance (R) with Reynolds number for different jet hole shapes 164

Figure 6.1 Schematic of experimental setup 175

Figure 6.2 Left figure: Two pass ribbed duct with bulk temperature measurement locations (red dots) in reference to channel centerline, green color indicates flow path. Right figure: assembly drawing for in-situ temperature measurements on leading side, trailing side and blade tip underside in one run 175

Figure 6.3 Mesh generated using ICEM software 176

Figure 6.4 (a) Variation of normalized pressure (p^*) with Reynolds number (Ro = 0), (b) variation of normalized pressures (p^* and p^{**}) with Rotation number (numerically predicted). 177

Figure 6.5 Mainstream temperature variation with time, (a) smooth two pass channel, (b) ribbed two pass channel 178

Figure 6.6 Detailed Nusselt number enhancement contours under stationary Conditions 180

Figure 6.7 Detailed Nusselt number enhancement(Nu/Nu_0) contour for smooth and ribbed two-pass duct at Re = 25000 and Ro = 0.063 (700 RPM). 182

Figure 6.8 Iso-surface of Q criterion colored by vorticity: Re= 25000 and Ro = 0 for the ribbed configuration 183

Figure 6.9 Iso-surface of Q criterion colored by vorticity: Re= 25000 and Ro = 0.063 for the ribbed configuration 183

Figure 6.10 Streamtraces superimposed with normalized TKE for Ro=0 and 0.063 cases. 185

Figure 6.11 Streamtraces superimposed with normalized TKE, plotted near endwall 186

Figure 6.12 Iso-surface of Q-criterion colored by vorticity 188

Figure 6.13 Blade tip underside heat transfer – numerical predictions 189

Figure 6.14 Regionally averaged normalized Nusselt number for smooth two-pass channel under stationary conditions 190

Figure 6.15 Regionally averaged normalized Nusselt number for ribbed two-pass channel under stationary conditions 191

Figure 6.16 Streamlines showing turbulent kinetic energy in the flow near the rib, also shown is the normalized TKE contour with streamtraces in a plane orthogonal to bulk flow direction. (The planes were drawn just downstream of the rib, left plane

corresponds to first rib and right plane corresponds to third rib of the first pass): Re = 25000, Ro = 0 192

Figure 6.17 (a) Regionally averaged Nusselt number (Nu/Nu_s) at Ro = 0 - experiment versus CFD, (b) regionally averaged Nusselt number ($Nu/Nu_{stationary}$) at Re = 25000, Ro = 0.063 – experiment versus CFD. 193

Figure 6.18 Regionally averaged Nusselt number (Nu/Nu_0) for rotation and stationary cases (smooth): experimental results 194

Figure 6.19 Regionally averaged Nusselt number (Nu/Nu_0) for rotation and stationary cases (ribbed): experimental results 195

Figure 7.1 Schematic of experimental setup 203

Figure 7.2 Rib details 204

Figure 7.3 Two-pass channel inlet conditions, rib angle of attack (Model A) 205

Figure 7.4 Model orientations with respect to direction of rotation and their locations in mid-chord region in turbine blade 206

Figure 7.5 Demonstration of channel orientation with respect to direction of rotation, and rib arrangement 207

Figure 7.6 Heat transfer measurement regions, bulk temperature measurement Locations 208

Figure 7.7 Mainstream temperature evolution with time, measurements carried out at four locations in the two pass channel 211

Figure 7.8 Camera orientation, lighting conditions, liquid crystal and black coating Locations 212

Figure 7.9 Calibration of wall temperature with Hue [LC part # R10C5W] 214

Figure 7.10 Detailed map of normalized Nusselt number (Nu/Nu_0), Model A- Smooth configuration 215

Figure 7.11 Detailed map of normalized Nusselt number (Nu/Nu_0), Model A- 2RW 216

Figure 7.12 Detailed map of normalized Nusselt number (Nu/Nu_0), Model B- Smooth [White stripe : NO data] 217

Figure 7.13 Detailed map of normalized Nusselt number (Nu/Nu_0), Model B - 1RW [White stripe : NO data] 218

Figure 7.14 Detailed map of normalized Nusselt number (Nu/Nu_0), Model B - 2RW [White stripe : NO data] 220

Figure 7.15 Regionally averaged normalized Nusselt number variation with increasing streamwise distance from inlet [Model A - Smooth] 223

Figure 7.16 Regionally averaged normalized Nusselt number (Nu/Nu_0 and Nu/Nu_s) variation with increasing streamwise distance from inlet [Model A - 2RW] 224

Figure 7.17 Regionally averaged normalized Nusselt number (Nu/Nu_s) with corresponding smooth channel configuration 226

Figure 7.18 Regionally averaged normalized Nusselt number (Nu/Nu_0) variation with increasing streamwise distance from inlet [Model B - Smooth] 227

Figure 7.19 Regionally averaged normalized Nusselt number (Nu/Nu_0 and Nu/Nu_s) variation with increasing streamwise distance from inlet [Model B 1RW] 228

Figure 7.20 Regionally averaged normalized Nusselt number (Nu/Nu_0 and Nu/Nu_s) variation with increasing streamwise distance from inlet [Model B: 2RW] 230

Figure 7.21 Nusselt number enhancement (Nu/Nu_0) in bend region (# 7 and # 8) for all configurations: variation with Rotation number 231

Figure 7.22 Nusselt number enhancement (Nu/Nu_0) comparison between Model A and B smooth configurations 232

Figure 7.23 Nusselt number enhancement (Nu/Nu_0) comparison between Model A and B ribbed configurations 233

Figure 7.24 Globally averaged Nusselt number enhancement (Nu/Nu_0 and Nu/Nu_s) with Rotation number 234

Figure 7.25 Globally averaged Nusselt number enhancement (Nu/Nu_0) with total Pumping power [Watts] requirements 235

LIST OF TABLES

Table 2.1	Correlation coefficients from Eq. 10	72
Table 2.2	Correlation coefficients from Eq. 11	73
Table 3.1	Comparison of measured total pressure drop with numerical predictions	88
Table 5.1	Geometrical parameters	149

PREFACE

The dissertation is presented in manuscript format and is divided into two parts – (1) heat transfer studies under stationary conditions, (2) heat transfer studies under rotating conditions. Part 1 of this work was focused towards development of novel concepts for heat transfer enhancement for internal cooling passages of gas turbine airfoils. Different rib turbulator shapes, rib dimpled compound channels, jet impingement hole shapes, impingement heat transfer performance under various crossflow schemes, has been investigated experimentally and numerically in order to develop cooling configurations which have high thermal hydraulic performance. The numerical work as carried out by Bharath Viswanath Ravi, Weihong Li and Yongbin Ji. Heat transfer coefficients were experimentally calculated using transient liquid crystal thermography. In some papers, both experiments and numerical results have been used in conjunction to understand the heat transfer characteristics.

Part 2 of the dissertation is focused towards evaluation of rotational effects on heat transfer on internal flows in two-pass ducts. Similar to stationary studies, the heat transfer coefficients were measured using transient liquid crystal thermography for the rotation studies as well. Traditional two pass duct (AR 1:2) featuring V-shaped rib turbulators was investigated under rotating conditions to quantify the effects of Coriolis and centrifugal buoyancy forces on heat transfer enhancement and reduction on leading and trailing sides. The understanding from this work was used to develop a novel two-pass channel cooling design which uses rotation for enhancement of heat transfer on both the leading and trailing walls subjected to heat loads in real gas turbine engines.

The selected research articles presented in this dissertation has been published/under review in International Journal of Heat and Mass Transfer (Elsevier) and conference proceedings of ASME IGTI Turbo Expo.

BACKGROUND

Development of highly efficient gas turbines is imperative in order to achieve increased power while still keeping the fuel consumption economically viable. Higher efficiencies of gas turbines are associated with higher turbine inlet temperatures. The components of high pressure turbine (HPT) stages are hence subjected to increased thermal loads. These thermal stresses are further aggravated for rotating components, particularly, the blades of HPT stages. Continued exposure of turbine hot gas path components to high thermal loads results in increase in maintenance cost and in some cases in permanent failure. In order to keep the turbine airfoil temperatures under safe limits of operation, about 30% of relatively colder high-pressure air is bled off from the compressor section. The extraction of pressurized air results in penalty to the thermodynamic efficiency of gas turbine. The pressurized coolant is then routed to complex passages inside turbine airfoils and finally exiting into hot gas path via film cooling holes. The airfoil internals feature jet impingement for leading edge cooling, turbulence promotors for mid-chord section, pin fin array for trailing edge cooling etc. All of these cooling technologies are designed to increase the heat transfer between the coolant and the internal walls of the airfoils. However, cooling is achieved at a cost of higher supply pressures and increased coolant flow rates, which has a direct effect on the thermodynamic efficiency.

Gas turbine cooling is a slowly progressing research field where any new concept is challenged based on its manufacturability and integration in the existing cooling design. Hence, there exists a need to develop simple yet effective concepts keeping in view, the applicability of cooling designs in the existing blade designs. Efforts have been made in the present study to address these issues by utilizing the existing concepts in an intelligent way to yield more efficient cooling, while still being easy to implement. Some of the cooling designs have also been tested under rotating conditions for realistic evaluation of their thermal hydraulic performance – which depends on both, overall heat transfer enhancement and net pressure drop. Attempts have been made to come up with a rib turbulated two-pass channel configuration which has high thermal hydraulic performance under rotating conditions by arranging the coolant direction and rotation vector such that heat transfer was enhanced on both trailing and leading side internal walls.

Present study is particularly focused on the mid-chord region of a gas turbine blade. This region is typically cooled by serpentine passages featuring rib turbulators or array of impinging jets. Hence, the present work can be broadly categorized as rib turbulator studies and jet impingement studies under both, non-rotating and rotating conditions.

The mid-chord region of turbine blade has been extensively studied in the past and several concepts have been tested and heat transfer enhancement levels have been quantified in perspective of friction factor enhancement. Figure 0.1 shows the heat transfer enhancement levels for different existing cooling concepts in reference to their pumping power requirements. It can be observed from the figure that heat transfer enhancement comes at an increased pumping cost. Heat transfer enhancement (Nu/Nu_0) level of 5.0 is typically achieved at friction factor enhancement levels ranging from 10 to 15 for different shapes of rib turbulators.

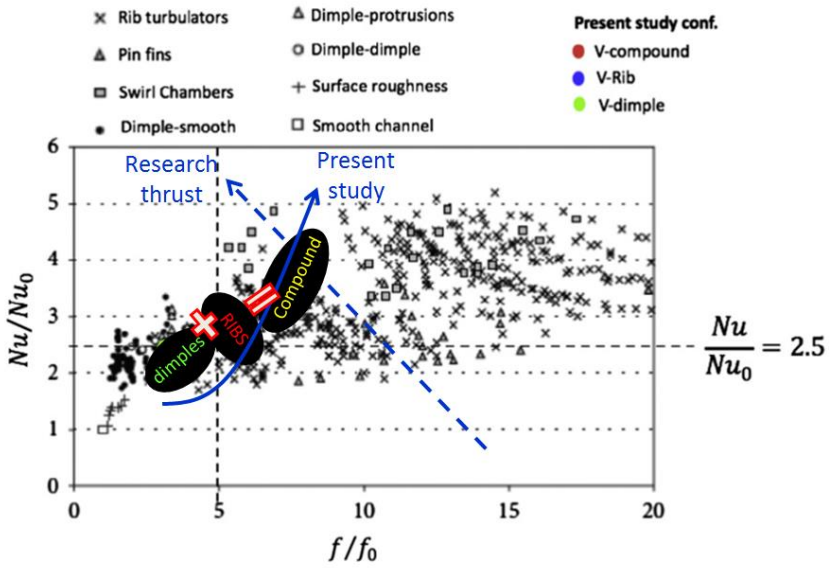

Figure 0.1 Heat transfer enhancement levels versus friction factor enhancements for different existing cooling concepts, also shown is the contribution of present study aimed towards achieving higher heat transfer enhancement levels at relatively lower enhancement in friction factor [0.1]

As mentioned earlier, the present study is focused on the mid-chord section of turbine blades, which feature serpentine passages having rib turbulators on opposite internal walls. The commonly known rib shapes which are 90°, 45°, 60°, 45° V, 60° V, broken 45°, broken 60°, delta and wedge shaped ribs, W shaped ribs, M shaped, truncated ribs, etc. Heat transfer experiments

are designed to evaluate the heat transfer enhancement levels with respect to Dittus-Boelter correlation for developed turbulent flow in circular duct (Nu_0). 90° rib shape has been found to have lowest levels of (Nu/Nu_0) ~ 2. Also, in many prior studies it has been found that the heat transfer enhancement levels decrease with increasing Reynolds numbers. The angled ribs have been found to have (Nu/Nu_0) ranging from 2.5 to 3.5. Dimples are also commonly used to enhance heat transfer due to periodical vortex shedding. The levels of HT enhancements (Nu/Nu_0) are typically around 2.0, however, the pressure penalty is also minimal. With the advancements in additive manufacturing, fabrication of complicated ribs and dimples are now possible and opens up new possibilities for novel design development. One example of advance cooling technique is demonstrated in the present study by employing combination of rib turbulators and dimples in a unique patter for heat transfer enhancement at minimal increment in pumping power requirements. An attempt was made to combine merits of ribs and dimples to develop a feature which has higher HT enhancement levels compared to both ribs and dimples. In order to realize this goal, four rib shapes, viz. 45°, V, W and M, employed in a two-pass square channel, were tested for a range of Reynolds number from 19500 to 69000. The basic mechanism of heat transfer enhancement due to rib turbulators is due to the increase in wall shear due to rib induced secondary flows and the turbulent mixing resulting in transport of relatively hotter air from the heated walls. The corresponding dimpled channel featured cylindrical dimples arranged in a form of corresponding rib shape. The heat transfer enhancement in dimpled channels occurs due to periodic shedding of secondary flows induced inside the dimples. The transport of these secondary flows to the upper endwall results in increased heat transfer. Dimples are associated with relatively lower pressure penalty and also lower levels of heat transfer enhancement compared to rib turbulators. The compound channel resulted from direct addition of rib alone and dimple alone configurations. Increased heat transfer was expected from the compound channels due to the interaction of rib induced secondary flows with periodically shed secondary flows from the cylindrical dimples. A complete study of above mentioned four configuration resulted in 12 test plates with one additional smooth two pass channel as a baseline case. A total of 56 heat transfer and pressure experiments were carried out in order to measure detailed heat transfer coefficients and static pressure streamwise variation for all configurations.

From Figure 0.1, it can be seen how the present study utilized the merits of two different heat transfer enhancement concepts, ribs and dimples, to achieve higher overall heat transfer enhancement. The dissertation provides the thermal hydraulic performances of ribs, simples and the compound channels and it is concluded that the combination has higher thermal hydraulic performance compared to rib-alone and dimple-alone concepts. The direction of heat transfer enhancement levels with respect to friction factor enhancement observed in the present study agrees with the research thrust direction.

As mentioned earlier, the mid-chord region of the turbine airfoil can also be equipped with array of impinging jets. Jet impingement is typically used in applications which require high rates of heat removal. One demerit associated with this impingement is the effect of crossflow on the impingement effectiveness. Hence, it is imperative to design jet impingement hole shapes which have high impingement heat transfer and an arrangement of jets which have minimal effects of crossflow on the degradation of jet impingement effectiveness. The study on jet impingement hole shape was limited due to limitations from the manufacturing side. The traditional cast method was not deemed effective in fabrication of complex impingement hole shapes at the length scales required in turbine blades.

The present study investigates the application of jet impingement in the mid chord region of gas turbine airfoils. Jet impingement is a well-established cooling concept for applications demanding fast heat removal rates. In the past, several researchers have investigated different facets of this concept and detailed correlations of heat transfer by impinging jets are available in the currently available literature. However, due to manufacturing limitations, only circular, racetrack, square and rectangular hole shapes were studied in the past. An attempt has been made in order to develop novel jet impingement hole shapes by modifying the circular holes by keeping the physical area same. A new hole shape in the form of "V" has been studied along with circular and racetrack shapes. Due to the design constraint of same physical area of jet holes, the hydraulic diameters of different hole shapes were different. Detailed Nusselt numbers were measured experimentally using transient liquid crystal thermography for Reynolds number ranging from 2500 to 10000. The normalized spanwise and streamwise pitch was 6 (based on hydraulic diameter of circular holes) and the normalized jet to target plate spacing was kept at 4. It has been found that V shaped holes had highest heat transfer followed by circular and

racetrack hole shapes. The discharge coefficient of shaped holes was lower than the circular holes. This study gives promising results and motivation for further pursuance of new hole shapes.

In the mid-chord section of turbine blade, double-wall cooling concepts are also used to cool the internal walls. Typically, an array of impinging jets is used for such application. Array of impinging jets lead to different types of crossflow scheme, and each crossflow scheme has different effects on local and global heat transfer levels. Present study also investigates all the crossflow schemes in an impingement alone and in an impingement-effusion system. Different spent air removal schemes have been experimentally tested in order to evaluate the globally averaged heat transfer enhancement levels with respect to pumping power requirements. Two types of target plates – (1) without effusion holes, (2) with effusion holes have been tested for jet Reynolds numbers ranging from 3500 to 10000. It has been found that the minimum crossflow scheme with and without effusion holes was the most efficient configuration and the maximum crossflow scheme with target surface without the effusion holes was the least efficient configuration for the range of Reynolds numbers studied.

The other aspect of turbine internal cooling study is to characterize the heat transfer under rotating conditions. Combined effects of Coriolis force and centrifugal buoyancy forces lead to increase in heat transfer on the trailing side of the radially outward passage and reduction in heat transfer levels on the leading side of the radially outward passage. Reverse trends in heat transfer enhancements on the leading and trailing walls was observed in the second pass, where the coolant flows radially inwards. The direction of Coriolis force depends on the relative angle between the coolant flow and the rotation vector. The heat transfer enhancement levels (Nu/Nu_0) of typical angled rib turbulators can be enhanced to as high as 4 to 5 and can be degraded to as low as 1. This leads to non-uniform cooling and potentially results in local hot spots, resulting in increase in thermal stresses and eventually leading to blade failure. Hence it is imperative to carry out detailed measurements of (Nu/Nu_0) under rotating conditions. Rotation studies are also combined with the model orientation effects since internal cooling passages are arranged according to blade external profile. It has been found that a 45° inclined channel with the axis of rotation has reduced effects of Coriolis force and Buoyancy forces, thus reducing the difference between the heat transfer enhancement levels on pressure and suction side internal

wall heat transfer. These factors need to be taken into account to develop a high performance ribbed configuration which works under rotating conditions as well.

First part of the rotation studies carried out in the present study was to investigate detailed heat transfer coefficients for a two-pass rib roughened duct (AR 1:2). Stationary experiments were carried out for Reynolds numbers ranging from 25000 to 75000. Rotation experiments were carried out for the lowest Reynolds number of 25000 and at Rotation numbers of 0.036 and 0.063. It was found that rotation had significant effects on the leading and trailing walls. AR 1:2 was investigated since this aspect ratio is suited for the mid-chord section of as turbine blade.

The second study which was carried out was focused on using the rotation in favor of heat transfer enhancement on both leading and trailing walls of 1^{st} and 2^{nd} pass. The coolant flow orientation in the 2^{nd} pass was adjusted such that the leading side facing the direct heat load had higher heat transfer enhancement due to Coriolis force acting in a favorable direction. The two pass channel featured V-shape rib turbulators and a total of five configurations were studied for a Reynolds number of 25000 and Rotation numbers of 0, 0.05 and 0.1. The new proposed design of two-pass rib roughened duct was compared against the traditional two-pass channel, and it was experimentally found that the globally averaged Nusselt number for the new design was 11% higher than the conventional design of two-pass channel at 8% reduction in the pumping power requirements.

Overall, the present study has been focused on investigating new concepts for internal cooling passages of gas turbine blades. Efforts have been made towards using rotation in favor of heat transfer enhancement with an aim to achieve increased as well as uniform cooling on the pressure and suction side internal walls at lower pumping power requirements.

REFERENCE

[0.1] Singh, P. and Ekkad, S., 2017. Experimental study of heat transfer augmentation in a two-pass channel featuring V-shaped ribs and cylindrical dimples. Applied Thermal Engineering, 116, pp.205-216.

[0.2] Han, J.C., Dutta, S. and Ekkad, S., 2012. Gas turbine heat transfer and cooling technology. CRC Press.

CHAPTER 1

Experimental and Numerical Study of Heat Transfer due to Developing Flow in a Two-pass Rib Roughened Square Duct

Prashant Singh, Bharath Viswanath Ravi, Srinath V. Ekkad
Advanced Propulsion and Power Laboratory, Virginia Tech
Blacksburg, VA, USA, 24061

International Journal of Heat and Mass Transfer, pp. 1245-1256

ABSTRACT

Experimental and numerical study of flow and heat transfer in a two-pass channel featuring different rib geometries has been carried out. The thermal hydraulic performance of four different rib geometries- 45° angled, V, W and M-shaped ribs, have been reported and analyzed. The tests were performed over a Reynolds number range from 19500 to 69000. The channel aspect ratio was 1:1 (square), the rib-pitch-to-rib-height ratio (p/e) was 16 and the rib-height-to-channel hydraulic diameter ratio (e/D_h) was 0.125. The detailed Nusselt number distributions on the ribbed wall were obtained using transient liquid crystal thermography. Numerical simulations (using ANSYS Fluent) have been carried out to resolve the complex flow field peculiar to rib turbulator shapes, for detailed understanding of the experimentally measured heat transfer coefficients. For the numerical simulations, realizable version of k-ε model was chosen because of its ability to predict separated flows behind ribs. Also, CFD simulations have been validated with experimentally obtained pressure measurements at several locations in the two pass channel. In addition to flow validation, the numerically obtained heat transfer results are validated and compared with the experiments and discussion has been presented on the role of secondary flows, turbulent kinetic energy etc., on heat transfer augmentation due to the presence of the ribs.

Keywords: Thermal Hydraulic Performance; Liquid crystal thermography; secondary flows; turbulent kinetic energy.

Introduction

Increasing need for improved performance and efficiency is pushing turbine inlet temperatures to higher levels. Turbine blades in rotation are subjected to high thermal stresses and thus innovative blade internal cooling concepts need to be developed. Internal cooling passages

(connected via 180° bends) feature different types of turbulence promoters, which induce secondary flows which increase near-wall turbulence resulting in enhanced heat transfer. The ribs maximize the heat transfer by breaking down the laminar sub-layer thereby minimizing the thermal resistance between the coolant and surface. However, enhancement in heat transfer comes at a cost of increased supply pressure requirement, thus imposing higher load on the compressor of actual gas turbine engine. Hence there exists a need to identify turbulence promoters which have high thermal hydraulic performance. Therefore it is important to accurately predict the heat transfer and friction characteristics so as to assess the performance of the roughening features.

Heat transfer characteristics of rib turbulators have been studied in detail in the past. Several parameters affecting the heat transfer, such as, rib-pitch-to-rib-height ratio, channel aspect ratio, blockage ratio, rib shape, etc. have been studied [1.1-1.7]. Detailed heat transfer coefficients were also presented which helped understanding the role of secondary flow and bend in heat transfer augmentation [1.8-1.14]. Several numerical studies have been carried out in the past to study three-dimensional fluid flow behavior and its effect on heat transfer [1.15-1.22].

Earlier studies carried out on rib turbulators focused mainly on different rib shapes in a single pass channel. The present paper reports detailed heat transfer measurements in a two-pass channel (aspect ratio of unity) and numerical simulation results for four different rib configurations, viz. 45˚ angled, V, W and M-shaped for Reynolds numbers ranging from 19500 to 69000. To the best of authors' knowledge, there hasn't been such detailed experimental and numerical study on above mentioned configurations in a two-pass channel. The rib-pitch-to-rib-height ratio (p/e) in the present study was chosen to be 16. The high Reynolds number is typical of land based gas turbines. Smaller p/e values at higher Reynolds numbers lead to high pressure penalty. The current configurations and experimental conditions caters to the land-based gas turbines, hence higher value of p/e was chosen and a wide range of Reynolds numbers were investigated. The 45˚ angled rib configuration in the present study has also been studied by [1.4] for Reynolds number of 30000 and the present study extends this to much higher Reynolds number. Tanda [1.12] investigated the effects of p/e on heat transfer enhancement for single pass channel (single ribbed-wall) and reported an optimal value of p/e = 13.33. The particular W rib arrangement in the present study has not been investigated for a two-pass channel in the existing literature. The M rib in the present study has been studied by Lamont et al. [1.29] (where the

authors referred this configuration as "W"), at a Reynolds number of 16000 and for a low p/e value of 8 (ribs on top and bottom wall). Further, detailed numerical investigation of fluid flow and heat transfer carried out in the current study provides valuable insight into the development of novel rib turbulator shapes and geometrically optimized two-pass channels.

Experimental Setup

The schematic of the experimental setup is shown in Fig. 1.1. Working fluid in the experiments was air, discharged from the compressor at around 300 K and 1-2.7 atm. The pressure downstream of the tank discharge was controlled by a pressure regulator depending upon the flow rate requirements of the tests. The fine tuning of the air flow rate is carried out by an inline globe valve. An orifice meter was located (~ 35 times the pipe diameter) downstream of the flow control valve, where the differential pressure (Dwyer 477-4-FM; 0 to 10 psi range) across the orifice was metered to calculate the mass flow rate. Also, the temperature (T-type thermocouple) of the air and the high pressure (Dwyer DPG – 103, range 0 to 30 psi) was metered at the orifice, to account for the variations in density during different runs. Downstream of the orifice plate, one additional pressure regulator was installed for further fine tuning of the airflow rate. A couple of solenoid valves were located downstream of the pressure regulator. These solenoid valves worked in pair and acted as a 3-way valve based on the binary command signal from LabVIEW. Downstream of the Solenoid valve #1, a fitting was provided for liquid Nitrogen (LN_2) intake. Mixture of air and Nitrogen was used to chill the path between the solenoid valve (#1) and vent valve (V1). Once the thermal reservoir is suitably cooled, the nitrogen supply was cut off and all the remaining nitrogen in the line was vented into the ambient through V1.

Further, the solenoid valve direction was switched towards the atmosphere and the combination of ball valve (B1) and gate valve (V1) was used to open the line towards test section. The flow rate was set to the desired value and the test commenced once the solenoid valves were flipped towards the test section.

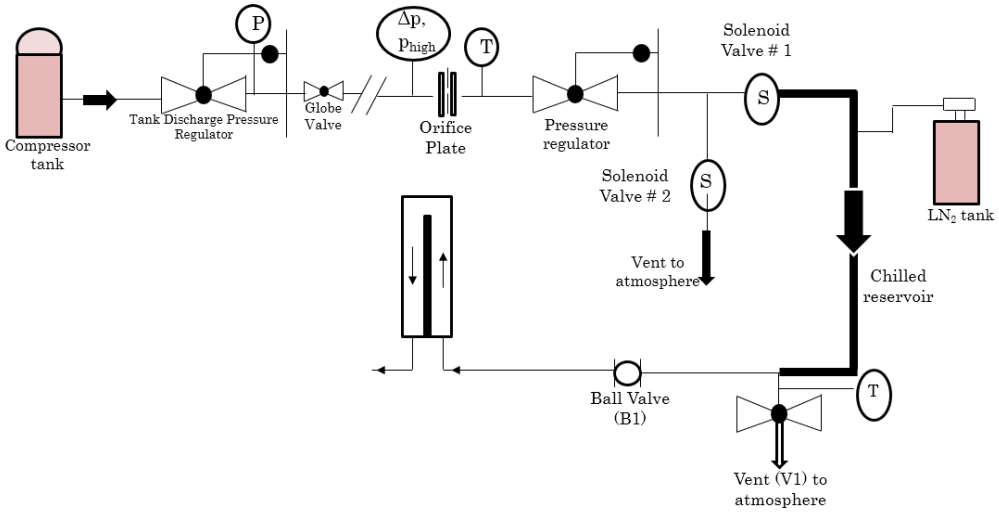

Figure 1.1 Schematic of experimental setup

Description of Test Configurations

Both the first pass and second pass have five ribs each, and the 180˚ bend featured a 90° rib (Fig. 1.2). The channel aspect ratio was 1:1, with ribs attached only to the bottom wall. The rib-pitch-to-rib height ratio (p/e) was 16 and the rib-height-to-channel hydraulic diameter ratio (e/D_h) was kept at 0.125. V-shaped ribs have been studied by many investigators and have been summarized in [1]. This particular configuration (V) has been chosen so as to have a reference with already established heat transfer and friction characteristics in the existing literature.

Computational Methodology, Grid Independence Study and Flow Data Validation

The turbulent flow field in the two–pass ribbed channel was modeled using realizable version of k-ε model with enhanced wall treatment. The computations were carried out using a commercial CFD software package, Fluent which is a finite-volume based solver and the fluid domain was meshed using ANSYS CFX meshing software. The realizable version of the k- ε model was chosen for computations since it has been known to perform well for rib induced secondary flows. In addition, Siddique et al. [1.18] have shown good agreement with experimental results for ribbed two-pass channels using the realizable version of the k- ε model. Shevchuk et al. [1.19] observed that the k-ε model was able to capture the predominant flow physics accurately in the 180° bend region. This is critical for a two-pass channel wherein the

bend strongly influences the heat transfer and flow characteristics in the 2nd pass. Second order discretization scheme has been used for the governing equations.

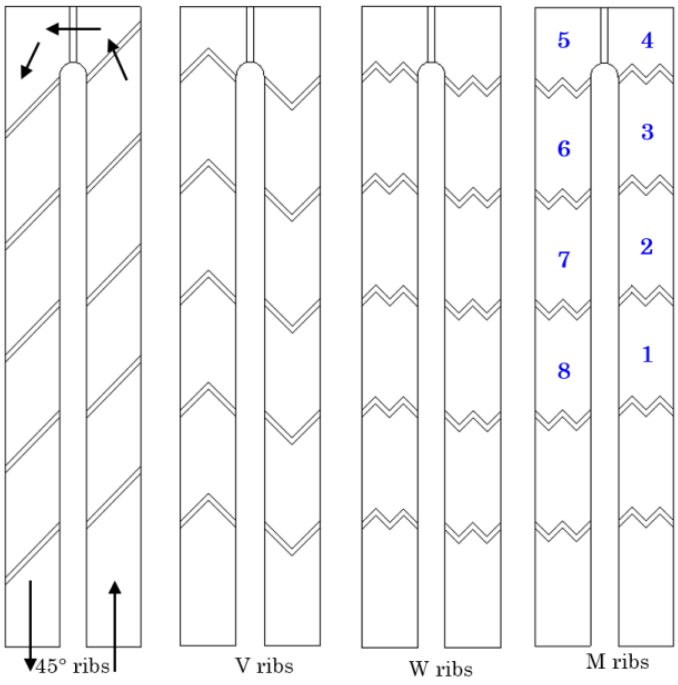

Figure 1.2 Four rib configurations studied (45°, V, W, and M), also indicated are the region #s in M rib (smooth channel was the baseline case, which is not shown here)

Figure 1.3 shows the computational grid which was used for the study. Meshing in the near wall region is critical so as to ensure that the chosen turbulence model is able to accurately capture the flow physics hence correctly predicting heat transfer. For all the cases, it was ensured that the wall y+ values were in the range of 1-3 which is one of the requirements for proper implementation of realizable k-ε turbulence model with enhanced wall treatment.

The numerically obtained normalized static pressures have been compared with those obtained experimentally (Fig. 1.4(a)), to validate the flow predictions through CFD. For grid independence study, three different grid sizes were considered- 5 million, 7.5 million and 11.5 million elements. The grid independence study was carried out for only one configuration (45° ribs) at the maximum Reynolds number. Figure 1.4(b) shows the comparison of average normalized Nusselt number (Nu/Nu_s) for the different mesh sizes considered (45° ribs). A difference of less than 2% was observed in the average normalized Nusselt number between the

finest and coarsest mesh. To maintain a balance between computational economy and accuracy, a grid system with 7.5 million elements was chosen for all the computations.

Boundary Conditions

A uniform velocity (calculated based on experimental Reynolds number) and uniform bulk fluid temperature was specified at the inlet. The turbulence intensity of 5% was specified at the inlet. The pressure at the outlet was set to zero (gauge). A constant and uniform heat flux of 5000 W/m^2 was specified on the bottom wall and the ribs for all the cases. The other walls were specified to be adiabatic. No slip boundary condition was imposed on all the walls. The working fluid (air) was modelled as an incompressible fluid and the flow was considered to be steady, three-dimensional and non-rotating.

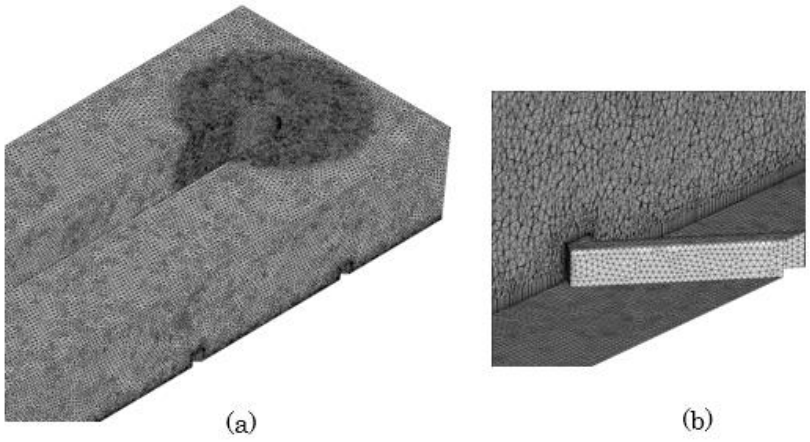

Figure 1.3 (a) Overview of mesh, (b) zoomed-in view of the cut section near ribs

Heat Transfer Coefficient Measurement Theory and Procedure

Heat transfer coefficient on the ribbed wall was calculated using the transient liquid crystal technique with 1-D semi-infinite conduction model assumption. The solution of this model after incorporating Duhamel's superposition principle is given by Eq. 1.1 [1.30].

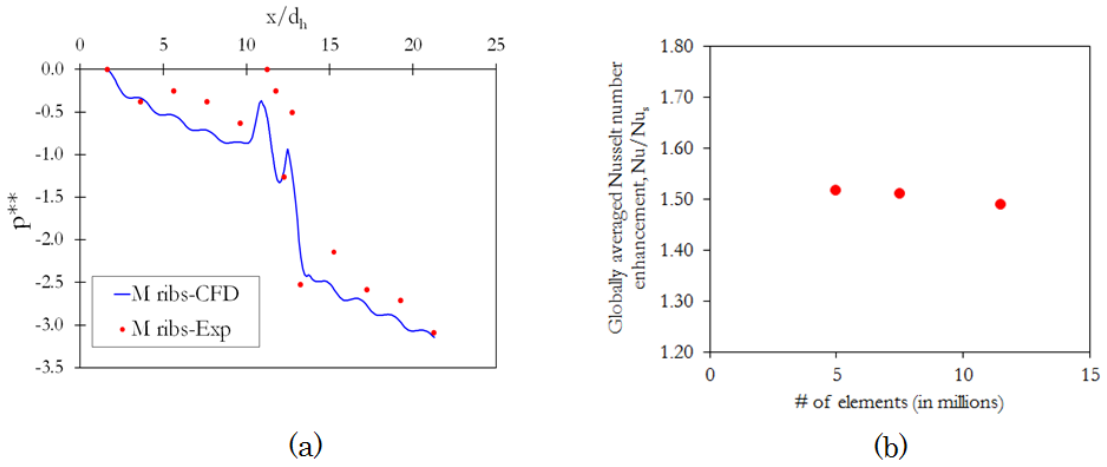

Figure 1.4 (a) Comparison of numerically predicted normalized static pressure with experiments, (b) summary of grid independence study (for 45˚ ribs)

$$T_w = T_i + \sum (T_{m,i} - T_{m,i-1}) \times \left[1 - \exp\left(\frac{h^2(t-t_i)}{\rho c k}\right) erfc\left(h\sqrt{\frac{(t-t_i)}{\rho c k}}\right)\right] \quad (Eq.\,1.1)$$

The mainstream temperature (after the step change) keeps dropping as the test proceeds (Fig. 1.5), hence Duhamel's superposition principle has been incorporated in the solution of 1-D semi-infinite solid conduction equation. The time varying mainstream temperature is divided into small time steps during which that particular mainstream temperature could be assumed to be constant. Duhamel's superposition was used where mainstream temperature was resolved at 200 Hz which was quite higher than the expected frequency of the change in mainstream temperature.

The mainstream temperature was measured by fast response T-type thermocouples (bead diameter: 0.0762 mm) and the data acquisition was carried out using LabVIEW interface which linked the computer to a National Instrument chassis (cDAQ9174) housing thermocouple module (NI9214). Two more T-type thermocouples were taped onto ribbed wall for in-situ calibration of wall temperature with color change in the nearby region of 5 x 5 pixel. In this region, the RGB data obtained from the video recording was converted into the corresponding HSV data. The Hue was averaged over the entire calibration region (25 pixels) and this value was considered to be representative of Hue near the wall temperature measurement.

$$t_{max} = 0.1\frac{\rho c t_{target}{}^2}{k} \quad (Eq.\,1.2)$$

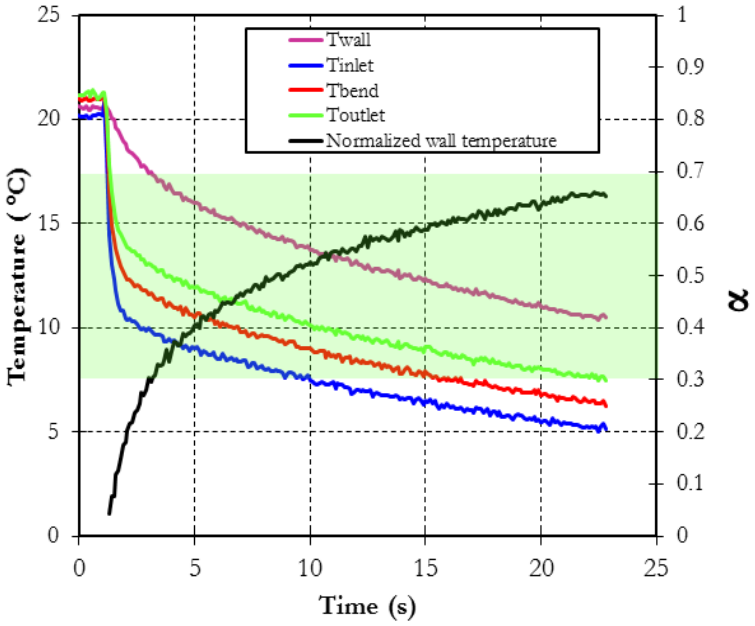

Figure 1.5 History of mainstream temperatures measured at inlet, bend and outlet of two-pass channel, normalized wall temperature (α) measured at the inlet plotted with time, green region indicating 0.3 <α< 0.7.

A sample Hue versus temperature plot for the calibration region is shown in Fig. 1.6(a). The hue based wall temperature calculation has been proven to be robust and less sensitive to illumination angles, lighting intensity etc. Also, the maximum permissible time for the transient liquid crystal experiment without violating the 1-D semi-infinite conduction model assumption was found from Eq. (1.2). The typical run time of experiments was well under t_{max}.

For the video recording of the color change of the target surface, a GoPro Hero 3 camera was used which captured the color change at ~30 frames per second. LCR Hallcrest liquid crystals with color play in the range 10°C to15°C was used for the transient heat transfer tests. The room temperature (T_i) was above the color play band of the liquid crystal used in these experiments. The video processing was carried out using an in-house MATLAB code. The R, G and B information for each pixel at each frame was obtained, which was then converted into the corresponding Hue, Saturation and Value (H, S and V). A time-matrix was built by calculating the time taken for each pixel to reach a particular hue corresponding to the temperature being tracked. The minimum threshold on saturation and value was set at 0.25 to ensure that each pixel

had decent color change. Figure 1.6(b) shows the HSV variation with time and it can be seen that saturation and value were always higher than the threshold value from the start of the experiment.

The heat transfer coefficient was then calculated from Eq. (1.1) using an error minimization routine based on the secant method. The Nusselt number (based on channel hydraulic diameter) was calculated using Eq. 3.

$$Nu_d = \frac{hd_h}{k_f} \quad (Eq.\,1.3)$$

where, k_f is the thermal conductivity of air at the film temperature.

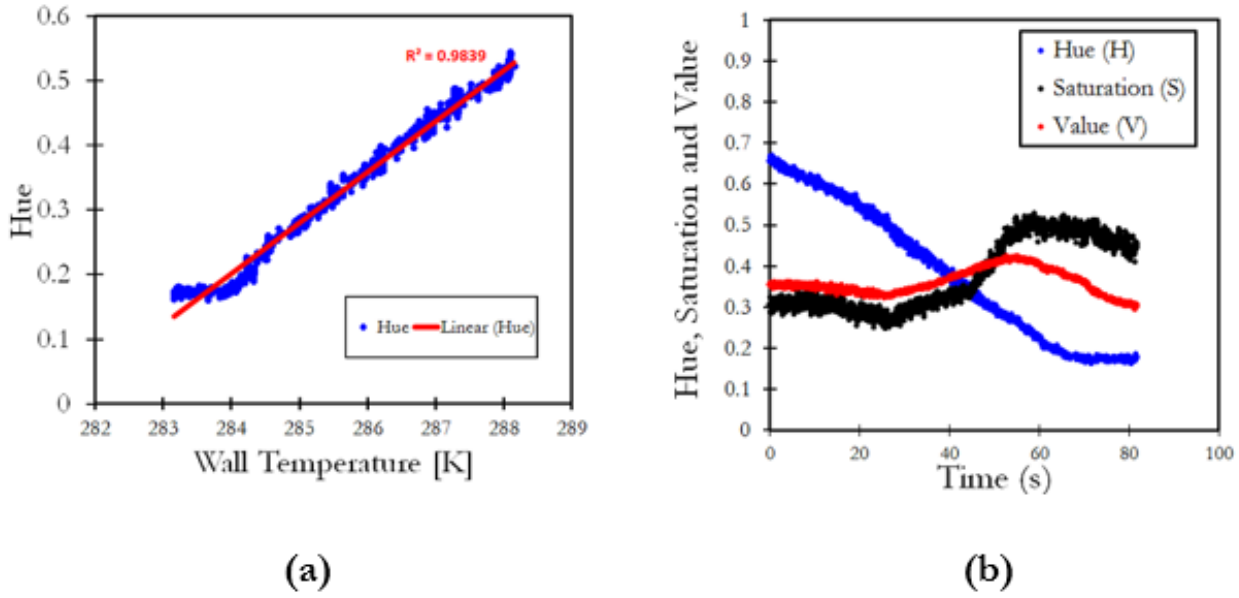

Figure 1.6 (a) Typical Hue versus Wall Temperature relationship observed during experiments, (b) Hue (H), Saturation (S) and (V) time history

Uncertainty Analysis

The uncertainty in the measurement of Nusselt number and Reynolds number was calculated using the sequential perturbation method described by Moffat [1.24]. In the calculation of Nusselt number, the measurements contributing to the overall uncertainty are T_w, T_i, T_m, t and $\sqrt{\rho ck}$. The contribution of T_w, T_i, T_m was taken to be 0.5°C and the contribution of t was taken to be 0.033 seconds. The contribution of $\sqrt{\rho ck}$ was taken to be 5% of the calculated value. For a

typical Nusselt number of 236, the uncertainty was found to be 13.74%. Figure 5 shows the normalized wall temperature (α) variation with time. Yan and Owen [1.25] carried out detailed uncertainty analysis for transient experiments using liquid crystal technique. They concluded that the uncertainty levels depend on the normalized wall temperature variation and concluded that low levels of uncertainties can be achieved just by judicious selection of wall-calibration temperature and mainstream temperature such that α lies between 0.3 and 0.7 during most the test duration. The normalized wall temperature shown in Fig. 1.5 is calculated by taking the surface temperature (T_w) measurement at the rib pitch upstream of region 1 and the mainstream temperature (T_{ref}) measured at the inlet of the test section. It can be seen that for significant duration of testing time, α lies in the green region ($0.3 < \alpha < 0.7$). Higher levels of uncertainties can be expected for the regions which reach the calibration temperature (T_{tlc}) in a very short time or simply the regions with high heat transfer coefficient values. Such regions are typically the edges of the ribs, which constitutes a very small fraction of the total region of interest. Hence, the effects of higher uncertainty levels at the edges of the ribs will have negligible effect on the region-wise averaged Nusselt number values. The uncertainty in the calculation of Reynolds number (based on channel hydraulic diameter) of 35500 was found to be 4.34%.

Validation of Numerical Prediction of Heat Transfer Coefficient with Experiments

Figure 1.7(a) shows the development of flow in the first pass for smooth channel. At this point, it is important to discuss the difference between the Nusselt number predicted by the numerical simulations and those measured experimentally in the 1st pass. A uniform velocity profile was specified at the inlet for the numerical simulations. However, the experimental test section (as shown in Fig. 1.1) was oriented at an angle of 90° to the inlet flow followed by a short entrance length ($4d_h$). Hence, this difference in the inlet velocity profile results in deviation in the downstream heat transfer in the 1st pass. The flow gets developed at around ten hydraulic diameters (equivalent to $x/d_h=6$ in Fig. 1.7(a)) for both experiment and CFD but due to the difference in the inlet velocity condition in experiments and numerical simulations, the rate of the decay of normalized Nusselt number is higher for experiments. This is the reason why the comparison of heat transfer enhancement between experiments and CFD have been made in reference to the smooth plate data and not the Dittus-Boelter correlation (for developed turbulent flow in smooth circular ducts).

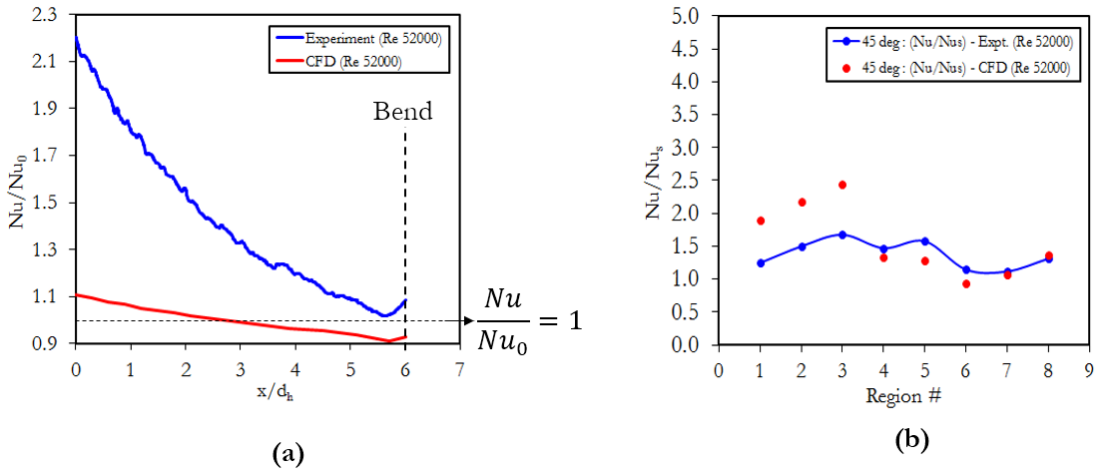

Figure 1.7 (a) Smooth plate spanwise averaged Normalized Nusselt number (Nu/Nu_0) variation in first pass, $x/d_h = 0$ corresponds to start of Region 1 and $x/d_h = 6$ corresponds to end of region 3; (b) region-wise averaged normalized Nusselt number (Nu/Nu_s) for 45˚ angled rib for Reynolds number of 52000

Figure 7(b) presents the area averaged normalized Nusselt number (Nu/Nu_s) for 45˚ angled ribs for both experiments and CFD (for Reynolds number of 52000). Equation 1.4 presents a comparison between Nusselt number measured experimentally and predicted numerically. It can be concluded that enhancement in heat transfer caused by rib turbulators when normalized with smooth plate heat transfer data, will lead to higher values of enhancement in case of CFD in the first pass in comparison to experiments (Fig. 7(b)).

$$\text{From Fig. 7(a)}, \frac{Nu_{s_{CFD}}}{Nu_0} < \frac{Nu_{s_{EXPT.}}}{Nu_0} \equiv \frac{1}{Nu_{s_{CFD}}} > \frac{1}{Nu_{s_{EXPT.}}} \qquad (Eq.\,1.4)$$

The agreement between experimentally measured area averaged Nusselt number in bend region and 2nd pass was within the uncertainties of experiments. However, reasons for slight departure between experiment and CFD are discussed in subsequent sub-sections.

Results and Discussions

The detailed Nusselt number contours for Re = 35500 are shown in Fig. 1.8. Nusselt number data has been presented only for the last three rib pitches in the first pass, the first three rib pitches in the second pass and the bend region. The smooth channel Nusselt number contour shows the development region in the first pass. The heat transfer near the right and left sidewalls

are lower because of the development of thermal boundary layer on those walls and the contour shows the top view of that thermal boundary layer in the form of lower heat transfer (here, right and left sidewalls are in reference to the direction of coolant flow). Also, the effect of the orientation of channel flow with the inlet flow, results in slightly skewed velocity profile near the inlet region, and this effect remain to about four times the hydraulic diameter of the channel. This effect can only be seen in the smooth channel Nusselt number contour where slightly higher heat transfer is observed along the left sidewall in the first pass. The inlet condition for the experiments was chosen to simulate an actual gas turbine blade featuring multi-pass channels, where the flow remains under-developed while it passes over the ribs. Very few studies have been carried out which reports the heat transfer enhancement of turbulence promotors with reference to a smooth channel. Most of the studies present heat transfer enhancement by normalizing the Nusselt number by the Dittus-Boelter correlation for developed turbulent flow in circular duct. The current paper presents the heat transfer enhancement from two points of views – (1) Nusselt number normalized with Dittus-Boelter correlation, (2) Nusselt number normalized with smooth channel heat transfer. These two different point of views lead to interesting observations, particularly in the bend region, where the major factor responsible for heat transfer enhancement is the 180° sharp turn. In a two pass channel, the bend region has the maximum contribution to the overall heat transfer coefficient and this contribution is subjective to the rib shape present in first and second pitch. This fact somewhat skews the performance of the ribs when only Nu/Nu_0 is compared, and hence it is suggested that heat transfer augmentation should be evaluated in reference to smooth plate as well.

For the smooth channel, the Nusselt number near the bend region (1^{st} pass) tends to the Nusselt number corresponding to the correlation of Dittus-Boelter. However, the normalized Nusselt number approaches a value slight greater than unity, just upstream of the bend region corresponding to first pass (Fig. 1.7). This is because of the precursor effects of bend on the upstream heat transfer in the first pass. The contour in the bend explains that the flow hits the endwall of the passage (corresponding to the first pass), resulting in increased heat transfer due to a sort of impingement effect. The turning flow closer to the divider wall, separates and results in lower heat transfer. However, the flow after 180° turn hits the right sidewall (2^{nd} pass) and travels along that, resulting in increased heat transfer. The purpose of presenting the Nu/Nu_0 contours predicted by CFD and measured experimentally, is to qualitatively comment on the

flow in the two pass channel. CFD predictions have very good qualitative match with experiments for the Nu/Nu_0 comparison. However, in later sub-sections, it is shown that when the Nu/Nu_s values are compared, there exists a very good quantitative match as well.

From the contour plots of ribbed configurations, the general trend which could be observed is that the heat transfer enhancement with respect to Dittus-Boelter decreases as the flow moves in the streamwise direction in the first pass. The bend, however, witnesses an increase in heat transfer due to the sharp turn and the presence of a 90° rib. The heat transfer enhancement in the bend region is subjected to the type of rib present upstream and downstream of the bend. The first pitch in the second pass, witnesses a lower enhancement with slight increment as the flow moves downstream of the second pass. The highest heat transfer region in the entire fluid domain is the bend region (region #s 4 and 5, in the line plots). The bend region has significant effect on the overall heat transfer enhancement values and thus it might skew the evaluation of any particular rib shape with respect to Dittus-Boelter correlation, as the rib shape has very nominal role in bend heat transfer. Specific heat transfer enhancement peculiar to particular rib configuration is elaborated in the subsequent subsections.

Figure 1.9 shows the streamtraces at a plane ($z/d_h = 0.04$, very close to the bottom wall where the heat transfer coefficient is calculated) parallel to the bulk flow direction. The stream traces are representative of the probable path taken by a massless particle if introduced in the flow (without any initial energy). The rib turbulators lead to heat transfer enhancement due to the formation of secondary flows induced from the interaction of bulk fluid with the ribs.

In the case of 45° rib, the secondary flow travels along the rib, as can be seen (from the Nu contour) on the ribs, the heat transfer decays as the secondary flow strength reduces along the rib. The stream traces also show the separation and re-attachment, which leads to low and high heat transfer, respectively. Nusselt number contours indicate that the strength of secondary flow diminishes as the bulk flow dominates towards the right endwall (1^{st} pass). Experimentally obtained Nusselt number contour indicates low heat transfer region near the right endwall (1^{st} pass), indicating minimal effect of secondary flow as thermal boundary layer is prevalent along the right endwall. This phenomena can also be explained via the stream trace contour plot where the particles seem to travel along the rib, then hit the right endwall and then travel along that.

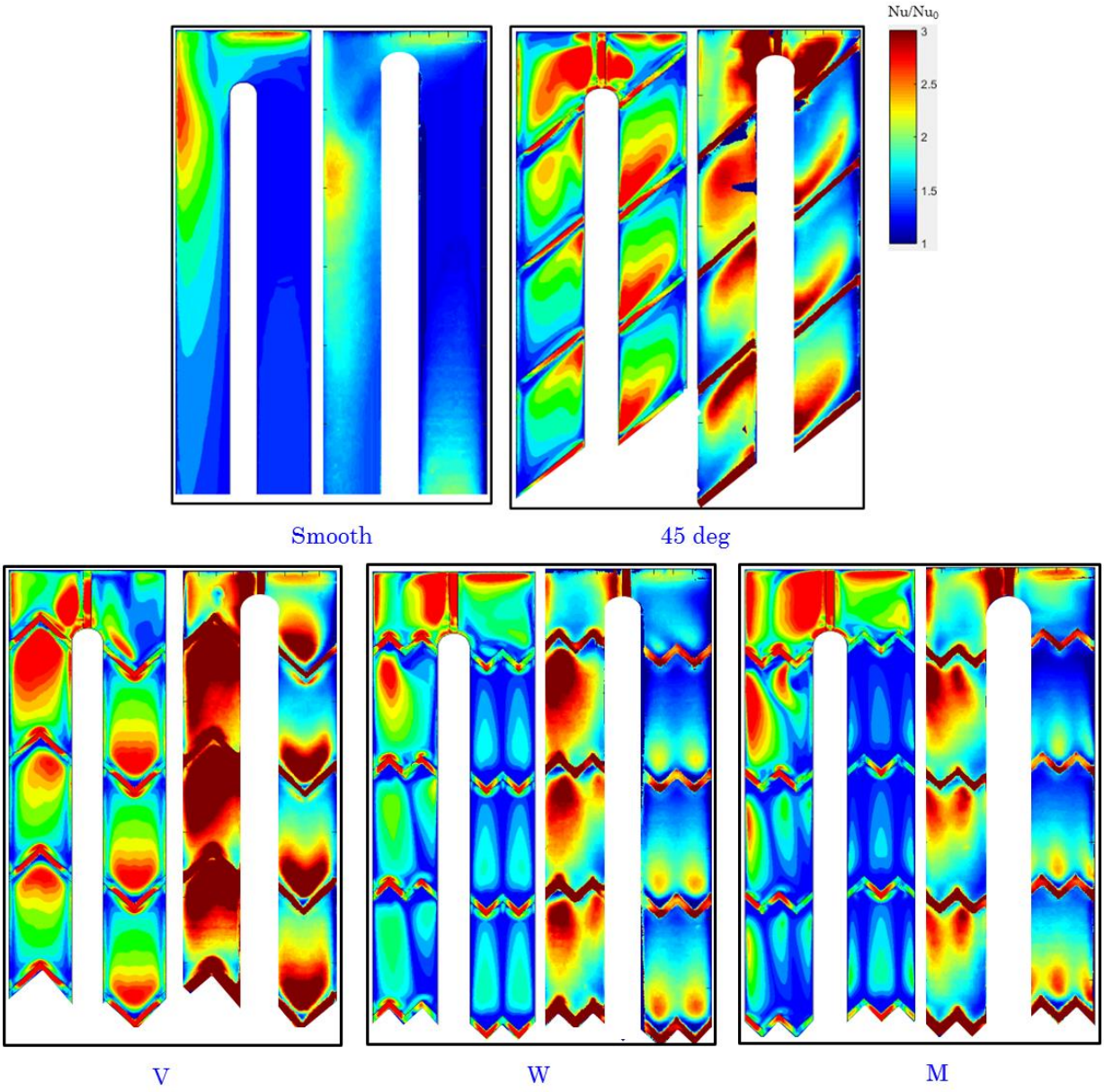

Figure 1.8 Normalized Nusselt number contour plots for four rib configurations, and the baseline smooth channel (Re 35500); left contour: CFD and right contour: experiments, direction of flow specified in Fig. 1.2

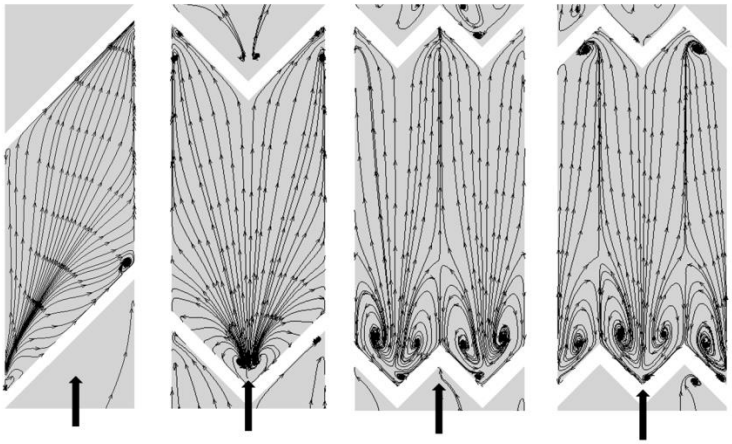

Figure 1.9 Streamtraces plotted at a plane located at $z/d_h = 0.04$ from the bottom wall (3rd rib pitch in 1st pass)

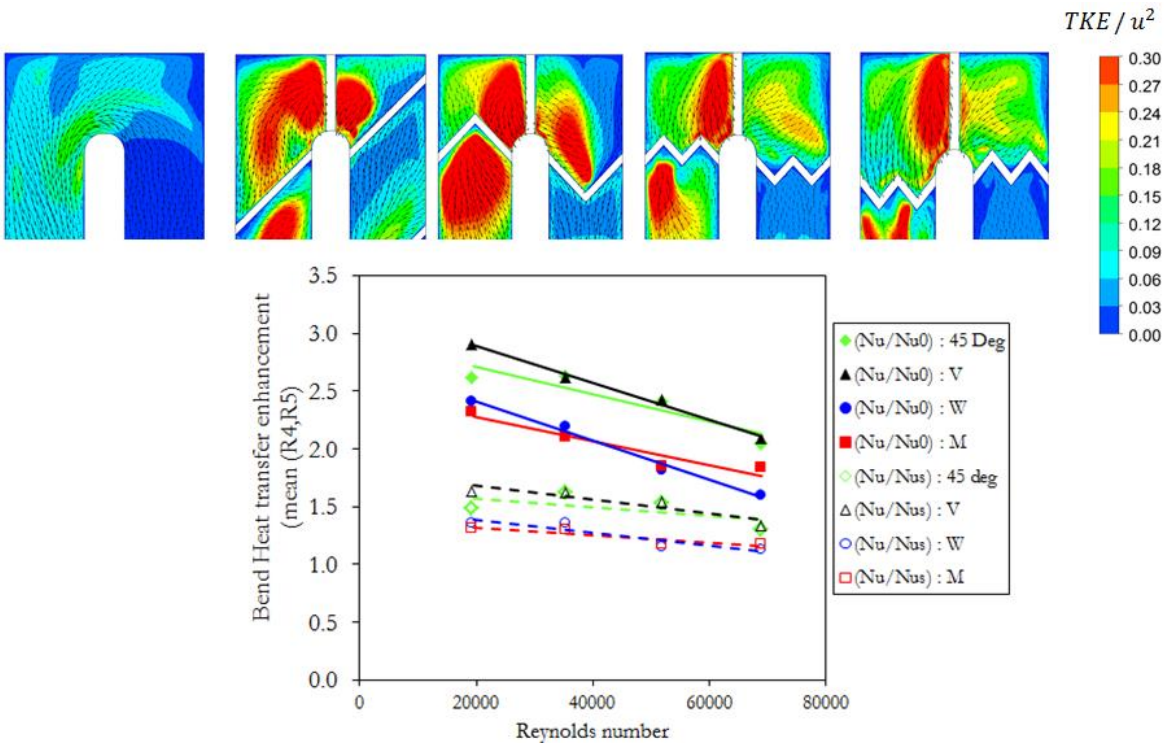

Figure 1.10 Velocity vectors superimposed by normalized turbulent kinetic energy at a plane located at z/dh = 0.04 above the bottom wall, and normalized heat transfer enhancement in the bend region (mean of region # 4 and 5)

Similarly the heat transfer due to V-shaped ribs can be explained by the stream traces which indicate that flow after separation due to rib, re-attaches immediately downstream of the

rib resulting in increased local heat transfer and the secondary flows travel towards the left and right endwall (1st pass), resulting in more uniform spread across the channel span. Also, the flow hits the downstream rib, resulting in regions of high heat transfer (shear along the rib, after being diverted). This feature is fairly well captured in numerical simulations.

In the case of W-shaped ribs, two pairs of counter rotating vortices (CRVPs) could be seen downstream of each rib. From the contour plots, it can be seen that the re-attachment length in numerical simulations is overpredicted when compared to experiments. This might also be possible due to slight skewness in the video capture due to camera angle with respect to the location of interest. These CRVPs after mutual interaction travels along with the bulk fluid causing increased shear along the bottom wall. Similar to W-shaped rib, one counter rotating vortex pair is observed downstream of the center corner, and two separate vortices along the endwall and the left and right corner of the M-shaped rib. In this case as well, the re-attachment length is overpredicted by CFD.

Bend Heat Transfer and Fluid Flow

Figure 1.10 presents the area averaged Nusselt numbers (mean of regions 4 & 5) normalized with Dittus-Boelter and corresponding smooth channel Nusselt number. The turbulent kinetic energy contour is one way of explaining localized high and low heat transfer regions. In the case of 45˚ and V ribs, the secondary flows are being guided by the bulk fluid turning by 180˚ resulting in higher heat transfer compared to W and M-shaped ribs, wherein the secondary flows are not affected by the turning phenomena occurring in the bend region. The turbulence model used in the current study is realizable k-ε, as a result of which, the turbulence features which are direct consequences of anisotropic phenomena occurring in the bend region, are not fairly well captured, e.g. the first pass endwall region, second pass right endwall region [1.24-1.26]. However, a qualitative agreement of turbulent kinetic energy with the heat transfer resulting from turbulent eddies can be established.

Bulk Fluid Distribution (1st pass, 3rd pitch)

Bulk temperature distribution along with stream traces plotted in a plane perpendicular to the direction of flow at a location just downstream end of the 3rd rib in the first pass has been presented in Fig. 1.11. The bulk temperature distribution is the result of the disturbances caused

in the flow due to the turbulence promotors. It can be seen that lower temperatures near the bottom wall for the cases of 45° angled ribs and V-shaped ribs explains the higher heat transfer associated with these rib shapes, in comparison with W and M shaped ribs. It should be noted that in the numerical simulations, the heat transfer boundary condition for the left, right and top endwall was adiabatic and a constant heat flux was imposed on the bottom wall.

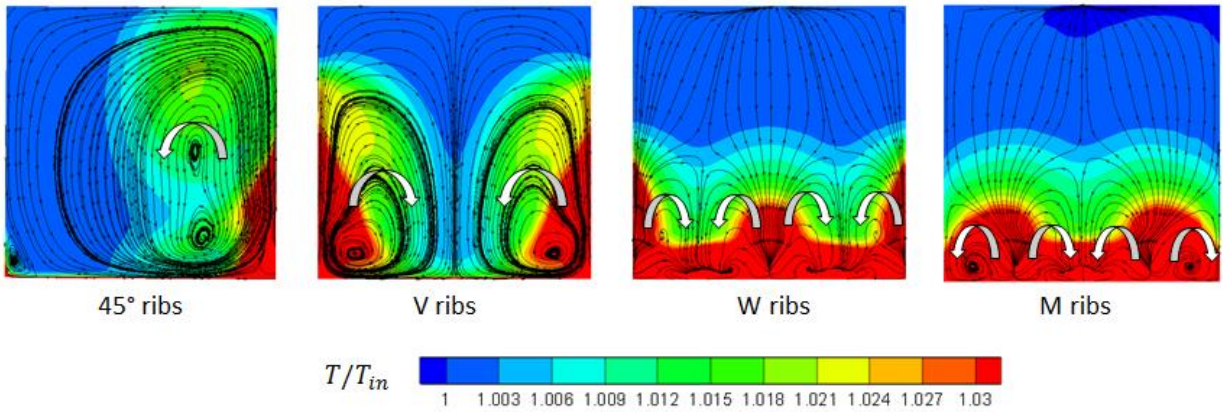

Figure 1.11 Streamtraces superimposed with normalized bulk fluid temperature at a plane just downstream of the 3rd rib in the first pass (shown plane is normal to the direction of bulk flow)

These contours of normalized flow temperatures are better representatives of the thermal boundary layer which develops on the side walls (and or bottom wall). Although, the region of interest for heat transfer calculations is the bottom wall, it is still important to look into the thermal boundary layer formation along the side walls adjacent to the bottom walls. Especially, for the cases of 45° and V shaped ribs, the thermal boundary layer on the sidewall and the bottom wall interact, which has direct effect on heat transfer on the bottom wall. The stream traces plotted in this plane and the resultant bulk fluid temperature distribution gives the gas turbine blade designers, an interesting view point of how to arrange the ribs on all four walls so as to obtain the best possible heat transfer scenario.

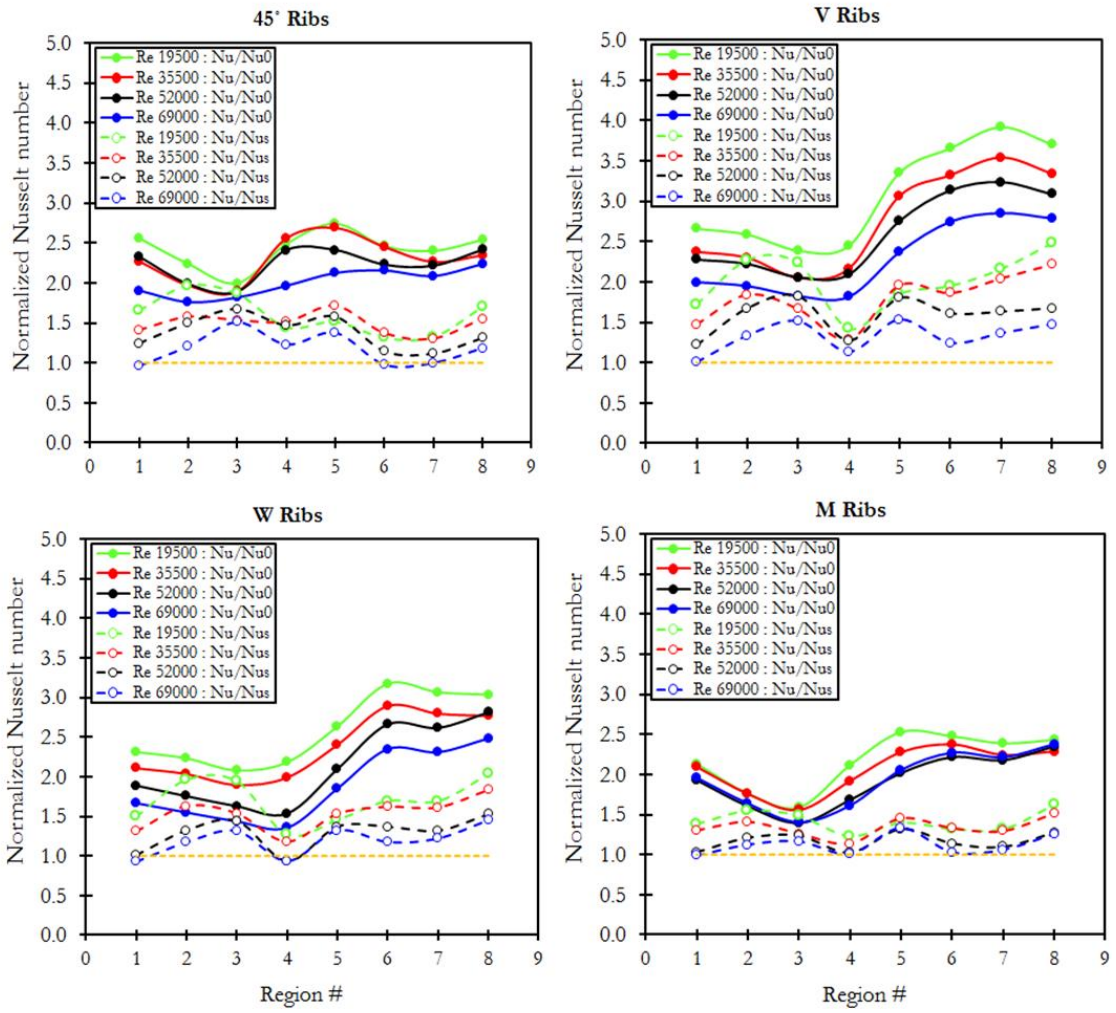

Figure 1.12 Area averaged Heat transfer enhancement, Nu/Nu_0 and Nu/Nu_s for four rib configurations

Area averaged Nusselt number

Figure 1.12 shows the region-wise averaged Nusselt numbers for the four rib configurations studied. The region #s are indicated in Fig. 1.2. It can be seen that the bend region has the highest contribution to the overall heat transfer. It is observed that the Nusselt numbers when normalized with smooth channel resulted in lower enhancements when compared to those normalized with Dittus-Boelter correlation (for fully developed turbulent flow in smooth circular tubes). The Nu/Nu_0 plots show a decreasing trend in the first pass as they are normalized with a constant number whereas Nu/Nu_s plots show an increasing trend in the first pass as they are

normalized with smooth channel heat transfer which gets developed along the streamwise direction- this is an expected trend. This way of representing enhancement in Nusselt number provides the reader, the individual contribution of rib and bend region in the globally averaged Nusselt number enhancement. The bend featured a 90˚ rib and it can be seen that the heat transfer enhancement with respect to smooth plate in the bend region varied between ~1.5 to 1.1. The Nu/Nu_s values for Regions 1 through 3 and 6 through 8 presents the contribution of rib alone on the heat transfer enhancement by separating the effects of inlet conditions and the after effects of turbulence/mixing caused by the 180˚ bend on 2nd pass heat transfer. One of the main focuses of the present study is to evaluate the heat transfer and friction characteristics in reference to smooth two pass channel. Hence, for the present test configurations, Nu/Nu_s provide a more realistic evaluation of heat transfer enhancement by a particular rib shape.

Globally averaged Nusselt number

Figure 1.13 shows the globally averaged Nusselt numbers, normalized with Dittus-Boelter correlation and with smooth channel. V-shaped ribs have shown maximum heat transfer enhancement followed by 45° ribs. W and M-shaped ribs have shown lower heat transfer enhancements in comparison to V and 45° ribs. Both Nu/Nu_0 and Nu/Nu_s ratios have been observed to decrease with increasing Reynolds number, which is consistent with many studies carried out on ribs in the past. The authors would like to point out an important observation at this point. Wright et al. [1.31] have reported heat transfer enhancements of W-shaped ribs at around 3.5 times the Dittus-Boelter correlation. However, this level of heat transfer enhancement has not been seen in the present study, where the globally averaged Nu/Nu_0 levels for W and M-shaped ribs have been found to be around 2.3 times the Dittus-Boelter correlation. One factor responsible for deviation from [1.31] is that the investigators in [1.31] used the area of smooth surface for the calculation of heat flux for ribbed cases. The area addition due to W ribs (25.7%) was neglected and hence resulted in over-calculation of heat transfer coefficient. The other reason of lower Nu/Nu_0 level is the high p/e value in the present study. The present study is consistent with Lamont et al. [1.32] who studied heat transfer in developing flow featuring W and M-shaped ribs, and the authors reported enhancement levels (Nu/Nu_s) to be around 1.2 times for both W and M-shaped ribs for a Reynolds number of 12000.

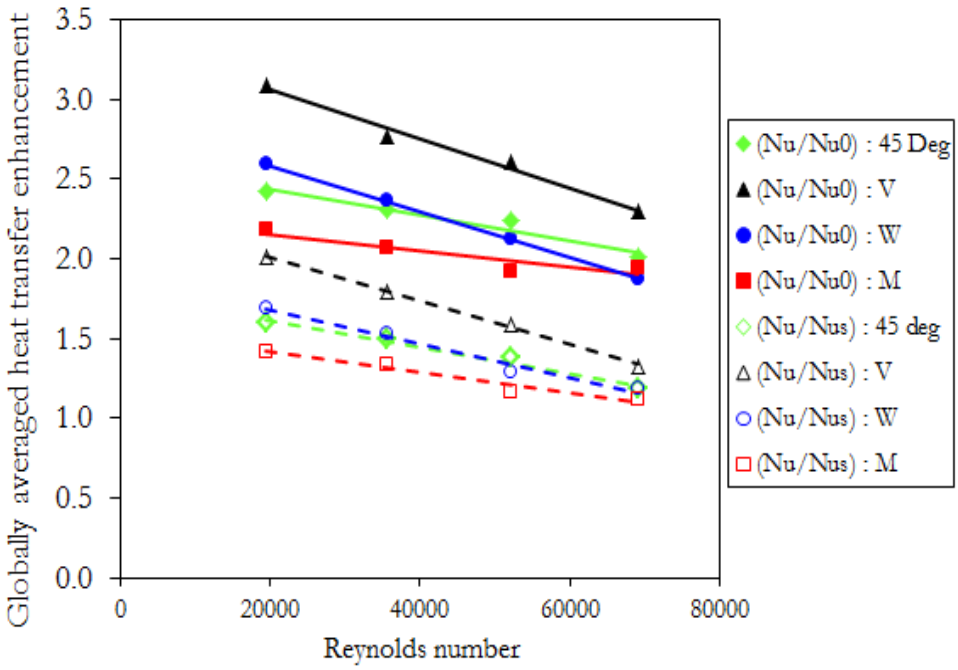

Figure 1.13 Globally averaged heat transfer enhancement, Nu/Nu_0 and Nu/Nu_s for four rib configurations

Comparison between Experimental Measurements and Numerical predictions of Globally Averaged Nusselt Number Enhancement (Nu/Nu_s)

Figure 1.14 shows the comparison between the globally averaged Nusselt numbers predicted by CFD and those calculated experimentally. A decent match is observed between experiments and numerical results. For about 75% of the experimental cases, the deviation in globally averaged normalized Nusselt number (Nu/Nu_s) was under 15%. One reason for this deviation is that the turbulence model used in the numerical simulations, only models the flow physics which is isotropic in nature and the configurations studied can lead to very complex flows, particularly in the bend region and initial portions of the second pass. Also, only Nu/Nu_s values have been compared between experiments and CFD for the reasons discussed in above sections. This close agreement between heat transfer enhancement predicted by the CFD and measured by experiments allows us to understand the fluid dynamics associated with rib features as predicted by the CFD. For more complete understanding of complex flows, several other turbulence models should be studied, such as k-ω (SST), $\overline{v^2} - f$ etc.

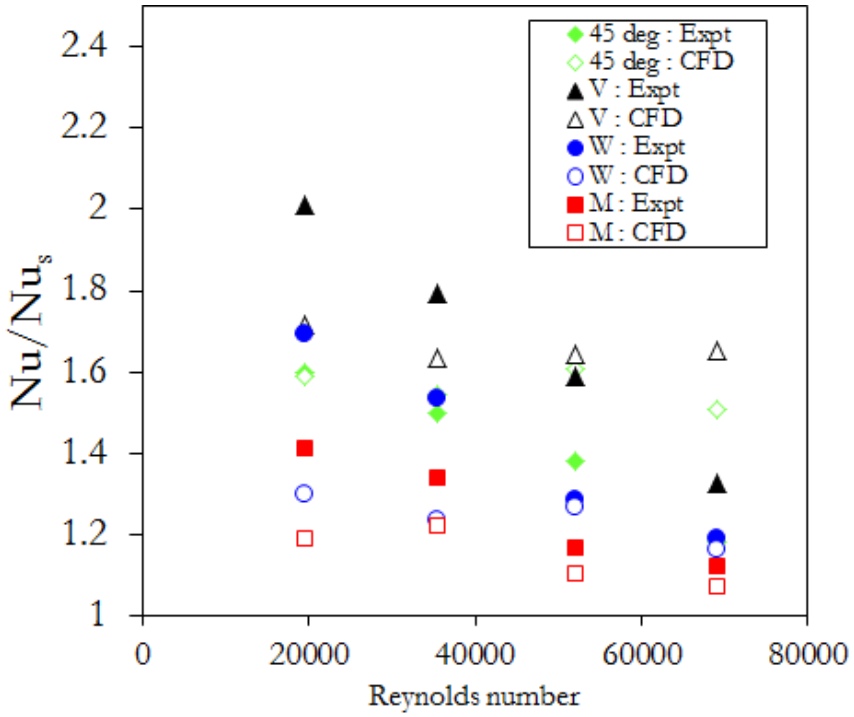

Figure 1.14 Globally averaged Nusselt number enhancement: Experiment versus CFD

Friction factor and Thermal Hydraulic Performance (THP)

The baseline friction factor is calculated using the correlation for the smooth tube as given by the Blasius equation.

$$f_0 = 0.079Re^{-0.25} \quad (Eq.1.5)$$

The friction factor for the two-pass channel is calculated by measuring the total pressure drop across the geometry and using Eq. 6.

$$f = \frac{\Delta p D_h}{2\rho u^2 L} \quad (Eq.1.6)$$

The normalized friction factor plots for four rib configurations have been presented in Fig. 1.15. As expected, the normalized friction factor increases with Reynolds number. V-shaped ribs have the highest frictional loss followed by W, M and 45° angled ribs. An asymptotic nature has been observed for all rib configurations for Reynolds number higher than 40000 for the f/f_s plots.

The thermal hydraulic performance of the two pass channels is shown in Fig. 1.16 and is given by the following equations:

$$THP_0 = (Nu/Nu_0)/(f/f_0)^{1/3} \qquad (Eq.1.7)$$

$$THP_s = (Nu/Nu_s)/(f/f_s)^{1/3} \qquad (Eq.1.8)$$

The $(THP)_0$ of V and 45° angled ribs are slightly higher than those of W and M-shaped ribs particularly at lower Reynolds number, while the difference in $(THP)_0$ between different rib configurations seem to diminish at high Reynolds number.

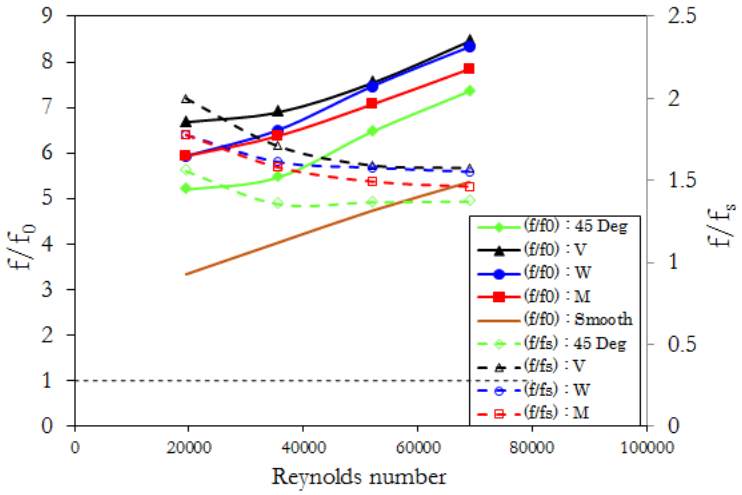

Figure 1.15 Normalized friction factor

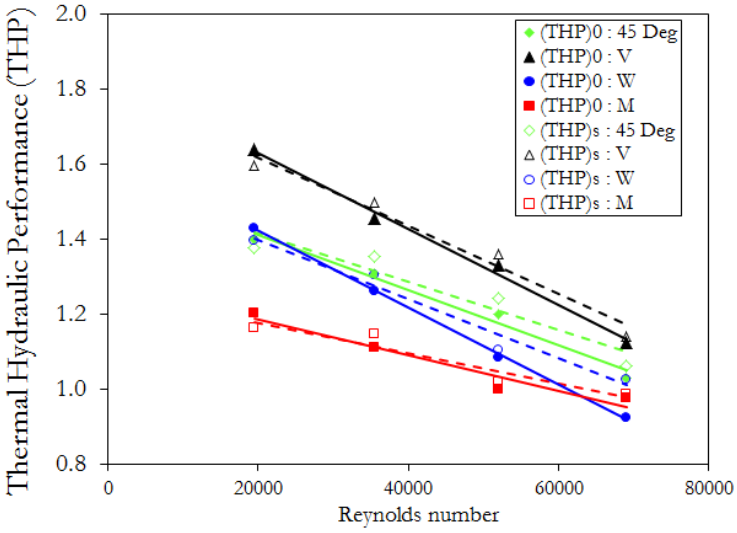

Figure 1.16 Thermal Hydraulic Performances

An overall decreasing trend in the thermal hydraulic performance is seen with increase in Reynolds number which is consistent with many earlier studies. Similar trends have been observed for the $(THP)_s$ plots, and the performance levels compared to THP_0 are very similar.

Conclusions

Present study reports heat transfer and frictional characteristics of rib turbulated two-pass channels, featuring 45° angled, V, W and M-shaped ribs. A large Reynolds number range from 19500 to 69000 was tested for each geometry. Experiments were carried out using transient Liquid crystal thermography to calculate detailed heat transfer coefficients at the bottom wall which featured different rib shapes. Numerical simulations were carried using ANSYS Fluent solver using realizable k-ε turbulence model. For the validation of numerically obtained results, experimentally measured static pressure in the channel is compared with those computed by numerical simulations. Further, important flow phenomena peculiar to a particular rib, occurring in the two-pass channel is studied using numerical results to explain heat transfer characteristics typical to a particular rib shape. Heat transfer and friction characteristics of the two pass channels is presented in two ways, (1) heat transfer normalized with Dittus-Boelter correlation for developed turbulent flow in smooth circular tube and friction factor with Blasius correlation (for friction factor in smooth tubes), (2) heat transfer normalized with smooth channel, friction factor normalized with smooth channel. In a typical gas turbine blade featuring multi-pass channels, the scope of fully developed flow is limited. From the understanding of present study, the authors recommend that heat transfer enhancements due to rib shapes should also be evaluated based on the normalized results with a geometrically similar smooth channel. The heat transfer enhancements and thermal hydraulic performance (Nu/Nu_0 and Nu/Nu_s, THP_0 and THP_s) have been presented for developing flow in ribbed two-pass channel for wide range of Reynolds numbers. It has been observed that V-shaped ribs and 45° angled ribs have slightly higher heat transfer enhancement and thermal hydraulic performance when compared to W and M-shaped ribs. Also, Nu/Nu_s levels for all rib configurations are lower than the corresponding Nu/Nu_0 values. However thermal hydraulic performance (THP_0 and THP_s) levels were similar to each other.

Overall, this is the first study to look at new rib shapes for a large Reynolds number range with comprehensive CFD analysis to understand experimentally measured detailed heat transfer

coefficients for rib turbulated two-pass channel. A better understanding of complex flow structures and their impact on surface heat transfer can help cooling designers to optimally use coolant for turbine cooling purposes and improve overall efficiency of gas turbine engines.

Nomenclature

c specific heat capacity

d_h hydraulic diameter

f friction factor

f_0 friction factor from Blasius correlation

h heat transfer coefficient

k_f thermal conductivity

L total length of two-pass channel

Nu Nusselt number

Nu_0 Nusselt number from Dittus-Boelter correlation for developed turbulent flow in smooth circular duct

p^{**} normalized pressure, $(p_x - p_{in})/0.5\rho v^2$

Re Reynolds number (based on channel hydraulic diameter)

T temperature

t_{target} thickness of the target plate

T_i initial wall temperature

t time taken to reach T_{tlc}

T_{tlc} temperature of wall corresponding to the Hue to be tracked

T_m bulk fluid temperature at the inlet on test section

TKE turbulent kinetic energy

THP thermal hydraulic performance

u speed of working fluid in channel

Greek symbols

α normalized wall temperature, $(T_w(t) - T_i)/(T_m(t) - T_i)$

ρ density

Subscripts

i	initial
in	inlet
w	wall
m	mainstream
0	Dittus-Boelter/ Blasius correlation
s	smooth surface
x	cumulative streamwise distance

References

[1.1] Han, J. C., Dutta, S., and Ekkad, S., 2012, Gas turbine heat transfer and cooling technology, CRC Press.

[1.2] Taslim, M. E., Li, T., and Kercher, D. M., 1994, "Experimental heat transfer and friction in channels roughened with angled, V-shaped and discrete ribs on two opposite walls," ASME IGTI 1994, pp. V004T09A018-V004T09A018.

[1.3] Zhang, Y. M., Gu, W. Z., and Han, J. C., 1994, "Heat Transfer and Friction in Rectangular Channels With Ribbed or Ribbed-Grooved Walls," J. Heat Transfer, Vol. 116(1), pp. 58-65.

[1.4] Mochizuki, S., Murata, A., and Fukunaga, M., 1997, "Effects of Rib Arrangements on Pressure Drop and Heat Transfer in a Rib-Roughened Channel With a Sharp 180 deg Turn," J. Turbomach., Vol. 119(95), pp. 610–616.

[1.5] Chandra, P. R., Alexander, C. R., and Han, J. C., 2003, "Heat transfer and friction behaviors in rectangular channels with varying number of ribbed walls," Int. J. Heat Mass Transfer, Vol. 46(3), pp. 481–495.

[1.6] Lee, E., Wright, L. M., and Han, J.C., 2003, "Heat transfer in rotating rectangular channels (AR= 4: 1) with V-shaped and angled rib turbulators with and without gaps," ASME IGTI Paper No. GT2003-38900.

[1.7] Han JC, Zhang YM, Lee CP., 1991, "Augmented Heat Transfer in Square Channels With Parallel, Crossed, and V-Shaped Angled Ribs", ASME. J. Heat Transfer. Vol. 113(3), pp. 590-596. doi:10.1115/1.2910606.

[1.8] Ekkad, S. V, and Han, J. C., 1997, "Detailed heat transfer distributions in two-pass square channels with rib turbulators," Int. J. Heat Mass Transfer, Vol. 40(11), pp. 2525–2537.

[1.9] Jenkins, S. C., Zehnder, F., Shevchuk, I. V., von Wolfersdorf, J., Weigand, B., and Schnieder, M., 2013, "The Effects of Ribs and Tip Wall Distance on Heat Transfer for a Varying Aspect Ratio Two-Pass Ribbed Internal Cooling Channel," J. Turbomach., Vol. 135(2), pp. 021001-1-021001-9.

[1.10] Won, S. Y., Burgess, N. K., Peddicord, S., & Ligrani, P. M., 2004, "Spatially resolved surface heat transfer for parallel rib turbulators with 45 deg orientations including test surface conduction analysis", ASME Journal of Heat Transfer, Vol. 126(2), pp. 193-201.

[1.11] Tanda, G., & Abram, R., 2009, "Forced convection heat transfer in channels with rib turbulators inclined at 45 deg", Journal of Turbomachinery, Vol. 131(2), 021012.

[1.12] Tanda, G., 2011, "Effect of rib spacing on heat transfer and friction in a rectangular channel with 45 angled rib turbulators on one/two walls", International Journal of Heat and Mass Transfer, Vol. 54(5), pp. 1081-1090.

[1.13] Astarita, T., & Cardone, G., 2003, "Convective heat transfer in a square channel with angled ribs on two opposite walls", Experiments in Fluids, Vol. 34(5), pp. 625-634.

[1.14] Lee, D.H., Rhee, D.-H., Kim, K, M., Cho, H.H., Moon, H.K., 2009, "Detailed measurement of heat/mass transfer with continuous and multiple V-shaped ribs in rectangular channel", Energy, Vol. 34(11), pp. 1770-1778.

[1.15] Stephens, M. A., Shih, T. I. P., & Civinskas, K. C., 1995, "Computation of flow and heat transfer in a rectangular channel with ribs," *AIAA paper* 95-0180.

[1.16] Lin, Y.-L., Shih, T. I.-P., Stephens, M. a., and Chyu, M. K., 2001, "A Numerical Study of Flow and Heat Transfer in a Smooth and Ribbed U-Duct With and Without Rotation," J. Heat Transfer, Vol. 123(2), pp. 219-232.

[1.17] Shih, T. I. P., Lin, Y. L., and Stephens, M. A., 2001, "Fluid flow and heat transfer in an internal coolant passage," International Journal of Rotating Machinery, Vol. 7(5), pp. 351-364.

[1.18] Siddique, W., Shevchuk, I. V., El-Gabry, L., Hushmandi, N. B., and Fransson, T. H., 2013, "On flow structure, heat transfer and pressure drop in varying aspect ratio two-pass rectangular channel with ribs at 45˚," Heat Mass Transfer, Vol. 49(5), pp. 679–694.

[1.19] Shevchuk, I. V., Jenkins, S. C., Weigand, B., von Wolfersdorf, J., Neumann, S. O., and Schnieder, M., 2011, "Validation and Analysis of Numerical Results for a Varying Aspect Ratio Two-Pass Internal Cooling Channel," J. Heat Transfer, Vol. 133(5), pp. 051701-1-051701-8.

[1.20] Xie, G., Liu, J., Zhang, W., Lorenzini, G., and Biserni, C., 2014, “Numerical Prediction of Turbulent Flow and Heat Transfer Enhancement in a Square Passage With Various Truncated Ribs on One Wall,” J. Heat Transfer, Vol. 136(1), pp. 011902-1-011902-11.

[1.21] Pape, D., Jeanmart, H., von Wolfersdorf, J., & Weigand, B., 2004, “Influence of the 180 bend geometry on the pressure loss and heat transfer in a high aspect ratio rectangular smooth channel,” ASME Paper No. GT2004-53753.

[1.22] Chung, H., Park, J. S., Park, S., Choi, S. M., Rhee, D.-H., and Cho, H. H., 2015, “Augmented heat transfer with intersecting rib in rectangular channels having different aspect ratios,” Int. J. Heat Mass Transfer, Vol. 88, pp. 357–367.

[1.23] Maurer, M., Wolfersdorf, J. Von, and Gritsch, M., 2007, “An Experimental and Numerical Study of Heat Transfer and Pressure Losses of V-and W-Shaped Ribs at High Reynolds Numbers,” ASME Paper No. GT2007-27167.

[1.24] Moffat, R. J., 1988, “Describing the uncertainties in experimental results”, Experimental thermal and fluid science, Vol. 1(1), pp. 3-17.

[1.25] Yan, Y., & Owen, J. M., 2002, “Uncertainties in transient heat transfer measurements with liquid crystal”, Int. J. Heat Fluid Flow, Vol. 23(1), pp. 29-35.

[1.26] Sleiti, A. K., and Kapat, J. S., 2006, “Comparison between EVM and RSM turbulence models in predicting flow and heat transfer in ribroughened channels,” J. Turbulence, 7(29), pp. 1-21.

[1.27] Ooi, A., Iaccarino, G., Durbin, P. A., and Behnia, M., 2002, “Reynolds averaged simulation of flow and heat transfer in ribbed ducts,” Int. J. Heat Fluid Flow, 23, pp.750–757.

[1.28] Schüler, M., Dreher, H. M., Neumann, S. O., Weigand, B., and Elfert, M., 2012, “Numerical Predictions of the Effect of Rotation on Fluid Flow and Heat Transfer in an Engine-Similar Two-Pass Internal Cooling Channel With Smooth and Ribbed Walls,” ASME. J. Turbomach., 134(2), pp. 021021-1-021021-10.

[1.29] Lamont JA, Ekkad SV, Alvin M., 2012, “Detailed Heat Transfer Measurements Inside Rotating Ribbed Channels Using the Transient Liquid Crystal Technique”, J. Thermal Sci. Eng. Appl., Vol. 4(1), pp. 011002-011002-11. doi:10.1115/1.4005604.

[1.30] Ekkad, S. V., & Han, J. C., 2000, “A transient liquid crystal thermography technique for gas turbine heat transfer measurements”, Measurement Science and Technology, Vol. 11(7), pp. 957-968.

[1.31] Wright, L.M., Fu, W.-L., Han, J.-C., 2004, “Thermal Performance of Angled, V-shaped, and W-shaped Rib Turbulators in Rotating Rectangular Cooling Channels (AR=4:1)”, J. Turbomach. Vol. 126(4), pp. 604-614.

[1.32] Lamont, J.A., Ekkad, S.V., Alvin, M.A., 2014, “Effect of Rotation on Detailed Heat Transfer Distribution for Various Rib Geometries in Developing Channel Flow”, J. Heat Transfer, Vol. 136(1), 011901.

CHAPTER 2

Characterization of heat transfer enhancement and frictional losses in a two-pass square duct featuring unique combinations of rib turbulators and cylindrical dimples

Prashant Singh, Jaideep Pandit, Srinath V. Ekkad
Advanced Propulsion and Power Laboratory
Virginia Tech, Blacksburg VA USA 24061

International Journal of Heat and Mass Transfer, 106, pp.629-647.

ABSTRACT

Transient heat transfer experiments using liquid crystal thermography have been carried out on a two-pass square channel for testing several unique combinations of ribs and cylindrical dimples. Four different rib shapes, viz. 45° angled, V, W and M have been studied. In compound channels, the rib pitch accommodates cylindrical dimples arranged in the shape of the rib, hence following the direction of rib induced secondary flows. For each rib shape, three different configurations – rib alone, dimple alone and rib-dimpled compound cases were studied. The rib-height-to-channel hydraulic diameter ratio was 0.125 and rib-pitch-to-rib-height ratio was 16. The dimple-depth-to-print diameter ratio was 0.3. The experiments were carried out for a wide range of Reynolds number (19500 to 69000), covering a spectrum typically found in both land-based and air-breathing engines. A total of 52 experiments were carried out to measure detailed heat transfer coefficient on the bottom wall of the two-pass channel. A transient liquid crystal thermography technique was used for heat transfer measurement. Static pressure measurements were carried out to measure the overall pressure drop in the two pass channel. From globally averaged Nusselt number and overall pressure drop, thermal-hydraulic performance of the 13 configurations were determined, compared and analyzed. It has been observed that 45° angled and V compound configurations resulted in higher heat transfer augmentation as well as higher thermal hydraulic performance when compared with their corresponding ribs alone and dimples alone configurations.

Keywords: Liquid Crystal Thermography; Nusselt number; Thermal Hydraulic Performance

Introduction

Over the past few decades, increasing demand for higher overall efficiency of gas turbine engines has been pushing the turbine inlet temperatures to higher levels. Such elevated inlet temperatures to the turbine section have the potential to significantly increase the maintenance cost of airfoils, reduce their lifespans or even permanently damage them. In order to develop highly durable turbine airfoils which can withstand extreme thermal loads, innovative internal cooling technologies need to be developed. The present study is an attempt to identify novel heat transfer enhancement features, which are essentially the combination of two separate augmentation techniques. The most commonly used technologies for heat transfer enhancement in internal cooling serpentine passages are rib turbulators, concavities, pin-fins, jet impingement, etc. The present study investigates the heat transfer and pressure characteristics of rib-alone, dimple-alone and rib-dimpled compound channels. Following is a brief outline of some relevant studies reported earlier on rib turbulators, dimples and few very recent studies on the combination of ribs and dimples.

Han et al. [2.1] presented a detailed overview of the various geometric and flow parameters like rib spacing, their orientation, channel aspect ratio, rib shape etc., which influence ribbed channel heat transfer. Taslim et al. [2.2] compared the thermal-hydraulic performance of V-shaped ribs, 90° angled, 45° angled and other discrete angled ribs. They observed that the secondary flows generated by the angled ribs contribute to higher heat transfer enhancement compared to 90° ribs. Zhang et al. [2.3] investigated the effects of compound turbulators on the friction factor and heat transfer coefficient in rectangular channels. The heat transfer performance of rib-groove roughened duct was found to be significantly better than the rib-roughened channel with very little difference in pressure drop characteristics. Mochizuki et al. [2.4] experimentally studied the combined effects of 180° bend and rib patterns on the heat transfer and friction performance in a two-pass rib- roughened channel. They reported that the arrangement of ribs significantly alters the pressure drop and heat transfer performance of the entire channel due to the interactions between the bend-induced secondary flow and rib-induced secondary flow. Ekkad and Han [2.5] were the first to present detailed Nusselt number distributions for a two-pass square channel using transient liquid crystal technique. Their study provided useful insight into the role of rib induced secondary flow on local heat transfer. Chandra et al. [2.6] studied the effect of varying number of ribs on heat transfer and friction characteristics of a rectangular channel. They observed a decrease in heat transfer performance

with increasing Reynolds number and with each additional rib. Lee et al. [2.7] investigated the heat transfer distribution in a high aspect ratio rotating ribbed channel with V-shaped and angled ribs and observed that the parallel V-shaped ribs produce the maximum heat transfer enhancement. Jenkins et al. [2.8] used transient liquid crystal technique to investigate the heat transfer distribution and pressure losses for a ribbed two-pass varying aspect ratio cooling channel with different divider wall-to-tip wall distance. Furthermore, they also studied the effects of bend and rib induced enhancements separately and observed that the bend significantly contributes to the heat transfer enhancement in the outlet channel. Han et al. [2.9] carried out experiments on different angled crossed ribs and reported that 60 degree V shaped rib had the highest heat transfer augmentation. Won at al. [2.10] carried out experiments on 45 degree angled ribs and reported enhancements (normalized with Dittus-Boelter) from 3.53 to 1.79 times for Reynolds number range of 9000 to 76000. Tanda and Abram [2.11] carried out experiments using steady state liquid crystal thermography on 45 degree angled turbulators for a Reynolds number range from 9000 to 35500, and reported heat transfer augmentation in the range of 2.7 to 1.8. Steady state liquid crystal thermography technique was used by Tanda [2.12] to investigate the effects of pitch-to-height ratio of 45 degree ribs in a rectangular channel with aspect ratio of five. The author reported that a rib-pitch-to-rib-height (p/e) ratio of 13.33 was preferable for single wall ribbed case, particularly for higher Reynolds number. In the present study, the rib-pitch-to-height ratio of ribs was chosen to be 16. One reason for this choice is to encounter lower pressure penalties, particularly at high Reynolds number. At lower p/e values, the pressure penalty is significant at high Reynolds number. One aim of present study is to pack the dimples in a ribbed configuration in a particular way so as to achieve higher thermal hydraulic performance. More details on this topic has been presented in later sections. Astarita and Cardone [2.13] carried out experiments on 30 degree and 45 degree ribs using IR thermography for a range of 16000 to 60000 Reynolds number. The authors reported low heat transfer augmentation for p/e = 20 case, due to more probability of development of boundary layer within a rib pitch.

Several researchers have carried out numerical studies on two-pass channel featuring rib turbulators. The research has been focused on resolving complex flow physics in the sharp 180° turn and the secondary flows induced by rib turbulators. One such study was carried out Murata and Mochizuki [2.14] where the authors reported Large Eddy simulation (LES) results for the

effect of rib turbulators orientation on turbulent heat transfer. In this study, the computational domain included a sharp 90° turn before the coolant flows over rib turbulators in the first pass. This configuration is very similar to the present study's configuration in terms of inlet conditions. The authors reported that the heat transfer in the two pass channel was mainly dominated by the bend induced secondary flows. Lu and Jiang [2.15] carried out experimental and numerical investigation to study turbulent heat transfer in a rectangular channel featured ribs at different angles to the bulk flow. The SST k-ω turbulence model was chosen and it was concluded that heat transfer increased with increasing Reynolds number and decreasing rib pitch. Jang et al. [2.16] carried out computations to explore heat transfer and flow field in a two-pass channel featuring ribs inclined at an angle of 60° with the bulk flow. In order to resolve the turbulent flow, a RANS model in conjunction with near-wall second-order RSM with a two-layer k-ε isotropic eddy viscosity model was used. The authors reported that the angled turbulators produced strong anisotropic turbulence due to combined effects of angled ribs and 180° turn, which in turn had significant effect on heat transfer in the second pass. Similar turbulence effects were observed by Jang et al. [2.17]. Shih et al. [2.18] carried out numerical investigations to study three-dimensional flow and heat transfer in a U-shaped duct with a square cross-section featuring angled rib turbulators on both the walls. Their study encompassed Reynolds number ranging from 25000 to 350000 and the authors also studied the effects of rotation on heat transfer. Due to wide range of Reynolds numbers investigated by the authors, they reported that at lower Reynolds numbers, the bend induced pressure gradients had dominant effects on heat transfer, and at higher Reynolds number – the rib induced secondary flows dominated the heat transfer in the bend and 2^{nd} pass.

In the present compound channel study, the other method of enhancing heat transfer was dimples (also called concavities). Several experimental and numerical studies have been carried out in the past to explore heat transfer and fluid dynamics in a dimpled channel. However, experimental data on dimples in two pass channel is very sparse. One such study was carried out by Zhou and Acharya [2.19] where they carried out mass transfer experiments on a two-pass square duct featuring hemispherical dimples using Naphthalene-Sublimation technique. The authors reported heat transfer enhancement of less than 100% for a Reynolds number of 21000. The common observation in most of the studies on dimpled channel is that they have relatively lower heat transfer enhancement when compared to ribs but also lower pressure penalty. This

quality of dimples makes it a potential candidate in the compound channel studies where it can contribute more towards heat transfer enhancement while still imposing lesser pressure drop. More studies on dimples have been documented in [2.1].

Very recently, compound single pass channels featuring both ribs and dimples have been investigated by Chang et al. [2.20]. They studied the effects of V-shaped ribs and very closely spaced cylindrical dimples (referred to as “scales” in the original article) for relatively lower values of Reynolds numbers (max Reynolds number of 30000). The authors reported that the combination of ribs and dimples resulted in higher heat transfer enhancement when compared to the rib alone case. One other interesting observation made was that the normalized Nusselt number enhancement with respect to Dittus-Boelter correlation, remained uniform over the range of Reynolds number studied. Most of the enhancement features come with the demerit of reducing normalized Nusselt number enhancement with increasing Reynolds number, and hence rendered less effective for high Reynolds number applications such as those in land-based turbines. However, the maximum Reynolds number studied by [2.15] was still low to draw such general conclusions. Present study extends the Reynolds number range to 69000 which encompass the high Reynolds number application found in land-based gas turbines [1]. Choi et al. [2.21] studied the heat transfer characteristics of compound channel (single-pass) featuring 45° ribs and cylindrical dimples using liquid crystal thermography. The straight channel had aspect ratio of 2 and 4. Six configurations were studied at three Reynolds numbers and it was found that the compound channel with aspect ratio of 2 had the highest heat transfer enhancement and highest thermal hydraulic performance in comparison to other cases. Another parametric study carried out by Choi et al. [2.22] documents the effects of dimple configuration on heat transfer enhancement in compound channels. They have reported that the dimple depth-to-diameter ratio of 0.22 resulted in the best heat transfer augmentation. This result by Choi et al. was taken into design consideration of the presented study’s compound channel configuration. Zhang et al. [2.23] carried out numerical investigation of flow and heat transfer of rectangular duct featuring combination of 90° ribs, spherical concavities and spherical protrusions. The authors identified the optimum dimensions of protrusion and concavity for higher thermal hydraulic performance. Recently, Shen et al. [2.24] carried out numerical study of fluid flow and heat transfer in a U-shaped channel featuring combination of 90° ribs and dimples and combination of ribs and protrusions. The authors concluded that rib-protrusion combination

showed higher heat transfer enhancement over rib alone case, when compared to rib-dimpled combination.

The rib alone configuration in the present study is taken directly from [2.25]. Singh et al. [2.25] carried out detailed experimental and numerical studies on the four rib-alone configurations used in the present study. The authors in the present study used the knowledge gained from the numerical investigation carried out in [2.25] to explain the role of rib induced secondary flow in heat transfer enhancement due to combination of ribs and dimples. The streamtraces shown in [2.25], for the secondary flows induced by ribs, provided guidelines on arrangement of cylindrical dimples in order to have maximum enhancement in heat transfer. Section 5.3 documents detailed discussion on secondary flows induced by rib turbulators, and complex fluid dynamics in the bend region – this discussion is predominantly based on the work done in [2.25].

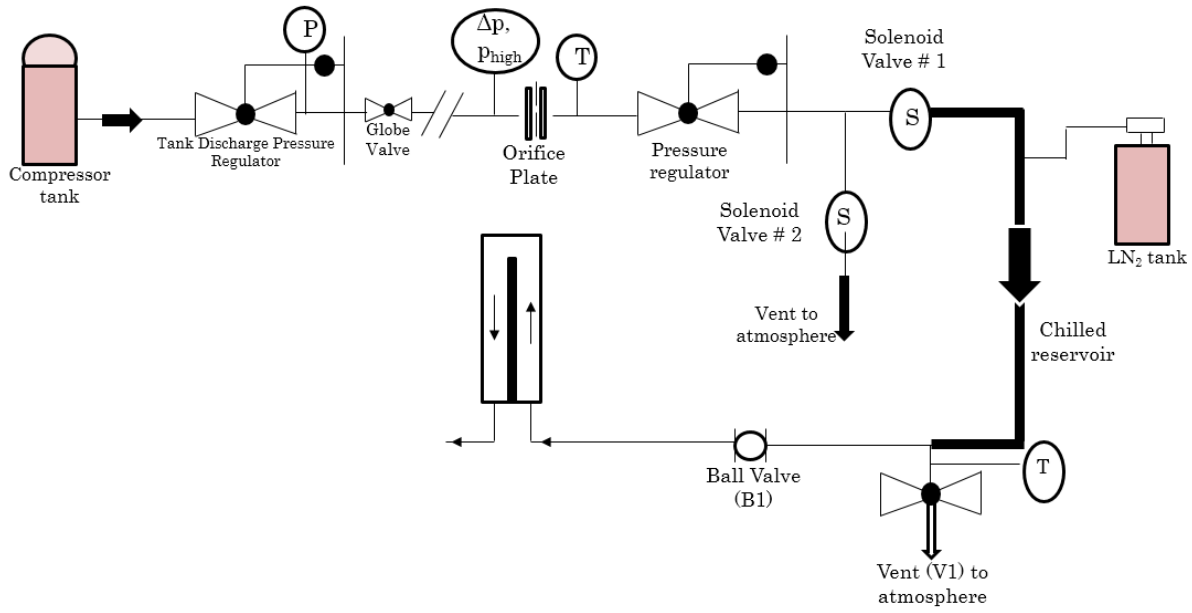

(a)

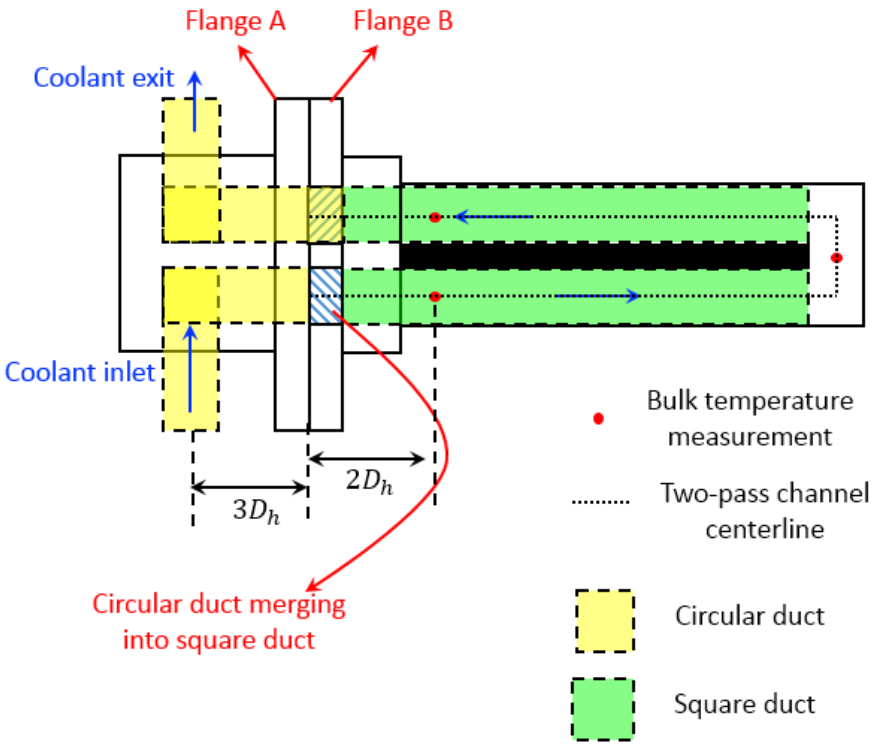

(b)

Figure 2.1 (a) Schematic of Experimental setup, (b) description of coolant flow prior to entering the test section, location of mainstream temperature measurement

Experimental Setup

The experimental setup for the present study is shown by a schematic in Fig. 2.1(a). The schematic shown in Fig. 2.1(b) describes the process of the coolant entrance into the two pass channel. Flange A houses the inlet port. The flow turns in the flange A by 90° and travels a distance of $3D_h$ before the circular duct merges into rectangular duct.

As mentioned earlier, a transient liquid crystal thermography technique was used for the detailed measurement of heat transfer coefficient on the bottom wall of the two pass channel. For this type of heat transfer experiment, a temperature differential between the working fluid (air) and the surface is required to calculate the heat transfer coefficient. The air is supplied by a compressor capable of maximum continuous supply of 1.36 kg/s of air at 150 psi (~1 MPa). For the current experiments, a buffer tank was installed downstream of the main compressor. The pressure in the buffer tank was maintained at about 40 psi (~270 kPa), which was sufficient for

constant supply of the desired mass flow rate. An inline globe valve was installed downstream of the buffer tank to allow fine control over the flow rate. The mass flow rate of air was measured by an orifice meter, which was located approximately 35 pipe diameters downstream of the flow control valve. The differential pressure across the orifice was measured by Dwyer 477-4-FM (10 psi (~70 kPa) range) and the high pressure at the orifice was measured by Dwyer DPG – 103 (30 psi (~206 kPa) range). The temperature of the air at the orifice meter was measured by a T-type thermocouple. Above measurements were used to calculate the mass flow rate, where the changes in the density of air during different inlet conditions in different runs was taken into account. Two solenoid valves were located downstream of the pressure regulator. These solenoid valves worked in conjunction to act as a 3-way valve, where the binary operating signal to solenoid valves was controlled using LabVIEW. In the present study, colder air has been chosen as working fluid because in the actual engine, the coolant is at a lower temperature than the wall. However, this type of experiment can be carried out by hot air as well and the heat transfer coefficient obtained from both these approaches should theoretically be the same. A fitting was provided downstream of the Solenoid valve #1, for the intake of liquid Nitrogen (LN2). A mixture of air and Nitrogen was used to cool the path between the solenoid valve (#1) and vent valve (V1), and thus creating a cold reservoir for the actual transient test. Several calibration runs were carried out to collect data for the minimum reservoir temperature required to achieve similar heat transfer experiments across the range of Reynolds number. The main aim was to keep the experiment run-time similar, and hence, different levels of reservoir temperatures were required for different runs. Once the thermal reservoir is suitably cooled, the nitrogen supply was cut off and all the remaining nitrogen in the reservoir line was purged out from the main line into the ambient through the valve V1.

Further, the solenoid valve direction was switched towards the ambient and the combination of Ball valve (B1) and gate valve (V1) was used to open the main line towards the test section. Afterwards, the flow rate was set to the desired value and the test commenced once the solenoid valves were flipped towards the test section. Several precautions were taken in order to make sure that the flow rate during the test was uniform and very close to the intended flow rate.

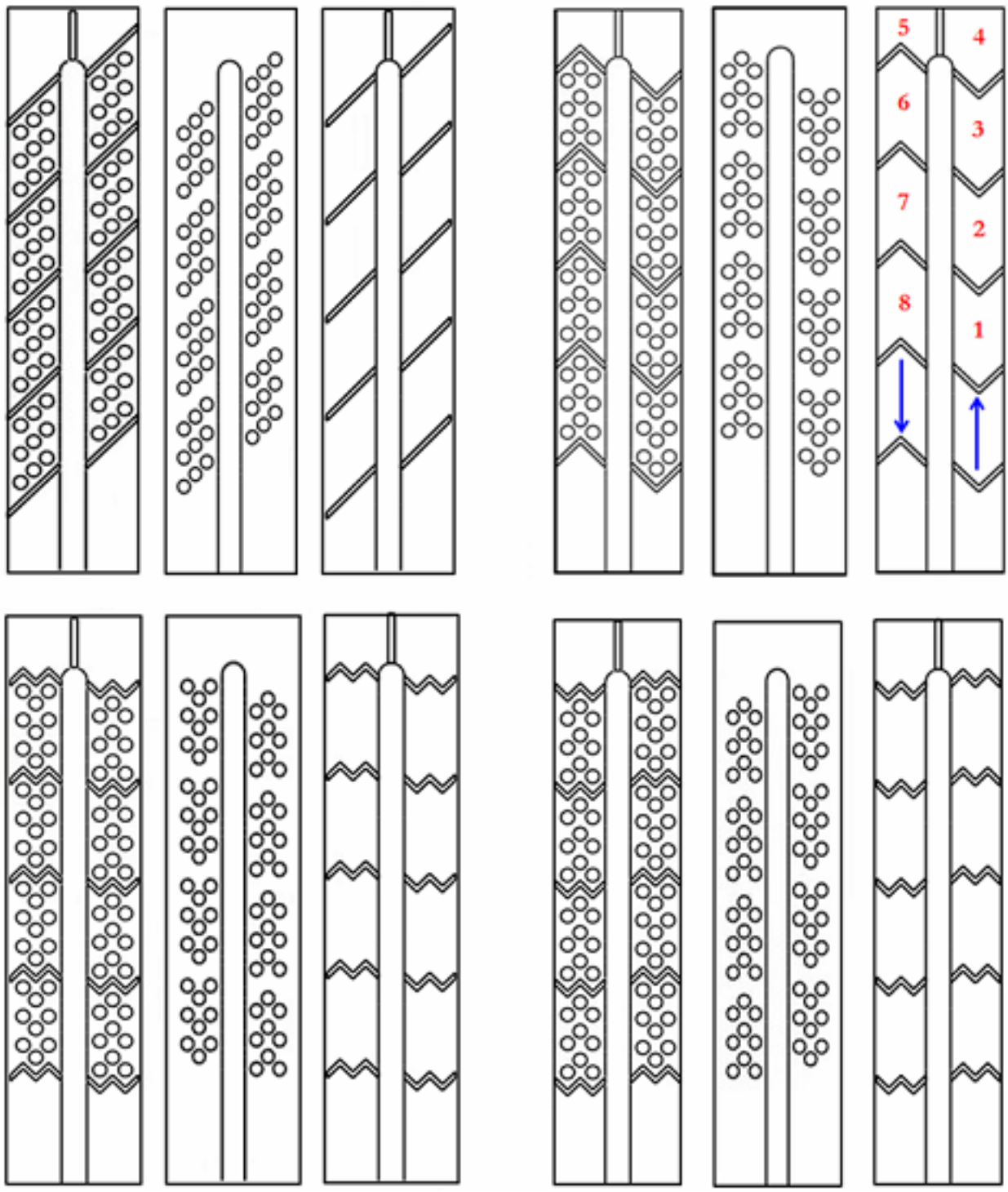

(a)

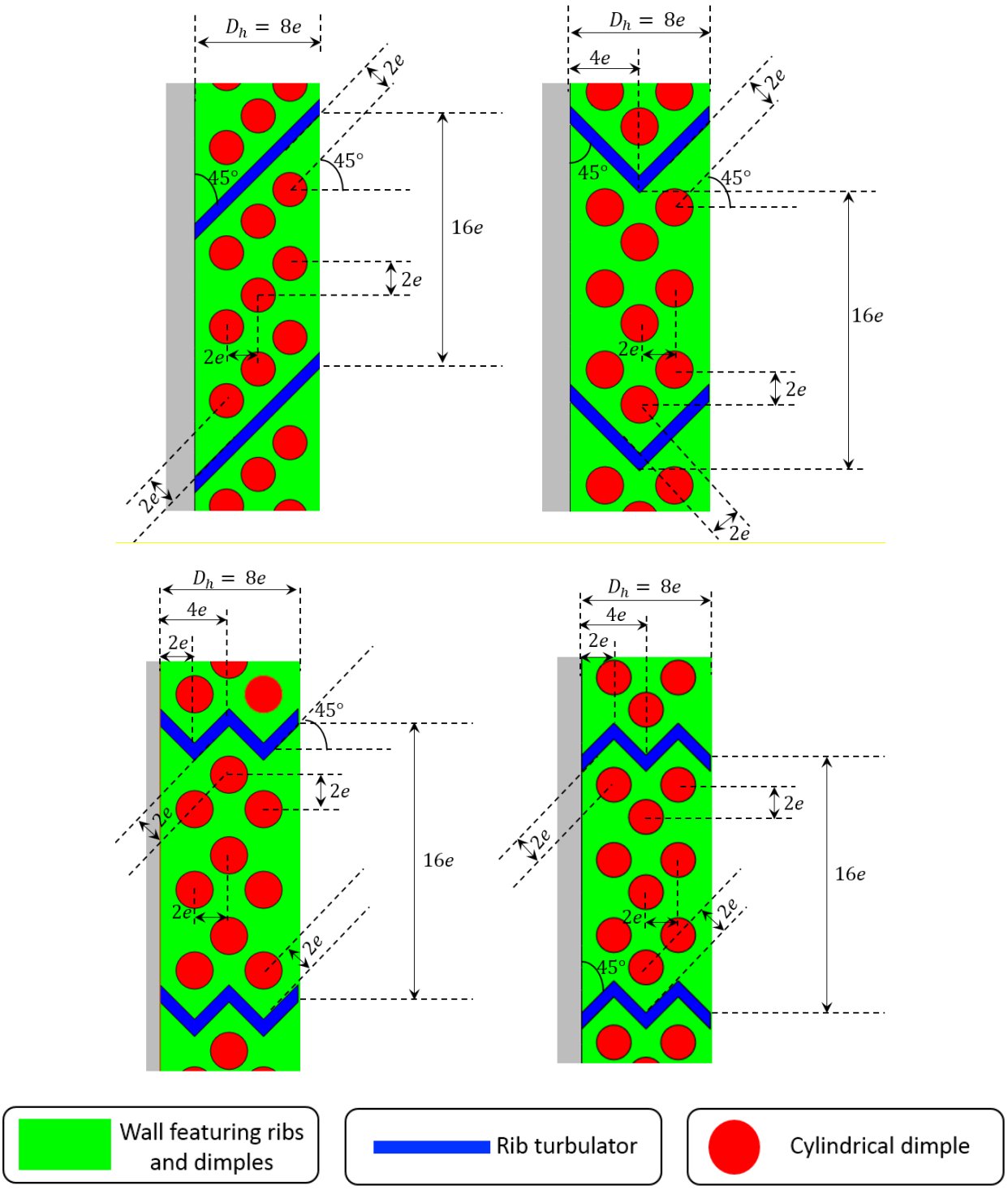

(b)

Figure 2.2 (a) Different rib, dimple and rib-dimple compound channel studied, (b) dimensions of rib and dimple relative to each other in terms of rib height

Description of Test Configurations, Experimental Conditions and Terminology

Figure 2.2(a) shows the twelve configurations studied. The two-pass channel was connected by a 180° bend and the bend featured a 90° rib in the ribbed case and the compound case. The aspect ratio of the two-pass channel was unity. The rib-pitch-to-rib-height ratio (p/e) was 16 and the rib-height-to-channel-hydraulic-diameter (e/d_h) was 0.125. Four different rib configurations, 45°, V, W and M were studied. The dimpled configuration comprises of three rows of dimples packed in a rib pitch.

The dimples were aligned in the direction of secondary flows induced by a particular rib shape in order to maximize the wall shear stress due to interaction of secondary flows induced by ribs and dimples with the bottom wall. The dimple depth-to-print diameter ratio was 0.3. The relative positioning of dimples with respect to the ribs for four different configurations has been shown in Fig. 2.2(b) in reference to rib height. The dimple print diameter was 6.86 mm.

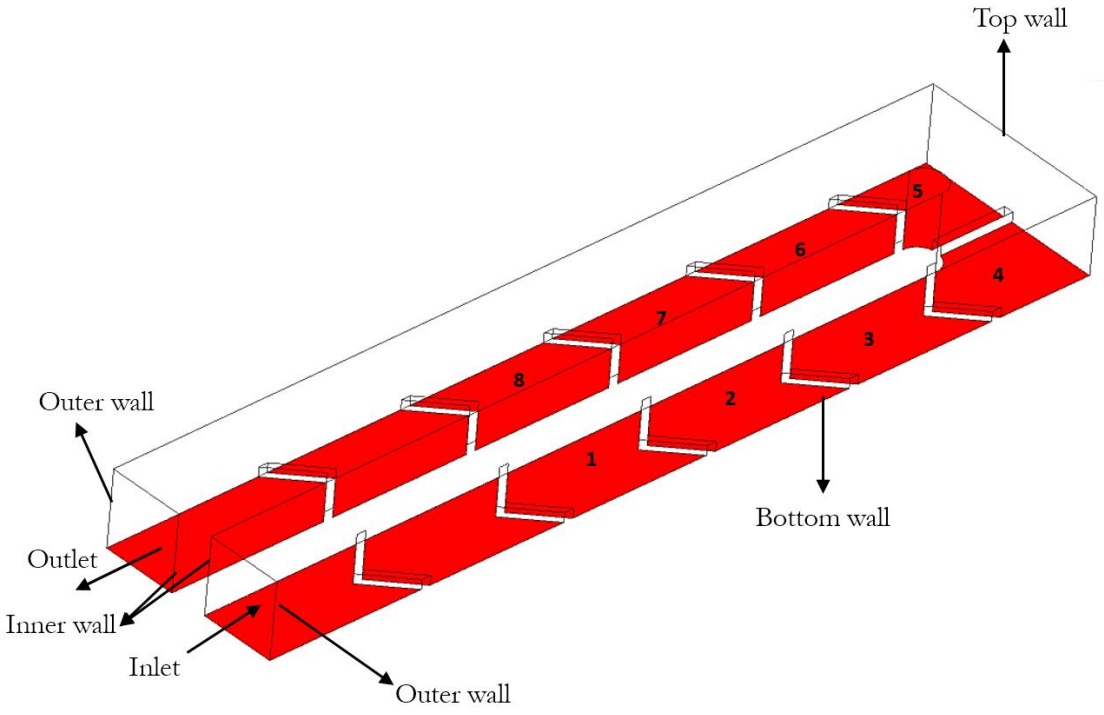

Figure 2.3 Two pass channel nomenclature

Heat Transfer Coefficient Calculation Methodology

The two-pass channel was made with combination of 3D printing material (ABS) and plexiglass. The heat transfer enhancement features were additively manufactured on the bottom

wall and the top wall was made of clear acrylic (assumed to be smooth and having good optical access). The thermal conductivity of the bottom wall was very low and the material was chosen such that 1-D semi-infinite transient heat conduction was valid for the chosen thickness over the span of the experiment. The analytical solution for the 1-D semi-infinite conduction model with convective heat transfer boundary condition on the coolant side and constant temperature boundary condition on the other side of the solid, is given by Eq. 2.1.

$$\frac{T_w - T_i}{T_m - T_i} = 1 - exp\left(\frac{h^2 t}{\rho c k}\right) erfc\left(h\sqrt{\frac{t}{\rho c k}}\right) \quad Eq.(2.1)$$

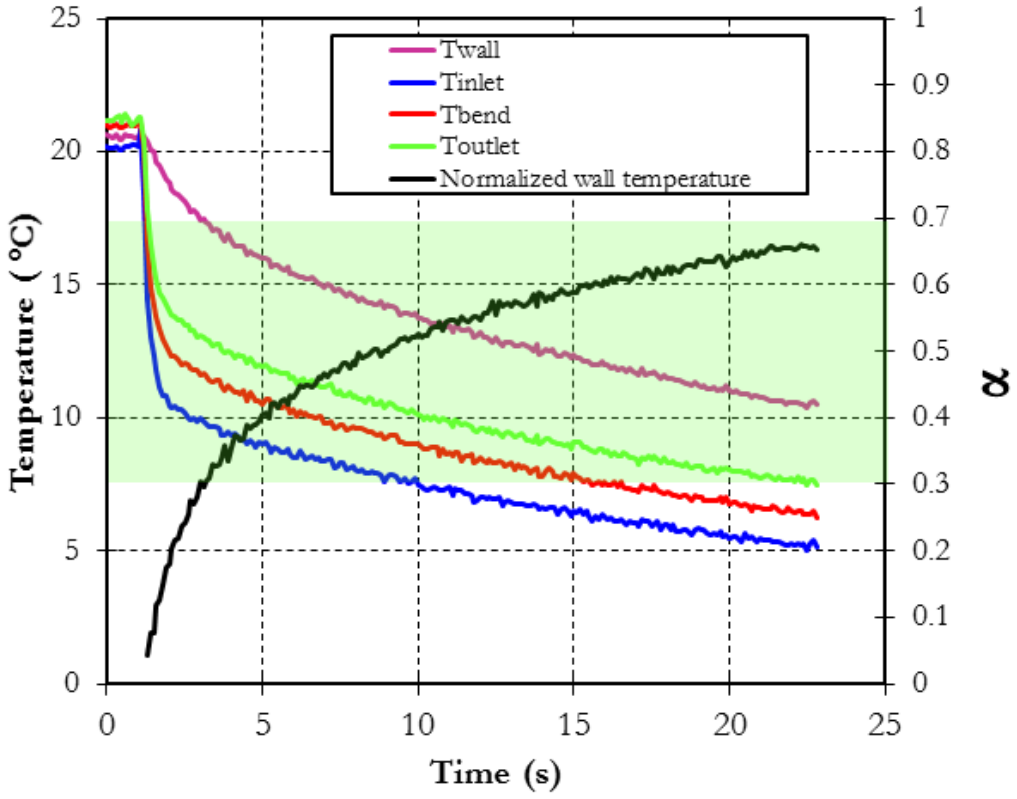

Figure 2.4 History of wall temperature and static temperature measured in plenum chamber, green region indicating $0.3 < \alpha < 0.7$.

Equation 2.1 is valid for constant mainstream temperature (T_m), which is practically impossible to achieve during transient experiments. In experiments, the mainstream temperature keeps decreasing after the step change. In order to take into account the transient nature of the mainstream temperature, Duhamel's superposition principle has been incorporated in the

solution of 1-D semi-infinite solid conduction equation (Eq. 2.1). The time varying mainstream temperature was divided into small time steps. The mainstream temperature during each time step was then assumed to be constant. After applying Duhamel's superposition principle, the Eq. (2.1) can be written as,

$$T_w = T_i + \sum_{i=1}^{i=n_{max}} (T_{m,i} - T_{m,i-1}) \times \left[1 - \exp\left(\frac{h^2(t-t_i)}{\rho ck}\right) erfc\left(h\sqrt{\frac{(t-t_i)}{\rho ck}}\right)\right] \quad (Eq.\ 2.2)$$

where, T_m represents the temperature of the working fluid (air) and 'i' is the summation index for time steps. Ti is the initial temperature of the target surface, which was calculated by averaging the sampled wall temperature till the commencement of the transient test. The maximum permissible time for the transient liquid crystal experiment without violating the 1-D semi-infinite conduction model assumption was found from Eq. 2.3. The typical run time of experiments was well under t_{max}.

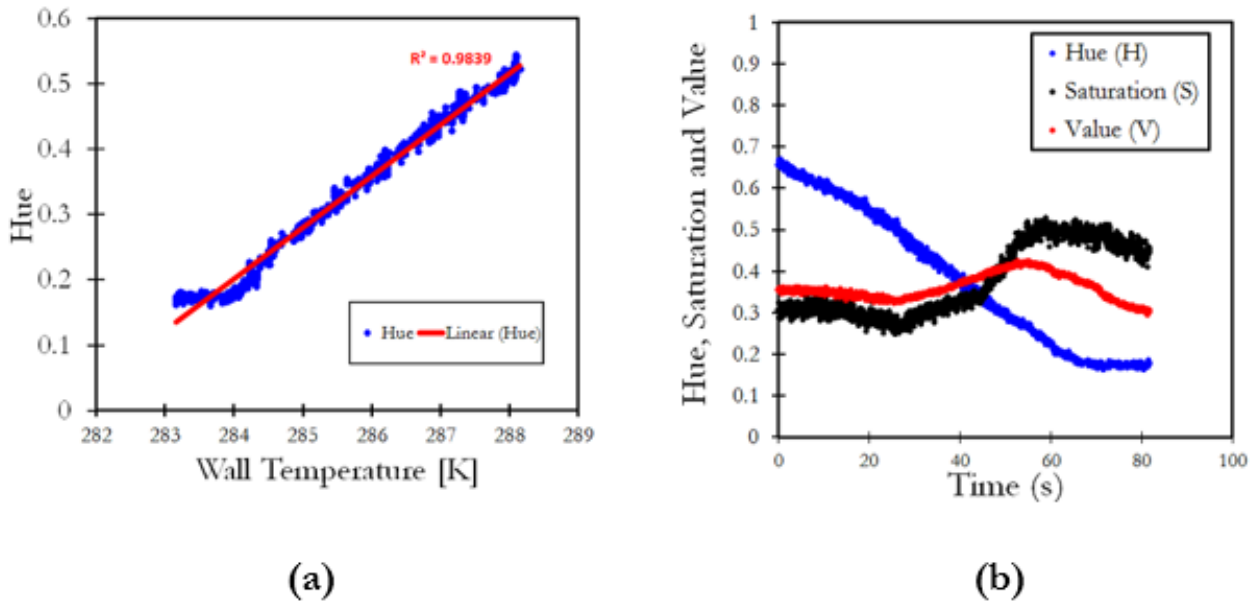

Figure 2.5 (a) Hue versus wall temperature, (b) Time evolution of Hue, Saturation and Value

$$t_{max} = 0.1\frac{\rho c {t_{target}}^2}{k} \quad (Eq.\ 2.3)$$

The spatial variation of bulk temperature in the first pass was modeled by linearly interpolating the temperatures measured at the inlet and the bend, and by linearly interpolating between the

bend and outlet temperature measurements for the second pass. The location of bulk temperature measurement is shown in Fig. 2.1(b).

The temperature of the coolant was measured by a fast response T-type thermocouple (bead diameter: 0.0762 mm) and the data acquisition was carried out using LabVIEW interface which linked the computer to a National Instrument chassis (cDAQ9174) housing thermocouple module (NI9214). The wall temperature was measured in the last pitch of the second pass for in-situ calibration. Figure 2.4 shows all the temperature measurements by thermocouples. Now, in Eq. (2.2), the only unknowns are T_w, t and h. These unknowns are determined as follows.

Liquid Crystal Thermography involves associating the color change of a thermochromic material (Thermochromic Liquid Crystal) to a temperature. TLC is sprayed onto the surface of interest. The color response of the TLC is within the manufacturer specified range (10°C-15°C in this case). Within this temperature range, TLC changes color which is captured by a video camera and examined in the HSV color space. In order to establish a relationship between Hue and measured wall temperature, a 5 x 5 pixel region in the vicinity of the wall thermocouple was chosen as the "calibration region". A flat region was installed in the last pitch only for the purpose of proper in-situ calibration and in a region close enough to regions of interests in order to have same illumination conditions. This is a relatively small region and the wall temperature measured by the thermocouple can be considered to be uniform across the calibration region (entire 25 pixels), because of low values of second order spatial derivative of spanwise and streamwise heat transfer coefficient in the calibration regime. It was ensured that the thermocouple had good contact with the wall, hence eradicating possibilities where wall thermocouple might have the effects of mainstream flow. For redundancy, two such wall thermocouples were secured on the target surface. It was found that very similar calibration curves were obtained for both the calibration regions. Figure 2.5(a) shows the relationship between Hue and wall temperature for the calibration region. It can be seen that a linear dependence of Hue on measured wall temperature was found and the range of Hue is wide. Figure 2.5(b) shows the normalized Hue (H), Saturation (S) and Value (V) on a scale of 0-1, and averaged over 25 pixels representing the 'calibration region'. The physical scale of Hue (H) is from 0°-360° (representing a circle) and normalized values are presented in Fig. 2.5(b). For data quality check, a minimum threshold of 0.25 was applied to Saturation (S) and Value (V). It can

be seen from Fig. 2.5 that both the S and V values were above 0.25 throughout the transient experiment.

A reference Hue (H_{ref}) was determined such that $H_{ref} = H_{min} + H_f(H_{max} - H_{min})$. A Hue factor ($H_f$) of 0.5 was chosen for the calculation of heat transfer coefficient. Different Hue factors were tested for the calculation of heat transfer coefficient and it was found that the variation of globally averaged heat transfer coefficient was less than 5% for $H_f \propto 0.5 \pm 0.3$. Tw is the wall temperature corresponding to the reference Hue value (H_{ref}). A GoPro camera recorder was used to record the color change video where the frame capture rate was approximately 30 frames per second. Standard MATLAB inbuilt functions were used to process the video and extract R, G, B information of each pixel for each frame.

Further, a time (t) matrix was built for the entire region of interest as follows. Each pixel was sequentially traversed, and the Hue information was extracted from RGB information using standard functions. For a particular pixel, each frame was then traversed to find the frame number where its Hue corresponds to H_{ref} (and S, V>0.27). Once all of these criteria were satisfied, the physical time ((frame#) x fps^{-1}) corresponding to the particular frame number was calculated and stored in the time matrix associated with the specific pixel location. At this stage, the only unknown left in Eq. 2.2 is the heat transfer coefficient (h). Heat transfer coefficient is then determined by a root finding algorithm (secant method).

The tolerance specified for the convergence of root determination was 0.01°C difference between T_w (calculated from H_{ref}) and T_w calculated from the substitution of calculated value of 'h' (through root finding algorithm) in Eq. 2.2. The Nusselt number (based on channel hydraulic diameter) was calculated using Eq. 4.

$$Nu_d = \frac{hd_h}{k_f} \quad Eq.(2.4)$$

where k_f is the thermal conductivity of air.

Uncertainty Analysis

The sequential perturbation method prescribed by Moffat [2.26] was used for the calculation of uncertainty in the measurement of Nusselt number and Reynolds number. The contributing parameters in the measurement of Nusselt number are, $T_w, T_i, T_m, t \; and \; \sqrt{\rho ck}$. The

temperatures were measured by T-type thermocouple and the uncertainty in the measurement of temperature was taken to be 0.5°C. Time taken (t) to reach a particular hue value has an uncertainty of two frames, and the worst case scenario was taken where the hue value was reached at a time instant common to two frames. Hence, depending upon the frame capture rate, the uncertainty in measurement of t was taken to be 0.067 seconds. The combined uncertainty in the solid properties, $\sqrt{\rho ck}$ was taken to be 5%. Using above individual contributions of different variables towards the overall uncertainty in the measurement of a typical Nusselt number of 236 was found to be 13.74%. Also, Yan and Owen [2.27] carried out detailed uncertainty analysis for transient liquid crystal experiments and reported that lower levels of uncertainties can be achieved if the normalized wall temperature (α) varies between 0.3 and 0.7. This can be obtained by thoughtful selection of mainstream operating temperatures, reference Hue to be tracked and liquid crystal color band. As can be seen in Fig. 2.4, the normalized wall temperature in the present study lies in the prescribed region ($0.3 < \alpha < 0.7$) for about last 85% of the run time. The above measures were taken in order to minimize the uncertainties in heat transfer coefficient measurements. However, the lateral conduction effects would still have some effects on measured heat transfer coefficient.

The uncertainty in the calculation of Reynolds number (of 35500) based on channel hydraulic diameter, was found to be 4.34%.

Results and Discussion

In this section, detailed Nusselt number contours are presented for all the configurations studied for a representative Reynolds number of 35500. Detailed Nusselt numbers provide valuable insight into fluid dynamics in the two-pass channel, and the secondary flows induced due to heat transfer enhancement features. Firstly, discussion has been provided for the baseline case, which is the smooth two-pass duct. Later, heat transfer and flow characteristics of different configurations has been discussed.

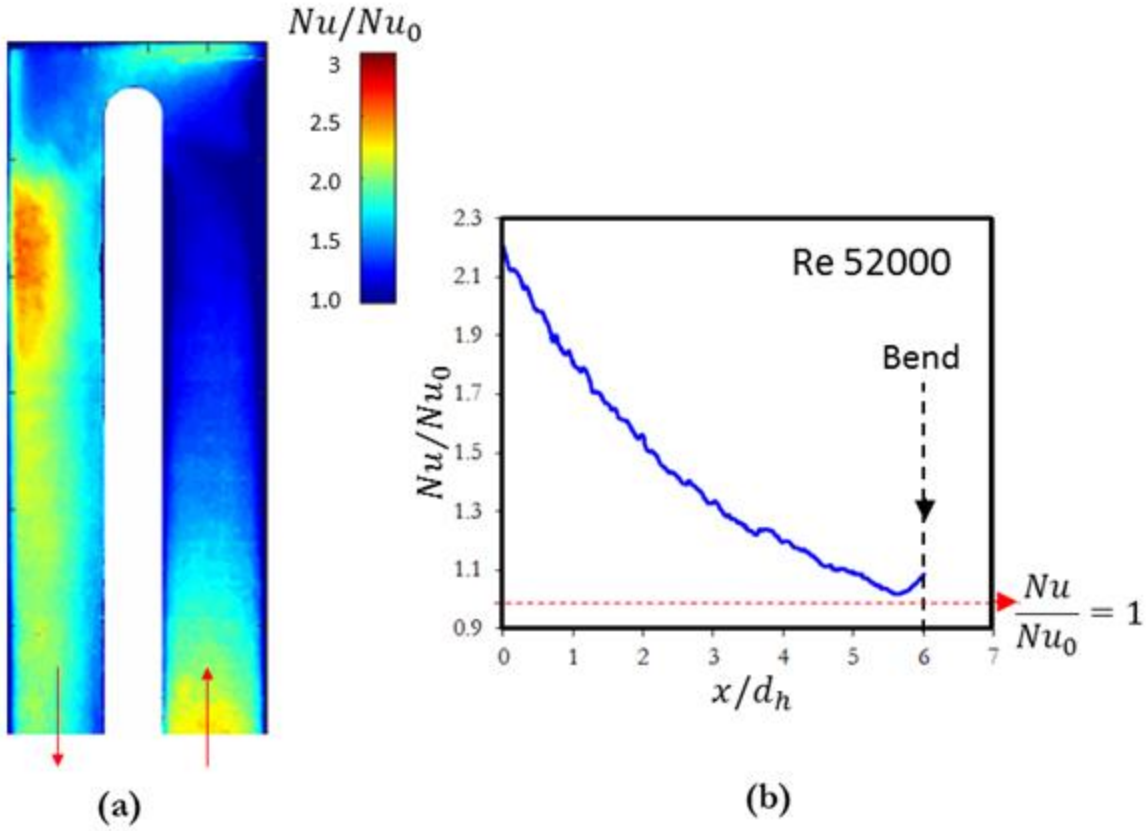

Figure 2.6 (a) Detailed Nusselt number contour (Nu/Nu0) at Re = 52000, (b) Spanwise averaged Nusselt number (1st pass) plotted in streamwise direction (x/dh = 0 corresponds to start of second rib pitch in the first pass, x/dh = 6 corresponding to end of last rib in the first pass)

Heat Transfer Characteristics of Smooth two-pass duct

Figure 2.6(a) shows the detailed Nusselt number contour for Reynolds number of 52000, and Fig. 2.6(b) shows the streamwise evolution of spanwise averaged Nusselt number (1st pass) normalized with respect to Dittus-Boelter correlation for developed turbulent flow in a circular duct.

From Fig. 6(a), it can be seen that the flow in the first pass was not developed, thus resulting in higher Nusselt number compared to that found from Dittus-Boelter correlation for fully developed turbulent flow in a circular duct. Also, the velocity profile was slightly skewed towards the inner wall (refer Fig. 2.3 for nomenclature of endwalls and sidewalls). This was because of the 90° orientation of the two pass channel with respect to the incoming coolant direction, as shown in Fig. 2.1. This particular arrangement was chosen to simulate the inlet flow condition existing in actual gas turbine airfoil internal cooling multiple serpentine passages. In

actual engine, the inlet conditions of the coolant are not similar to uniform velocity. The smooth channel results are important in the current study because the overall heat transfer enhancement in the first pass is due to a combination of heat transfer enhancement features and the under-developed turbulent flow. Similarly, the heat transfer enhancement in the second pass is due to a combination of bend induced secondary flows and the enhancement features. In order to obtain realistic evaluation of the performance of any heat transfer enhancement feature, the reference should be a similar configuration without the features, which in the current study, was the smooth two-pass channel. The flow in the first pass remained under-developed throughout the channel. The normalized Nusselt number reached a value of approximately 1.05 just upstream of the bend. The reason why the fully developed thermal boundary layer couldn't be achieved is because of the precursor effects of the bend. Also, the streamwise distance shown in the Fig. 2.6(b), was measured from the region of interest. In reality, the bend lies exactly at a distance of ten channel-hydraulic-diameters when measured from the inlet of the two-pass channel. Hence, a very good agreement has been found, between the Nusselt numbers predicted by correlations for fully developed turbulent flow in circular ducts and those measured experimentally. The flow while making the 180° turn, hits the outer endwall corresponding to the second pass, due to flow inertia. Post 180° turn, a part of flow hugs the outer wall in the second pass and travels along it for approximately one rib pitch. The next section provides discussion on heat transfer enhancement mechanism for ribs and dimples.

Basic Heat Transfer Augmentation Phenomena due to Ribs and Dimples

As mentioned in section 4, four different rib configurations have been studied. The corresponding dimpled channel features dimples arranged in a particular form, following the direction of corresponding rib induced secondary flows. The compound channel was obtained by adding the rib configuration and the dimple configuration. The bend featured a 90° rib for the ribbed and compound cases.

In a rib turbulated channel, the coolant near the ribs get tripped which disturbs the developing thermal boundary layer, resulting in separation immediately downstream of the rib. This leads to recirculating fluid in the downstream vicinity of the rib, resulting in lower heat transfer. The coolant then re-attaches resulting in increased heat transfer. The re-attachment length depends on Reynolds number, rib shape, and other geometrical parameters.

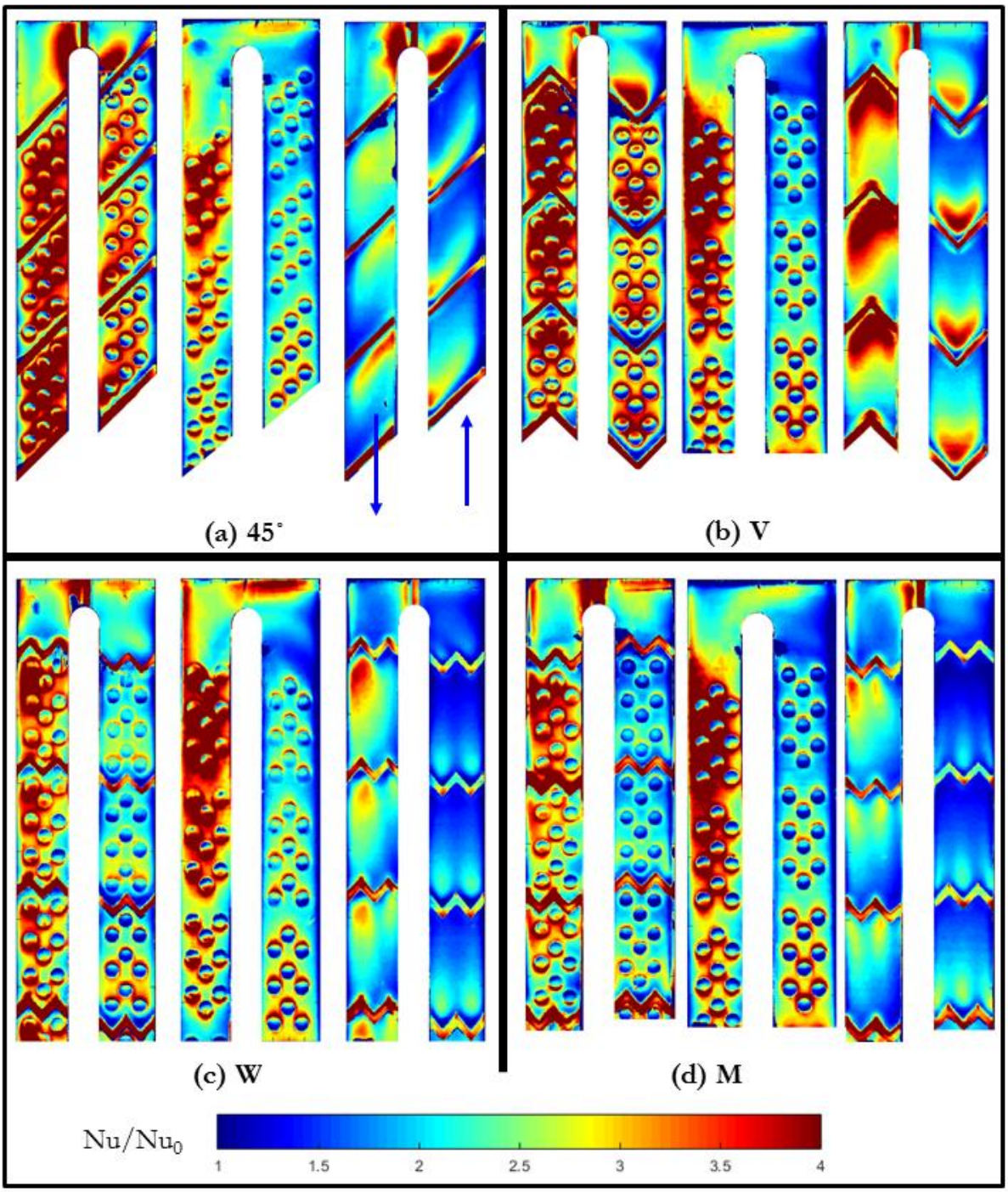

Figure 2.7 Detailed Nusselt number enhancement contours for all the configurations studied (Re = 35500) (first pass and second pass orientation as shown in Fig. 2.2)

The heat transfer mechanism due to dimples is different than that of ribs. Flow over dimples result in the occurrence of several periodical fluid dynamics phenomena. The frequency of the occurrence of these phenomena is function of dimple print diameter, dimple depth and Reynolds number of coolant flow. The primary vortex (formed inside a dimple) is shed periodically and this is followed by advection into the dimple cavity. The vortex shedding from the core of dimples result in heat transfer augmentation on the endwall just downstream of the dimple. Further discussion on rib specific and dimple specific heat transfer is provided in the following section.

Detailed Nusselt number Contours for Different Configurations Studied

Figure 2.7 (a) shows the detailed Nusselt number contour for 45° angled configuration. In this particular configuration, the 45˚ angled ribs induce secondary flows at an angle approximately 45˚ with the bulk fluid direction. This rib induced secondary flow travels along the rib, and has maximum strength along the ribs. Also, the bulk fluid interacts with the induced secondary flow and transports them downstream of the rib, thus causing heat transfer enhancement on the bottom wall due to increase in wall shear. The basic mechanism of heat transfer enhancement due to rib is because of the increase in wall shear from the increase in near-wall turbulence due to rib induced secondary flows, and due to transport of relatively hot fluid near the bottom wall (featuring ribs) to the core of the channel. The rate of transport of the hot fluid from ribbed wall depends upon the nature of rib induced secondary flows. The heat transfer mechanism by re-attachment of coolant separated due to ribs results in much higher augmentation, while the heat transfer due to coolant transport from bottom to top wall results in more uniform and persistent heat transfer augmentation, but the contribution towards the overall heat transfer augmentation by the later mechanism is smaller than the former. From the Nusselt number contour plot of 45˚ angled ribs, it can be seen that thermal boundary layer started to develop near the outer wall, as the strength of rib induced secondary flow started diminishing as it approached the outer wall (refer Fig. 2.3 for terminology).

The bend region features a strategically placed 90˚ rib which adds to the structural integrity of the gas turbine airfoil featuring multi-pass channel. The flow while making the 180˚ turn, interacts with the rib and results in high heat transfer due to combined effects of secondary flows induced due to last 45˚ angled rib in the first pass, the 90˚ rib in the bend and the bend

induced secondary flows. In a smooth two-pass duct without a 90˚ rib in bend region, dean-type vortices (symmetrical in nature) are formed in bend due to the combined effects of centrifugal force acting on turning fluid and pressure gradient induced by the curvature. These flow structures are affected both by the presence of 90˚rib and the rib shapes present upstream and downstream of the bend. Comparisons of heat transfer augmentation in the bend region have been shown in a later section. Post 180˚ turn, the greater part of the coolant momentum flux lies closer to the outer wall, which interacts with the secondary flow induced by the first 45˚ angled rib in the second pass, resulting in more uniformly spread heat transfer enhancement ascribed to the diminished thermal boundary layer development along the outer wall. As the flow travels further downstream, the coolant momentum flux distribution along the spanwise direction becomes more uniform and trend of heat transfer enhancement in the second pass starts to mimic that seen in the first pass.

The second configuration was the dimpled two-pass channel, where the dimples were packed between the two ribs, and aligned in the form of 45˚ angled rib. The reason behind such an arrangement is to enhance the rib induced secondary flow effects on heat transfer augmentation. As discussed earlier, the periodic vortex shedding from the core of the dimple results in higher heat transfer in the downstream endwall.

It can be seen that higher heat transfer enhancement regions are present downstream of each dimple, and one half of the dimple endwall. The first half of the dimple endwall witnesses lower heat transfer due to recirculating fluid.

The third configuration resulted from the simple addition of the previous two configurations. The ideology behind the design of the compound channel is to utilize the individual merits associated with ribs and dimples. Ribs are associated with higher heat transfer and higher pressure penalty whereas dimples are known to have higher thermal hydraulic performance. The aim of the present study is to evaluate the combined effects of ribs and dimples on the thermal hydraulic performance of the two pass channel. It can be seen from the compound channel case of 45˚ angled configuration, that when the rib induced secondary flow interacts with cylindrical dimples, it leads to increased enhancement in heat transfer. The turbulent kinetic energy associated with the rib induced secondary flows is higher than the normal channel flow. Hence a dimpled bottom wall in a channel flow will lead to lower enhancement in heat transfer compared to the case where the channel flow comprises of the high

TKE secondary flows, which in the present case happens to be induced by rib turbulators. The design of compound channels can be viewed from two perspectives, enhancing heat transfer of a dimpled channel by introducing ribs, or enhancing heat transfer of rib turbulated channel by packing the rib pitches with dimples. In a later section, the thermal hydraulic performance of rib alone, dimple alone and rib-dimple compound channel will be evaluated and discussed.

Figure 2.7 (b) shows the V configuration detailed Nusselt number contours. The V shape rib can be considered to be equivalent of two 45˚ ribs joined at the center of the channel, where each arm of the V shape is exactly half the length of the 45˚ angled configuration rib. The angle between two arms of hence formed V shape rib is 45˚. The bulk fluid interacts with the sharp corner of V and induces a counter rotating vortex pair (CRVP), which travels towards the inner and outer wall of the channel. The TKE associated with these secondary flows, however, will be lower than that of the single secondary flow induced by the 45˚ angled rib configuration due to the smaller length of the arm, hence secondary flows will have shorter distance to traverse. A low heat transfer region could be identified just downstream of the rib, due to flow separation. The distribution of enhanced heat transfer regime in this case is more uniform (attributed to symmetry of rib induced secondary flows) when compared to the 45˚ angled rib configuration.

The dimple arrangement in between two rib pitches in the form of V results in similar type of heat transfer enhancement and the dimple arrangement has no such distinguishable effect when compared with all four types of arrangements. The role of dimples become significant in the compound channel case where the rib induced secondary flow interacts with cavities to further enhance heat transfer. In the case of V compound channel, the rib induced secondary flows travelling in opposite directions towards the inner and outer wall, first interact with the cylindrical dimples strategically placed in the direction of these secondary flows, resulting in increased heat transfer enhancement.

Figure 2.7 (c) shows the three configurations for W shape. The W shape ribs can be considered as two V shaped rib connected at the center. The length of each arm will thus be one-fourth of the single 45˚ angled rib. Due to the nature of W shape, it produces two CRVPs but the TKE associated with them will be lower than both 45˚ angled rib and V shape rib because of the reduction in the length of the arm of the rib. It can be seen that the effect of the two CRVPs is felt only slightly downstream of each rib in the first pass. After the flow turns 180˚ in the bend region, the bulk of the momentum flux is higher towards the outer wall and combines with one of

the CRVPs induced by the W rib resulting in increased heat transfer skewed towards the outer wall. This effect, however, decays rapidly as the flow passes over downstream ribs. W ribs combined with dimples result in increased heat transfer when compared to rib alone and dimple alone cases. However, since the enhancement in heat transfer caused by ribs was lower in comparison to 45˚ angled ribs and V shaped ribs, the W compound case also resulted in lower heat transfer enhancement when compared to 45˚ angled compound and V compound. One important conclusion which can be drawn, is the heat transfer enhancement associated with the compound channel is dependent on the heat transfer characteristics of the rib. Dimples play an important role of further enhancing the heat transfer, but the base level of heat transfer is dictated by the particular rib shape.

Figure 2.7 (d) shows the three configuration for M shape. The M shape can be considered as inverted W shape or two inverted V ribs connected at the center. The length of the arm of M shape rib is same as W shape rib. Similar to W shape rib, the strength of the secondary flows for M shape rib is lower in comparison to 45° angled ribs and V shape ribs. Heat transfer characteristics of W and M shaped ribs are similar. The compound case of M shape configuration also witness increased heat transfer when compared to the dimple alone and rib alone cases of the same configuration. However, the rib induced secondary flows due to M shape rib are not that effective in enhancing the heat transfer when dimples are packed in the rib pitches, compared to cases of 45° angled rib configuration and V shape configurations. However, heat transfer characteristics of M and W were found to be similar.

Detailed Nusselt number contours help designers in locating hot and cold spots in a configuration and help in making decisions on the parameters associated with any configuration. For example, in the ribbed configurations, it should be noted that rib-pitch-to-height ratio was chosen to be 16, where the traditionally found ratios lie between 8 to 12. The reason behind choosing a high rib-pitch-to-rib-height ratio was to pack the dimples in a certain pattern while maintaining a particular (optimum) dimple-depth-to-dimple-diameter ratio. The other geometrical constraint which affected the design decision was the increased 2D conduction errors encountered in sharp corners or 1D semi-infinite assumption validation for the case of very closely spaced dimples. These factors together lead to the final design of the configurations in the present study. However, when only rib cases are considered, it can be seen that large regions of low heat transfer enhancement can be found. The ideology behind choosing such

configuration for further enhancement in heat transfer, is that the high p/e rib configurations impose lower pressure drop penalty, and dimples are known to have higher thermal hydraulic performance relative to ribs. A combination of sparsely arranged ribs and densely packed dimples, was hence chosen for achieving higher overall thermal hydraulic performance for the rib-dimpled compound channels. Subsequent sections provide details about regionally averaged Nusselt number variation with streamwise distance.

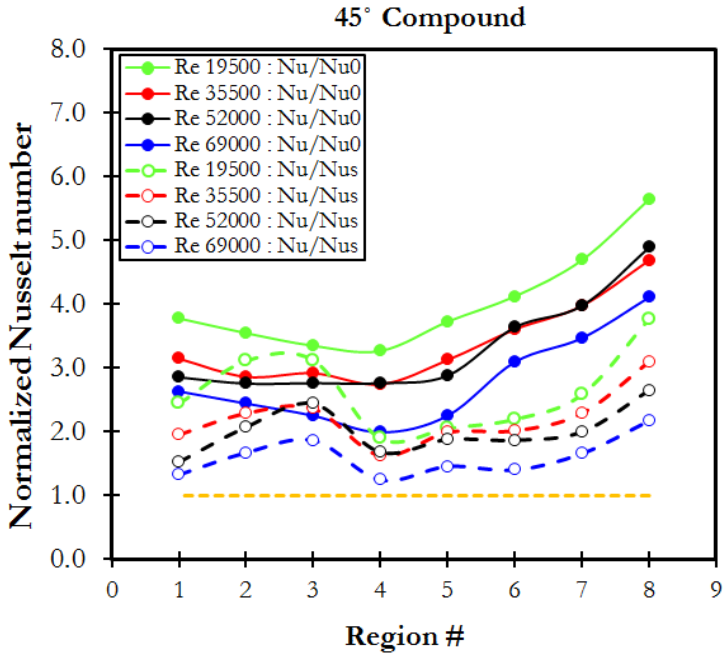

Figure 2.8 (a) Regionally averaged normalized Nusselt number for compound channels

Regionally Averaged Nusselt numbers

Figures 2.8, 2.9 and 2.10 show the regionally averaged Nusselt number variation with streamwise distance. The region numbers are indicated in Figs. 2.2 and 2.3. The data has been presented in two forms- Nu/Nu_0 (normalization with respect to Dittus-Boelter correlation for developed turbulent flow in smooth circular tube) and Nu/Nu_s (normalization with respect to regionally averaged Nusselt numbers obtained from experiments carried out on smooth two pass channel). This comparison provides insight into the importance of considering smooth plate normalization in order to evaluate the feature specific contribution to overall heat transfer enhancement.

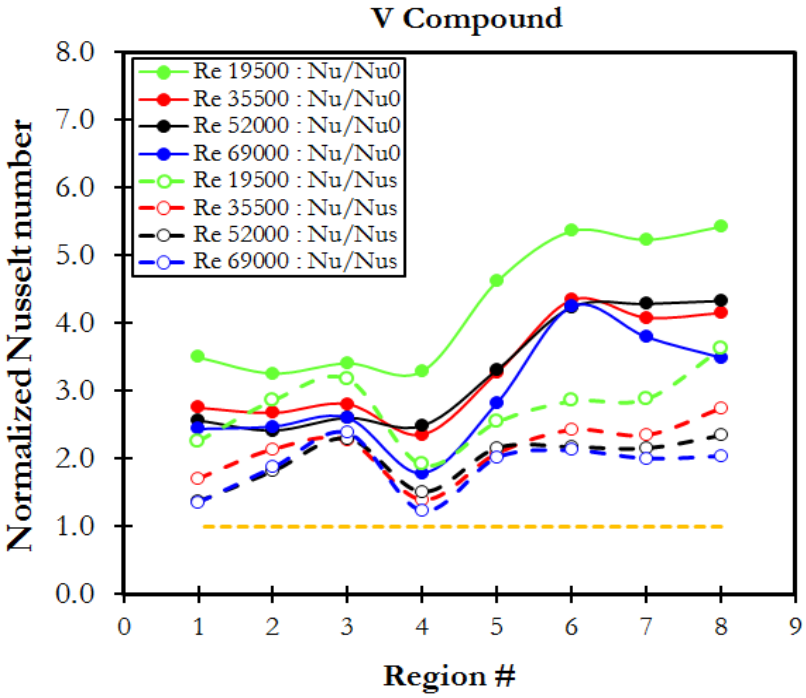

Figure 2.8 (b) Regionally averaged normalized Nusselt number for compound channels

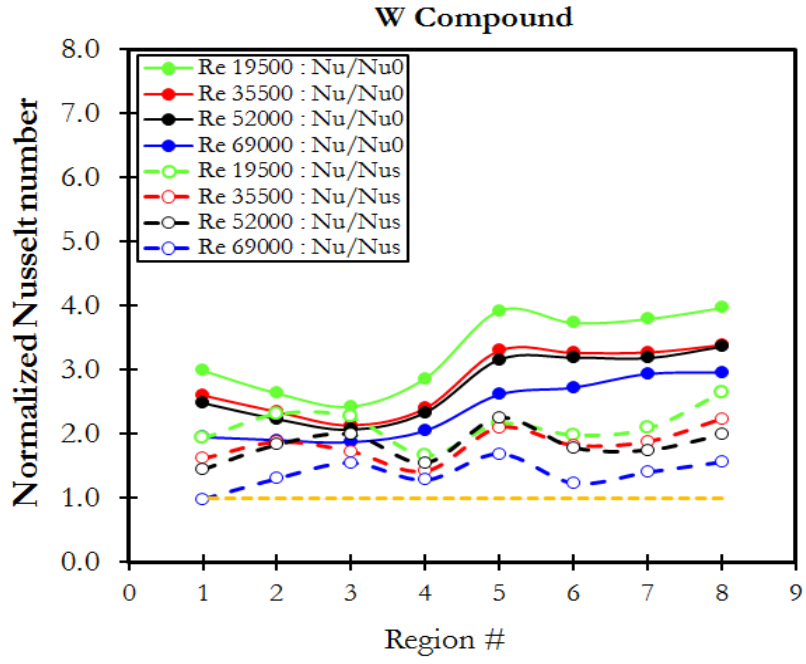

Figure 2.8 (c) Regionally averaged normalized Nusselt number for compound channels

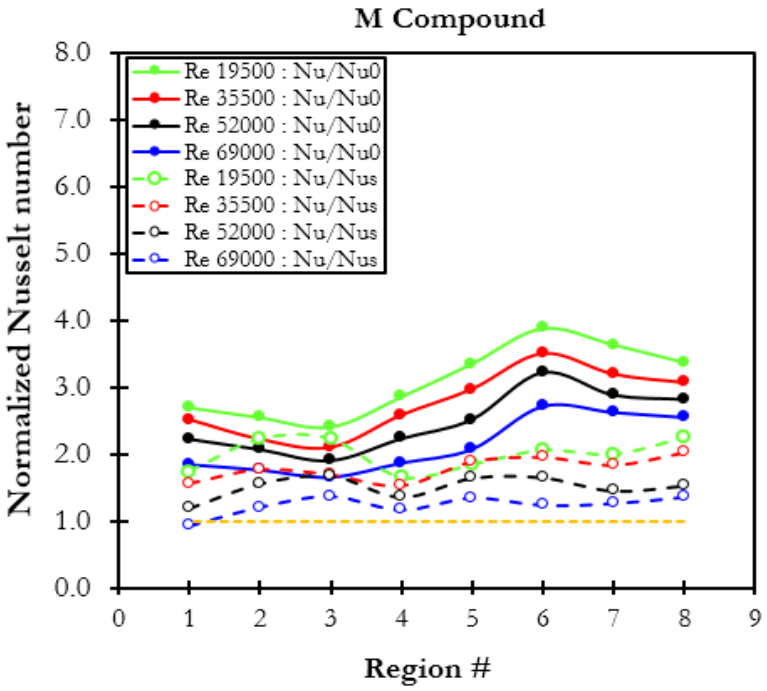

Figure 2.8 (d) Regionally averaged normalized Nusselt number for compound channels

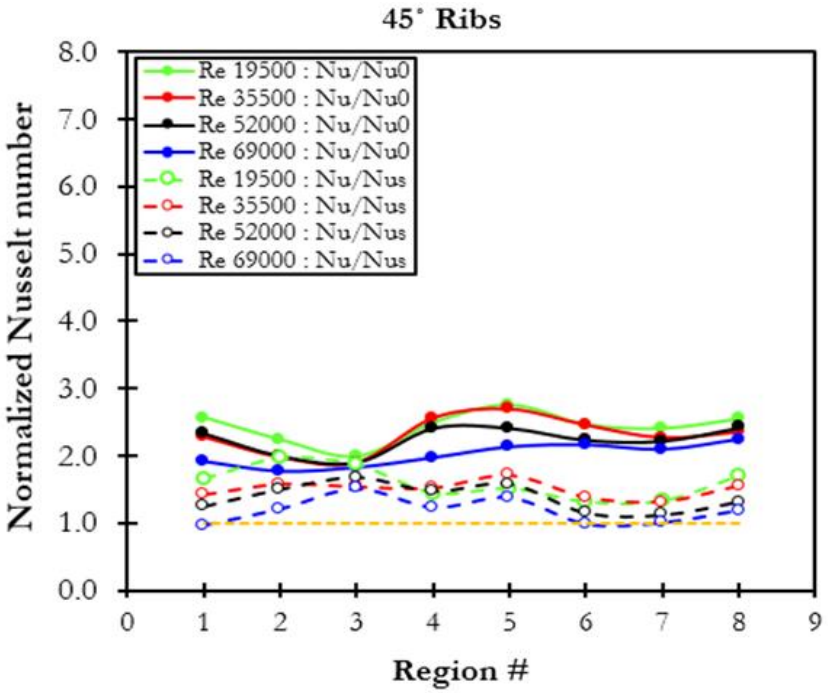

Figure 2.9 (a) Regionally averaged normalized Nusselt number for the ribbed channels

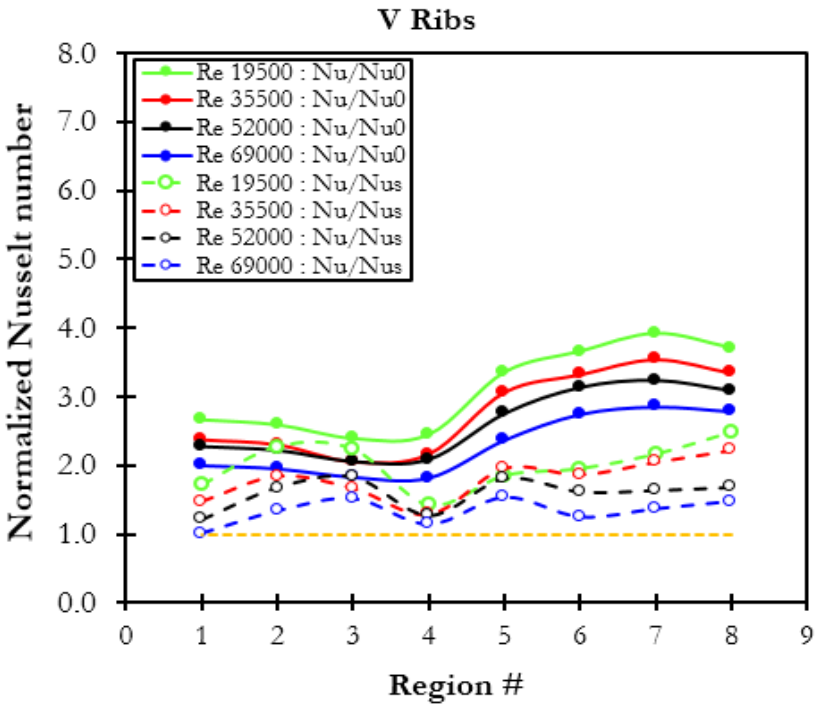

Figure 2.9 (b) Regionally averaged normalized Nusselt number for the ribbed channels

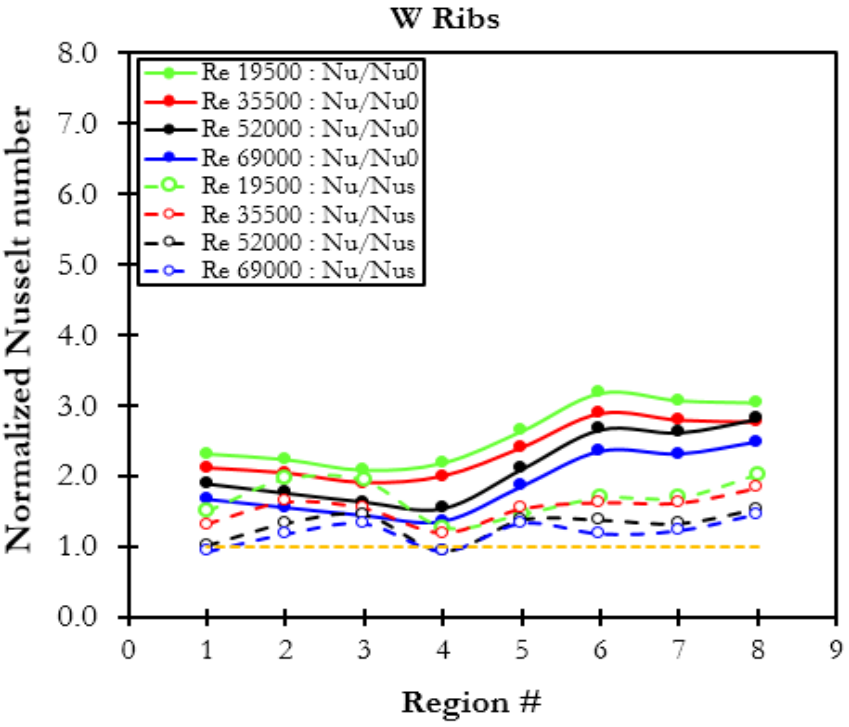

Figure 2.9 (c) Regionally averaged normalized Nusselt number for the ribbed channels

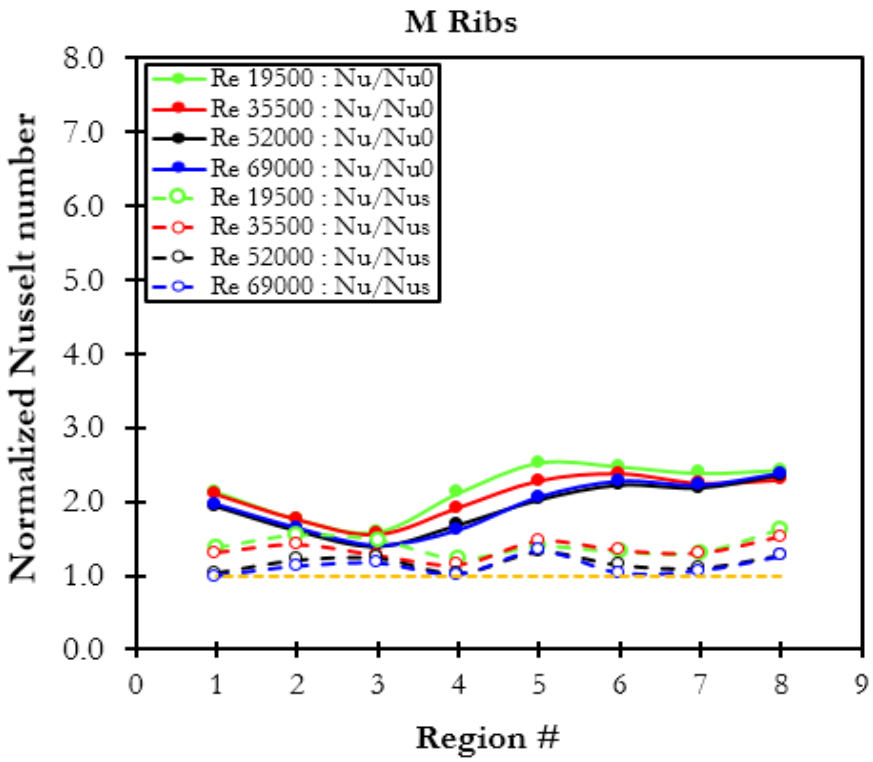

Figure 2.9 (d) Regionally averaged normalized Nusselt number for the ribbed channels

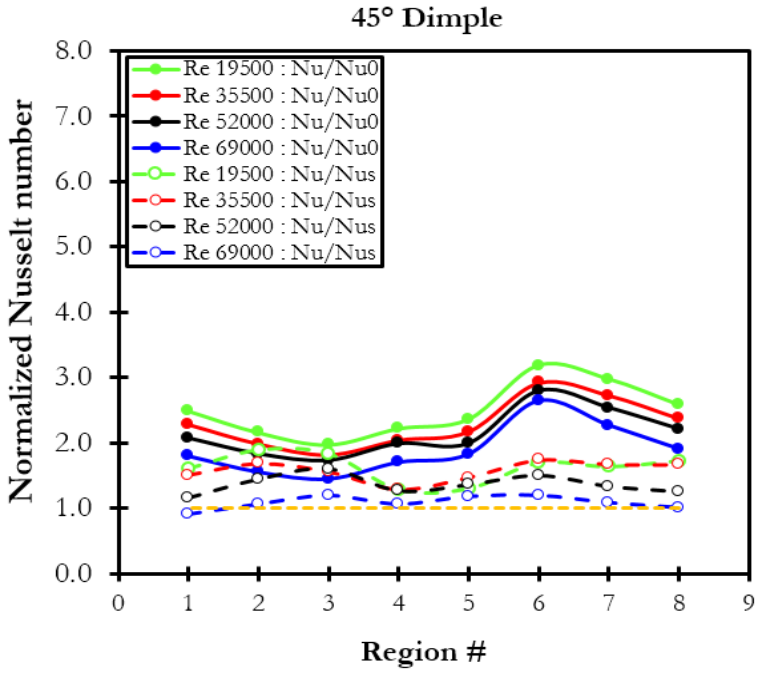

Figure 2.10 (a) Regionally averaged normalized Nusselt number for the dimpled channels

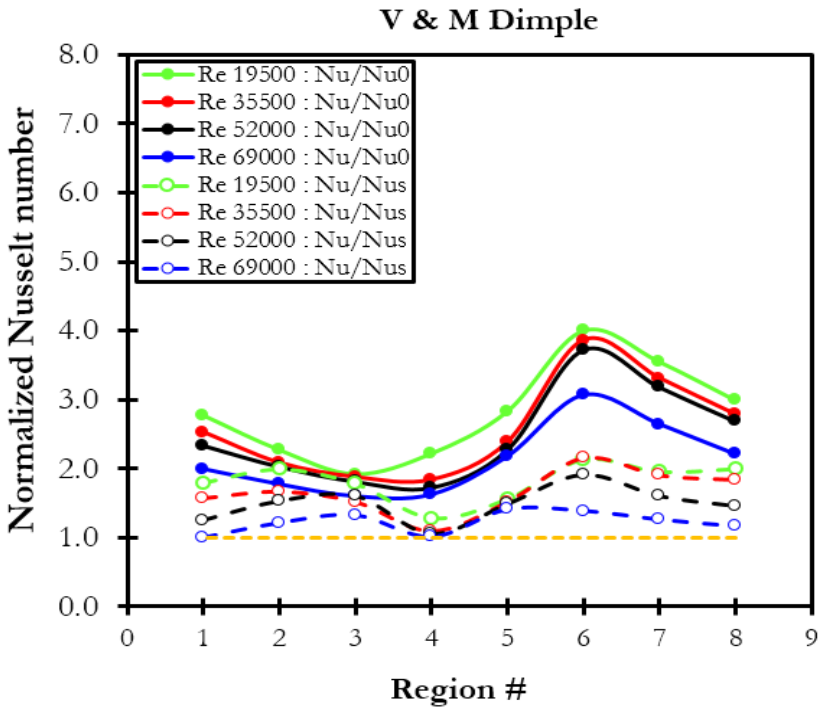

Figure 2.10 (b) Regionally averaged normalized Nusselt number for the dimpled channels

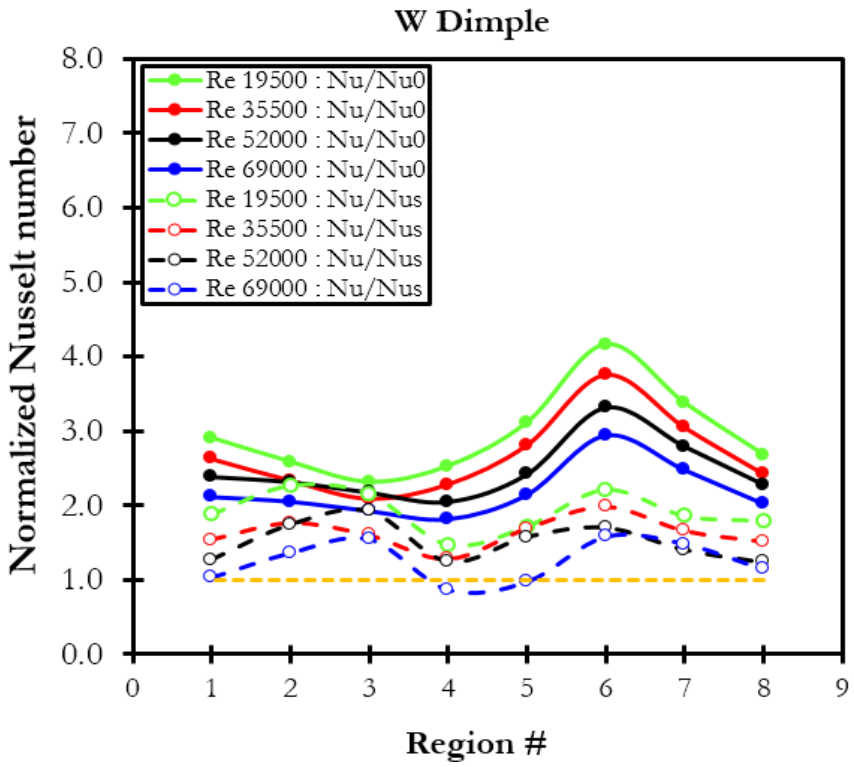

Figure 2.10 (c) Regionally averaged normalized Nusselt number for the dimpled channels

As expected, the Nu/Nu_0 trend for all configurations decrease in the first pass as the flow starts developing with increasing streamwise distance. The bend region (region #4 and 5) had an important role in the globally averaged heat transfer enhancement as it modifies the downstream heat transfer in the second pass. The heat transfer enhancement in the second pass stays more or less uniform as the flow moves downstream of the bend region for the V and W compound configurations, and decays for the M compound configuration.

Figure 2.8 shows the regionally averaged Nusselt number variation in the two pass channel featuring both ribs and dimples. The 45° compound configuration showed increasing heat transfer enhancement with increasing streamwise distance in the second pass because of the rib specific heat transfer characteristics of the configuration, which was further enhanced by the presence of dimples between the rib pitches and aligned in the direction of the secondary flows. As discussed earlier, the momentum flux of the coolant was skewed towards the outer wall in the second pass, and the rib induced secondary flows in the second pass also travelled from inner to outer wall. Hence, when the momentum flux of the coolant becomes more uniformly distributed (around region 6), the secondary flow travelling from inner to outer wall creates the extra turbulent mixing. Thus, the combined effects of bend induced turbulent mixing and rib induced secondary flows for the 45° angled configuration leads to increasing heat transfer enhancement trend in the second pass compared to other configurations, particularly W and M shapes. As discussed earlier, in the case of W and M shape compound configurations, the rib induced secondary flow strength was the weakest due to reduced rib arm length, and also the secondary flows induced by these rib shapes align in the direction of bulk coolant motion, hence leading to symmetric flow around the centerline of the channel. The secondary flows induced by the ribs present in the V compound configuration on the other hand has somewhat similar characteristics when compared to 45° angled compound configuration case. In this case, the secondary flow travels towards both, the inner wall and the outer wall, with strength slightly lower than the 45° angled compound configuration case. The combined effects of the skewed momentum flux, rib induced secondary flows, arrangement of dimples doesn't however accumulate to provide increasing trend of heat transfer enhancement with increasing streamwise distance in the second pass, in the case of V compound configuration.

The Nu/Nu_s trends provide some interesting information about heat transfer enhancement features. As can be seen from Fig. 2.6, the flow in the first pass of the smooth two pass channels

gets almost developed (thermally) when it approaches the bend region. This leads to decreasing heat transfer with increasing streamwise distance in the first pass (Fig. 2.6(b)). The gradient of decay of heat transfer for the smooth channel is greater than those configurations having heat transfer enhancement features. As a result, the regionally averaged Nusselt number normalized by those obtained from the smooth channel, shows an increasing trend in the first pass. This trend was observed for all the twelve configurations studied. The compound and the ribbed configurations featured a 90° rib in the bend region which connects the divider wall to the bend outer wall. The heat transfer enhancement in the bend region was only slightly higher when compared to the smooth channel, due to the presence of the 90° rib. For all the configurations and all the Reynolds number studied, the enhancement levels in heat transfer in the bend region converge to a value (close to unity), smaller than those obtained in the first and second pass. This implied that heat transfer enhancement evaluation of features in a two-pass channel must consider the contribution of bend and its effect on downstream heat transfer in the second pass.

Figure 2.9 shows the regionally averaged Nusselt number variation in the two pass channel featuring ribs alone. The trends of Nu/Nu_0 and Nu/Nu_s in first pass, bend and second pass for rib turbulated channels closely mimic to those observed for two-pass compound channels (Fig. 2.8). In rib turbulated channels also, the bend had a major contribution in heat transfer in the bend region and the second pass.

Figure 2.10 shows the regionally averaged Nusselt number for the dimpled channels. The trend of heat transfer enhancement for dimpled channels in the first and second pass, is similar to those of compound and rib turbulated channels. The dimpled channels did not feature a 90° rib in the bend region. In the bend region, the Nu/Nu_s tend towards unity for all the dimple configurations, which implies that arrangement of dimples in first and second pass didn't affect the heat transfer enhancement in the bend region. The reason behind this trend is that the mechanism of heat transfer enhancement due to dimples is different in comparison to ribs. In the case of dimples, the effect of one dimple is felt just downstream of the dimple and the enhancement in heat transfer due to one dimple decays at a much faster rate when compared to those of ribs.

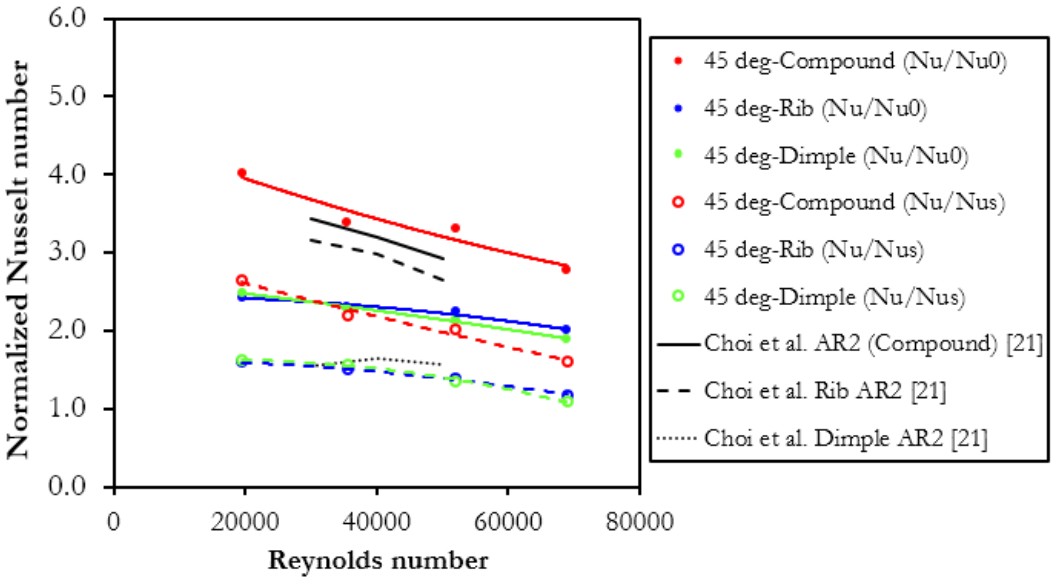

Figure 2.11 (a) Globally averaged Nusselt number variation with Reynolds number for 45° configuration

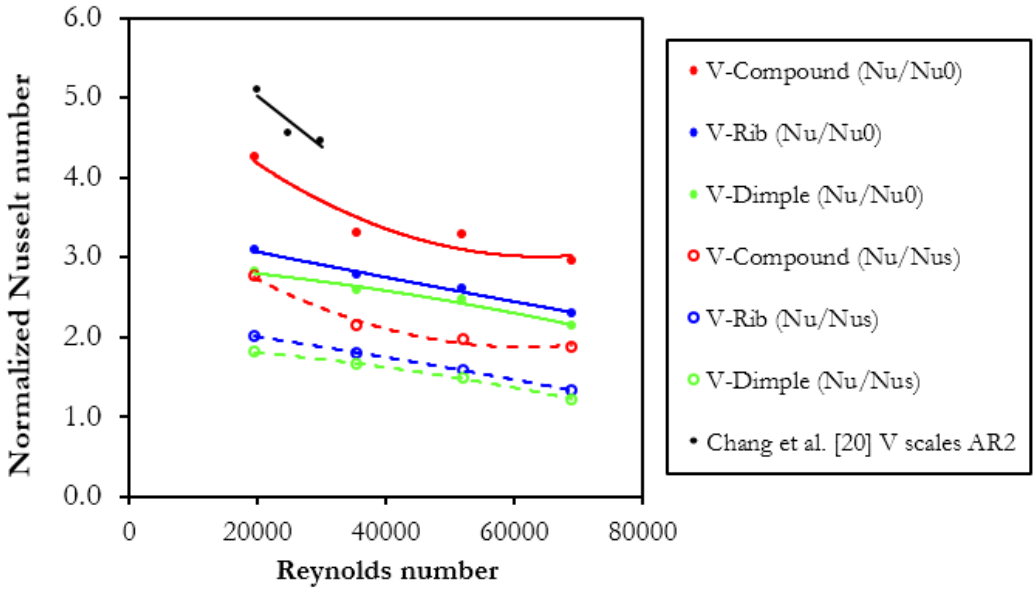

Figure 2.11(b) Globally averaged Nusselt number variation with Reynolds number for V configuration

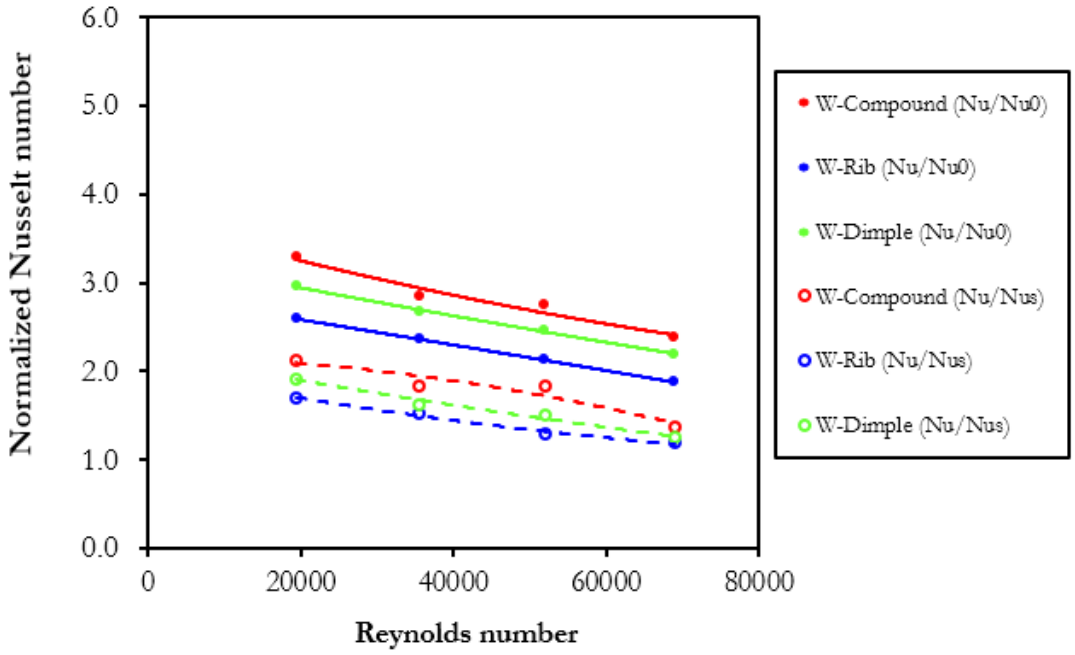

Figure 2.11(c) Globally averaged Nusselt number variation with Reynolds number for W configuration

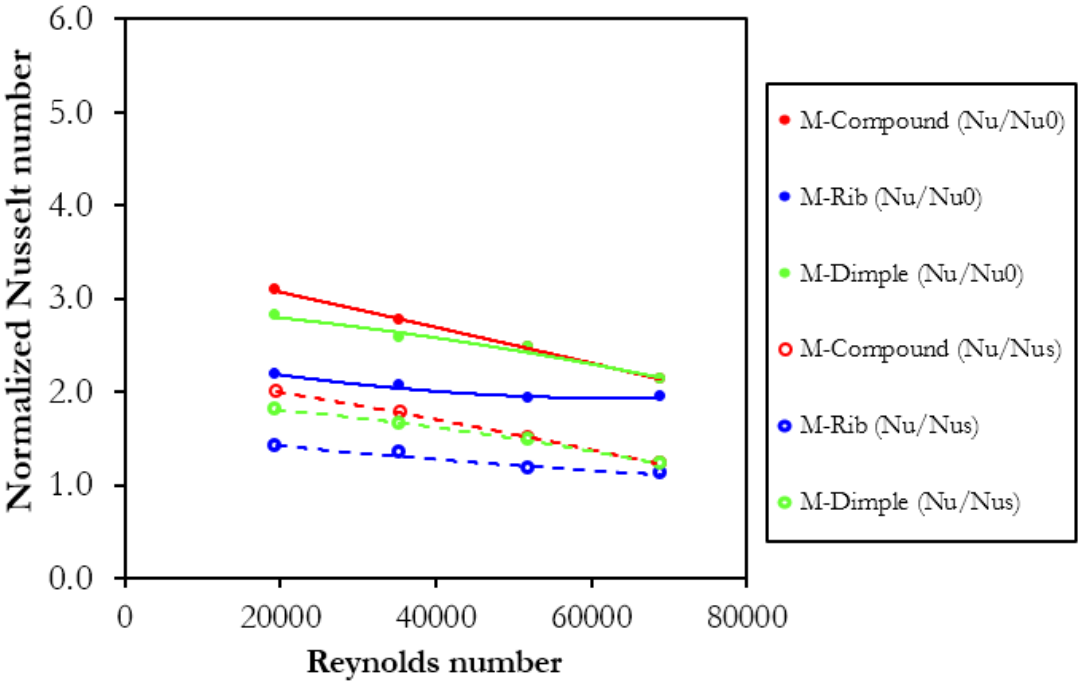

Figure 2.11(d) Globally averaged Nusselt number variation with Reynolds number for M configuration

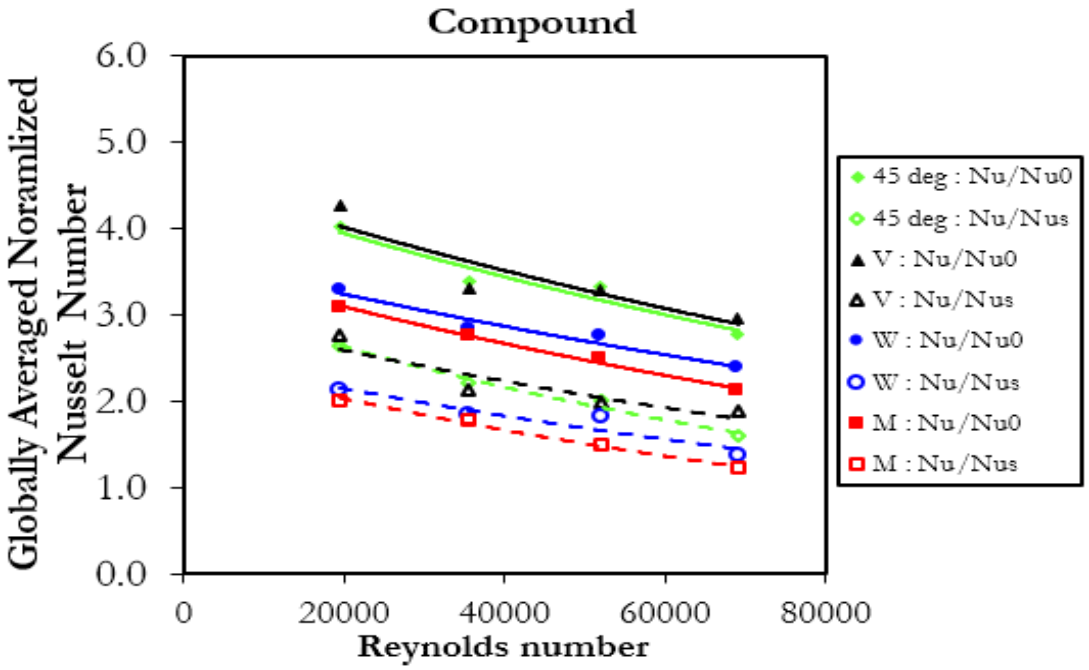

Figure 2.12 (a) Globally averaged normalized Nusselt number variation with Reynolds number for Rib-dimpled Compound configurations

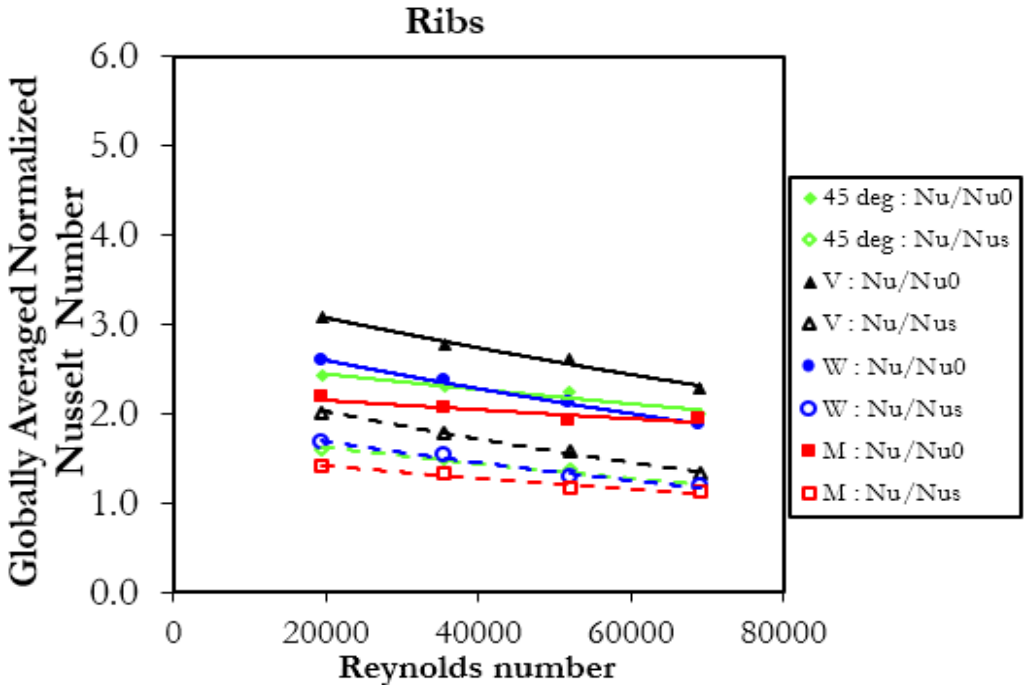

Figure 2.12 (b) Globally averaged normalized Nusselt number variation with Reynolds number for Ribbed configurations

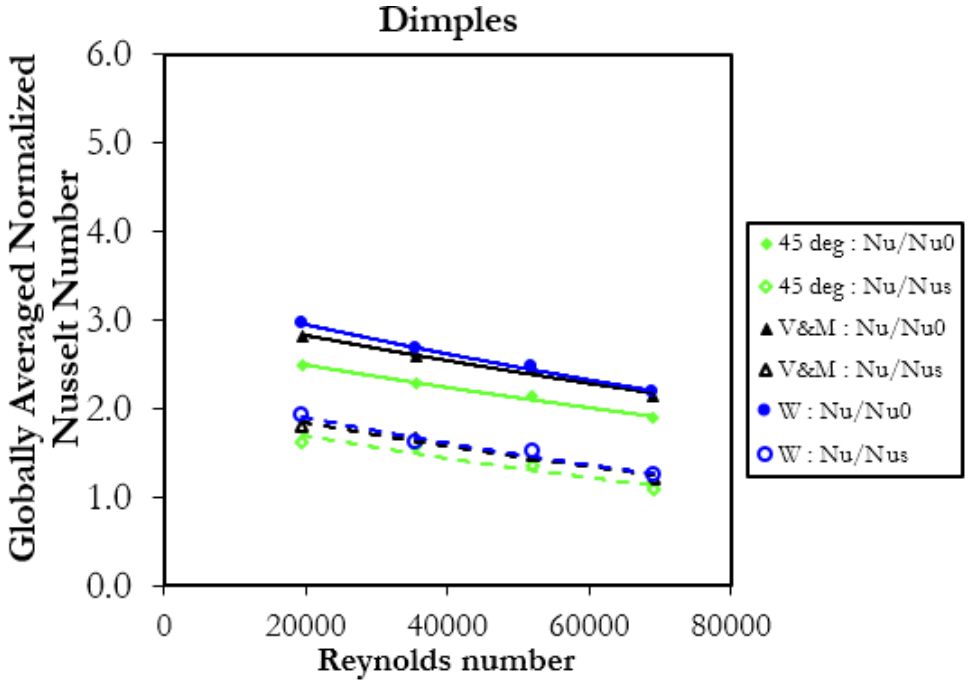

Figure 2.12 (c) Globally averaged normalized Nusselt number variation with Reynolds number for Dimpled configurations

Globally Averaged Nusselt number variation with Reynolds number

Figure 2.11 shows the variation of globally averaged Nusselt number with Reynolds number. The plots are arranged for comparison between compound, rib and dimpled channels for four different configurations studied. The compound channels had higher heat transfer enhancement for all the four configurations studied. Figure 2.11(a) shows the comparison of heat transfer enhancement of 45° compound channel with Choi et al. [2.16]. The order of heat transfer enhancement levels for compound, rib and dimpled channels have the same trend in the current study and the study carried out by Choi et al [2.16].

In their study [2.16], the configuration details were: p/e of 10, single pass channel, 60° angled ribs and spherical dimples. The present study has higher p/e compared to [2.16], hence the heat transfer enhancement due to rib turbulated channel is lower in the present case. The levels of heat transfer enhancement for the dimpled channel in the present study was higher when compared to [2.16] due to the shape and packing of dimples between two consecutive rib pitches.

Comparisons have been made for the V compound case with Chang et al. [2.15]. The globally averaged Nusselt number reported by [2.15] was found to be slightly higher in

comparison with the present study. The reason for the higher heat transfer enhancement levels in [2.15] can be attributed to the fact that the p/e was 10 and the dimples (referred as "deepened scales") were very closely packed in their study [2.15]. For both 45° and V configurations, the heat transfer enhancement levels by rib alone case and dimple alone case was similar, however these levels were much lower than the corresponding compound channel cases.

The heat transfer characteristics of W and M configurations were found to be similar to each other. For M configuration, the compound channel had similar levels of heat transfer enhancement when compared to their dimpled cases, where the compound configuration heat transfer enhancement was on the higher side. The ribbed cases of W and M channels had lower levels of enhancement compared to the compound and dimpled channels.

On comparison of all the four configurations, it can be noticed that addition of dimples in the rib pitches are effective when the heat transfer enhancement due to rib alone configurations are high. In other words, the rib shapes which have higher heat transfer enhancements, when combined with dimples, seem to result in higher levels of heat transfer enhancements in the present study.

Comparison of Globally Averaged Nusselt numbers for Different Types of Configurations

Figure 2.12 shows the comparisons among the compound, rib and dimple configurations. The 45° compound and V compound configurations have similar heat transfer enhancement levels and higher than W and M configurations. In the rib alone configurations, the decreasing order of heat transfer enhancement levels was, V, 45° angled, W and M. The arrangement of dimples also showed some effects on the globally averaged heat transfer enhancement. The total number of dimples in each configuration was same, and the decreasing order of heat transfer enhancement was, W, V&M and 45° angled arrangement of dimples. An interesting observation can be drawn for the 45° angled configuration. The 45° rib had lower enhancements in heat transfer when compared with V ribs, and 45° angled arrangement of dimples was lower than both W, V&M arrangement, but the combination of ribs and dimples aligned at 45° resulted in the highest level of heat transfer enhancement. Both 45° angled compound and V compound configurations showed promise and should be studied in more detail from parametric point of view. A systematic optimization study is required to come up with the normalized dimensions which define a particular configuration and which lead to highest heat transfer enhancement.

Friction losses and Thermal Hydraulic Performance of two-pass channel

The heat transfer enhancement comes at a cost of increased requirements of inlet pressure in order to maintain a particular Reynolds number across a configuration. The aim of heat transfer enhancement research is to develop configurations which have higher thermal hydraulic performance. The following definitions are important for further discussion on frictional losses and thermal hydraulic performance in a two-pass channel.

$$f = \frac{(\Delta p)_{two-pass}}{2\rho u^2}\frac{d_h}{L} \quad (Eq.\,2.5)$$

$$f_0 = 0.079Re^{-0.25} \quad (Eq.\,2.6)$$

$$f_s = \frac{(\Delta p)_{two-pass,smooth}}{2\rho u^2}\frac{d_h}{L} \quad (Eq.\,2.7)$$

$$THP_0 = \frac{(Nu/Nu_0)}{(f/f_0)^{1/3}} \quad (Eq.\,2.8)$$

$$THP_s = \frac{(Nu/Nu_s)}{(f/f_s)^{1/3}} \quad (Eq.\,2.9)$$

The normalized friction factor (f/f_0) increases with Reynolds number, and is an expected trend (Fig. 2.13). The friction factor normalized with smooth two-pass channel friction factor (f_s), resulted in a decreasing trend with increase in Reynolds number. For all the four configurations, the compound channels have the highest frictional losses, followed by rib and then the dimpled channels.

Figure 2.14 shows the thermal hydraulic performance of all the configurations studied. For 45° angled and V configurations, the compound channels have the highest THP followed by dimples and ribs, which have similar thermal hydraulic performances. The V compound channel in particular showed an asymptotic nature of THP with Reynolds number and thus might be considered as a potential candidate for high Reynolds number applications, such as land based gas turbines. For the W and M configurations, the dimpled channel showed highest thermal hydraulic performance followed by the compound and rib configurations. Since, the heat transfer enhancement for W and M compound channels are either similar, or slightly higher than the corresponding dimpled channels, the increased pressure penalty for the compound cases, led to corresponding lower levels of THP.

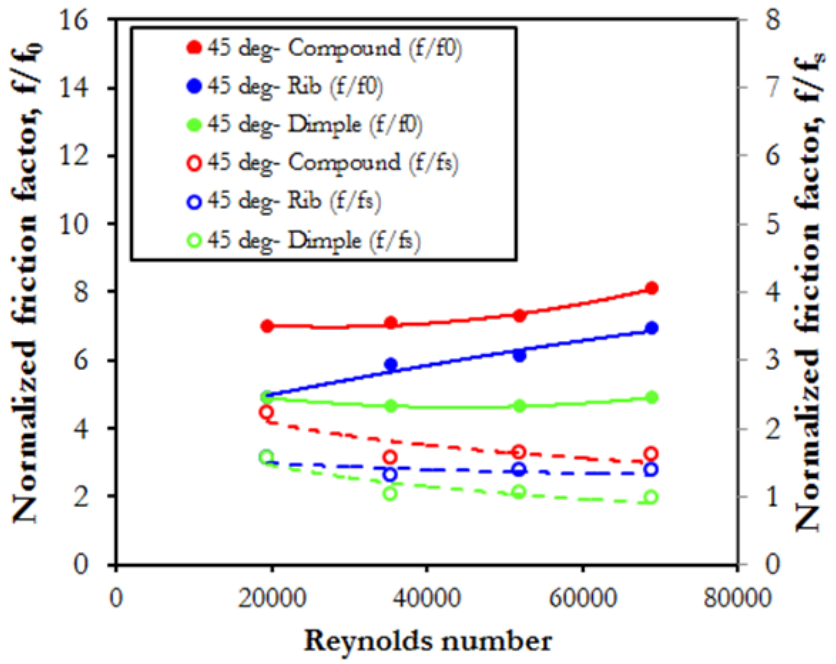

Figure 2.13 (a) Normalized Friction factors for 45° configuration

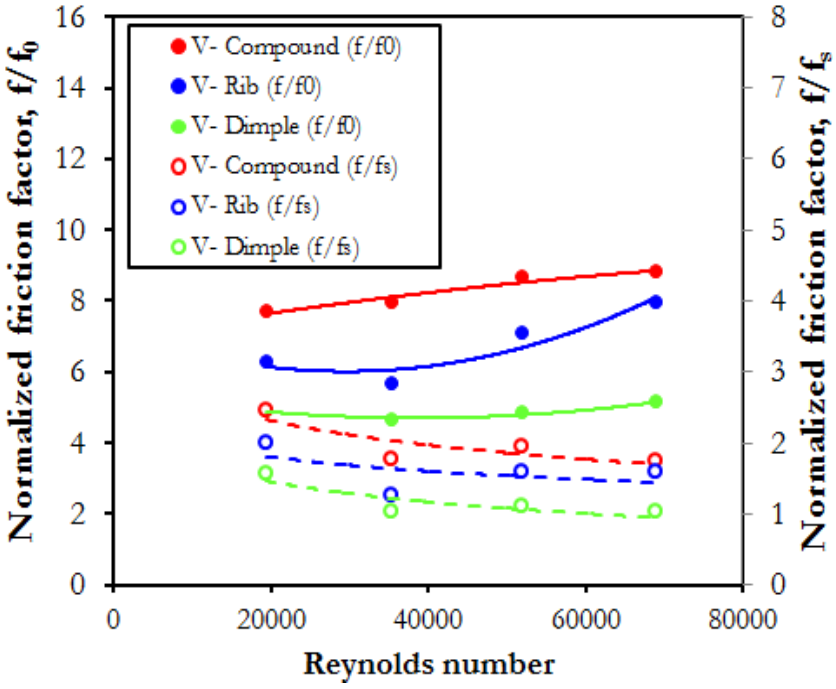

Figure 2.13 (b) Normalized Friction factors for V configuration

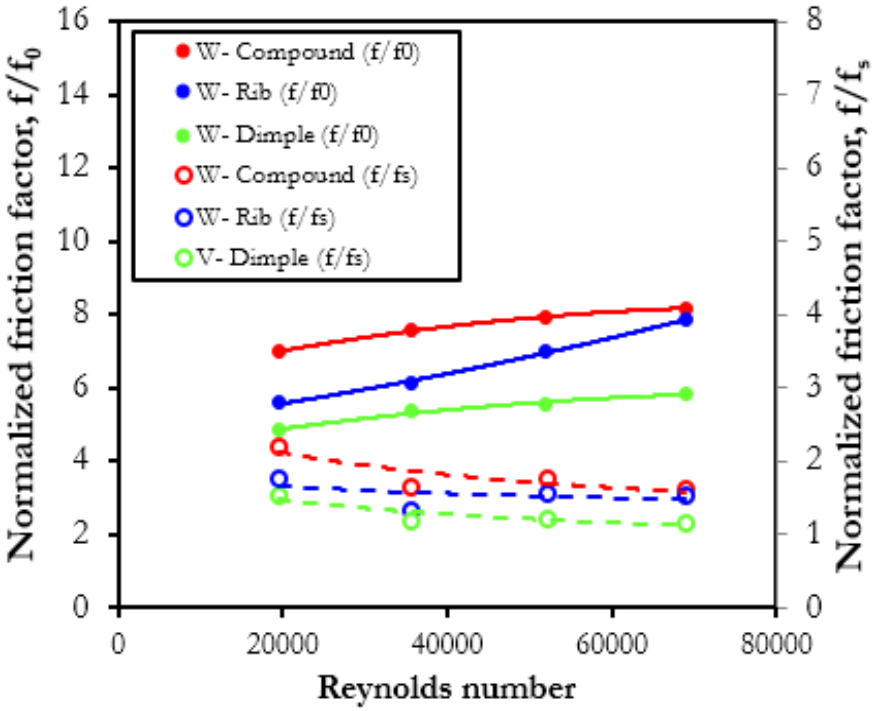

Figure 2.13 (c) Normalized Friction factors for W configuration

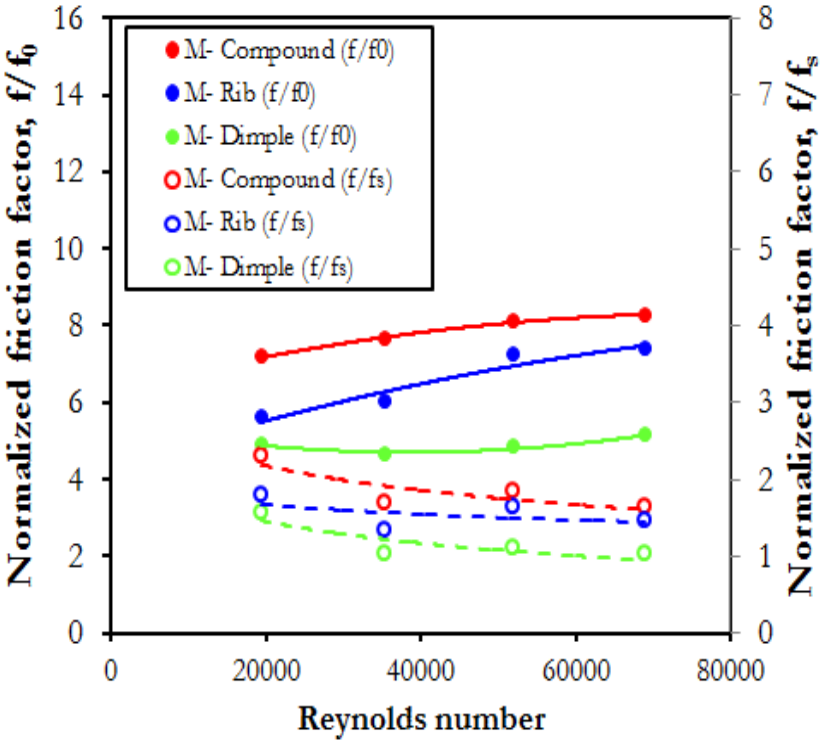

Figure 2.13 (d) Normalized Friction factors for M configuration

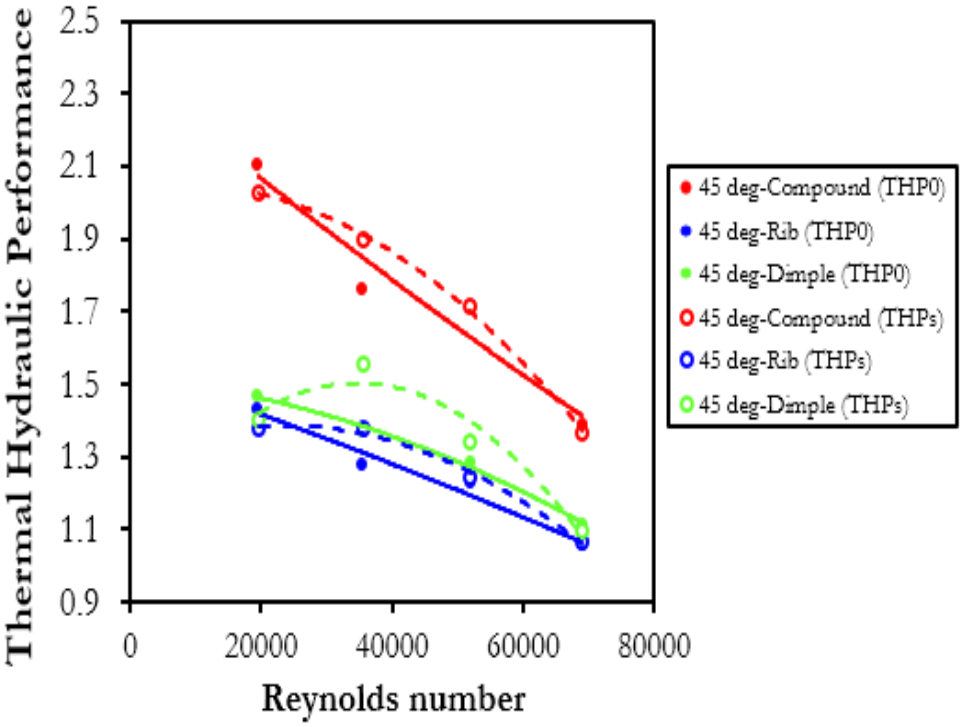

Figure 2.14 (a) Thermal Hydraulic Performance for 45° configuration

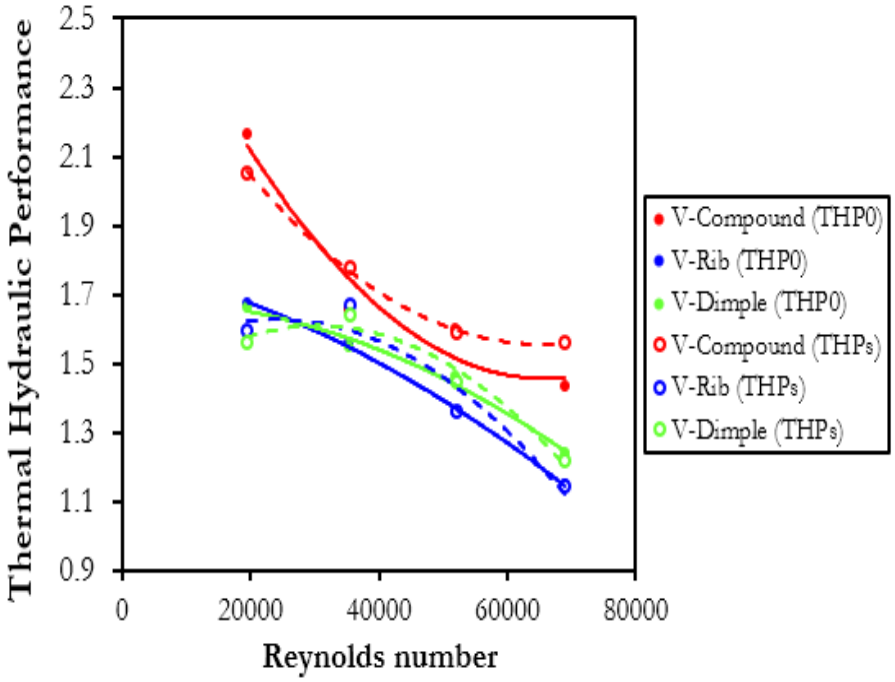

Figure 2.14 (b) Thermal Hydraulic Performance of V configuration

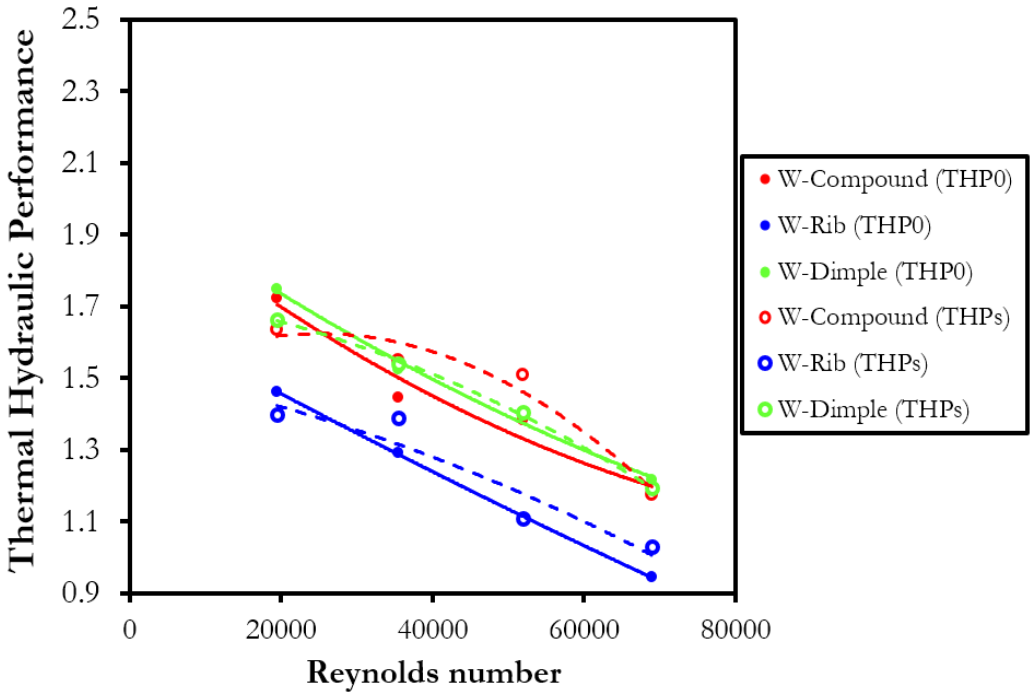

Figure 2.14 (c) Thermal Hydraulic Performance of W configuration

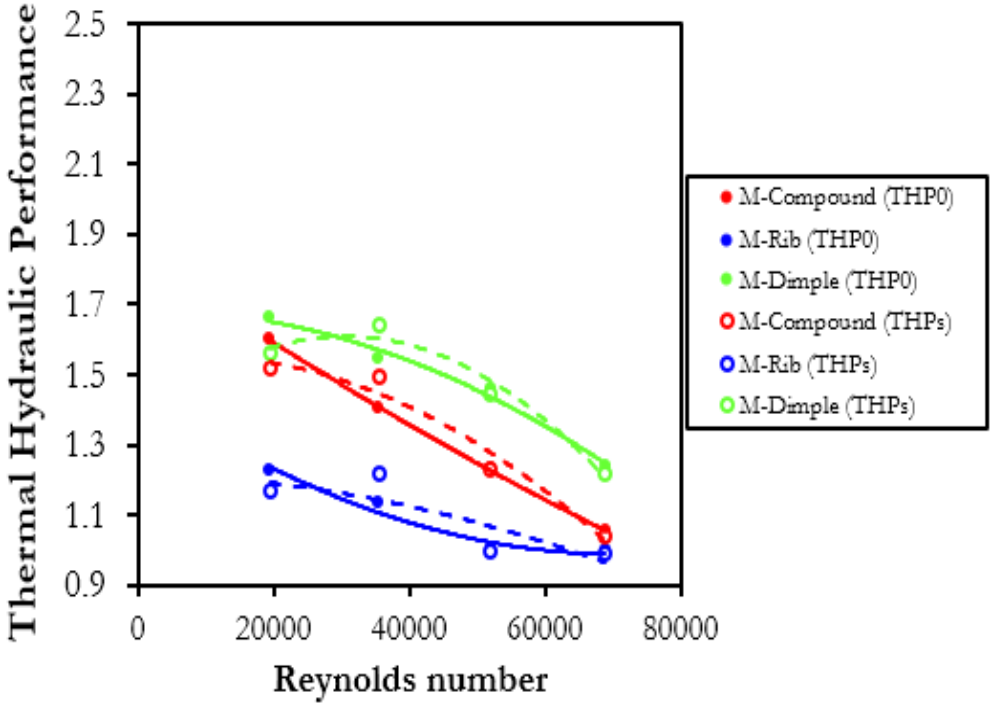

Figure 2.14 (d) Thermal Hydraulic Performance of M configuration

Heat transfer correlations

As shown earlier, the heat transfer enhancement has been presented in two forms, (a) normalized with respect to Dittus-Boelter correlation for developed turbulent flow in smooth circular duct, (b) Nusselt number normalized with corresponding smooth channel results. In this section, two different correlations are provided for globally averaged heat transfer. Following are the forms of correlation,

$$\overline{\overline{Nu}} = aRe^{b} \quad \forall \ Re \in [19500, 69000] \quad (Eq. 2.10)$$

$$\overline{\overline{\left(\frac{Nu}{Nu_s}\right)}} = a \ \times \exp\left(-b\sqrt{Re}\right) \quad \forall \ Re \in [19500, 69000] \qquad (Eq. 2.11)$$

Equation 2.10 represents scaling of globally averaged Nusselt number with Reynolds number. Since, Nusselt number from Dittus-Boelter correlation is known, hence only globally averaged Nusselt number has been correlated to Reynolds number. Figure 15 shows the scatter of globally averaged Nusselt number (Eq. 2.10) obtained from the correlation and those obtained experimentally. It can be seen that ~ 94% of the total data points lie in ±5% band and the rest lie in ±5% to ±10% band. The reader can use Eq. 2.10 in conjunction with Dittus-Boelter correlation to obtain $\overline{\overline{\left(\frac{Nu}{Nu_0}\right)}}$. The correlation coefficients for Eq. 2.10 has been provided in Table 2.1.

Equation 2.11, on the other hand, provides the globally averaged Nusselt number enhancement with respect to smooth channel heat transfer obtained experimentally in the present study. Since smooth channel heat transfer will be different for different studies, Eq. 2.11 will be proved helpful for CFD validation and confirmation of similar experimental studies. Also, for gas turbine blade designers, Eq. 2.11 provides enhancement factors for a wide range of Reynolds numbers from 19500 to 69000. Figure 2.16 shows the scatter of globally averaged Nusselt number (normalized with respect to smooth channel heat transfer) (Eq. 2.11) obtained from the correlation and those obtained experimentally. It can be seen that ~ 85% of the total data points lie in ±5% band and the rest lie in ±5% to ±10% band. The correlation coefficients for Eq. 2.11 has been provided in Table 2.

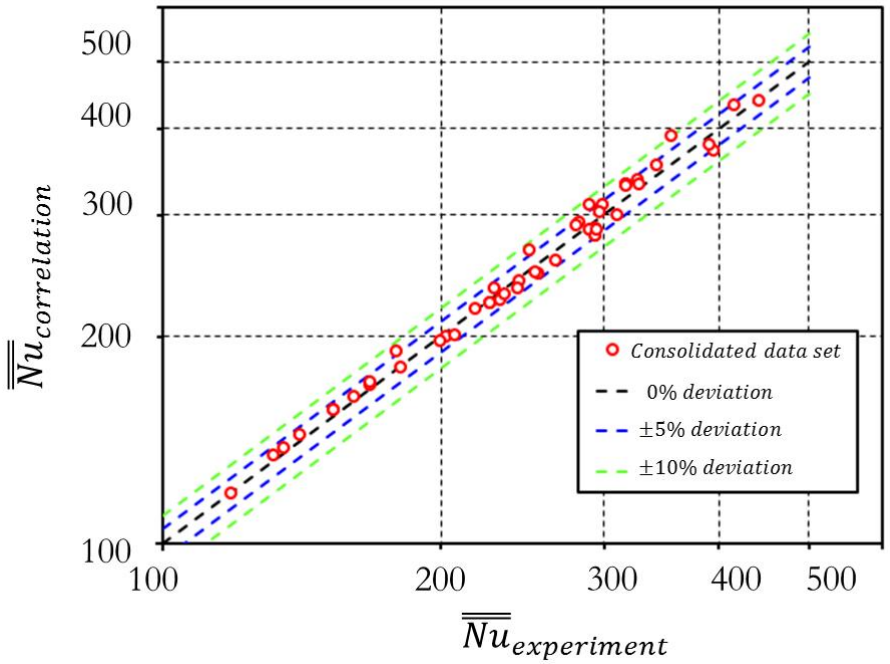

Figure 2.15 Comparison of globally averaged Nusselt number obtained from correlation shown in Eq. 10 with experiments

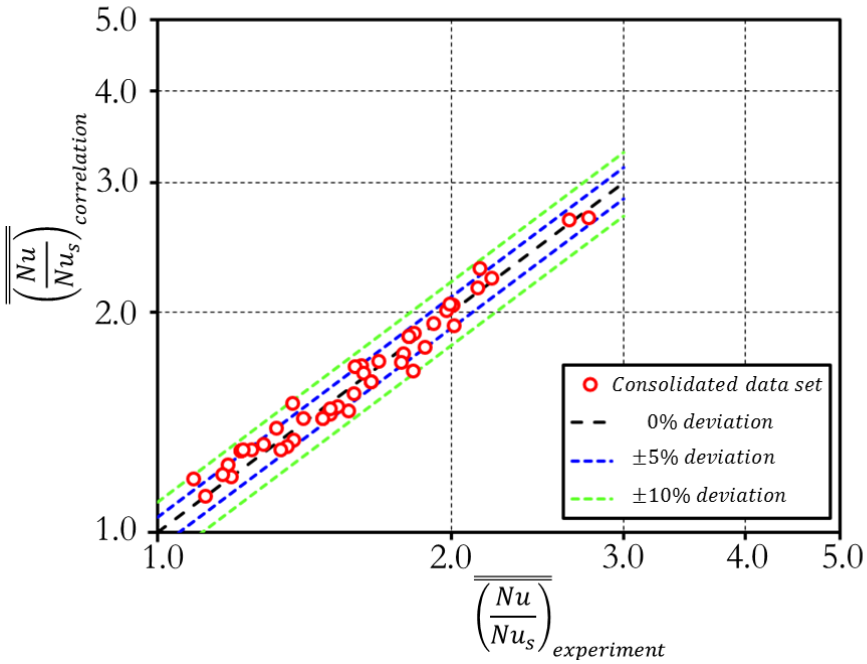

Figure 2.16 Comparison of heat transfer enhancement obtained from correlation shown in Eq. 11 with experiments

Table 2.1 Correlation coefficients from Eq. 10

Configuration	Type	Correlation Coefficients	
		a	b
45°	Rib	0.190	0.664
	Dimple	0.384	0.595
	Compound	1.090	0.537
V	Rib	0.559	0.579
	Dimple	0.424	0.598
	Compound	1.226	0.528
W	Rib	0.612	0.553
	Dimple	0.571	0.573
	Compound	0.685	0.569
M	Rib	0.119	0.698
	Dimple	0.424	0.598
	Compound	1.021	0.519
Smooth		0.013	0.889

Conclusions and Recommendations

Experiments have been carried out to investigate heat transfer and pressure characteristics of two-pass channel featuring several unique combinations of rib shapes with cylindrical dimples packed in the rib pitches. Four different rib shapes and dimple arrangements have been studied, viz. 45° angled, V, W and M. Detailed heat transfer coefficients were measured using transient liquid crystal thermography. Experiments were carried out for Reynolds number ranging from 19500 to 69000. Also, pressure drop was measured across the two pass channel in order to calculate the thermal hydraulic performance. Following conclusions can be drawn from the present study:

(a) For two pass channels, it is important to evaluate the heat transfer characteristics in reference to a similar two pass channel with no features, as the 180° bend has significant contribution in heat transfer and pressure loss in the second pass. Also, the thermally under-

developed flow in the first pass had significant contribution on heat transfer enhancement in the first pass, particularly in the initial few rib pitches.

Table 2.2 Correlation coefficients from Eq. 11

Configuration	**Type**	**Correlation Coefficients**	
		a	**b**
45°	Rib	2.232	2.250e-3
	Dimple	2.521	2.880e-3
	Compound	4.488	3.743e-3
V	Rib	3.174	3.157e-3
	Dimple	2.789	2.937e-3
	Compound	4.257	3.300e-3
W	Rib	2.586	2.952e-3
	Dimple	3.026	3.235e-3
	Compound	3.255	2.954e-3
M	Rib	1.888	1.993e-3
	Dimple	2.789	2.937e-3
	Compound	3.440	3.725e-3

(b) For 45° angled and V configurations, the compound channel had the highest heat transfer enhancement as well as the highest thermal hydraulic performance. Heat transfer enhancement by ribs and dimples were similar to each other and the thermal hydraulic performance of dimples was slightly higher than the corresponding ribbed configurations.

(c) W and M compound configurations had similar heat transfer enhancements compared to their corresponding dimpled configurations. W and M ribs had lowest enhancements compared to their corresponding dimple and compound configurations.

(d) 45° angled and V compound configurations had higher heat transfer enhancements and higher thermal hydraulic performances compared to W and M.

(e) Correlations have been provided for scaling of globally averaged Nusselt number with Reynolds number.

(f) Correlation have been provided for Nusselt number enhancement with respect to smooth channel heat transfer results, with respect to Reynolds number.

Some recommendations based on the understanding developed from the present study are as follows:

(a) Numerical studies are required for more detailed understanding of fluid dynamics of two-pass channel featuring combinations of ribs and dimples.

(b) Experimental or numerical optimization is required to find the geometrical parameters leading to higher thermal hydraulic performance.

(c) Experiments need to be carried out at higher Reynolds number (>69000) as V compound channels tend to show an asymptotic nature of heat transfer augmentation with increasing Reynolds number and it would be interesting to see whether the asymptotic trend is retained or not at higher Reynolds numbers.

Nomenclature

c	specific heat capacity
d_h	hydraulic diameter
f	friction factor
f_0	friction factor from Blasius correlation
h	heat transfer coefficient
k	thermal conductivity of test material
k_f	thermal conductivity of air
L	total length of two-pass channel
Nu	Nusselt number (based on channel-hydraulic-diameter)
$\overline{\overline{Nu}}$	Globally averaged Nusselt number
Re	Reynolds number (based on channel hydraulic diameter)
T	temperature
t_{target}	thickness of the target plate
T_i	initial wall temperature
t	time taken to reach T_{tlc}
T_m	bulk fluid temperature at the inlet on test section

TKE turbulent kinetic energy

THP thermal hydraulic performance

Greek symbols

α normalized wall temperature, $(T_w(t) - T_i)/(T_m(t) - T_i)$

ρ density

Subscripts

i initial

in inlet

w wall

m mainstream

0 Dittus-Boelter/ Blasius correlation

s smooth surface

x cumulative streamwise distance

References

[2.1] Han, J. C., Dutta, S., and Ekkad, S., 2012, Gas turbine heat transfer and cooling technology, CRC Press.

[2.2] Taslim, M. E., Li, T., and Kercher, D. M., 1994, "Experimental heat transfer and friction in channels roughened with angled, V-shaped and discrete ribs on two opposite walls," In ASME 1994 International Gas Turbine and Aeroengine Congress and Exposition, pp. V004T09A018-V004T09A018.

[2.3] Zhang, Y. M., Gu, W. Z., and Han, J. C., 1994, "Heat Transfer and Friction in Rectangular Channels With Ribbed or Ribbed-Grooved Walls," J. Heat Transfer, 116(1), pp. 58-65.

[2.4] Mochizuki, S., Murata, A., and Fukunaga, M., 1997, "Effects of Rib Arrangements on Pressure Drop and Heat Transfer in a Rib-Roughened Channel With a Sharp 180 deg Turn," J. Turbomach., 119(95), pp. 610–616.

[2.5] Ekkad, S. V, and Han, J. C., 1997, "Detailed heat transfer distributions in two-pass square channels with rib turbulators," Int. J. Heat Mass Transfer, 40(11), pp. 2525–2537.

[2.6] Chandra, P. R., Alexander, C. R., and Han, J. C., 2003, "Heat transfer and friction behaviors in rectangular channels with varying number of ribbed walls," Int. J. Heat Mass Transfer, 46(3), pp. 481–495.

[2.7] Lee, E., Wright, L. M., and Han, J.C., 2003, “Heat transfer in rotating rectangular channels (AR= 4: 1) with V-shaped and angled rib turbulators with and without gaps,” ASME IGTI Paper No. GT2003-38900.

[2.8] Jenkins, S. C., Zehnder, F., Shevchuk, I. V., von Wolfersdorf, J., Weigand, B., and Schnieder, M., 2013, “The Effects of Ribs and Tip Wall Distance on Heat Transfer for a Varying Aspect Ratio Two-Pass Ribbed Internal Cooling Channel,” J. Turbomach., 135(2), pp. 021001-1-021001-9.

[2.9] Han JC, Zhang YM, Lee CP., 1991, “Augmented Heat Transfer in Square Channels With Parallel, Crossed, and V-Shaped Angled Ribs”, ASME. J. Heat Transfer. Vol 113(3):590-596. doi:10.1115/1.2910606.

[2.10] Won, S. Y., Burgess, N. K., Peddicord, S., & Ligrani, P. M., 2004, “Spatially resolved surface heat transfer for parallel rib turbulators with 45 deg orientations including test surface conduction analysis”, ASME Journal of Heat Transfer, 126(2), 193-201.

[2.11] Tanda, G., & Abram, R., 2009, “Forced convection heat transfer in channels with rib turbulators inclined at 45 deg”, Journal of Turbomachinery, 131(2), 021012.

[2.12] Tanda, G., 2011, “Effect of rib spacing on heat transfer and friction in a rectangular channel with 45 angled rib turbulators on one/two walls”, International Journal of Heat and Mass Transfer, 54(5), 1081-1090.

[2.13] Astarita, T., & Cardone, G., 2003, “Convective heat transfer in a square channel with angled ribs on two opposite walls”, Experiments in Fluids, 34(5), 625-634.

[2.14] Murata, A. and Mochizuki, S., 2004, “Effect of rib orientation and channel rotation on turbulent heat transfer in a two-pass square channel with sharp 180° turns investigated by using large eddy simulation”, International Journal of Heat and Mass Transfer, Vol. 47(12), pp.2599-2618.

[2.15] Lu, B. and Jiang, P.X., 2006, “Experimental and numerical investigation of convection heat transfer in a rectangular channel with angled ribs”, Experimental Thermal and Fluid Science, Vol. 30(6), pp. 513-521.

[2.16] Jang, Y.J., Chen, H.C. and Han, J.C., 2001, “Computation of flow and heat transfer in two-pass channels with 60 deg ribs”, Journal of Heat Transfer, Vol. 123(3), pp. 563-575.

[2.17] Jang, Y.J., Chen, H.C. and Han, J.C., 2001, "Numerical prediction of flow and heat transfer in a two-pass square channel with 90 ribs", International Journal of Rotating Machinery, Vol. 7(3), pp. 195-208.
[2.18] Shih, T.I.P., Lin, Y.L. and Stephens, M.A., 2001, "Fluid flow and heat transfer in an internal coolant passage", International Journal of Rotating Machinery, Vol. 7(5), pp. 351-364.
[2.19] Zhou, F., & Acharya, S., 2001, "Mass/Heat Transfer in Dimpled Two-Pass Coolant Passages with Rotation", Annals of the New York Academy of Sciences, Vol. 934(1), pp. 424-431.
[2.20] Chang, S. W., Liou, T. M., Chiang, K. F., & Hong, G. F., 2008, "Heat transfer and pressure drop in rectangular channel with compound roughness of V-shaped ribs and deepened scales", International Journal of Heat and Mass Transfer, Vol. 51(3), pp. 457-468.
[2.21] Choi, E. Y., Choi, Y. D., Lee, W. S., Chung, J. T., & Kwak, J. S., 2013, "Heat transfer augmentation using a rib–dimple compound cooling technique", Applied Thermal Engineering, Vol. 51(1), pp. 435-441.
[2.22] Choi, E. Y., Choi, Y. D., & Kwak, J. S., 2013, "Effect of Dimple Configuration on Heat Transfer Coefficient in a Rib-Dimpled Channel", Journal of Thermophysics and Heat Transfer, Vol. 27(4), pp. 653-659.
[2.23] Zhang, D., Guo, S., Shen, Z. and Xie, Y., 2014, "Numerical study on flow and heat transfer performance of rectangular heat sink with compound heat transfer enhancement structures", Advances in Mechanical Engineering, Vol. 6, p.457650.
[2.24] Shen, Z., Xie, Y. and Zhang, D., 2015, "Numerical predictions on fluid flow and heat transfer in U-shaped channel with the combination of ribs, dimples and protrusions under rotational effects", International Journal of Heat and Mass Transfer, Vol. 80, pp. 494-512.
[2.25] Singh, P., Ravi, B.V. and Ekkad, S.V., 2016, "Experimental and numerical study of heat transfer due to developing flow in a two-pass rib roughened square duct", International Journal of Heat and Mass Transfer, Vol. 102, pp. 1245-1256.
[2.26] Moffat, R. J., 1988, "Describing the Uncertainties in Experimental Results", Experimental Thermal and Fluid Science, Vol. 1(1), pp. 3-17.
[2.27] Yan, Y., & Owen, J. M., 2002, "Uncertainties in transient heat transfer measurements with liquid crystal", Int. J. Heat Fluid Flow, Vol. 23(1), pp. 29-35.

CHAPTER 3

Experimental and Numerical Investigation of Heat and Fluid flow in a Square Duct Featuring Criss-Cross Rib Patterns

[a]Prashant Singh, [b]Yongbin Ji, [a]Srinath V. Ekkad
[a]Department of Mechanical Engineering, Virginia Tech, Blacksburg, VA USA
[b]Department of Mechanical Engineering, Shanghai Jiao Tong University, Shanghai, China

Under review: International Journal of Heat and Mass Transfer

ABSTRACT

This paper presents detailed experimental and numerical study of heat transfer and fluid flow in a straight square duct featuring rib turbulators in a criss-cross pattern formed by 45° angled ribs. Two ribbed configurations with Criss-Cross pattern – Inline and staggered, have been studied where the baseline case was smooth duct with no heat transfer enhancement feature. The effective rib-pitch-to-rib-height ratio (p/e) was 8.6 and rib-height-to-channel-hydraulic diameter ratio (e/d_h) was 0.1. The channel had a total length of 20 hydraulic diameters and the rib turbulators were installed at a distance of six hydraulic diameters from the inlet of the test section to allow flow development. Detailed heat transfer coefficients were calculated using transient liquid crystal thermography employing 1D semi-infinite conduction model. Heat transfer and pressure drop measurements and calculations were carried out for Reynolds number ranging from 30000 to 60000. Further, numerical investigations were carried out for all the test configurations and for all the test conditions. SST k-ω turbulence model was used in the numerical calculations. Numerical predictions of near wall fluid dynamics and turbulent transport has been used in conjunction with detailed heat transfer measurements to understand the heat transfer enhancement mechanism by criss-cross ribs. Regionally averaged Nusselt numbers normalized by corresponding smooth channel heat transfer results have been reported and comparisons have been made between experiments and numerical predictions. Globally averaged Nusselt numbers are calculated from the experimentally obtained heat transfer data and thermal hydraulic performance of configurations have been reported with respect to Reynolds number. Heat transfer roughness function is presented with respect to Roughness Reynolds number and comparisons have been made with correlations of Han and Park. Nusselt numbers normalized with respect to Dittus-Boelter correlation for developed turbulent flow in circular

duct varied from 3.1 to 2.7 for inline and staggered configurations for the range of Reynolds number studied.

Keywords: Rib turbulators; criss-cross; liquid crystal thermography; thermal hydraulic performance

INTRODUCTION

Applications of heat transfer enhancement concepts can be found in gas turbine airfoils, solar air heaters, electronic cooling etc. A common technique to enhance heat transfer is by installing turbulence promotors ("rib turbulators") on the smooth walls. The rib turbulators generate secondary flows which increase near-wall shear in the vicinity of the ribs and these secondary flows also interact with channel side walls to increase turbulent transport of energy from relatively hotter walls by forming vortex or vortices. One application of rib turbulators as heat transfer enhancement technique is found in gas turbine airfoils. The gas turbine airfoils are subjected to elevated heat loads on both pressure and suction side walls. Hence rib turbulators are installed on pressure and suction side internal walls to increase heat transfer in order to increase the heat transfer rates between internal walls and coolant. Rib turbulators also result in increase in wetted surface area which enhances the overall conductance. Several studies have been carried out in the past on heat transfer enhancement by various cooling designs, such as, ribbed channel with bleed holes, ribbed channel with grooves, rib dimpled compound channels, jet impingement, jet impingement with effusion holes, dimpled channel, jet impingement onto dimpled target surface etc. [3.1-3.11]. The use of artificial roughness on a surface is an effective technique to enhance heat transfer coefficient also has good application in design and development of efficient solar air heaters. Many investigations [3.12-3.21] have demonstrated the effects of different rib configurations on heat transfer coefficient between absorbers plate and air flowing in solar air heaters, numerically and experimentally, in order to improve the heat transfer capability of solar air heater ducts.

Heat transfer enhancement due to rib turbulators is affected by several parameters such as rib angle-of-attack, channel aspect ratio, rib pitch-to-height ratio, blockage ratio, and rib shape. Investigations on these aspects of rib turbulator design have been reported in [3.22-3.31]. In the past, researchers have studied the flow characteristics of ribbed duct, both, experimentally and numerically [3.32-3.37]. Some studies focused on the relative arrangement of ribs, e.g. parallel,

staggered, and criss-cross [3.38-3.40]. Gao and Sunden [3.38] used particle image velocimetry to reveal the flow characteristics in rectangular channels with aspect ratio of 1:8. Six different rib configurations were experimentally investigated, namely staggered parallel ribs, staggered-single parallel ribs, in-line parallel ribs, crossed ribs, V-ribs pointing downstream, and pointing upstream. Ekkad and Han [3.39] performed a detailed study on heat transfer characteristics with all rib parallel to each other in a non-rotating square channel using transient liquid crystals technique. Lee et al. [3.40] used naphthalene sublimation technique to measure detailed heat transfer enhancement contours using heat-mass transfer analogy. They tested continuous V shaped ribs and discrete V shaped ribs. Several investigations have been carried out in the past on rib turbulator as a method of enhancing heat transfer.

Several numerical investigations have been carried out to understand turbulent heat and fluid flow in rib roughened ducts. Murata and Mochizuki [3.41] carried out numerical investigation of laminar and turbulent heat transfer in a square duct featuring angled rib turbulators. Lu and Jiang [3.42] carried out experimental and numerical study on a rectangular channel featuring angled rib turbulators. The authors concluded that the SST $k-\omega$ turbulence model was more suitable for the prediction of turbulent heat transfer compared to RNG $k-\varepsilon$ model. Al-Qahtani et al. [3.43] used Reynolds Stress turbulence model in conjunction with near-wall second –moment turbulence closure to study heat transfer in rotating rectangular channels with rib turbulators. Eiamsa-ard and Promvonge [3.44] studied four turbulence models for prediction of heat transfer in a rectangular duct featuring grooves. The authors carried out computations using standard $k-\varepsilon$, RNG $k-\varepsilon$, standard $k-\omega$, SST $k-\omega$ turbulence models and found that the $k-\varepsilon$ model was better than the other turbulence models. For computations of heat transfer in a square duct roughened by discrete V-shaped ribs, Promvonge et al. [3.45] used RNG $k-\varepsilon$ model. Acharya et al. [46] compared nonlinear and standard $k-\varepsilon$ models for prediction of periodically developed heat and flow transfer in ribbed duct and concluded that the nonlinear model predicted realistic Reynolds stresses in the core flow region than the standard model. Peng et al. [3.47] studied different rib shapes numerically using SST $k-\omega$ turbulence model. Sewall and Tafti [3.48] carried out Large Eddy Simulations (LES) on a two-pass rib roughened duct featuring 90° rib turbulators and demonstrated that LES predicted flow and heat transfer was very accurate. However, LES comes at a significant computational cost. In order to maintain a balance between computational accuracy and cost, SST $k-\omega$ turbulence model was used in the present study.

Further, the choice of the turbulence model in the present study is based on relative comparisons of heat transfer predictions by four other turbulence models and experimentally obtained heat transfer data.

The present study reports a new ribbed configuration which has shown promise in terms of heat transfer and overall thermal hydraulic performance. Detailed heat transfer measurements have been carried out using transient liquid crystal thermography. The ribs were installed periodically in a single pass channel with aspect ratio of unity. The ribbed channel was constructed by aligning ribs at an angle of attack of 45° in a unique pattern, which is called as "criss-cross" in this paper. Two such ribbed configurations were studied – inline and staggered. Heat transfer experiments were also carried out on smooth duct with no heat transfer enhancement features in order to characterize the inlet conditions and its effect on the downstream heat transfer distribution. Heat transfer and static pressure measurements were carried out for Reynolds number ranging from 30,000 to 60,000. Heat transfer measurements have been presented as detailed contours, region-wise averaged Nusselt numbers normalized with D-B correlation and corresponding smooth channel results. Numerically predicted fluid flow has been used to explain the heat transfer enhancement characteristics of the configurations. Thermal hydraulic performance of the channel has also been reported along with the frictional losses in the channel due to the ribs. Detailed discussion on flow physics has been presented for better understanding of heat transfer in rib roughened duct.

EXPERIMENTAL SETUP

The experimental setup used in this paper has been schematically shown in Fig. 3.1. The working fluid (air) was supplied by a compressor which is capable of providing air flow rate of 1.36 kg/s at a pressure of 150 psi (1MPa). A buffer tank was installed downstream of the compressor to create a low pressure air reservoir for transient experiments. The air pressures in the buffer tank were typically around 40 psi (270 kPa). This buffer tank pressure was sufficient to provide the desired mass flow rate. The air flow rate was metered by an orifice meter installed downstream of the buffer tank. A total length of 35 pipe diameters was provided upstream of the orifice plate and about 10 pipe diameters downstream of the orifice plate to allow for complete development length, upstream and downstream of the orifice plate. In order to calculate the mass flow rate through the orifice plate, the pressure differential across the orifice, the high pressure at the

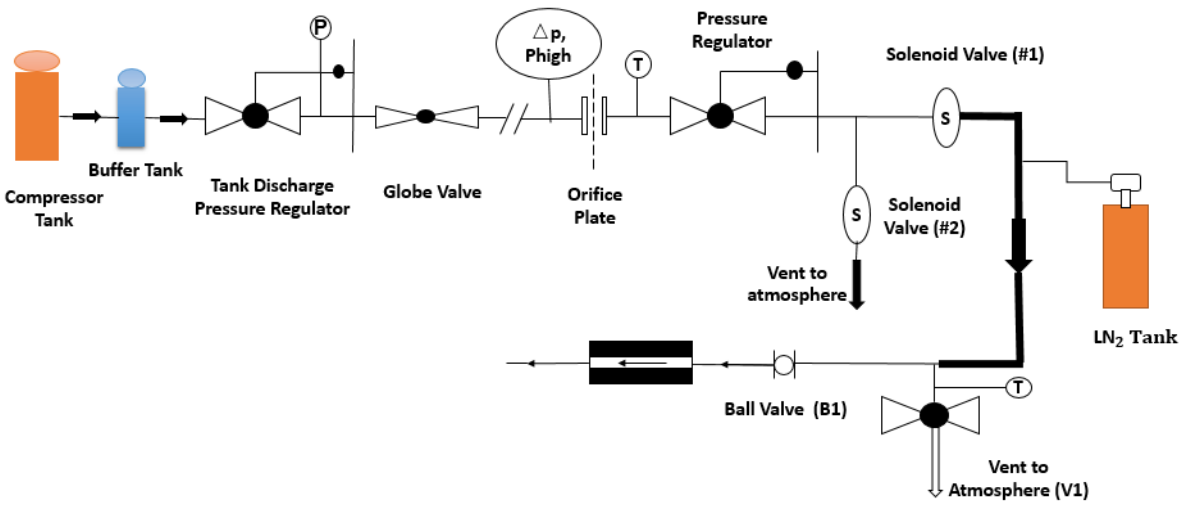

Fig. 3.1 Schematic of experimental setup

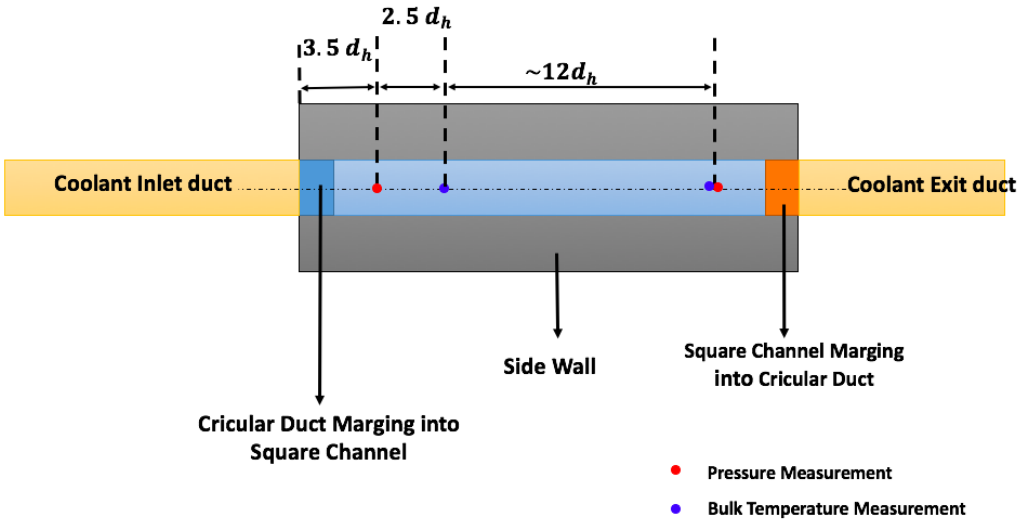

Fig. 3.2 Coolant inlet and exit conditions, bulk temperature measurement locations, static pressure measurement locations

orifice, and the air temperature at the orifice were measured. The devices used for above measurements were Dwyer 477-4-FM (10 psi, 70 kPa range), Dwyer DPG-103 (30psi, 206 kPa range), and T-type thermocouple, respectively. The high pressure at the orifice plate and the temperature of the air was measured in order to account for the density variation of air on different days. Two solenoid valves were installed downstream of the pressure regulator, controlled by binary operating signal using LABVIEW, which acted as a 3-way valve. Downstream of the solenoid valve #1, a fitting was provided for liquid Nitrogen (LN_2) intake. A mixture of air and liquid Nitrogen was used to chill the path between the solenoid valve (#1) and vent valve (V1). The chilled reservoir is shown by solid black line. Several experiment characterization runs were carried out to make sure that the reservoir was suitably cooled to the required temperature, achieving similar heat transfer experiments across the range of Reynolds number. Once the path was suitably cooled, the Nitrogen supply was cut off and all the remaining Nitrogen in the path is purged out from the main line into the ambient through the valve V1.

Further, the solenoid valve direction was switched towards the ambient and Ball valve (B1) and Vent valve (V1) were turned to open the main line towards the test section. The test was commenced through a single click system from a LabVIEW code. Detailed operational procedure can be found in [3.6].

DESCRIPTION OF TEST CONFIGURATIONS

Figure 2 shows the test section with inlet and outlet conditions, bulk temperature measurement locations and static pressure measurement locations.

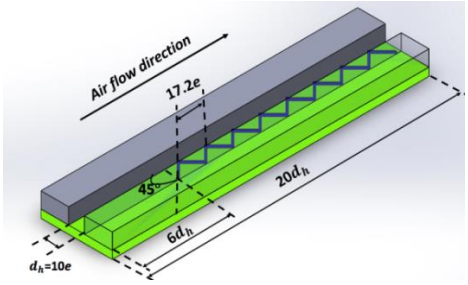

Fig. 3.3 Dimensions of the test section, rib turbulator, and orientation with respect to coolant flow

A circular duct merged smoothly into the square test section duct through an adapter fitting and similar fitting was provided at the outlet for smooth merging of the square duct into circular duct. An extra exit length was provided at the exit in order to avoid the back pressure effects on heat transfer on last few rib pitches. Fig. 3.3 shows the isometric view of the test section, where only one wall featuring rib turbulators has been shown. The important dimensions have been given in terms of rib height and channel hydraulic diameter. The square channel was 10e wide and $20d_h$ long. The ribs were installed at a distance of $6d_h$ from the inlet of the test section The angle between adjacent ribs is 90° and the cross section of the ribs was square. Ribs were installed on two opposite walls. The effective rib-pitch-to-rib-height ratio (p/e) is 8.6 and the rib-height-to-channel-hydraulic-diameter ratio (e/d_h) is 0.1.

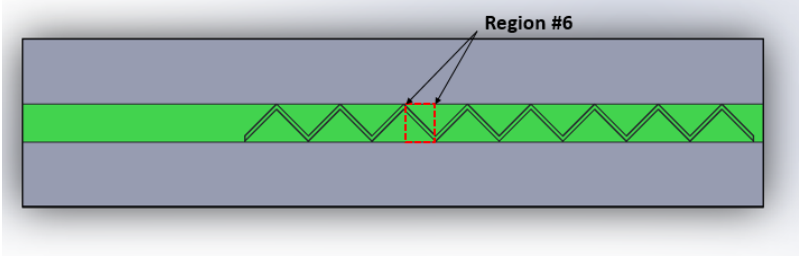

(a)

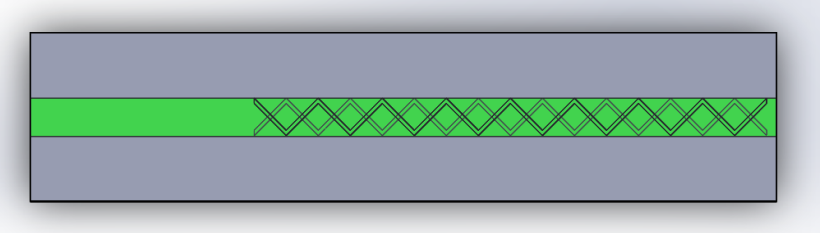

(b)

Fig. 3.4 (a) Inline configuration (a sample region # has been shown); (b) staggered configuration; coolant flow direction is from left to right

Figure 3.4 shows the two ribbed configurations studied. The configurations are named as Inline and Staggered. The channel was made with the combination of 3D printed ribs (ABS) and clear acrylic walls to allow optical access in order to capture the liquid crystal color change. From the top view, ribs on the opposite walls in inline configured channel were parallel to each other, and the ribs in staggered configured channel were crossed. A sample region has also been shown in the figure. This region definition was used in the presentation of regionally averaged Nusselt number data.

EXPERIMENTAL CONDITIONS

Transient liquid crystal thermography experiments have been carried out at three Reynolds numbers, viz. 30000, 45000 and 60000. Three configurations have been tested, viz. smooth, inline and staggered ribs. Static pressure measurements have been carried out at the inlet and outlet of the test section to determine the total pressure drop of the channel featuring heat transfer enhancement features.

Computational details

This section describes the computational procedure employed in the present study. Numerical studies were carried out at all the flow conditions mentioned earlier and for all the configurations – inline, staggered and smooth. Smooth channel computations were carried out in order to calculate normalized Nusselt numbers (Nu/Nu_s) for comparison with experimentally obtained Nusselt number enhancements. This type of comparison cancels out the difference in inlet conditions between numerical setup and experiments [3.6, 3.7, 3.10, 3.11].

Inlet conditions

A uniform velocity was specified at the inlet of the test section and the outlet was specified as zero gage pressure. A turbulence intensity of 5% was specified at the inlet. Note that the inlet condition of the coolant in numerical study was different from the experiments. In experiments, a developing flow existed in the initial regions of the fluid domain. More discussion on this has been presented in the Results and discussion section.

Selection of turbulence model

The flow field in the rib turbulated duct was turbulent and it was modeled using SST k-ω turbulence model. Five different turbulence models, viz., SST, RNG k-ε, k-ω, standard k-ε and RSM were investigated for both inline and staggered configurations at a Reynolds number of 30000. Figure 3.5 shows the model validation studies and its comparison with experimentally obtained normalized Nusselt number (Nu/Nu_s). Due to difference in the inlet conditions between numerical domain and experiments, region numbers 7 through 13 were used for comparison of experiments and numerically predicted heat transfer. Figure 5 shows the comparison of all the turbulence models investigated in the present study along with the experimentally obtained normalized Nusselt number. The SST turbulence model was found to have good agreement with the experimental results. The other four turbulence models significantly under-predicted the heat transfer enhancement and hence were not considered for further computations. The numerical calculations were carried out using commercial CFD software package, CFX which is a finite-volume based solver. The fluid domain was discretized using ICEM meshing software which is provided by ANSYS.

Computational grid details, mesh independence studies

Figure 3.6 shows four different views of the structured grid created to model the fluid flow. In order to accurately model the near wall fluid dynamics, a very fine structured grid was created near the endwalls and is also shown in Fig. 3.6 (a).

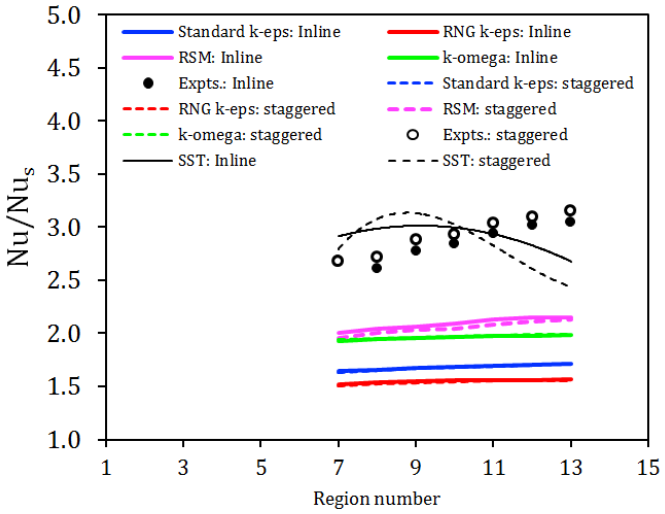

Fig. 3.5 Model validation with experimentally obtained normalized Nusselt number Nu/Nu_s (Re 30000)

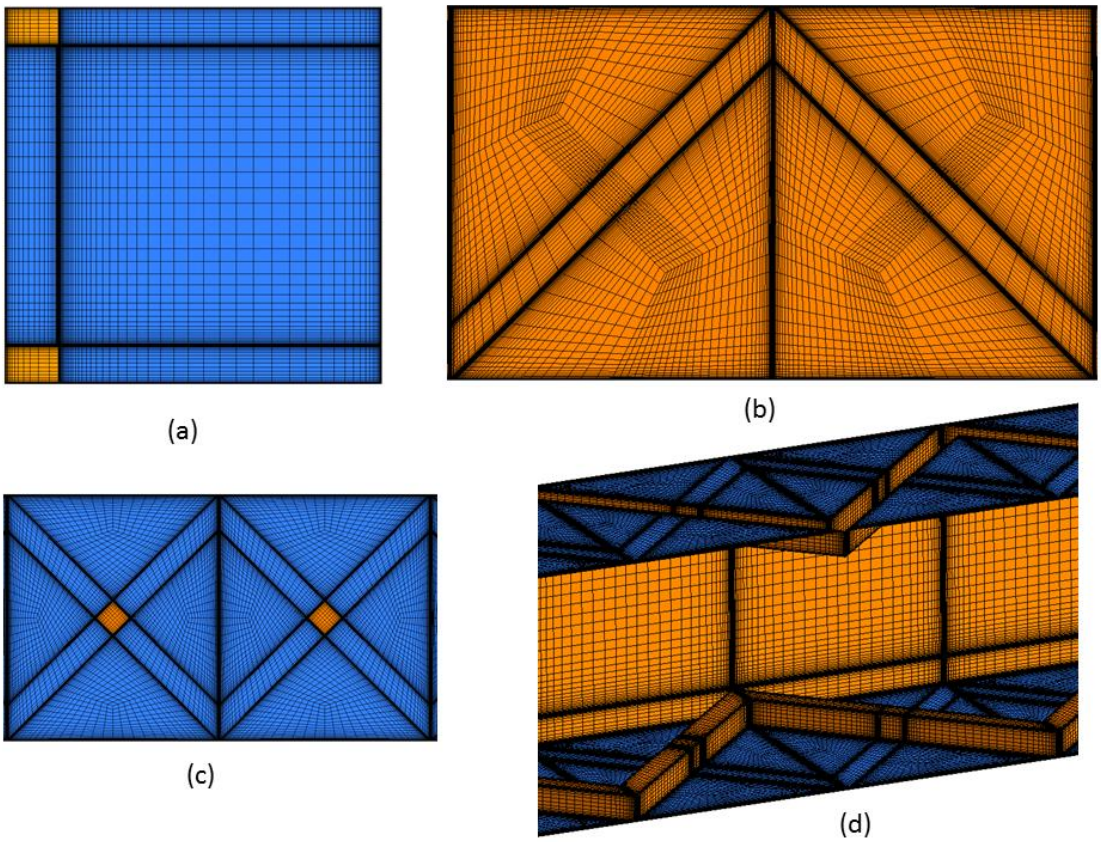

Fig. 3.6 Different views of structured grid employed for computations,

Table 3.1 Comparison of measured total pressure drop (Pa) with numerical predictions

Reynolds number	**Inline - Δp (Pa)**			**Staggered - Δp (Pa)**		
	Expts.	**CFD**	$\left\|100 \times \left(1 - \frac{(\Delta p)_{CFD}}{(\Delta p)_{Expts.}}\right)\right\|$	**Expts.**	**CFD**	$\left\|100 \times \left(1 - \frac{(\Delta p)_{CFD}}{(\Delta p)_{Expts.}}\right)\right\|$
30000	541.8	638.6	15.1	643.4	582.5	10.4
45000	1320.7	1481.9	10.8	1490.0	1314.3	13.3
60000	2268.9	2733.4	17.0	2607.5	2713.5	3.9

High quality three dimensional multiblock structured hexahedral mesh was generated to satisfy the convergence and resolution requirement for both inline and staggered cases. Especially, grids near walls and ribs were refined to accurately capture near wall fluid dynamics. Fig. 3.6 (a) is the side view of the ribbed channel, Fig. 3.6 (b) and (c) are the top views for inline and staggered cases in one pitch respectively, Fig. 3.6 (d) is the isometric view of the mesh. For all the computational cases, it was made sure that the y+ values were less than 1, which is one of the requirements for proper usage of the turbulence model used in this study. For flow validation, the supply pressure at a location (3.5 times the hydraulic diameter from the inlet) on the top wall was compared with the experimental measurements. Table 1 shows the comparison of the total pressure drop in the straight ribbed duct between experiments and computations.

Acceptable agreement has been observed between experiments and computationally predicted total pressure drop. Table 3.1 show the experimentally total pressure drop and numerically predicted pressure drop. The absolute percentage difference with predicted and measured total pressure drop ranged from 4% to 17%. The comparison between globally averaged normalized Nusselt number (Nu/Nu_s) between experiments and CFD has been shown at a later stage in this paper, due the suitability in discussion. For all the calculations of friction factor and thermal hydraulic performance, experimentally measured pressure drop is used.

Grid independence studies were carried out for three different grid schemes at the highest Reynolds number. The total number of elements were varied from 9 M, 13 M and 15 M for the inline configuration and 10 M, 15 M and 17 M for the staggered configuration. The area averaged integral of Nusselt number over the entire region of interest showed weak dependence on the considered grid schemes ($\pm 3\%$). In order to maintain a balance between computational accuracy and cost, the medium grid scheme 13 M for inline and 15 M for staggered configuration for chosen for all the computations.

Nusselt number calculations

A constant heat flux $5\,kW/m^2$boundary condition was provided for the heat transfer calculations. The heat flux was applied only on the endwalls, i.e. the ribs and the side walls were declared as adiabatic walls. The coolant inlet temperature was 300 K. Local wall temperatures were obtained from the computations and were used in the calculation of local heat transfer coefficient. The local heat transfer coefficient is defined as,

$$h(x,y) = \frac{q''}{T_w(x,y) - T_b(x)} \quad (Eq.\,3.1)$$

Due to addition of heat into the fluid domain, the coolant temperature was dependent on the spatial location. In order to account for the local spatial variation of bulk coolant temperature, a total of nine equally spaced planes were created orthogonal to the bulk flow direction. Mass weighted average temperatures (bulk fluid temperature) were calculated for these nine planes. Including the inlet and outlet, a total of 11 data points were obtained for the bulk fluid temperature. The local bulk fluid temperature $T_b(x)$ was calculated by linearly interpolating the obtained bulk fluid temperature data in the streamwise direction. Subsequently, the Nusselt number was calculated from the following equation.

$$Nu(x,y) = \frac{h(x,y)d_h}{k_f} \quad (Eq.\,3.2)$$

The thermal conductivity of the coolant was calculated at the film temperature, $T_f = 0.5(T_w + T_b)$.

HEAT TRANSFER COEFFICIENT CALCULATION METHODOLOGY IN EXPERIMENTS

Calculation of two-dimensional heat transfer coefficient distribution was carried out by transient liquid crystal thermography. A 1-D semi-infinite conduction model has been employed for the calculation of heat transfer coefficient at the boundary with forced convection condition. The evolution of wall temperature exposed to a constant mainstream temperature with a time-independent heat transfer coefficient is given by Eq. 3 [49].

$$\frac{T_w(t) - T_i}{T_m - T_i} = 1 - exp\left(\frac{h^2 t}{\rho c k_s}\right) erfc\left(h\sqrt{\frac{t}{\rho c k_s}}\right) \quad (Eq.\,3.3)$$

Here, T_m represents the reference mainstream temperature. In the present study, the mainstream temperature was measured at the channel centerline and has been assumed to be the representative of the bulk fluid temperature. During the transient experiment, the mainstream temperature was not constant with time. In order to incorporate the time dependence of the

mainstream temperature, Duhamel's superposition principle was employed in Eq. 3.3, where the mainstream temperature was discretized in small time steps. During each time step, the mainstream temperature can be assumed to be constant. The modified equation for wall temperature evolution is given by Eq. 4 [50].

$$T_w = T_i + \sum_{i=1}^{i=n_{max}} \left(T_{m,i} - T_{m,i-1}\right) \times \left[1 - exp\left(\frac{h^2(t-t_i)}{\rho c k_s}\right) erfc\left(h\sqrt{\frac{t-t_i}{\rho c k_s}}\right)\right] \quad (Eq.\,3.4)$$

Due to heat exchange between the coolant and the wall, the coolant temperature rises as it flows through the two-pass channel. In order to account for the streamwise variation of mainstream temperature, the mainstream temperature was linearly interpolated across the measurement locations.

Mainstream temperatures were measured at the inlet and outlet of the test section. The measurement locations have been shown in Fig. 3.2. The variation of mainstream temperature in the spanwise direction was very minimal and has been neglected in the heat transfer coefficient calculations. The temperature measurements were carried out by a fast response T-type thermocouple with bead diameter of 0.0762 mm. The transient experiment carried out in the present study has a relatively slower rate of change of temperature compared to typical mesh heater experiments. The time constant of these thermocouples were very low and were sufficient to capture the rate at which the temperature was changing with time. Figure 3.7 shows the evolution of mainstream temperature with time. Also shown in Fig. 3.7 is the evolution of normalized wall temperature with time. The wall temperature was measured by a T-type thermocouple taped on the endwall where rib turbulators were installed. At this stage, the unknowns in Eq. 3.4 are $T_w, t \; and \; h$.

Determination of T_w

T_w is the wall temperature which was tracked in order to calculate the heat transfer rate required to reach that particular temperature in a given time. In our calculations, same wall temperature (13 °C) was tracked for each pixel and for all the experimental conditions. The first step in the determination of T_w is the calibration of liquid crystal color change with wall temperature.

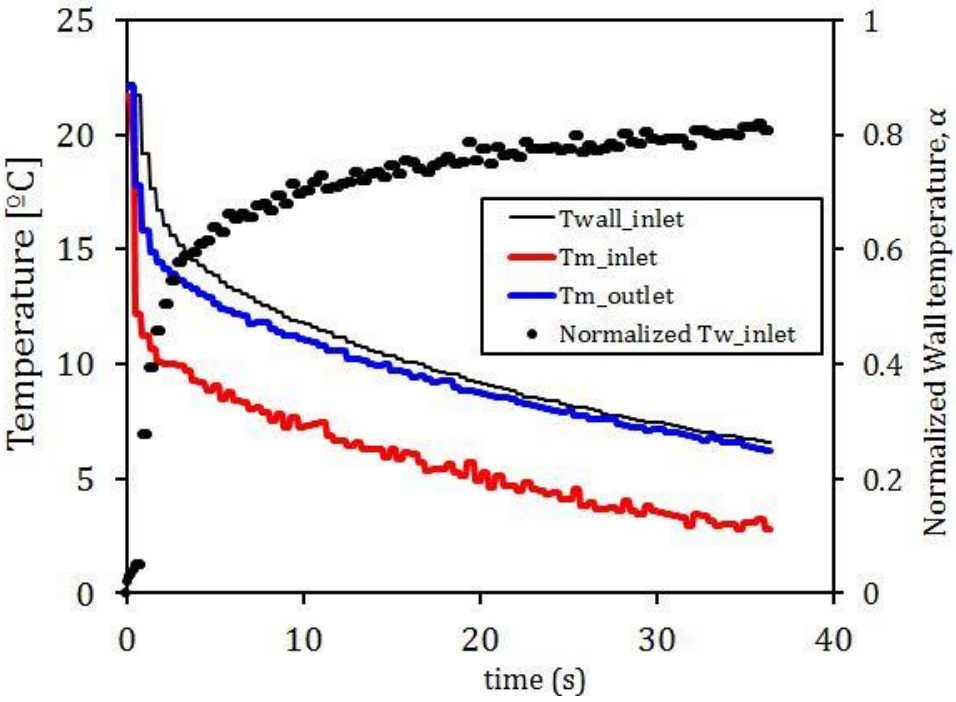

Fig. 3.7 Mainstream temperature evolution with time, wall temperature measured at inlet, normalized wall temperature (at inlet) versus time

The liquid crystal used in the present had a color play from 10°C to 15°C. A Hue based calibration technique was used in order to establish a relationship between the LC color change with measured wall temperature. Two T-type thermocouples were used in order to calibrate the LC. The wall temperature measurement thermocouples were taped at the inlet and outlet sections in order to cover the entire region of interest.

The Hue-based technique has been proven to be very robust with lighting conditions, camera inclination angles [3.51], it was observed that the two calibration curves of the LC color change were very similar to each other. A sample calibration curve has been shown in Fig. 3.8. The aim of calibration of LC color change is to establish a relationship between wall temperature and Hue. Also, the calibration was carried out in-situ for every heat transfer experiment to make sure that there were minimal effects of changes in lighting conditions, LC degradation in different runs on heat transfer coefficient determination.

In the close vicinity of the thermocouple, a 5 x 5 pixel region was chosen to be the ‘calibration region’. The Hue was calculated at each of the 25 pixels and averaged to one value. This

averaged value of Hue has been obtained for each frame of the video which was recorded at 30 frames per second. In order to make sure that the lighting conditions were diffused and uniform across the region of interest, a minimum threshold of 0.3 for saturation and intensity was applied to each pixel, for that pixel to qualify for heat transfer data reduction procedure.

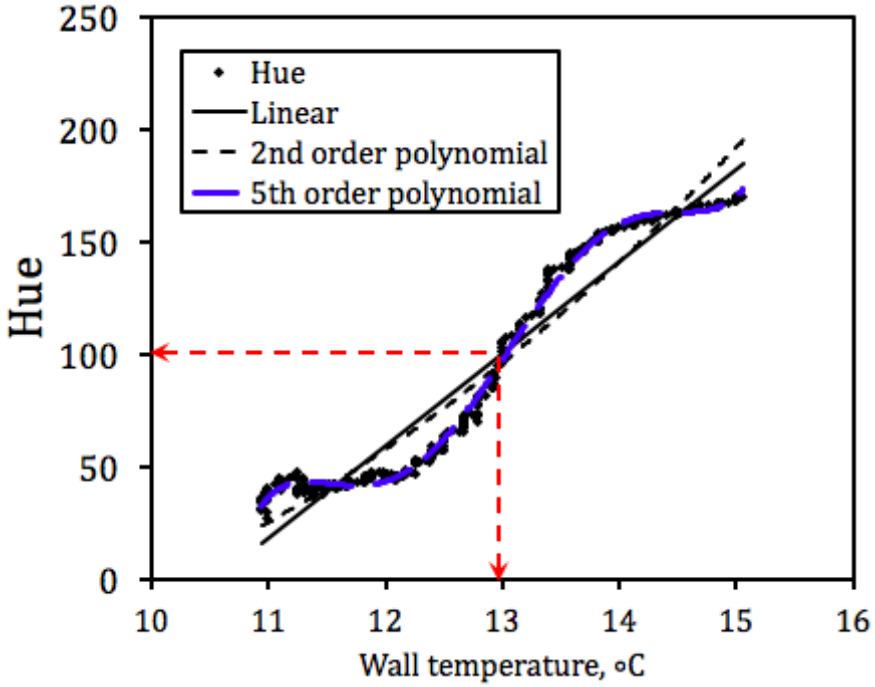

Fig. 8 Calibration of wall temperature with Hue [LC part # R10C5W]

Once the relationship between Hue and measured wall temperature was established, each pixel was traversed frame by frame in order to check for the reference Hue value (corresponding to a particular wall temperature), saturation and intensity values. The frame at which all the criterions on Hue, saturation and intensity were satisfied, that particular frame number was stored in a frame matrix, which was eventually converted to time matrix since the frame capture rate was known. At this stage, the only unknown in Eq. 4 is the heat transfer coefficient.

The heat transfer coefficient was then determined by an error minimization routine (secant method). The Nusselt number is given by Eq. 3.5.

$$Nu(x,y) = \frac{h(x,y)d_h}{k_f} \quad (Eq.3.5)$$

The thermal conductivity for air was obtained at the film temperature $T_f = 0.5(T_w + T_b)$.

UNCERTAINTY ANALYSIS

The uncertainty in the measurement of Nusselt number and Reynolds number has been carried out using sequential perturbation method described by Moffat [3.52]. The factors contributing to uncertainty in Nusselt number are $T_w, T_i, T_m, t, \sqrt{\rho c k_s}$. The contribution of temperature measurements was taken to be 0.5°C. The contribution of time (t) was taken to be 0.033 seconds. The uncertainty for a typical Nusselt number of 100 was found to be to around 12%.

The uncertainty in the measurement of Reynolds number was about 2.85%

RESULTS AND DISCUSSION

Detailed normalized Nusselt number contours have been presented for all the configurations and for all the Reynolds number studied. Different configurations have been compared for their heat transfer characteristics through regionally averaged Nusselt number enhancement (Nu/Nu_0). Fluid flow in the duct has been discussed in order to understand the heat transfer enhancement mechanisms by the criss-cross rib turbulators. In the end, globally averaged Nusselt number enhancement, friction factor and thermal hydraulic performance is reported and compared with existing rib turbulator designs.

Smooth channel heat transfer: effects of inlet conditions on heat transfer

As shown in Fig. 3.2, the circular duct merged into the square duct through an expansion adapter. The flow was developing in nature. Figure 9 shows the regionally averaged Nusselt number ratio plotted with region numbers for Reynolds number ranging from 30000 to 60000. The Nusselt number ratio was about 75% higher than the D-B correlation Nusselt number for Reynolds number of 30000 at the inlet of the test section. For the Reynolds number of 45000 and 60000, the enhancement in Nusselt number at the inlet was about 50% higher than the D-B correlation. The enhancement in heat transfer in the initial few hydraulic diameters was because of the merging of circular duct into a square duct. This effect decayed rapidly as the flow got developed in the square duct. The developed length of the flow can be defined as the streamwise distance after which the change in Nusselt number ratio was less than 10%. The development length was found to be different for different Reynolds numbers. For the higher two Reynolds number

conditions, the flow developed faster than the lowest Reynolds number case. For Reynolds numbers 45000 and 60000, the flow can be considered as developed downstream of region # 6. The investigation of heat transfer and fluid flow in a smooth channel with no heat transfer enhancement feature is important in order to evaluate the real contributions of the heat transfer enhancement configurations [3.6, 3.10, 3.11, 3.27].

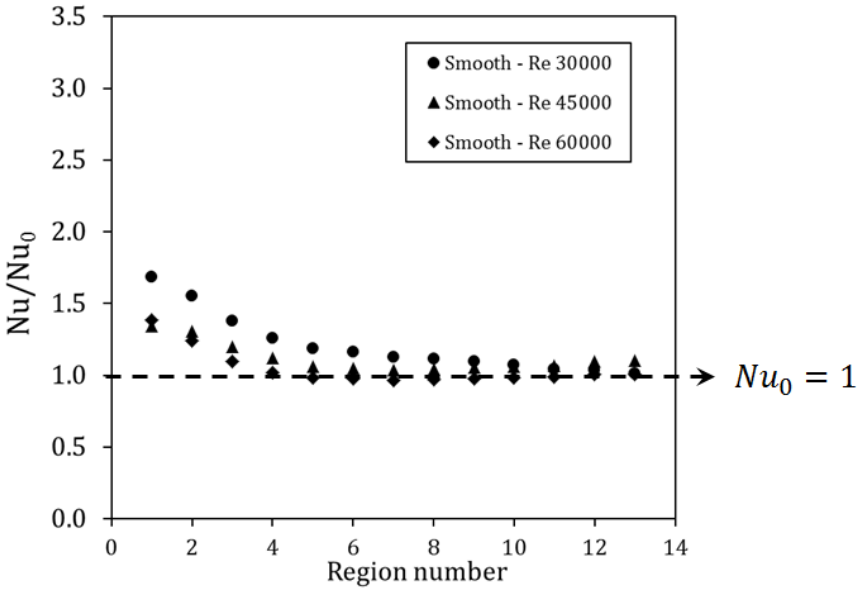

Fig. 3.9 Spanwise averaged Nusselt number ratio ($\mathrm{Nu}/\mathrm{Nu}_0$) plotted with normalized streamwise distance

Detailed measurements of Nusselt number ratio for Inline and Staggered configurations

Figure 3.10 shows the detailed measurement of normalized Nusselt number (Nu/Nu_0) for the inline configuration shown in Fig. 3.4(a). The ribs were inclined at an angle of 45° with respect to the direction of bulk coolant flow. The heat transfer enhancement mechanism of rib turbulator is through the increase in near wall shear due to rib induced secondary flows and the increase in turbulent mixing leading to energy exchange between enclosure walls and coolant. The secondary flows get induced due to the angle of attack of the ribs with respect to flow. The coolant while passing over the ribs, gets attached with the endwall slightly downstream of the

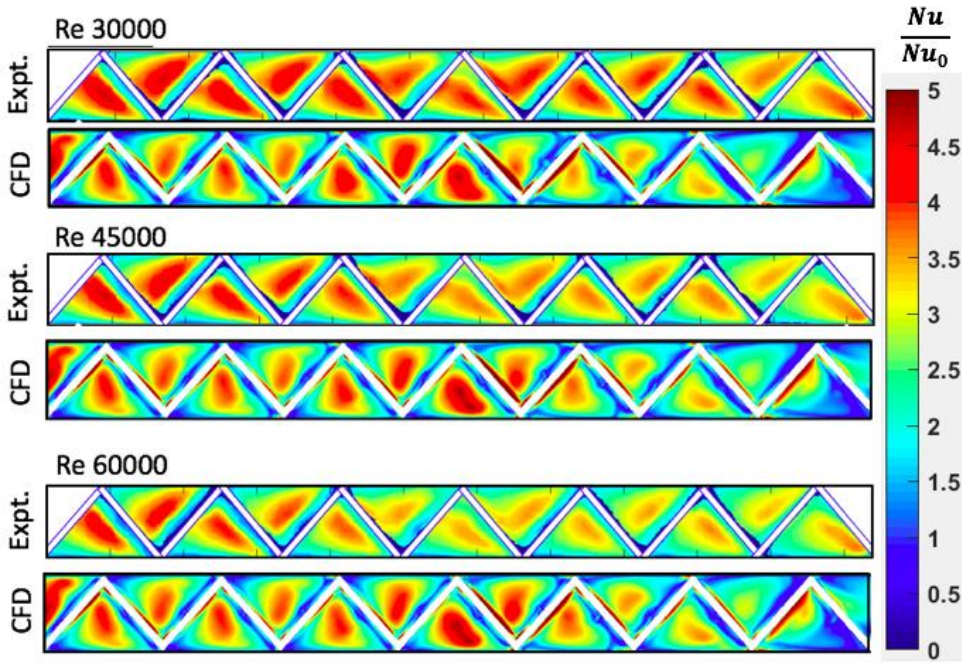

Fig. 3.10 Detailed Nusselt number ratio ($\mathrm{Nu}/\mathrm{Nu}_0$) contour for the Inline configuration for all Reynolds numbers - experiment versus CFD

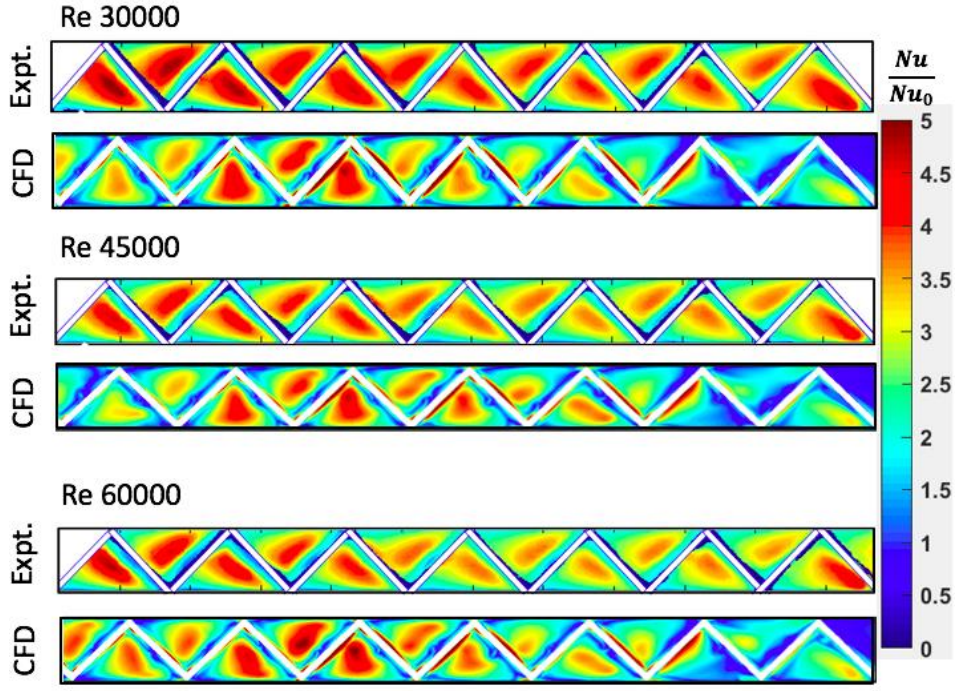

Fig. 3.11 Detailed Nusselt number ratio ($\mathrm{Nu}/\mathrm{Nu}_0$) contours for the Staggered configuration for all Reynolds numbers – experiment versus CFD

rib. The space between the reattachment location and the rib undergoes fluid recirculation, which leads to relatively lower heat transfer. Consider the first rib for any Reynolds number condition in Fig. 3.10. The high heat transfer region is shown by reddish color in the contour. It can be seen that the reattachment length for the first rib was about negligible and the direction in which the high heat transfer values were found was at angle greater than 45°. This was because of the combined effects of the bulk flow and the rib induced secondary flows.

A unique pattern of secondary flows was developed due to interaction of bulk flow and the ribs arranged in a new format. The secondary flows originated from both corners of the side walls and travelled inwards towards the channel centerline.

The secondary flows induced by the ribs directly resulted in increase in near wall shear stress which lead to enhancement of heat transfer on the endwalls featuring rib turbulators. As the flow progressed in the single pass, the secondary flows originating from the two corners started to interact with each other as well as with the bulk coolant flow. The resultant heat transfer characteristics in the mid-section of the region of interest, was hence, slightly different from that found in the initial few rib pitches. On relative comparison of Nusselt number enhancement, it can be seen that with increasing Reynolds number, the enhancement in heat transfer decreased. This is a common trend for most of the studies on heat transfer enhancement features [3.1, 3.2, 3.3, 3.5, 3.6, 3.10-3.13, 3.22-3.30 etc.].

The heat transfer characteristics as seen in Fig. 3.11 for the staggered configuration were similar to the inline configuration. The nature of secondary flows induced due to rib turbulators were similar on both the endwalls, however, the turbulent mixing for this configuration was different compared to the inline configuration.

The combined effects of rib induced secondary flows and turbulent mixing resulted in enhancement heat transfer for the staggered case when compared to inline case. The enhancement in near wall shear stress for the staggered and inline cases were similar to each other, however the nature of turbulence mixing which results from pair of counter-rotating vortex pairs were different. The turbulent transport characteristics for the two configurations are discussed in the following section.

Numerically predicted flow field in planes orthogonal and parallel to bulk flow direction

Figure 3.12 shows the numerically predicted velocity vectors for two different planes for inline and staggered configurations. The planes were drawn orthogonal to the direction of bulk coolant flow. The streamwise locations are presented in the figure to the left. The general heat transfer enhancement mechanism of angled rib turbulators is by increase in near wall shear due to rob induced secondary flows and enhancement in turbulent transport due to vortices formed post the interaction of rib induced secondary flows and the channel side walls.

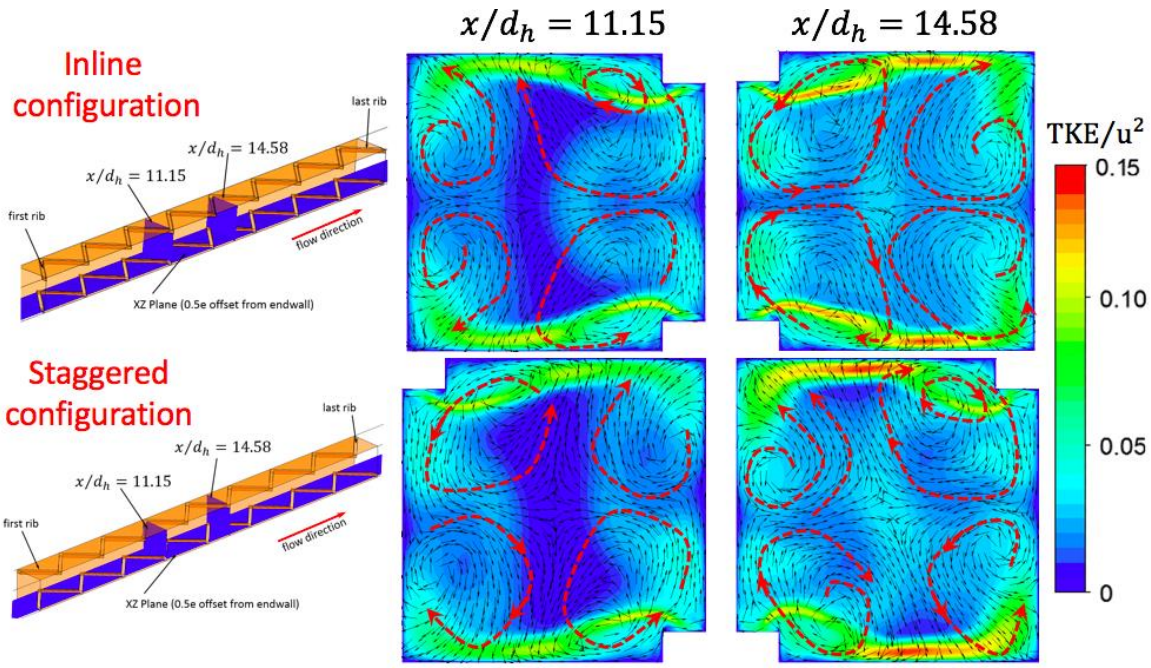

Fig. 3.12 Velocity vectors superimposed with normalized turbulent kinetic energy for two different orthogonal planes for inline and staggered configurations (Re = 30000): coolant flow is into the plane

From Fig. 3.12, it can be seen that four vortices have been formed for both inline and staggered configurations. These velocity vectors indicate the transport of colder fluid from the core towards the wall with heat flux boundary condition. Also, shown is the near wall normalized turbulent kinetic energy. It can be seen that the turbulent kinetic energy was higher near the ribs for all the planes and for both inline and staggered configurations. The large vortices while interacting with the wall break down into smaller length scale vortices, which results in increase in near wall

turbulent kinetic energy. This phenomenon is one contributor towards enhancement in heat transfer.

A different view of near wall turbulent kinetic energy has been shown in Fig. 3.13.

The breakdown of large vortices (shown in Fig. 3.12) when they approach the endwall results into small length scale eddies. This results in increase in near wall shear. Hence, increase in near wall turbulent kinetic energy results in increase in heat transfer. It can be seen that the local maxima and minima of normalized turbulent kinetic energy mimics the trend of local high and low heat transfer regions as shown in contour plots in Figs. 3.10 and 3.11. Just downstream of the rib, lower levels of heat transfer were observed due to separation of coolant from the top of the rib, hence resulting in recirculation.

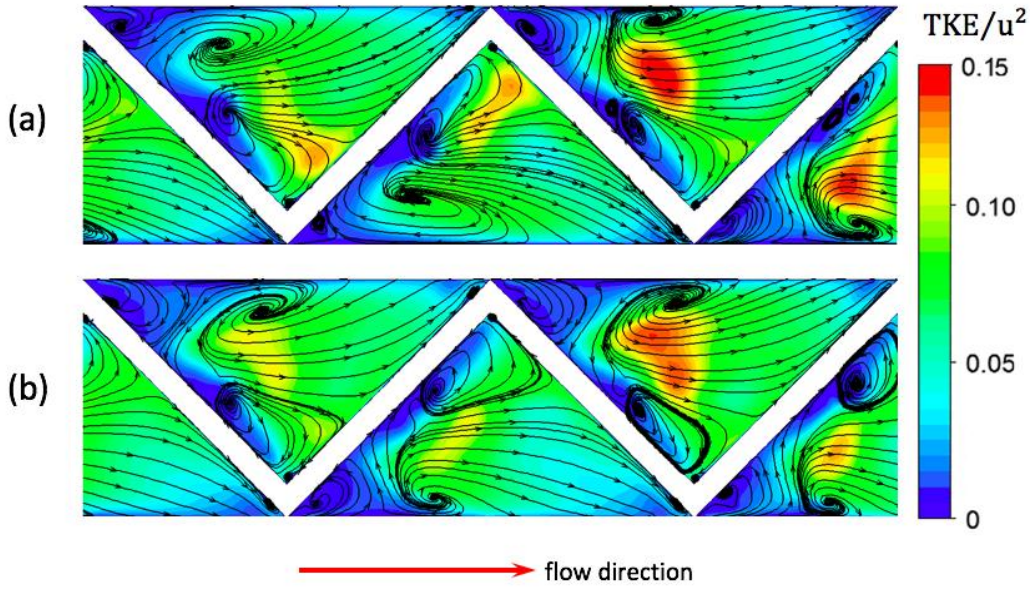

Fig. 3.13 Streamlines superimposed with normalized turbulent kinetic energy at a plane parallel to bulk flow and at a normal distance of 0.5e from the endwall featuring rib turbulators, (a) Inline, (b) staggered.

The streamlines show the probable path taken by a massless particle introduced at a given point without any initial energy. The ribs were placed at an angle of attack of 45°, hence the flow near the wall is expected to travel at an angle to the bulk flow. However, due to the interaction of secondary flows and the core coolant flow, the resultant flow directions near the wall can be seen from the streamlines.

Spanwise averaged, regionally averaged and globally averaged Nusselt number enhancement

Figure 3.14 shows the regionally averaged Nusselt number enhancement plotted in streamwise direction for the inline and staggered configurations. Length of one rib pitch was 17.2 times the rib height. The rib pitch is defined in Fig. 3.3. The definition of region is shown in Fig. 3.3.

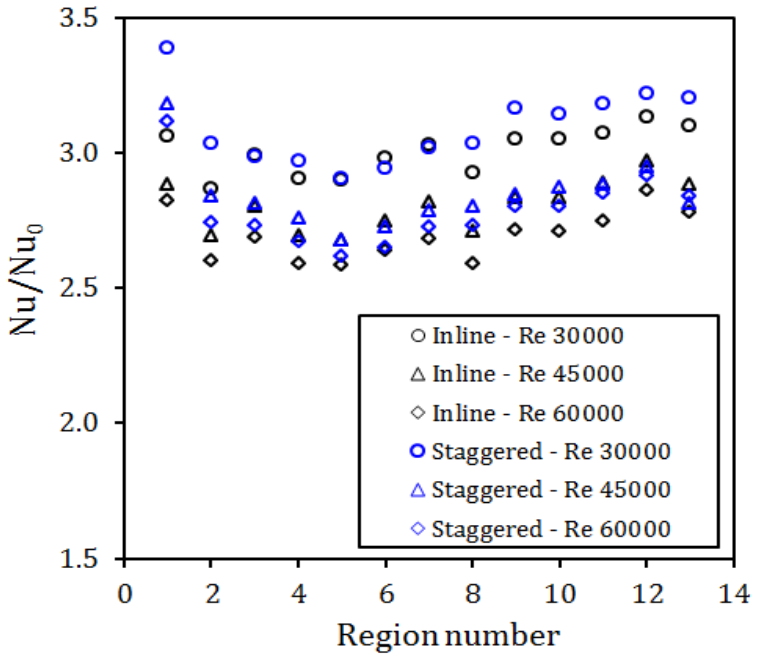

Fig. 3.14 Region-wise averaged Nusselt number enhancement plotted in streamwise direction – Inline and Staggered configurations (experimental results)

Region-wise averaged Nusselt number enhancement provides comparison between different Reynolds number on a broader scale with respect to spanwise averaged. The enhancement in heat transfer was fairly uniform across the single pass channel. The test section was designed in a way that real contributions of heat transfer enhancement features could be captured and measured with minimal variations in streamwise direction. The effects of developing flow towards the inlet of the test section can be seen as high heat transfer enhancement.

The effect of Reynolds number on Nusselt number enhancement can be seen more clearly through region based averaging. The entrance effects were found to be more pronounced for the ribbed configurations than that compared to the smooth channel. Due to the sudden expansion of the coolant while merging from the circular duct to the square duct, a much higher heat transfer

enhancement was found for the ribbed configuration. Figs. 3.9 and 3.14 are used in conjunction to determine the regions for reporting the globally averaged enhancement levels in heat transfer. For global averaging, regions 7 through 13 were taken since the entrance effects get cancelled out as seen from the heat transfer plot in Fig. 3.9. Also, the heat transfer enhancement levels were found to become periodic after region 7 for the ribbed configurations as seen in Fig. 3.14.

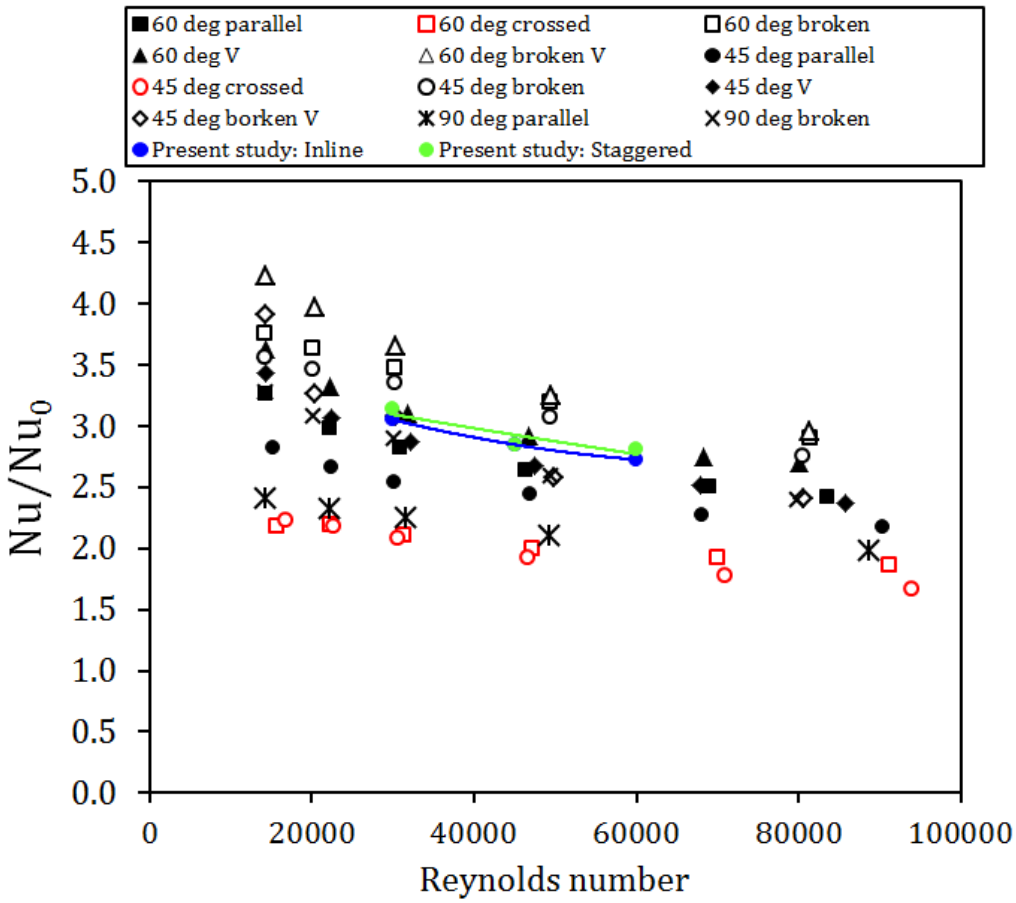

Fig. 3.15 Experimentally obtained globally averaged Nusselt number enhancement versus Reynolds number – Inline and Staggered configuration, comparison with different rib shapes from [3.53, 3.54]

Fig. 3.15 shows the globally averaged Nusselt number for the two configurations with respect to Reynolds number. Comparisons have been made with several different concepts of rib turbulators studied in [3.53, 3.54]. The staggered configuration had slightly higher heat transfer enhancement compared to the inline configuration. However, the difference between their respective heat transfer enhancements lie within the uncertainty limits of the transient liquid

crystal experiments. Hence, it can be concluded that overall heat transfer was similar for both these configurations. The enhancement in heat transfer was about 3 times of D-B correlation Nusselt number for 30000 Reynolds number and it decreased to about 2.7 times for the Reynolds number of 60000.

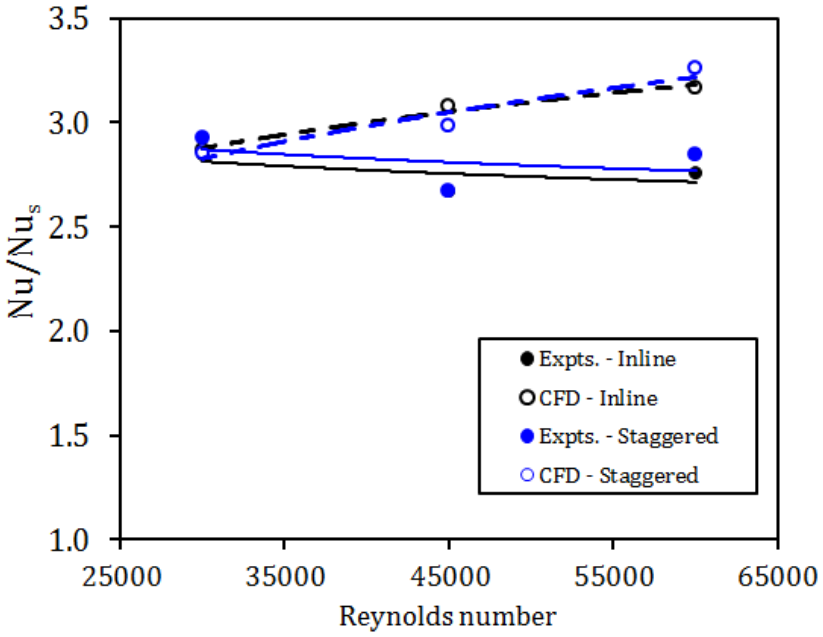

Fig. 3.16 Comparison of globally averaged normalized Nusselt number $\left(\overline{\mathrm{Nu}}/\mathrm{Nu_s}\right)$ between experiments and CFD

Figure 3.16 shows the comparison between experiments and numerically predicted normalized Nusselt number $(\overline{Nu}/Nu_s)$. A very good agreement was observed at the lowest Reynolds number of 30000. The deviation between experiments and CFD heat transfer results was found to be increasing with increasing Reynolds number. However, the difference between the predictions and measurements was still reasonable at the highest Reynolds number of 60000. One reason for this trend might be the increase in complexity to capture near wall eddies at highest Reynolds numbers. Efforts has been made towards refining the near wall grid for the highest Reynolds number in order to keep the y+ values less than one, which is one the requirements of the selected turbulence model. The equations of heat transfer enhancement versus Reynolds number has been shown in the brackets. It can be seen that the heat transfer enhancement $(\overline{Nu}/Nu_s)$ for the experiments had a weak dependence on Reynolds number. It

was observed from Fig. 3.15, that the ($\overline{\overline{Nu}}/Nu_0$) tend to decrease with increasing Reynolds number. Hence, normalization with respect to smooth channel heat transfer results provide better and more realistic representation of heat transfer enhancement as it cancels the effects of inlet conditions and only includes the effect of heat transfer enhancement features.

Comparison with established correlation of Han and Park [3.55]

Figure 17 shows the plot of heat transfer roughness function (G) with Roughness Reynolds number (e+). The correlation for G was provided by Han and Park [3.55]. The general form of the correlation was reduced to present study configuration, which is the double ribbed wall. Also, the rib pitch to rib height ratio (P/e) was taken to be half of 17.2 (Fig. 3.3) for comparison with Han and Park [3.55] correlation. The effective P/e for the present study was 8.6 since there was one rib turbulator between a length of 17.2e.

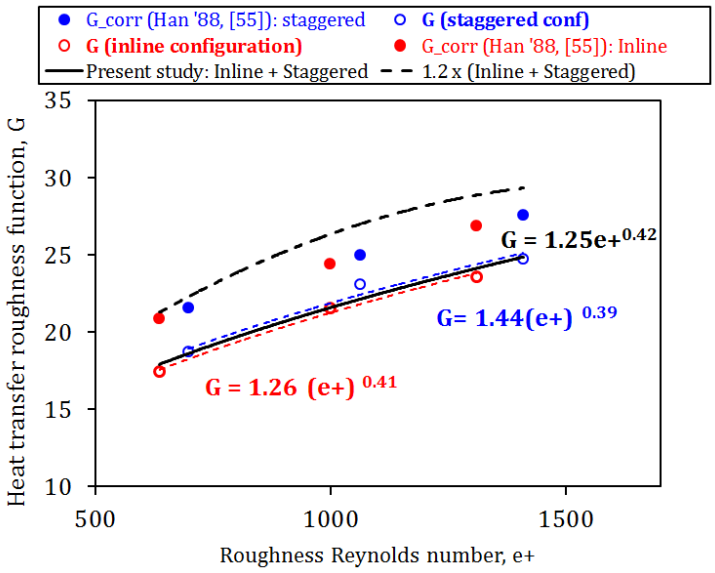

Fig. 3.17 Heat transfer roughness function (G) versus Roughness Reynolds number (e+) – correlation from present study and its proximity to Han and Park [3.55]; based experimental data of present study

The roughness Reynolds number is directly proportional to the friction factor and it is known that the heat transfer is usually proportional to the friction factor. Hence, an increasing trend of heat transfer roughness function versus roughness Reynolds number was expected. It can be seen that the data for the two configurations studied, fall on a single curve shown by black solid line.

An effective heat transfer roughness function ($\bar{\bar{G}}$) has been provided based on the data from the present study. Also, shown is the $1.2\bar{\bar{G}}$ line which encompasses the correlation of Han and Park [3.55].

Centerline static pressure (numerical), Normalized friction factor (experimental) and thermal hydraulic performance (experimental)

Figure 18 shows the variation of centerline static pressure at the endwall.

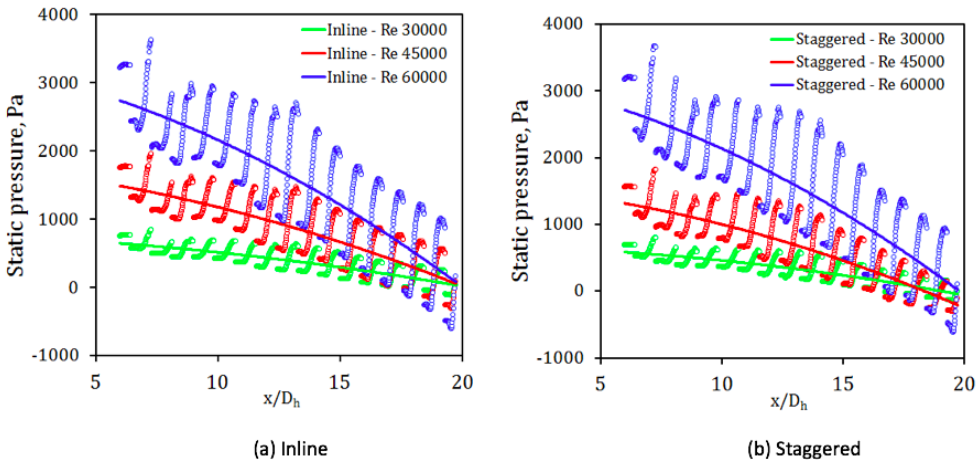

Fig. 3.18 Static pressures at the endwall centerline predicted by numerical calculations

Also shown are the trendlines (solid lines) for the static pressure variations in the streamwise direction. Since, the outlet of the channel was specified as zero gage pressure, the trendlines for all the Reynolds number converge to zero near the exit.

Figure 3.19 shows the combined plot of normalized friction factor and thermal hydraulic performance for both the configurations and for all the Reynolds numbers. The normalized friction factor and the thermal hydraulic performance is given by following equations,

$$f/f_0 = (\Delta p d_h/2\rho u^2 L)/(0.046 Re^{-0.2}) \quad (Eq. 3.6)$$

$$THP_0 = \frac{\overline{\overline{Nu}}/_{Nu_0}}{\left(f/_{f_0}\right)^{1/3}} \quad (Eq. 3.7)$$

The friction factor was expected to increase with the Reynolds number. The staggered configuration had higher friction factor than the inline configuration. As shown in Fig. 3.16, the globally averaged Nusselt number enhancement was slightly higher for the staggered configuration compared to the inline configuration. The combined effect of the globally Nusselt number enhancement and frictional losses can be combined together into thermal hydraulic performance (Eq. 3.7).

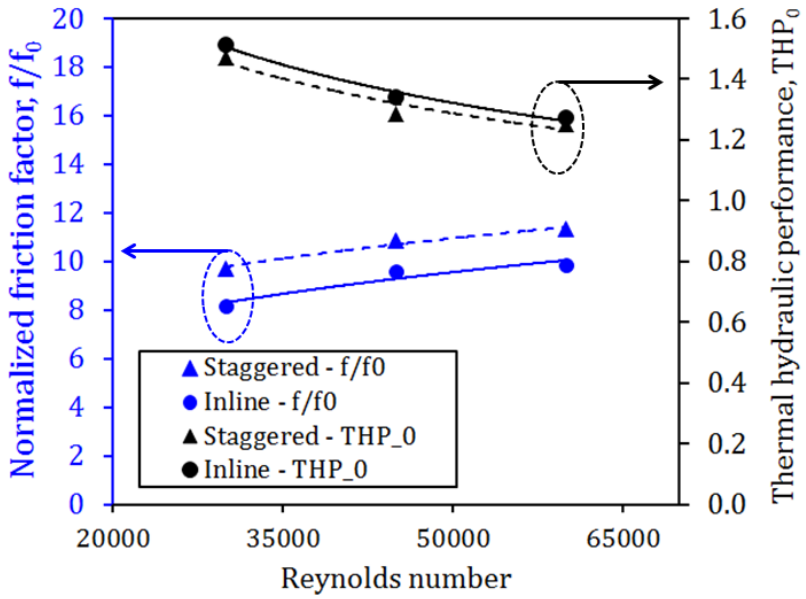

Fig. 3.19 Normalized friction factor (f/f_0) and thermal hydraulic performance (THP_0); based on experimental data from present study

The inline configuration had slightly better thermal hydraulic performance compared to the staggered configuration. However, the authors would like to caution that these THP values for inline and staggered configurations are within the uncertainty limits of each other and can be considered similar for both the configurations.

CONCLUSIONS AND RECOMMENDATIONS

The paper presents detailed measurement of heat transfer coefficient using transient liquid crystal thermography. Heat transfer and pressure drop experiments were carried out for Reynolds number ranging from 30000 to 60000. The heat transfer measurements have been presented in detailed format, spanwise averaged, regionally averaged and globally averaged. Comparison of

roughness heat transfer function with roughness Reynolds number has been made with the correlation provided by Han and Park [3.55] and an effective correlation for present study configurations have been presented in a similar format. Some of the important conclusions of the present study are as follows:

(a) The heat transfer enhancement varied from 3.1 times D-B correlation to 2.7 times, for Reynolds number changing from 30000 to 60000. The enhancement levels for both inline and staggered configurations were similar to each other.

(b) The friction factor for the inline configuration was relatively lower than the staggered configuration.

(c) The thermal hydraulic performance of both the inline and staggered configurations were similar to each other and the values changed from ~1.5 to ~1.2 for Reynolds number ranging from 30000 to 60000.

The criss-cross pattern proposed in the present study has shown promise in terms of heat transfer enhancement at a relatively lower frictional penalty. Parametric studies can be carried out to obtain optimum non-dimensional parameters (which define the configurations) which have higher thermal hydraulic performance.

NOMENCLATURE

c specific heat capacity of solid

d_h channel hydraulic diameter

e rib height

f friction factor

f_0 friction factor from modified Blasius correlation

h heat transfer coefficient

k_s thermal conductivity of solid

k_f thermal conductivity of air

L length of the test section

Nu local Nusselt number

Nu_0 Nusselt number (D-B correlation)

$\overline{\overline{Nu}}$ globally averaged Nusselt number

p rib pitch

Δp pressure drop across test section

Re Reynolds number, ud_h/v

T_i initial wall temperature

t time

T_w wall temperature

T_m mainstream temperature

THP_0 thermal hydraulic performance

u average coolant velocity in the duct

Greek symbols

ρ density of air

v kinematic viscosity of air

Subscripts

s smooth surface

Abbreviations

D-B Dittus-Boelter correlation

HT heat transfer

LC liquid crystal

LN_2 liquid nitrogen

M million

REFERENCES

[3.1] Choi, E. Y., Choi, Y. D., Lee, W. S., Chung, J. T., and Kwak, J. S., 2013, "Heat transfer augmentation using a rib-dimple compound cooling technique" Applied Thermal Engineering, 51, pp. 435-441.

[3.2] Chang, S. W., Liou, T. M., Chiang, K. F., and Hong, G. F., 2008, "Heat transfer and pressure drop in rectangular channel with compound roughness of V-shaped ribs and deepened scales" Int. J. Heat Mass Transfer, 51, pp. 457-468.

[3.3] Ekkad, S. V., Huang, Y. Z., and Han, J. C., 1998, "Detailed heat transfer distributions in two-pass square channels with rib turbulators and bleed holes" Int. J. Heat Mass Transfer, 41, pp. 3781-3791.

[3.4] Kumar, S., Amano, R. S., and Lucci, J. M., 2013, "Numerical simulations of heat transfer distribution of a two-pass square channel with V-rib turbulator and bleed holes" Int. J. Heat Mass Transf. Vol. 49, pp. 1141-1158.

[3.5] Zhang, Y. M., Gu, W. Z., and Han, J. C., 1994 "Heat transfer and friction in rectangular channels with ribbed or ribbed grooved walls" J. Heat Transfer, 116, pp. 58-65.

[3.6] Singh, P., Pandit, J. and Ekkad, S.V., 2017. Characterization of heat transfer enhancement and frictional losses in a two-pass square duct featuring unique combinations of rib turbulators and cylindrical dimples. International Journal of Heat and Mass Transfer, 106, pp.629-647.

[3.7] Singh, P., Ravi, B.V. and Ekkad, S., 2016, June. Experimental Investigation of Heat Transfer Augmentation by Different Jet Impingement Hole Shapes Under Maximum Crossflow. In ASME Turbo Expo 2016: Turbomachinery Technical Conference and Exposition (pp. V05BT16A018-V05BT16A018). American Society of Mechanical Engineers.

[3.8] Singh, P. and Ekkad, S., 2016, June. Effects of Rotation on Heat Transfer due to Jet Impingement on Cylindrical Dimpled Target Surface. In ASME Turbo Expo 2016: Turbomachinery Technical Conference and Exposition (pp. V05BT16A010-V05BT16A010). American Society of Mechanical Engineers.

[3.9] Singh, P. and Ekkad, S.V., 2017. Effects of spent air removal scheme on internal-side heat transfer in an impingement-effusion system at low jet-to-target plate spacing. International Journal of Heat and Mass Transfer, 108, pp.998-1010.

[3.10] Ravi, B.V., Singh, P. and Ekkad, S.V., 2017. Numerical investigation of turbulent flow and heat transfer in two-pass ribbed channels. International Journal of Thermal Sciences, 112, pp.31-43.

[3.11] Singh, P. and Ekkad, S., 2017. Experimental Study of Heat Transfer Augmentation in a Two-pass Channel Featuring V-shaped Ribs and Cylindrical Dimples. Applied Thermal Engineering, 116C, pp. 205-216.

[3.12] Varun, Saini R.P., Singal S.K., 2007, "A review on roughness geometry used in solar air heaters" Solar Energy, 81, pp. 1340–1350.

[3.13] Tanda G., 2011, "Performance of solar air heater dust with different types of ribs on the absorber plate" Energy, Vol. 36, pp. 6651-6660.

[3.14] Saini, R. P., and Verma, J., 2008, "Heat transfer and friction factor correlations for a duct having dimple-shape roughness for solar air heaters" Energy, 33, pp. 1277-1287.

[3.15] Bhushan, B., and Singh, R., 2010, "A review on methodology of artificial roughness used in duct of solar air heaters" Energy, Vol. 35, pp. 202-212.

[3.16] Mittal, M. K., Varun, Saini, R.P., Singal S.K., 2007, "Effective efficiency of solar air heaters having different types of roughness elements on the absorber plate" Energy, 32, pp. 739–745.

[3.17] Singh, S., Chander, S., and Saini J. S., 2011 "Heat transfer and friction factor of discrete V-down rib roughened solar air heater ducts" J. Renewable Sustainable Energy, Vol. 3, 10.1063/1.3558865

[3.18] Kumar, A., Saini, R. P., Saini, J. S., 2016, "Numerical simulation of effective efficiency of a discrete multi V-pattern rib solar air channel" Heat and Mass Transfer, Vol 52, pp. 2051-2065.

[3.19] Yadav, A. S. and Bhagoria, J. L., 2014, "A numerical investigation of square sectioned transverse rib roughened solar air heater" Int. J. Thermal Sciences, Vol. 79, pp. 111-131.

[3.20] Gill, R. S., Hans, V. S., Saini, J. S., and Singh, S., 2016, “Investigation on performance enhancement due to staggered piece in a broken arc rib roughened solar air heater duct” Renewable Energy, Vol. 104, pp. 148-162.

[3.21] Lanjewar, A. M., Bhagoria, J. L., and Sarviya, R. M., 2001, “Performance analysis of W-shaped rib roughened solar air heater”, J. Renewable Sustainable Energy, Vol. 3, 10.1063/1.3595740

[3.22] Han, J.-C., Zhang, Y. M., and Lee, C. P., 1991, ‘‘Augmented heat transfer in square channels with parallel, crossed, and V-shaped angled ribs,’’ ASME J. Heat Transfer, 113, pp. 590–596.

[3.23] Chandra, P. R., Niland, M. E., and Han, J.-C., 1997, “Turbulent flow heat transfer and friction in a rectangular channel with varying number of ribbed walls” ASME J. Turbomachinery, 119, 374-380.

[3.24] Han, J.-C., Ou, S., Park, J. S., and Lei, C. K., 1988, “Augmented heat transfer in rectangular channels of narrow aspect ratios with rib turbulators” Int. J. Heat Mass Transfer. Vol. 32. No. 9, pp. 161-163.

[3.25] Park, J. S., Han, J.-C., Huang, Y., and Ou, S., 1992, “Heat transfer performance comparisons of five different rectangular channels with parallel angled ribs” Int. J. Heat Mass Transfer., Vol. 35, No. 11, pp. 2891-2903.

[3.26] Taslim, M. E., Li, T., and Kercher, D. M., 1996, “Experimental heat transfer and friction in channels roughened with angled, V-shaped, and discrete ribs on two opposite walls” ASME J. Turbomach, Vol. 118, pp. 20-28.

[3.27] Singh, P., Ravi, B. V., and Ekkad, S. V., 2016, “Experimental and numerical study of heat transfer due to developing flow in a two-pass rib roughened square duct” Int. J. Heat Mass Transfer, 102, pp. 1245-1256.

[3.28] Tanda, G, 2011, “Effect of rib spacing on heat transfer and friction in a rectangular channel with 45 deg angled rib turbulators on one/two walls”, Int. J. Heat Mass Transfer, 54, pp. 1081-1090.

[3.29] Tanda, G., 2004, “Heat transfer in rectangular channels with transverse and V-shaped broken ribs” Int. J. Heat Mass Transfer, 47, pp. 229-243.

[3.30] Sparrow, E. M., and Tao, W. Q., 1983, “Enhanced heat transfer in a flat rectangular duct with streamwise-periodic disturbances at one principal wall”, ASME, J. Heat Transfer, 105, pp. 851-861.

[3.31] Jia, R. G., Saidi, A., and Sunden, B., 2002, “Heat transfer enhancement in square ducts with V-shaped ribs of various angles” ASME Turbo., pp. 469-476.

[3.32] Astarita, T., and Cardone, G., 2003, “Convective heat transfer in a square channel with angled ribs on two opposite walls” Experiments in Fluids, Vol. 34, pp. 625-634.

[3.33] Xie, G. N., Liu J., Zhang, W. H., Lorenzini G., and Bisemi C., 2013 “Numerical prediction of turbulent flow and heat transfer enhancement in a square passage with various truncated ribs on one wall” J. Heat Transfer 136(1), 011902 paper No: HT-12-1612.

[3.34] Bonhoff, B., Parneix, S., Leusch, J., Johnson B. V., Schabacker J., and Bolcs A., 1999, ‘‘Experimental and numerical study of developed flow and heat transfer in coolant channels with 45° ribs,’’ Int. J. Heat Fluid Flow, 20, pp. 311–319.

[3.35] Xie, G. N., Zheng, S. F., Sunden, B., 2015, “Heat transfer and flow characteristic in rib-/deflector-roughened cooling channel with various configuration parameters” Numerical heat transfer, Vol. 67, pp. 140-169.

[3.36] Mohamed, A. M. I., Hoettiba, R., and Saif, A. M., 2011, “The effect of the corrugation rib angle of attack on the fluid flow and heat transfer characteristics inside corrugated ribbed passages” J. Heat Transfer, 133(8), 081901, doi: 10.1115/1.4003668

[3.37] Sato, H., Hishida, K., and Maeda, M., 1992 “Characteristics of turbulent flow and heat transfer in a rectangular channel with repeated rib roughness” Experimental Heat Transfer, Vol. 5, pp. 1-16.

[3.38] Gao, X., and Sunden, B., 2004, “PIV measurement of the flow field in rectangular duct with 60 degrees parallel, crossed and V-shaped ribs” Exp. Thermal Fluid Sci., 28, pp. 639-653.

[3.39] Ekkad, S. V., and Han J. C., 1997, ‘‘Detailed heat transfer distribution in two-pass square channels with rib turbulators,’’ Int. J. Heat Mass Transf. 40, No. 11, pp. 2525–2537.

[3.40] Lee, D. H., Rhee, D. H., Kim, K. M., Cho, H. H., and Moon, H. K., 2009, “Detailed measurement of heat/mass transfer with continuous and multiple V-shaped ribs in Rectangular channel” Energy, Vol. 34, pp. 1770-1780.

[3.41] Murata, A. and Mochizuki, S., 2001. Comparison between laminar and turbulent heat transfer in a stationary square duct with transverse or angled rib turbulators. International Journal of Heat and Mass Transfer, 44(6), pp.1127-1141.

[3.42] Lu, B. and Jiang, P.X., 2006. Experimental and numerical investigation of convection heat transfer in a rectangular channel with angled ribs. Experimental Thermal and Fluid Science, 30(6), pp.513-521.

[3.43] Al-Qahtani, M., Chen, H.C. and Han, J.C., 2002, January. A numerical study of flow and heat transfer in rotating rectangular channels (AR= 4) with 45 rib turbulators by Reynolds stress turbulence model. In ASME Turbo Expo 2002: Power for Land, Sea, and Air (pp. 533-542). American Society of Mechanical Engineers.

[3.44] Eiamsa-ard, S. and Promvonge, P., 2008. Numerical study on heat transfer of turbulent channel flow over periodic grooves. International Communications in Heat and Mass Transfer, 35(7), pp.844-852.

[3.45] Promvonge, P., Changcharoen, W., Kwankaomeng, S. and Thianpong, C., 2011. Numerical heat transfer study of turbulent square-duct flow through inline V-shaped discrete ribs. International Communications in heat and mass transfer, 38(10), pp.1392-1399.

[3.46] Acharya, S., Dutta, S., Myrum, T.A. and Baker, R.S., 1993. Periodically developed flow and heat transfer in a ribbed duct. International Journal of Heat and Mass Transfer, 36(8), pp.2069-2082.

[3.47] Peng, W., Jiang, P.X., Wang, Y.P. and Wei, B.Y., 2011. Experimental and numerical investigation of convection heat transfer in channels with different types of ribs. Applied Thermal Engineering, 31(14), pp.2702-2708.

[3.48] Sewall, E.A. and Tafti, D.K., 2006. Large Eddy Simulation of Flow and Heat Transfer in the 180-Deg Bend Region of a Stationary Gas Turbine Blade Ribbed Internal Cooling Duct. Journal of turbomachinery, 128(4), pp.763-771.

[3.49] Incropera, F.P. and De Witt, D.P., 1985. Fundamentals of heat and mass transfer.

[3.50] Ekkad, S.V. and Han, J.C., 2000. A transient liquid crystal thermography technique for gas turbine heat transfer measurements. Measurement Science and Technology, 11(7), p.957.

[3.51] Camci, C., Kim, K. and Hippensteele, S.A., 1991, June. A new hue capturing technique for the quantitative interpretation of liquid crystal images used in convective heat transfer studies. In ASME 1991 International Gas Turbine and Aeroengine Congress and Exposition (pp. V004T09A009-V004T09A009). American Society of Mechanical Engineers.

[3.52] Moffat, R.J., 1985. Using uncertainty analysis in the planning of an experiment. ASME, Transactions, Journal of Fluids Engineering (ISSN 0098-2202), 107, pp.173-178.

[3.53] Han, J.C., Zhang, Y.M. and Lee, C.P., 1991. Augmented heat transfer in square channels with parallel, crossed, and V-shaped angled ribs. *Journal of Heat Transfer*, *113*(3), pp.590-596.

[3.54] Han, J.C. and Zhang, Y.M., 1992. High performance heat transfer ducts with parallel broken and V-shaped broken ribs. *International Journal of Heat and Mass Transfer*, *35*(2), pp.513-523.

[3.55] Han, J.C. and Park, J.S., 1988. Developing heat transfer in rectangular channels with rib turbulators. International Journal of Heat and Mass Transfer, 31(1), pp.183-195.

CHAPTER 4

Effects of spent air removal scheme on internal-side heat transfer in an impingement-effusion system at low jet-to-target plate spacing

Prashant Singh & Srinath V. Ekkad
Advanced Propulsion and Power Laboratory,
Virginia Tech, Blacksburg, VA 24061

Int. J. Heat Mass Transfer, 108, pp. 998-1010

ABSTRACT

Present study reports detailed measurements of heat transfer coefficient for jet impingement in an impingement-effusion system at low jet-to-target plate spacing. The heat transfer coefficients were measured experimentally by transient liquid crystal thermography. Heat transfer experiments were carried out at three jet Reynolds numbers – 3500, 6000 and 9000. The jet plate featured 8 x 9 circular jets with normalized streamwise (x/d_j) and spanwise (y/d_j) spacing of 6. The configurations are divided into two segments based on the characteristics of target surface. The first target surface was smooth without effusion holes, and the second target surface was smooth with effusion holes. The arrangement of effusion holes was staggered with respect to jet plate and the ratio of effusion hole diameter to jet hole diameter was unity. For the smooth target surface without effusion holes, three crossflow schemes were studied – minimum, intermediate and maximum. For the smooth target surface with effusion holes, four different crossflow schemes were studied – zero, minimum, intermediate and maximum. Interesting heat transfer characteristics are reported for different crossflow schemes as it was found that low z/d_j (=1) played an important role in the spent air removal from the system. Discharge coefficient of jets are also reported for wide range of plenum pressure ratio. Also reported are the pumping power requirements for each configuration across full range of flow conditions. It has been found that the minimum crossflow scheme (with and without effusion holes) has been the most efficient configuration and the maximum crossflow scheme with target surface without effusion holes has been the least efficient configuration.

Keywords: Nusselt number; transient liquid crystal thermography; impingement; effusion; pumping power

Introduction

Jet impinging has been widely used for applications requiring high rates of heat removal. Some of the common applications of jet impingement can be found in gas turbine blade leading edge, electronic cooling, combustor liner cooling, food processing industry, etc. Over the past few decades, several studies have been carried out to understand jet impingement heat transfer under various conditions. Jet impingement heat transfer depends upon several parameters, such as, spanwise and streamwise spacing between jets, jet-to-target plate spacing, nozzle contouring, crossflow (spent air) removal scheme, roughness of target surface, initial crossflow, etc. Earlier studies on jet impingement were focused on single jet, in order to establish standard definitions of heat transfer coefficient for jet impingement systems. Goldstein and Behbahani [4.1] studied heat transfer characteristics of single jet with and without crossflow. The authors established fundamental definition of heat transfer coefficient for jet impingement. They also provided definitions of recovery factor and emphasized on the accurate knowledge of adiabatic wall temperature in the determination of heat transfer coefficient. Viskanta [4.2] described the fairly complex fluid dynamics peculiar to jet impingement. The author concluded that thermal boundary layer is thinnest near the stagnation region and hence will have maximum heat transfer compared to other radially outboard locations. More details about research on jet impingement prior to 1992 can be found in the review paper by Jambunathan et al. [4.3].

Impingement/Effusion systems have also been widely studied. Some of the important studies carried out prior to 2005 has been listed from [4.4-4.9]. Andrews et al. [4.4] reported overall heat transfer coefficient for impingement/effusion system using a transient cooling technique. The authors found that the heat transfer coefficient for impingement/effusion system on the effusion inner wall was higher than the impingement alone case by 30% to 45%. The reason accounted for higher heat transfer was due to the pressure loss from the effusion walls. Dabagh et al. [4.5] studied the effects of number of impingement holes and pressure loss on heat transfer coefficient in an impingement/effusion cooling system. The authors used computer code to analyze the fluid dynamics in the impingement channel. Their measurements indicated that the interaction between the target and the jet plate resulted in a convective heat transfer to the jet plate and this

heat transfer was about half of the convective heat transfer on the target wall. The authors also concluded that increasing the number of impingement holes resulted in decrement in heat transfer coefficient by about 20%. Cho and Rhee [4.6] investigated the effects of jet-to-effusion plate distance on heat transfer on the effusion inner wall. The authors found high heat transfer region at the stagnation point and at the mid-line between two jets due to secondary flows. In general, for low values of z/d, the heat transfer was higher. In this study, the crossflow was guided through the effusion holes only. Rhee et al. [4.7] studied the heat transfer in an impingement/effusion system with initial crossflow for a z/d of 2. A mass transfer technique was used to calculate the mass transfer coefficient and then the heat transfer coefficient from the heat-mass transfer analogy. The authors reported shifting of stagnation points due to strong effects of crossflow. One interesting observation from this study was the heat/mass transfer coefficients for impingement/effusion cooling with crossflow were similar to impingement cooling with the same initial crossflow. Ekkad et al. [4.8] investigated the effect of the presence of film cooling holes on target plate. The authors studied three different crossflow schemes and reported that the presence of film cooling holes helped in the regulation of crossflow but the effect of film holes for maximum crossflow case was not discernable. The heat transfer comparisons in [4.8] were made with an earlier study carried out by Huang et al. [4.9].

Rhee et al. [4.10] carried out experimental and numerical investigation of heat/mass transfer for impingement/effusion system at low jet-to-target plate spacing. The authors reported that strong crossflow effects in the case of impingement alone configuration can be regulated by having effusion holes where all the spent air was forced to pass through the effusion holes. Cho et al. [4.11] investigated the effects of hole arrangement on local heat/mass transfer in an impingement/effusion cooling system. The authors studied three types of relative arrangement of jet and effusion holes – staggered, shifted in one direction and inline. The authors reported that overall averaged Sherwood number for staggered and shifted arrangement was approximately 70% higher than the in-line configuration.

Post 2005 studies on impingement/effusion cooling have been listed from [4.12-4.14]. Hong et al. [4.12] studied the effects of fin shapes and their arrangements on heat transfer for impingement/effusion cooling system with crossflow. The authors reported that as the crossflow strengthened, the effects of fins became more dominant and resulted in enhanced heat transfer,

however, the pressure losses also increased due to increase in the channel blockage ratio due to the addition of the fins. Hong et al. [4.13] studied heat transfer characteristics of impingement/effusion cooling with rib turbulators under rotating conditions. The authors reported that for leading and trailing edges, the deflection of jets because of crossflow reduced, due to presence of ribs. Hoberg et al. [4.14] carried out heat transfer measurements for jet impingement arrays with local coolant extraction. Correlations were provided for Nusselt number as function of jet Reynolds number for different cases studied.

Current paper documents detailed study of all the possible crossflow schemes in order to determine a configuration which has highest thermal hydraulic performance. The jet-to-target plate distance was kept low in order to simulate configurations which can be used in double wall cooling arrangements in turbine airfoils where space is one of the major constraints. An interesting way of evaluating efficiency of impingement/effusion cooling system has been shown in the present study by plotting global Nusselt number with the pumping power requirement. Separate effects of crossflow regulation and nature of target surface (with and without effusion holes) have been studied. The present study reports detailed measurements of heat transfer coefficient on target plates, with and without effusion holes. The jet-to-target plate spacing was kept at one jet diameter. For the target plate with no effusion holes, three different crossflow schemes were tested – minimum, intermediate and maximum crossflow. For the target plate with effusion holes, four different crossflow schemes were tested – minimum, intermediate, maximum and zero crossflow. For all the above crossflow schemes, the jet Reynolds number was varied from 3500 to 9000. This study investigates the effect of spent air removal scheme on jet impingement heat transfer in an impingement/effusion system at low jet-to-target plate spacing. Following section documents the details of the experimental setup, data reduction procedure, uncertainty and sensitivity analysis, and result and discussion.

Details of Experimental Setup

The experimental setup was designed for transient liquid crystal thermography experiments and is very similar to [4.15]. For these transient experiments, a step change in the fluid temperature is required in order to calculate heat transfer coefficient by monitoring the response of the target surface towards sudden change in the form of surface temperature measurement. The working fluid used in these experiments was air. Air was discharged from the building

compressor at around 300 K and 7 atm (~0.710 MPa) and was used to feed a buffer tank inside the test cell. The pressure in the buffer tank was regulated by a pressure regulator located at the exit of the tank. Depending upon the mass flow rate requirements of the transient tests, the pressure in the buffer tank was adjusted in order to ensure that the supply pressure (and mass flow rate) during the transient experiment was close to the intended value and remained constant throughout the experiment. A flow control valve was installed downstream of the buffer tank for flow rate adjustment. The mass flow rate was metered by an orifice meter. The orifice meter was located about 35 pipe diameters downstream of the flow control valve. The differential pressure at the orifice meter was measured by Dwyer 477-4 FM (10 psi (~70 kPa) range). The higher pressure at the orifice meter was measured by DPG-103 (30 psi (~210 kPa) range) and the fluid temperature was measured by a T-type thermocouple. The high pressure and temperature of the fluid was measured in order to calculate the density of the air so that the slight variations in the density due to change in ambient conditions can be accounted for in the mass flow rate calculations. Another flow control valve was installed about 10 pipe diameters downstream of the orifice plate for more control over the flow rate adjustment. A couple of solenoid valves were used in tandem as a 3-way valve. Since a step change is required in the mainstream temperature for transient liquid crystal experiments, a chilled thermal reservoir was created at the beginning of each experiment. The thermal reservoir is highlighted by dark black line in Fig. 4.1. In the present study, colder air has been chosen for the transient experiment. However, the same experiment can also be carried out using hot air and the heat transfer coefficients will only change slightly due to change in the direction of heat transfer. A fitting was provided downstream of the solenoid valve #1 for the intake of liquid nitrogen. A mixture of liquid nitrogen and lab ambient air was used in order to create the chilled thermal reservoir. Once the desired temperature of the reservoir was obtained, the remaining nitrogen in the reservoir was purged out through vent V1.

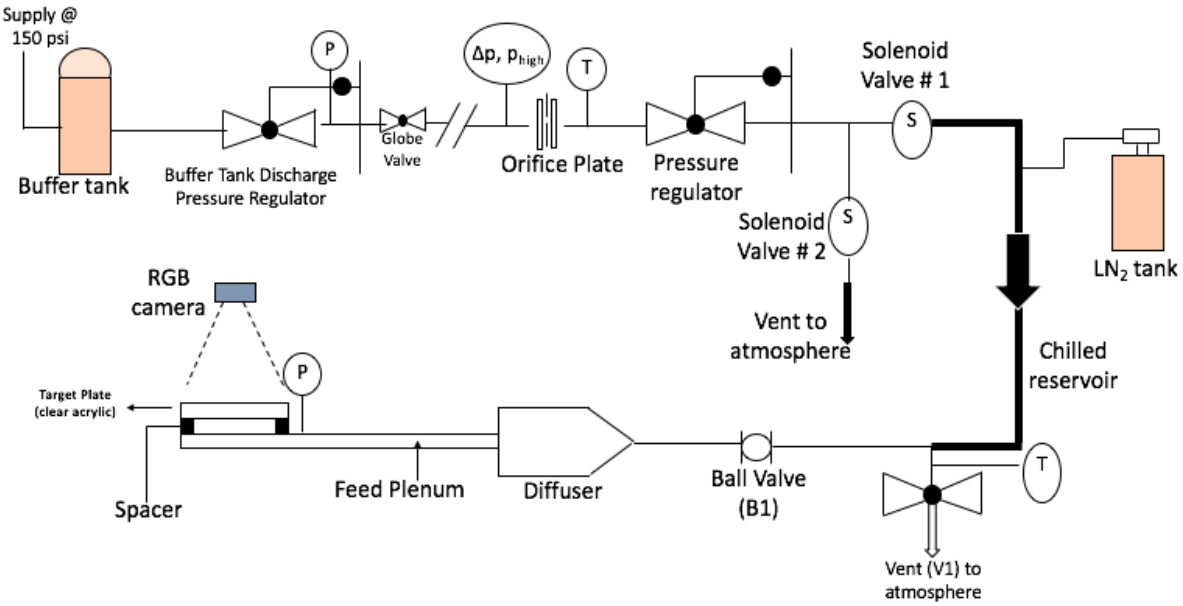

Fig. 4.1(a) Schematic of the experimental setup

The temperature of the chilled reservoir was selected based on the total mass flow rate required for an experiment. Higher the jet Reynolds number for a particular experiment, smaller was the temperature differential required to get the liquid crystal color because of the high heat transfer coefficients associated with high Reynolds numbers. It was made sure that the experimental run times were similar across all the Reynolds numbers studied.

Before the commencement of the transient experiment, the solenoid valve pair was switched towards the atmosphere. The ball valve (B1) and the gate valve (V1) was set towards the test section. The flow rate was set at desired value and the test was commenced with single LabVIEW signal which flipped the solenoid valves towards the test section. Single click procedure for transient test commencement removed any possibility of lag between the actual start time of the test and the time at which temperature measurement recording was started. The flow rate was continuously monitored during the transient experiment and it was made sure that the flow rate was constant and very close to the intended value.

The details of the test section, camera location, plenum chamber length and liquid crystal location has been shown in Fig. 4.1(b). Sufficient length was provided in order to obtain a uniform pressure in the feed chamber/plenum. The target surface was made out of smooth acrylic

which is optically clear and has low thermal conductivity. The first layer of coating on the clear acrylic was thermochromic liquid crystal which was sprayed by air-brush. The supply pressure of the air-brush and the quantity of liquid crystal was maintained the same across different test runs in order to achieve uniform thickness of liquid crystal. A fine layer of water soluble black paint was also sprayed on top of the liquid crystal layer in order to provide good contrast color change.

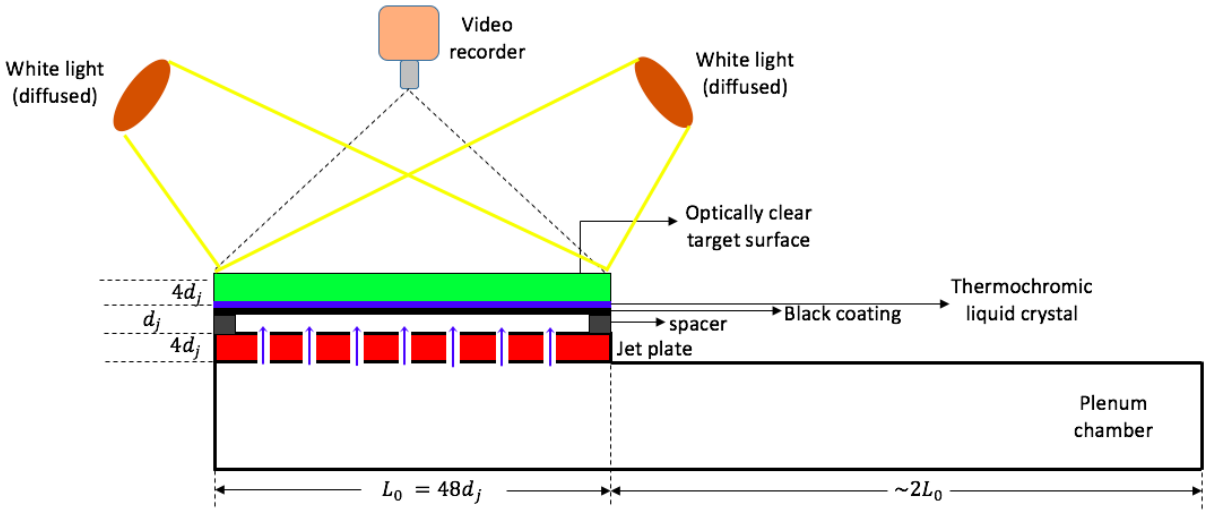

Fig. 4.1(b) Details of test section, camera location, plenum chamber length, liquid crystal location (not drawn to scale)

Description of Test Configurations and Experimental Conditions

The impingement/effusion system in the present study comprises of jet plate, target plate, spacer, plenum chamber. The jet consists of 72 jets in total, where 9 rows of jets were arranged in spanwise (y) direction and 8 rows of jets were arranged in streamwise (x) direction. The x and y directions have been shown in Fig. 4.2(a).

The effusion plate consists of 56 jets where 8 jets were arranged in spanwise direction and 7 jets were arranged in streamwise direction. The relative positioning of effusion and impingement holes was staggered (Fig. 4.2(a)). The diameter of impingement hole and effusion hole was equal to 3.175 mm. The target surface can be divided in two types – (a) target surface without effusion holes, (b) target surface with effusion holes. This study focuses on the effect of

spent air removal of impingement heat transfer. Three different crossflow schemes were investigated for target surface with no effusion holes – minimum, intermediate and maximum crossflow. Four different crossflow schemes were investigated for target plate with effusion holes – minimum, intermediate, maximum and zero crossflow. The crossflow schemes are shown in Fig. 4.2(b). For all the above configurations, detailed heat transfer measurements were carried out using transient liquid crystal thermography. The jet-to-target plate spacing was one jet diameter. The jet Reynolds number considered in the present study ranges from 3500 to 9000. Following section describes the data reduction procedure for heat transfer coefficient measurement and discharge coefficient measurement.

Data Reduction Procedure

In the present study, detailed Nusselt numbers have been experimentally measured using transient liquid crystal thermography. Also, the discharge coefficient of the jet, jet exit Mach number and pumping power has been experimentally measured for a wide range of plenum pressure ratios. This section describes the procedure involved in the measurement and calculation of above mentioned quantities.

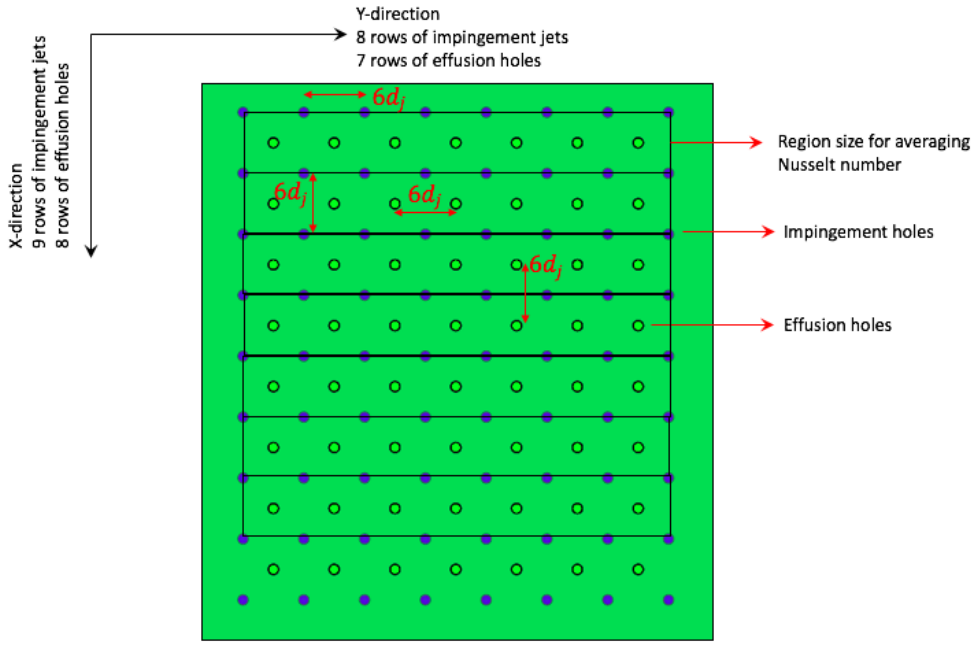

(a)

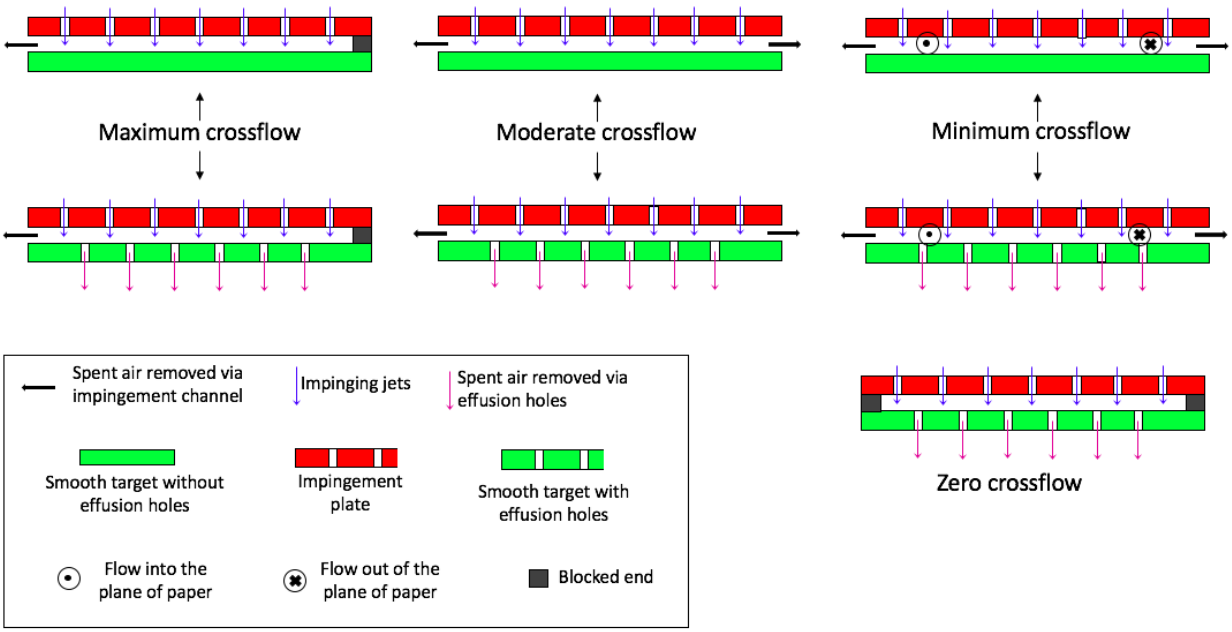

(b)

Fig. 4.2 (a) Relative arrangement of impingement and effusion holes (top view), also indicated is the region size for area averaged Nusselt number, (b) different crossflow schemes studied (side view).

Heat Transfer Coefficient Calculation

The heat transfer coefficient is calculated using transient liquid crystal thermography by treating the target surface as 1D semi-infinite solid. The one dimensional transient heat conduction partial differential equation when solved with convective boundary condition on the target side, constant temperature on the other side of target surface, yields the following equation.

$$\frac{T_w(t) - T_i}{T_m - T_i} = 1 - exp\left(\frac{h^2 t}{\rho c k_t}\right) erfc\left(h\sqrt{\frac{t}{\rho c k_t}}\right) \quad Eq.(4.1)$$

The maximum permissible time for the experiment without violating the 1D semi-infinite assumption is given by Eq. 2. It was ensured that the total duration of the experiment was well within t_{max}. For the present study, the maximum permissible time of the transient experiment

was 147 seconds. However, the typical duration of transient experiment did not exceed 60 seconds.

$$t_{max} = 0.1\frac{\rho c {t_{target}}^2}{k_t} \quad (Eq. 4.2)$$

Also, Eq. 1 is valid for a constant mainstream temperature (T_m). During the transient experiment, the mainstream temperature was not constant, and was both time and space dependent. Figure 4.3 shows the mainstream temperature variation with time in a typical transient experiment.

Now, the Eq. 1 can be modified in order to account for the time varying mainstream temperature using Duhamel's superposition principle. The time dependent mainstream temperature can be divided into small time steps, and it has been assumed that the mainstream temperature during each time step was constant. The modified form of Eq.1 can be written as,

$$T_w = T_i + \left(\sum_{i=1}^{i=n_{max}} (T_{m,i} - T_{m,i-1})\right) \times \left[1 - exp\left(\frac{h^2(t-t_i)}{\rho c k_t}\right) erfc\left(h\sqrt{\frac{t-t_i}{\rho c k_t}}\right)\right] \quad Eq. (4.3)$$

In Eq. 3, T_m is the static temperature measured in the plenum chamber and "i" indicates the summation index over entire test duration. The coolant speed in the plenum chamber was about 3% of the jet velocity. Usually in transient liquid crystal experiments, the jet total temperature is taken as the driving fluid temperature. In present study, an isentropic expansion of jets has been assumed. Due to low speed of coolant flow in the plenum chamber, the temperature measured in the plenum chamber can be assumed to be static and under isentropic expansion of jets, the measured static temperature of coolant is equal to jet total temperature. The static temperature in the plenum chamber was measured by a fast response T-type thermocouple with a bead diameter of 0.0763 mm. The data acquisition was carried out through a LabVIEW program which linked the computer storage to a National Instrument (NI) chassis (cDAQ9174) housing thermocouple module (NI9214). The mainstream temperature or the plenum static temperature was measured at two locations – (1) just underneath the first row in x-direction (location 1), (2) just underneath the last row in the x-direction (location 2). From several plenum temperature measurements in the plenum chamber across different Reynolds numbers, it was deduced that the spatial variation in the y-direction was negligible. The variation in streamwise direction was due to the coolant extraction in the streamwise direction and other heat transfer losses which were

transient in nature. This spatial variation of time dependent mainstream temperature was taken into account by linear interpolation from the first row to the last row (9^{th} row) in streamwise direction. However, the difference in the mainstream temperatures measured at these two locations were within 1°C, but it was still accounted for, in the heat transfer coefficient calculations.

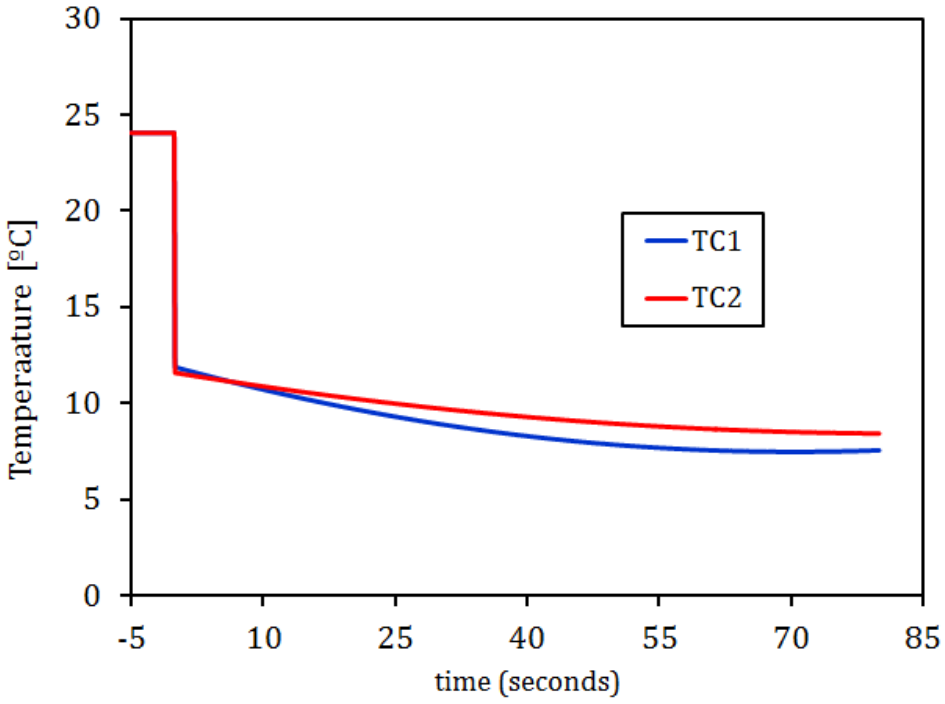

Fig. 4.3 Time history of typical plenum temperatures measured at location 1 and location 2, the transient test started at t = 0 seconds, TC measurements shown for maximum crossflow condition

In Eq. 4.3, T_i is the initial temperature of the solid. T_i was calculated by averaging the wall temperature measured till the commencement of the transient experiment. At this stage, the unknowns in Eq. 4.3 are T_w, t and h. Following discussion addresses the procedure for determination these three unknown quantities.

The TLC color change video was recorded using a GoPro Hero 3 camera at 30 frames per second. The raw video was processed using standard MATLAB functions and RGB information was extracted. The RGB information was then used to calculate Hue, Saturation and Intensity for each pixel at each frame. The relationship between Hue and wall temperature was established by

calibrating the LC color change by thermocouple measurement at the wall. Two thermocouples (T-type) were taped on the target wall for LC color change to wall temperature calibration. It was found that the two calibrations were very similar to each other and the Hue versus wall temperature method used in the present study was found to be very robust in terms of lighting conditions.

A 5 x 5 region was chosen in the close vicinity of the wall thermocouple, and an average Hue value was calculated over 25 pixels at each frame. This Hue was plotted against the measured wall temperature and hence a relationship between Hue and wall temperature was established (Fig. 4.4). The thermochromic liquid crystal used in the present study was manufactured by Hallcrest and the part number was R10C5W. The liquid crystal color play region was between 10°C to 15°C. A typical calibration curve between Hue and measured wall temperature has been shown in Fig. 4. Once the relationship between Hue and wall temperature was established, a reference Hue value was chosen for further data reduction.

Now, T_w in Eq. 4.3 is a wall temperature corresponding to a particular Hue value. Each pixel was sequentially traversed individually and the frame number was recorded at which a particular hue value (H_{ref}) was reached. Also, at each frame, the saturation and intensity values were checked and a filter for a minimum threshold of 0.3 was applied on saturation and intensity values for each pixel in order for it to qualify for HTC data reduction. Once all three conditions of Hue, Saturation and intensity were satisfied for a particular pixel, the corresponding frame number was then converted to real time by dividing the frame number by the frame rate at which the video was recorded. The real time hence obtained was stored in a two dimensional matrix, which is referred as 'time matrix'. At this stage, the only unknown in Eq. 4.3 was the heat transfer coefficient. Heat transfer coefficient was determined through an error minimization routine, which in the present study was the secant method. Once the heat transfer coefficient was determined, Nusselt number was calculated from Eq. 4.4.

$$Nu_d = \frac{hd_j}{k_f} \quad (Eq.\,4.4)$$

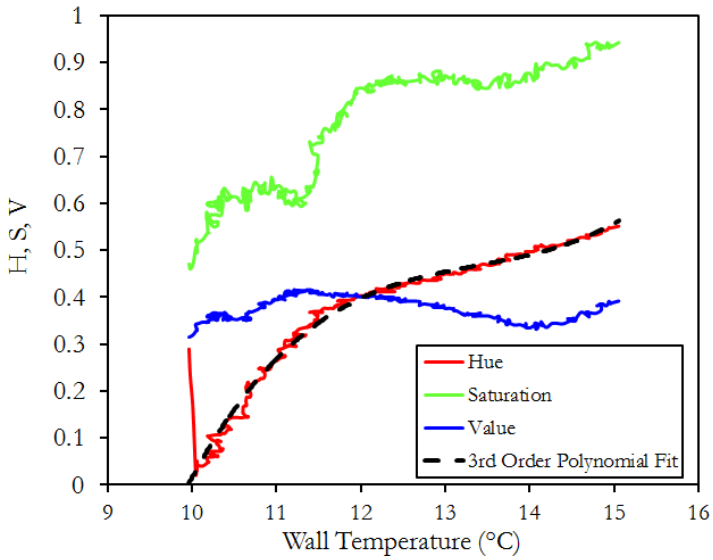

Fig. 4.4 Calibration of Hue with measured wall temperature, also shown is the saturation and intensity variation with wall temperature

The thermal conductivity of fluid (air) near the wall was calculated at the film temperature which was the mean of the average wall temperature (during transient experiment) and the jet total temperature.

Discharge Coefficient, Jet Exit Mach Number and Pumping Power Calculations

The discharge coefficient of the round jets was measured by exposing the jet plate to ambient and measuring the pressure in the plenum chamber. The discharge coefficient is only a function of the plenum pressure ratio and many studies have confirmed that the discharge coefficient has a weak dependence on the plenum pressure ratio. Hence, this simple method was designed for the discharge coefficient determination. Static pressure measurements were carried out in the plenum chamber at several locations, and the mean of these static pressures was taken as the static pressure for the discharge coefficient calculation. The discharge coefficient is given by Eq. 5.

$$C_d = \frac{G_{actual}}{G_{ideal}} \quad (Eq. 4.5)$$

The ideal mass flux was calculated from Eq. 6.

$$G_{ideal} = \left(\frac{p_{m,abs}}{R_a T_m}\right)\sqrt{\gamma R_a T_m}\sqrt{\frac{2}{\gamma - 1}\left[(p_{r,m^*})^{(\gamma-1)/\gamma} - 1\right]} \quad (Eq.\,4.6)$$

The actual mass flux was determined from the total mass flow rate measurement at the orifice plate. The actual mass flux is given by,

$$G_{actual} = \frac{\dot{m}_{actual}}{A_j N} \quad (Eq.\,4.7)$$

Figure 4.5 shows the variation of discharge coefficient with the plenum pressure ratio. The range of plenum pressure ratio encompasses different plenum pressures for the range of jet Reynolds number investigated for heat transfer measurements. Due to the uniformity of discharge coefficient, it can be concluded that discharge coefficient was only dependent on the shape of the jet, which in turn dictates the plenum pressure ratio. It can be seen that the discharge coefficient was uniform (~0.7) for the range of plenum pressure ratios investigated – this trend is in conformity with many other similar studies where discharge coefficient of an orifice/jet has been determined. Also shown is the variation of jet exit Mach number for a wide range of plenum pressure ratios.

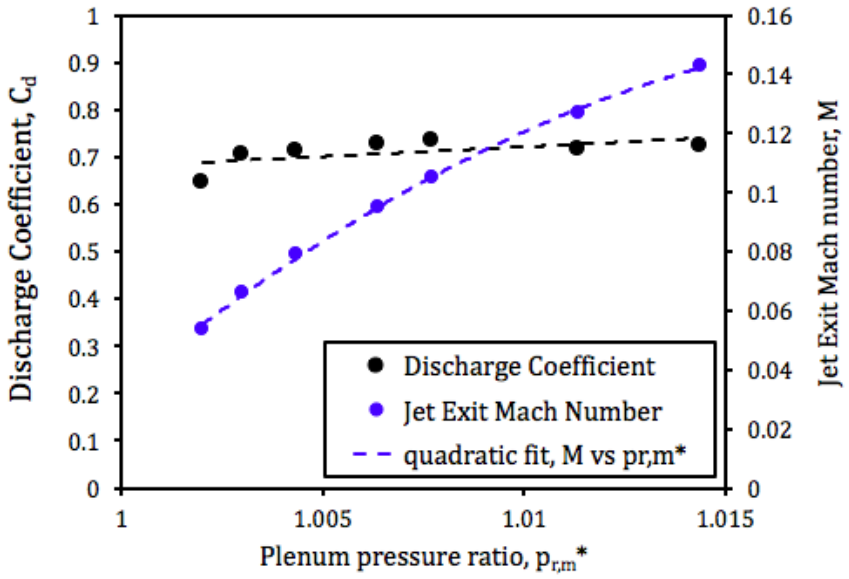

Fig. 4.5 Variation of discharge coefficient and jet exit Mach number with plenum pressure ratio

Pumping Power Calculations:

For the measurement of pumping power, a separate flow experiment was carried out. In this case, the target surface was assembled with the corresponding spacer for different crossflow schemes. Static pressure measurements in the plenum chamber were then carried out for all the configurations for both types of target surfaces- with and without effusion holes. A wide range of average jet Reynolds number (upto 9000) were investigated for the pumping power measurements to develop trendlines with high regression coefficient. The pumping power required to maintain certain plenum pressure ratio is given as,

$$Total\ Pumping\ power\ [W], Q = \dot{\forall}\Delta p = \frac{\pi \mu d_{jet} NRe \Delta p}{4\rho} \quad (Eq.\ 4.8)$$

Here, Δp is the total pressure drop between the plenum and the ambient, to provide an overall pumping power. Figure 4.6 shows the variation of pumping power with jet Reynolds number. It can be seen that the target plate with effusion holes under zero crossflow setting requires the maximum pumping power relative to other configurations. Also, for all the cases, the corresponding pumping power required in the case of target plate with effusion holes, for a given crossflow scheme, is always lower than the case of target surface without effusion holes. The intermediate data points provide more confidence in the trend of pumping power versus average jet Reynolds number. More discussion has been provided in a later section, where globally averaged Nusselt number has been compared in reference with pumping power.

Uncertainty Analysis

The uncertainty in the measurement of Nusselt number and jet Reynolds number was calculated by the sequential perturbation method prescribed by Moffat [4.16]. The factors which contribute in the uncertainty of Nusselt number are T_w, T_i, T_m, t, $\sqrt{\rho c k_t}$. The uncertainty in the measurement of temperatures was taken to be 0.5°C. The uncertainty in the time (t) taken to reach a particular temperature was taken to be the time taken to record two frames (0.067 seconds). The uncertainty in the solid properties was taken to be 5% of their nominal value. The uncertainty in a typical Nusselt number of 24 was found to be 12.2% based on the normalized wall temperature found during the experiments. Yan and Owen [4.17] carried out a detailed study to analyze uncertainties in typical transient liquid crystal thermography experiments and

prescribed methods which can yield lower levels of uncertainties. From there analysis, the authors recommended that if the normalized wall temperature varies between 0.3 and 0.7, it will lead to lower levels of uncertainties In the present study, the choice of liquid crystal color band and mainstream temperature variation was taken such that most of the pixels follow the recommendations of [4.17]. The uncertainty in the measurement of jet Reynolds number of 6000 was found to be 4%.

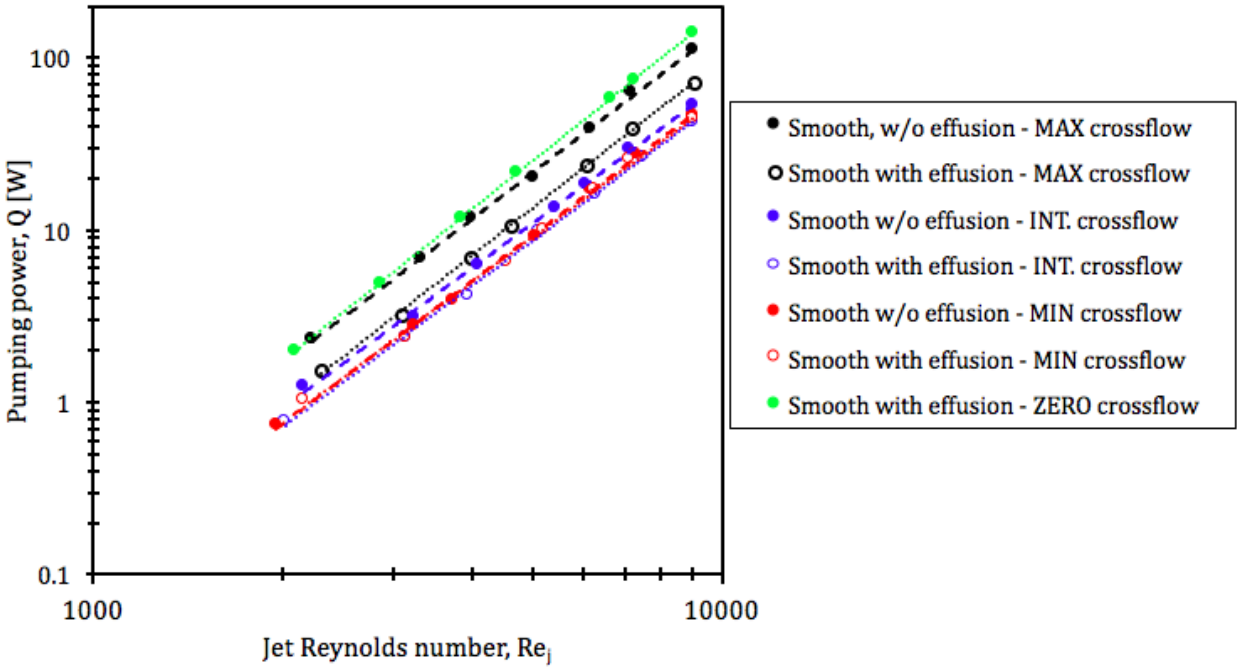

Fig. 4.6 Pumping power versus jet Reynolds number for all configurations for full range of jet Reynolds number investigated in heat transfer experiments (measurements were also carried out at intermediate jet Reynolds numbers in order to obtain high regression coefficient) (Note: Q is the total pumping power required for maintaining an average jet Reynolds number of Re_j across N jets)

VALIDATION OF EXPERIMENTAL DATA WITH CORRELATIONS

The experimental configuration of jet impingement onto smooth target under maximum crossflow condition was chosen for validation of current experimental data with the existing correlations. The correlation for Nusselt number provided by Florschuetz et al. [4.18] is valid for jet impingement on a target plate without film/effusion holes under maximum crossflow condition. The present study also investigates one such configuration and the comparison with [4.18] is shown in Fig. 4.7. The correlation prescribed by [4.18] is empirically constructed with a

basic nature of decreasing heat transfer with increasing streamwise distance because of crossflow accumulation and its release. The downstream jets in maximum crossflow condition suffer jet deflection and hence reducing the jet effectiveness. In the present study, at very low jet-to-target plate spacing, it has been observed that spent air underwent strong acceleration in the streamwise direction that subsequently led to increasing heat transfer in the downstream direction. This observation is consistent with [4.19] where the authors studied the effects of jet-to-target plate spacing on impingement heat transfer by an array of 5 jets under maximum crossflow condition. The authors in [4.19] observed decreasing heat transfer with streamwise distance for z/d greater than 1, but heat transfer coefficients increased with increasing streamwise distance for z/d of 0.5 and 1. The globally averaged Nusselt number for the maximum crossflow condition for impingement onto target surface with and without effusion holes is compared with similar studies carried out by [4.8], [4.9] and [4.18].

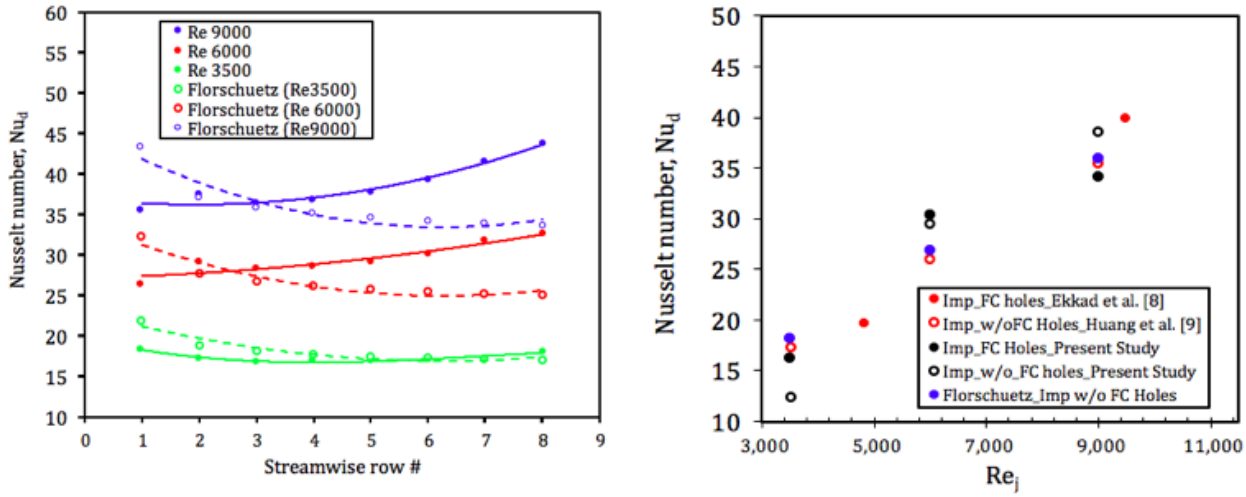

Fig. 4.7 Left figure: Comparison of Nusselt number with correlation prescribed by Florschuetz et al. [4.18]; Right figure: comparison of heat transfer data with similar past studies

RESULTS AND DISCUSSION

This section reports the heat transfer results obtained experimentally using the transient liquid crystal thermography. The detailed 2D map of heat transfer coefficient has been analyzed in detail to point out important observations which will be useful for designers while choosing a particular crossflow scheme.

Detailed Heat transfer coefficient contours

Figure 4.8 shows detailed heat transfer coefficient contours for all the configurations studied and for the full range of jet Reynolds number. Figure 4.8(a) shows the heat transfer results for Re 3500. The target surface, as mentioned in the earlier sections, was of two types (a) smooth target (without effusion holes), and (b) smooth target (with effusion holes). The contours for smooth target (without effusion holes) has been arranged in the top half and the contours for the smooth target (with effusion holes) has been arranged in the bottom half.

For the maximum crossflow condition in smooth target (without effusion holes), it can be seen that the jet footprint is distinctly round shaped in the first row (the innermost row). This is due to the fact that first row is not affected by crossflow. As the crossflow accumulates, the footprints of jets change there shape from round to slightly distorted in the direction of crossflow. The crossflow interacts with the incoming jet and reduces the jet effectiveness. One way to identify the effects of crossflow is to analyze the footprints of the circular jets. Compared to smooth target (without effusion holes), the corresponding case of smooth target (with effusion holes) undergoes reduced effects of crossflow buildup and its release. This is because of the coolant extraction between impingement locations. Due to sharp local pressure gradient, the spent air gets transported towards the effusion holes. This mechanism also helps in increase in heat transfer around the effusion holes, as the spent air undergoes slight acceleration as it leaves the impingement channel via the effusion holes. This effect has been seen for the full range of jet Reynolds number investigated. This effect of coolant extraction on local heat transfer becomes dominant with increasing jet Reynolds number, because of increased crossflow mass flux escaping the impingement channel through the effusion holes.

For the intermediate crossflow, the spent air was allowed to escape the impingement channel from two sides for the case of smooth target (without effusion holes). For the smooth target (with effusion holes), the spent air was allowed to escape through two opposite sides and via effusion holes. Considering the intermediate crossflow case for impingement onto smooth target (without effusion holes), it can be seen that the heat transfer contour was divided uniformly in two identical parts which might be referred to as “mirror images” about the centerline of the region of interest.

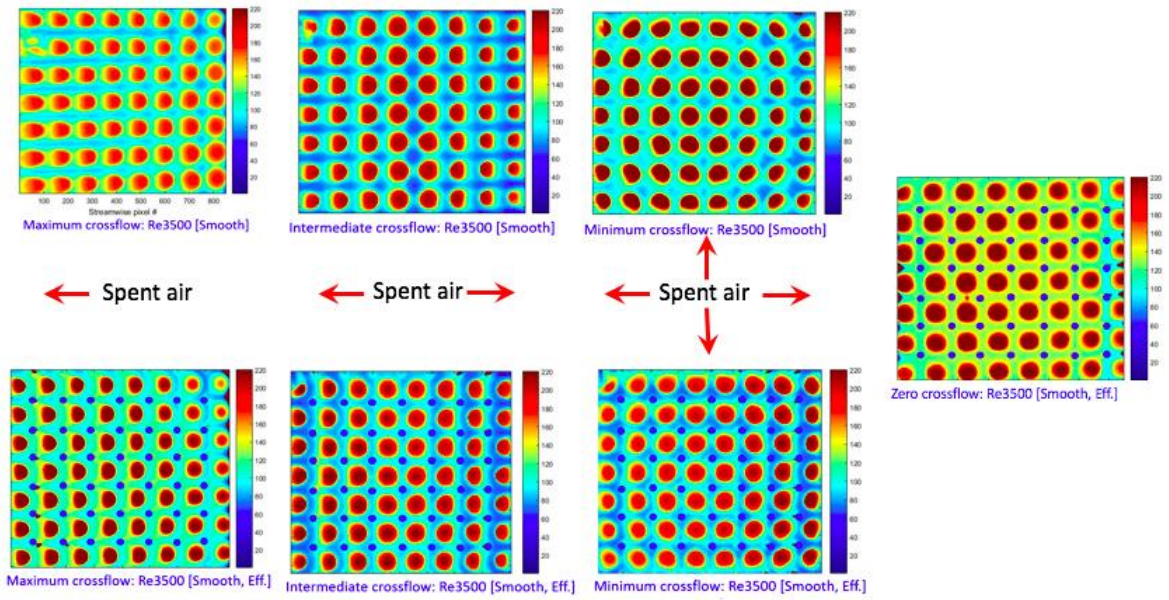

Fig. 4.8(a) Detailed heat transfer coefficient contours for all the configurations at $Re_j = 3500$

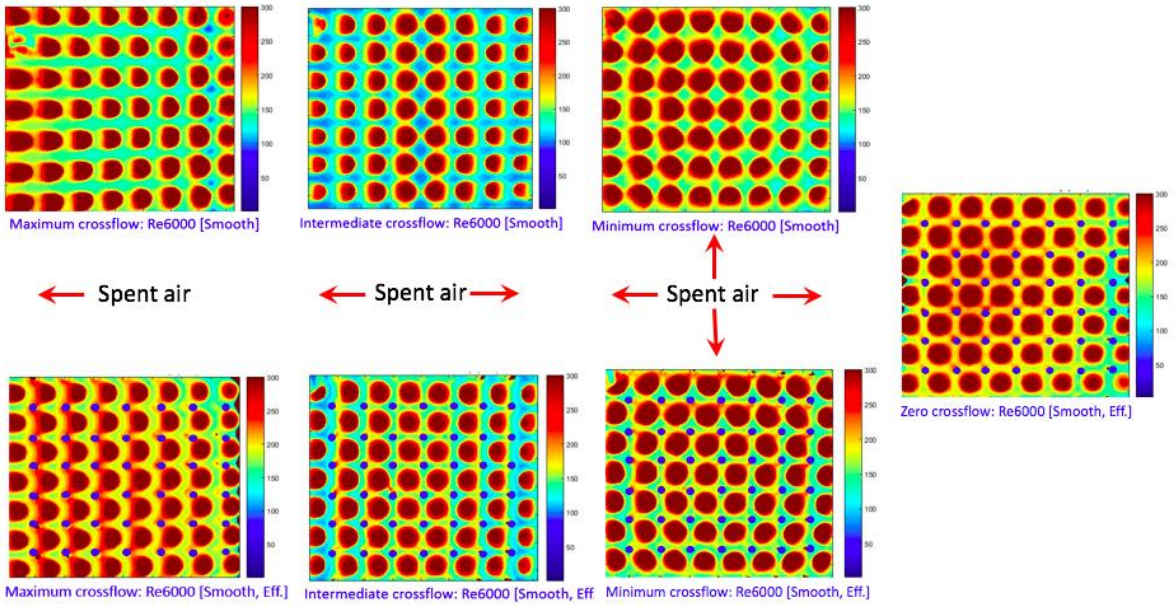

Fig. 4.8(b) Detailed heat transfer coefficient contours for all the configurations at $Re_j = 6000$

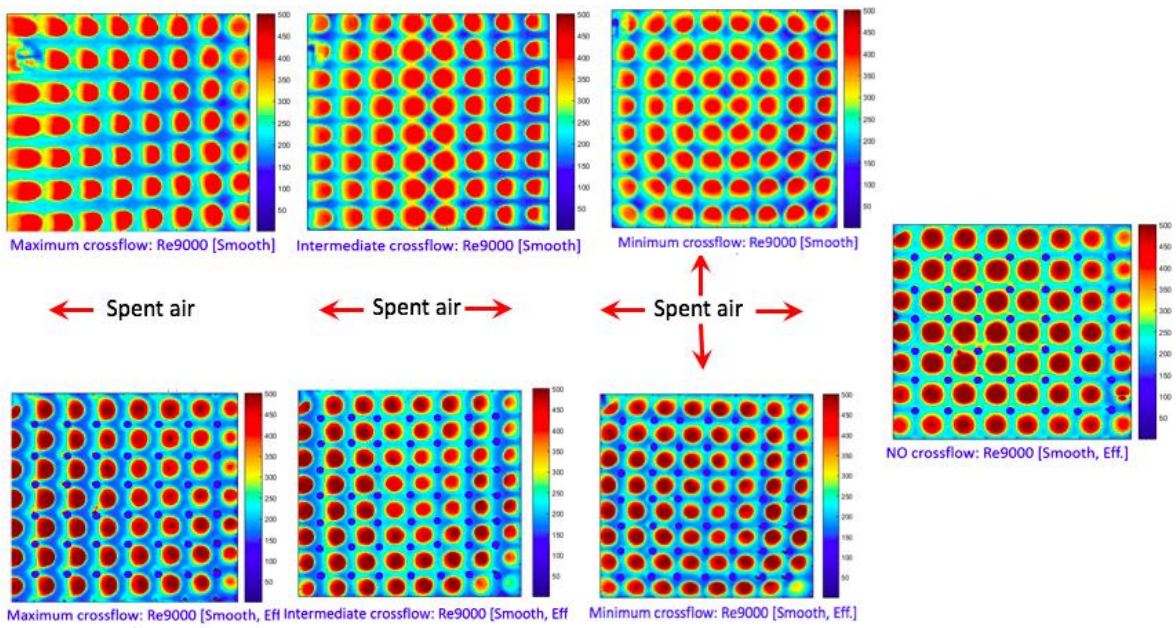

Fig. 4.8(c) Detailed heat transfer coefficient contours for all the configurations at Re_j = 9000

The footprints of jet impingement in the intermediate crossflow situation closely mimics the shape of the round jet for the first rows about the either side of the centerline of the region of interest. The crossflow accumulation in this crossflow scheme, starts from the first row closest to the centerline and has only half of the impingement channel to traverse. Hence, the crossflow accumulation at the last row on either ends of the impingement channel, will be about half of that of the maximum crossflow condition. This reason explains the reduced deterioration of jets which were closer to the exit of the impingement channel. However, for the low value of z/d, the acceleration of accumulated crossflow will also be lower when compared to maximum crossflow condition. Considering the case of impingement onto target surface (with effusion holes) in the intermediate crossflow exit scheme, similar trends related to jet footprints on the either side of the centerline, have been observed. The combined effect of spent air removal through intermediate crossflow scheme and via the effusion holes, resulted in increased heat transfer compared to the corresponding case where effusion holes were not present. The reason being the presence of effusion holes, helped escape the spent air and thus reducing the effect of spent air on the jet effectiveness reduction, particularly in the rows closer to the exit of the impingement channel. On the comparison of maximum and intermediate crossflow scheme, for impingement

onto smooth target (with effusion holes), it has been observed that as the crossflow strength gets reduced in the intermediate crossflow case, the local heat transfer around the effusion holes becomes higher than the corresponding locations for the maximum crossflow case.

For the case of minimum crossflow case for impingement onto smooth target surface (without effusion holes), the spent air was allowed to escape from all four sides of the impingement channel. It can be seen that high heat transfer values in the region of interest was arranged such that the corresponding isolines of high heat transfer values would lie in the form of concentric circles. The jets which are closest to exit escape immediately through the path having steepest gradient in the static pressure. This path would be the shortest path available to any jet. Compared to the corresponding case of intermediate crossflow for impingement onto smooth target (without effusion holes), it can be seen that the jet effectiveness was higher because of reduced effects of crossflow. Also, the distortion in the jet shape was found only for the jets which were closest to the exit, since they witnessed the accumulated crossflow from the radially inboard jets. Note that the nature of crossflow for the minimum crossflow case is different in comparison to both intermediate and maximum crossflow. For the later two crossflow schemes, the crossflow escapes the impingement channel via a linear path aligned in the direction of one or two exits, whereas in the case of minimum crossflow scheme, the spent air follows a radial path. This leads to an interesting case of crossflow accumulation and its ejection from the impingement channel. On comparison of impingement onto two different target surfaces for the minimum crossflow scheme, it can be observed that the basic footprint shape of the jets remain the same, where in the case of the no effusion case, the footprints were smaller and sharper, whereas in the case of effusion case, the footprints were larger and more diffused. The reason behind this heat transfer trend was the combined effect of crossflow evacuation through impingement channel and via the effusion holes. Also, for the minimum crossflow scheme and impingement onto smooth target (with effusion holes), due to the peculiar nature of crossflow escape compared to the maximum and the intermediate crossflow schemes, the feed of the spent air through the effusion holes was different in the minimum crossflow case.

For the zero impingement configuration, only target plate that could be tested, was the one with effusion holes. It can be clearly seen from the detailed heat transfer coefficient contours that the spent air when allowed to escape the impingement channel only through the effusion

holes resulted in more uniform round footprint with increased local heat transfer around the effusion holes. The high local heat transfer around the effusion holes is more dominant in the inner part of the region of interest compared to radially outboard region. Since, the spent air was vented out off the impingement channel via effusion holes, the round shape footprint of jets prevailed throughout the region of interest. More details about the relative heat transfer performance for different crossflow schemes have been presented in the following section.

Region-wise averaged Nusselt number distribution

The region size has been indicated in Fig. 4.2(a). The averaging has been done by considering all pixels on the target surface for the smooth target without effusion holes. For the smooth target with effusion holes, the averaged Nusselt number has been calculated by excluding the pixels acquired by the effusion holes.

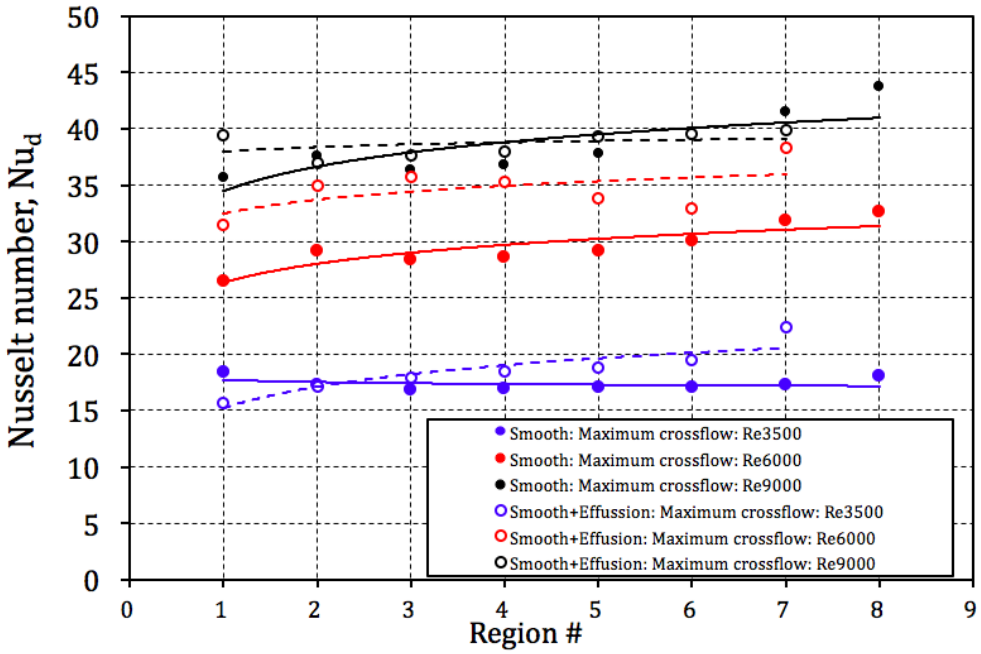

Fig. 4.9(a) Region-wise averaged Nusselt number for maximum crossflow condition, region 1 (blocked end), crossflow direction – region 1 through 8.

Figure 4.9(a) shows the region-wise averaged Nusselt number for the maximum crossflow condition.

An increasing trend for Nusselt number has been observed with increasing streamwise distance. This observation is consistent with [4.19] and is typical of low jet-to-target plate spacing (in present case, z/d=1). The accumulated spent experienced an acceleration while being purged out of the impingement channel. The spent air reduced the impingement effectiveness but when combined with channel flow heat transfer enhancement, resulted in overall incremental heat transfer in streamwise direction. The target plate with effusion holes had higher heat transfer compared to the target plate without effusion holes.

Figure 4.9(b) shows the region-wise averaged Nusselt number for the intermediate crossflow condition. In this case, a more uniform heat transfer behavior is observed for jet Reynolds numbers of 3500 and 6000 when compared to maximum crossflow condition. In the intermediate crossflow condition, the target plate with effusion holes showed higher heat transfer when compared to the target plate without effusion holes.

Figure 4.9(c) shows the region-wise averaged Nusselt number for the minimum crossflow condition. In this crossflow condition, a mixed trend of heat transfer was observed for the two types of target surfaces. For the lowest jet Reynolds number of 3500, the target surface without effusion holes showed higher heat transfer. With increasing jet Reynolds number, it has been observed that the target plate with effusion holes has higher heat transfer. This effect might be the outcome of combined effect of spent air acceleration through effusion holes and jet impingement effectiveness. For the lowest jet Reynolds number, the strength of accumulated crossflow was not significant, as a result of which, the target surface without effusion holes showed higher heat transfer due to high impingement effectiveness. The presence of effusion holes reduced the impingement effectiveness to some extent, but also helped in crossflow regulation. The combined effects of all the different phenomena discussed in this section, resulted in interesting deductions from the regionally averaged Nusselt numbers.

Figure 4.9(d) shows the region-wise averaged Nusselt number for the zero crossflow condition. The spent air accumulated in the impingement channel was purged out via the effusion holes. A result of which, higher heat transfer has been observed in the middle of the region of interest. Also, the heat transfer distribution is very uniform because of reduced interference of the spent air. The next section describes the globally averaged Nusselt number

where all the configurations will be compared with each other, in terms of heat transfer and pumping power requirements.

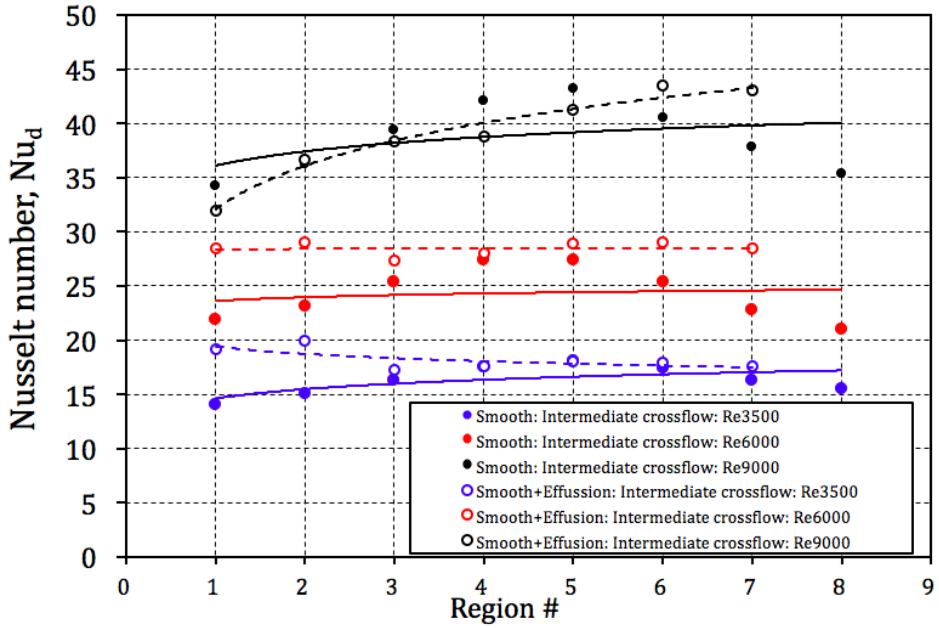

Fig. 4.9(b) Region-wise averaged Nusselt number for intermediate crossflow condition, region 1 (open end) and region 8 (open end).

Globally averaged Nusselt number and corresponding pumping power

Figure 4.10 shows the globally averaged Nusselt number for the full range of jet Reynolds number investigated in the present study. The net heat transfer results for all the configurations were very close to each other. However, the case of zero crossflow with effusion target plate resulted in highest heat transfer. For all crossflow schemes, the target plate with effusion holes had higher heat transfer compared to the target plate without effusion holes for any given crossflow scheme. This implies that effusion holes play a beneficial role in terms of spent air regulation, without significantly affecting the basic characteristics of jet impingement heat transfer. The moderate crossflow scheme showed lower heat transfer compared to other crossflow schemes, for both types of target surfaces. One reason behind this trend was the peculiar behavior of spent air for the maximum crossflow condition, where it has been observed that the accumulated spent air underwent accelerated removal from the impingement channel, hence increasing channel heat transfer. Note that this effect is only observed at low jet-to-target

plate spacing of 1. The present study is focused on only one z/d and hence, the trends observed in heat transfer characteristics are not to be extrapolated to higher values of z/d in other similar studies. The low jet-to-target plate spacing applications are found in double wall cooling structures in high pressure stage turbine airfoils, where thin slots are available for impingement and evacuation of spent air through film cooling holes.

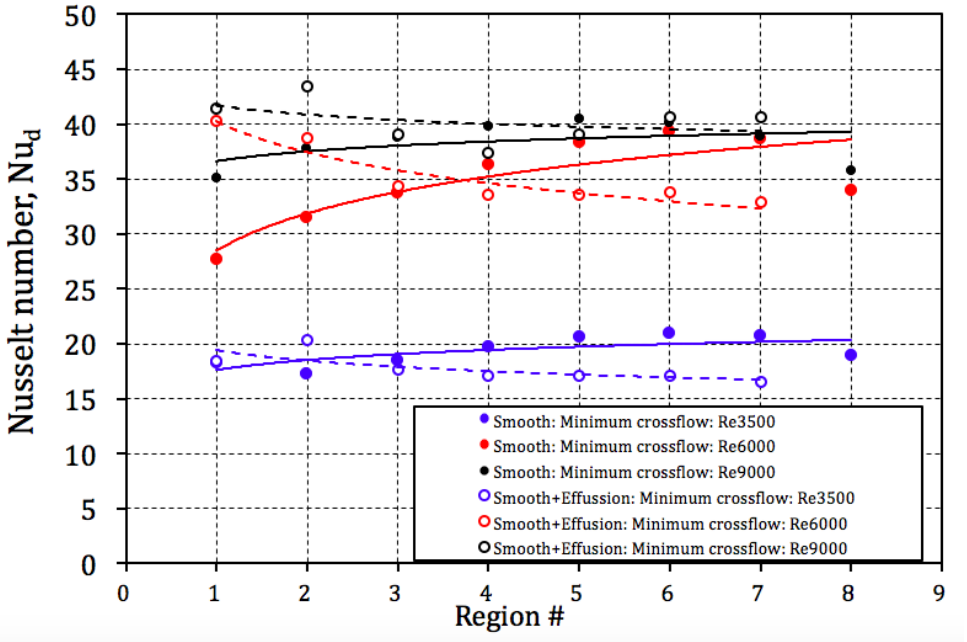

Fig. 4.9(c) Region-wise averaged Nusselt number for intermediate crossflow condition

The interesting results obtained for the maximum crossflow condition, provides a venue for further exploration of heat transfer characteristics to study the effects of other variables, such as x/d, y/d etc. The maximum crossflow configuration is most commonly found in the existing designs of double wall cooling concepts. The present study, hence provides important guidelines for gas turbine designers who aim to optimize cooling in thin internal cooling slots.

While it is important to look at the globally averaged heat transfer results in order to identify the configuration which has higher heat transfer characteristics, it is also imperative to investigate the cost at which the increment in heat transfer is obtained. The additional cost comes

in terms of increased pumping power requirements, which in turn implies, increased supply pressure requirements – which has a direct effect on the overall efficiency of gas turbine engines.

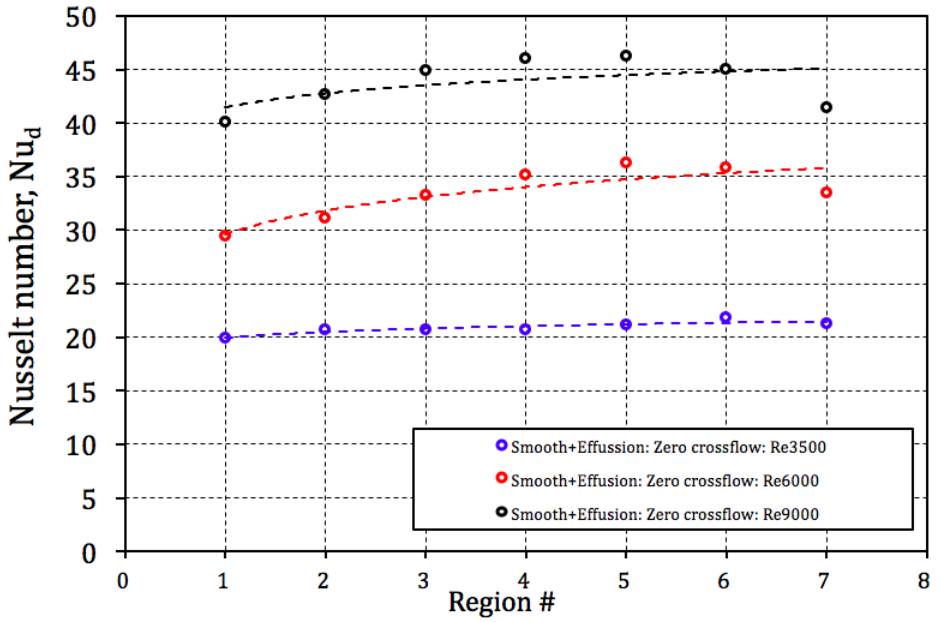

Fig. 4.9(d) Region-wise averaged Nusselt number for zero crossflow condition

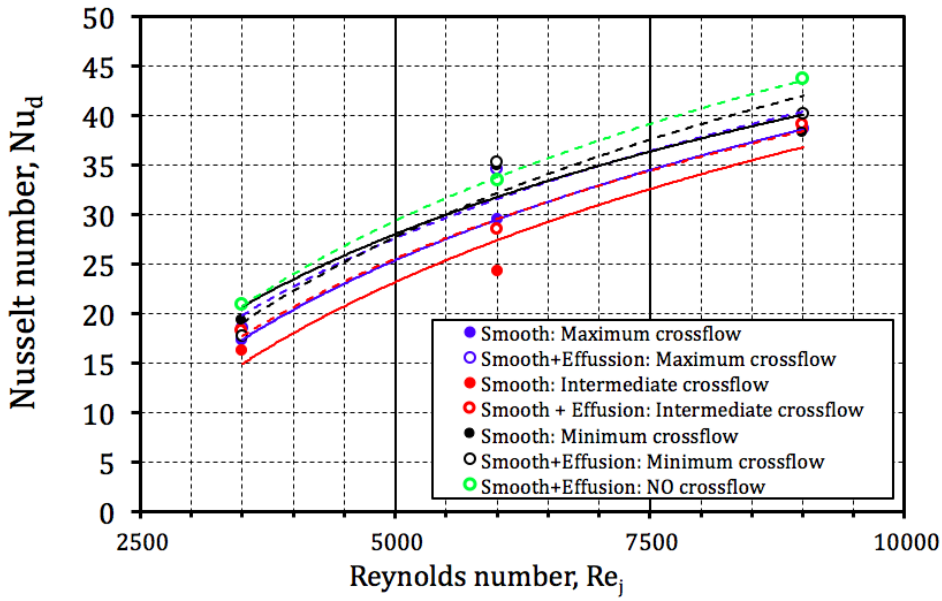

Fig. 4.10 Globally averaged Nusselt number variation with jet Reynolds number

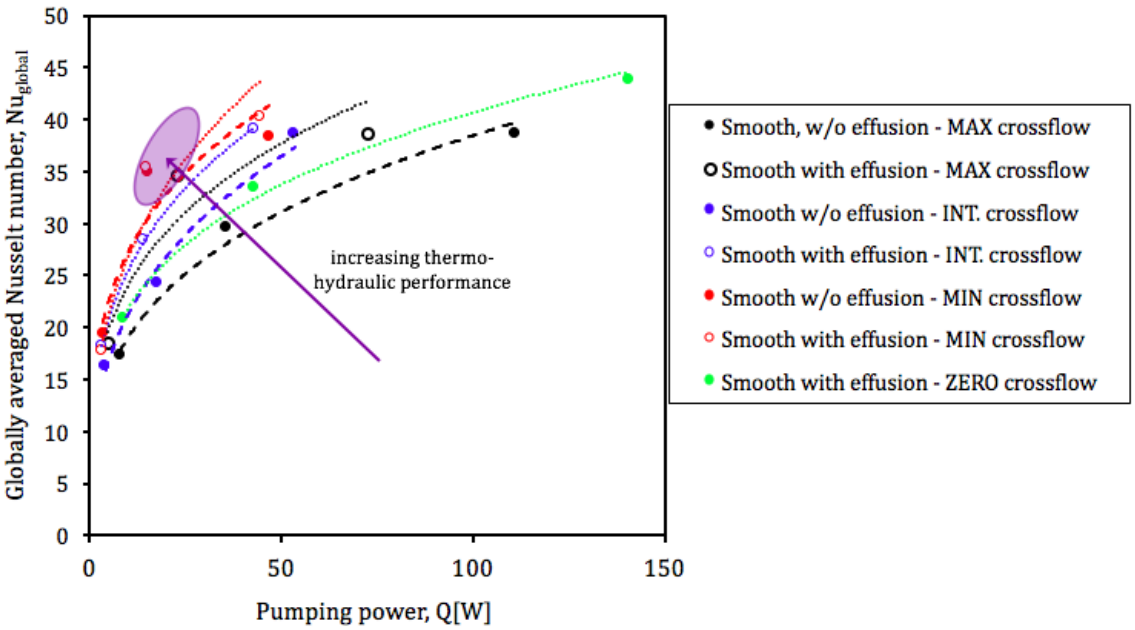

Fig. 4.11 Globally averaged Nusselt number with pumping power requirements for full range of Reynolds number investigated in the present study (Note: Q is the total pumping power required for N jets)

Figure 4.11 shows the globally averaged Nusselt number versus the pumping power required. The pumping power has been calculated using the curve fit equations (power fit) obtained from Fig. 4.6. The values of pumping power have been calculated at jet Reynolds numbers of 3500, 6000 and 9000. Interesting observations can be made from Fig. 4.11, on the heat transfer gain in reference to the pumping power.

The arrow shows the direction for increasing thermo-hydraulic performance. At this point of time, no attempt has been made to quantify the thermo-hydraulic performance, however Fig. 4.11 is an acceptable representation of qualitative trends of thermo-hydraulic performance. The minimum crossflow scheme had been the most efficient crossflow scheme, when both heat transfer and pumping requirements were taken into consideration. The maximum crossflow scheme for target surface without effusion holes had been the least efficient configuration in the present study.

Conclusions

Experimentally measured two-dimensional heat transfer coefficient map of internal-side of the target wall of the impingement-effusion system has been presented. The heat transfer coefficients were measured using transient liquid crystal thermography. A wide range of flow experiments were carried out to measure the discharge coefficients and pumping power requirements for each configuration over full range of plenum pressure ratios.

Following key observations have been noted in the present study:

(a) The low jet-to-target plate spacing (z/d=1) has shown interesting trends in heat transfer, as maximum crossflow scheme (without effusion holes) had higher heat transfer compared to the similar configuration at intermediate crossflow scheme.

(b) Effusion holes played vital role in crossflow regulation in all the crossflow schemes studied. It is recommended that more study needs to be carried out at higher z/d values to understand the effects of effusion holes on crossflow regulation.

(c) The target plate with effusion holes under zero crossflow scheme had the highest heat transfer while the intermediate crossflow with target plate without effusion holes was found to have lowest heat transfer amongst the configurations under consideration.

(d) The minimum crossflow scheme (target plate with and without effusion holes) has been the most efficient configuration in terms of thermo-hydraulic performance, while the maximum crossflow scheme with target plate without effusion holes was the least efficient configuration in the same terms as former.

(e) It is recommended that in jet impingement heat transfer studies, the globally averaged Nusselt numbers should also be evaluated in contrast with the pumping power requirements.

NOMENCLATURE

c specific heat capacity of target surface

c_p specific heat capacity at constant pressure

c_v specific heat capacity at constant volume

C_d discharge coefficient

d_j diameter

G	mass flux
h	heat transfer coefficient (W/m^2K)
H_{ref}	hue value to be tracked
k_f	thermal conductivity of air at film temperature
k_t	thermal conductivity of clear acrylic
M	jet exit Mach number
$\dot{m}$	mass flow rate
N	number of holes
Nu_{d_h}	Nusselt number (based on jet hydraulic diameter)
$p_{m,abs}$	absolute ambient pressure
$p_{r,m}$ *	absolute plenum pressure to absolute ambient pressure ratio
R_a	universal gas constant
Re_j	average jet Reynolds number (based on hydraulic diameter of jet)
t	time taken to reach T_{tlc}
t_{target}	thickness of the target plate made of clear acrylic
T	temperature
T_m	mainstream temperature
T_{tlc}	temperature of target wall corresponding to H_{ref}

Greek symbols

ρ	density of clear acrylic
γ	c_p/c_v

Subscripts

abs	absolute
i	initial
j	jet
m	mainstream
w	wall

REFERENCES

[4.1] Goldstein, R.J. and Behbahani, A.I., 1982, "Impingement of a circular jet with and without cross flow", International Journal of Heat and Mass Transfer, Vol. 25(9), pp.1377-1382.

[4.2] Viskanta, R., 1993, "Heat transfer to impinging isothermal gas and flame jets", Experimental Thermal and Fluid Science, Vol. 6(2), pp.111-134.

[4.3] Jambunathan, K., Lai, E., Moss, M.A. and Button, B.L., 1992, "A review of heat transfer data for single circular jet impingement", International Journal of Heat and Fluid Flow, Vol. 13(2), pp. 106-115.

[4.4] Andrews, G.E., Asere, A.A., Hussain, C.I., Mkpadi, M.C. and Nazari, A., 1988, June. Impingement/effusion cooling: overall wall heat transfer. In ASME 1988 International Gas Turbine and Aeroengine Congress and Exposition (pp. V004T09A036-V004T09A036). American Society of Mechanical Engineers.

[4.5] Andrews, G.E. and Nazari, A., 1999. Impingement/Effusion Cooling: Influence of the Number of Holes on the Cooling Effectiveness for an Impingement X/D of 10.5 and Effusion X/D of 7.0. In Proceedings of the International Gas Turbine Congress (pp. 639-646).

[4.6] Cho, H.H. and Rhee, D.H., 2000, May. Local heat/mass transfer measurement on the effusion plate in impingment/effusion cooling system. In ASME Turbo Expo 2000: Power for Land, Sea, and Air (pp. V003T01A058-V003T01A058). American Society of Mechanical Engineers.

[4.7] Rhee, D.H., Choi, J.H. and Cho, H.H., 2003. Flow and heat (mass) transfer characteristics in an impingement/effusion cooling system with crossflow. Journal of turbomachinery, 125(1), pp.74-82.

[4.8] Ekkad, S.V., Huang, Y. and Han, J.C., 1999. Impingement heat transfer on a target plate with film cooling holes. Journal of Thermophysics and Heat transfer, 13(4), pp.522-528.

[4.9] Huang, Y., Ekkad, S.V. and Han, J.C., 1998. Detailed heat transfer distributions under an array of orthogonal impinging jets. Journal of Thermophysics and Heat Transfer, 12(1), pp.73-79.

[4.10] Rhee, D.H., Yoon, P.H. and Cho, H.H., 2003. Local heat/mass transfer and flow characteristics of array impinging jets with effusion holes ejecting spent air. International Journal of Heat and Mass Transfer, 46(6), pp.1049-1061.

[4.11] Cho, H.H., Rhee, D.H. and Goldstein, R.J., 2008. Effects of hole arrangements on local heat/mass transfer for impingement/effusion cooling with small hole spacing. Journal of Turbomachinery, 130(4), p.041003.

[4.12] Hong, S.K., Rhee, D.H. and Cho, H.H., 2007. Effects of Fin Shapes and Arrangements on Heat Transfer for Impingement/ Effusion Cooling with Crossflow. Journal of heat transfer, 129(12), pp.1697-1707.

[4.13] Hong, S.K., Lee, D.H. and Cho, H.H., 2009. Heat/mass transfer in rotating impingement/effusion cooling with rib turbulators. International Journal of Heat and Mass Transfer, 52(13), pp.3109-3117.

[4.14] Hoberg, T.B., Onstad, A.J. and Eaton, J.K., 2010. Heat transfer measurements for jet impingement arrays with local extraction. International Journal of Heat and Fluid Flow, 31(3), pp.460-467.

[4.15] Singh, P., Ravi, B.V. and Ekkad, S., 2016, June. Experimental Investigation of Heat Transfer Augmentation by Different Jet Impingement Hole Shapes Under Maximum Crossflow. In ASME Turbo Expo 2016: Turbomachinery Technical Conference and Exposition (pp. V05BT16A018-V05BT16A018). American Society of Mechanical Engineers.

[4.16] Moffat, R.J., 1988. Describing the uncertainties in experimental results. Experimental thermal and fluid science, 1(1), pp.3-17.

[4.17] Yan, Y. and Owen, J.M., 2002. Uncertainties in transient heat transfer measurements with liquid crystal. International Journal of Heat and Fluid Flow, 23(1), pp.29-35.

[4.18] Florschuetz, L.W., Truman, C.R. and Metzger, D.E., 1981, March. Streamwise flow and heat transfer distributions for jet array impingement with crossflow. In ASME 1981 International Gas Turbine Conference and Products Show (pp. V003T09A005-V003T09A005). American Society of Mechanical Engineers.

[4.19] Li, W., Li, X., Ren, J., Jiang, H., Yang, L. and Ligrani, P., 2016, June. Effect of Reynolds Number, Hole Patterns and Hole Inclination on Cooling Performance of an Impinging Jet Array: Part I—Convective Heat Transfer Results and Optimization. In ASME Turbo Expo 2016: Turbomachinery Technical Conference and Exposition (pp. V05BT16A003-V05BT16A003). American Society of Mechanical Engineers.

CHAPTER 5

Experimental Investigation of Heat Transfer Augmentation by Different Jet Impingement Hole Shapes under Maximum Crossflow

Prashant Singh, Bharath Viswanath Ravi, Srinath V. Ekkad
Advanced Propulsion and Power Laboratory,
Department of Mechanical Engineering,
Virginia Tech, Blacksburg, VA (US) 24061

Published in Conference proceedings of ASME – IGTI TurboExpo 2016, GT2016-57874
Re-printed with permission from ASME

ABSTRACT

The present study is focused on exploring new hole shapes for jet impingement, in an arrangement, typical of mid-chord region in a double wall cooling concept for high pressure turbine airfoils. Transient liquid crystal experiments were carried out to measure heat transfer augmentation by jet impingement on smooth target where the spent air was allowed to exit in one direction, thus imposing maximum crossflow condition. The averaged Reynolds number (based on jet hydraulic diameter) was varied from 2500 to 10000. The jet plate had a square array of jets with 7 jets in one row (total number of jets = 49), featuring hole shapes – Racetrack and V, where the baseline case was the round hole. The non-dimensional streamwise (x/dj) and spanwise (y/dj) spacing was 6, and the nozzle aspect ratio (L/dj) was 4. The criteria for the hole shape design was to keep the effective area of different hole shapes to be the same, which resulted in slightly different hydraulic diameters across different configurations. The jet-to-target plate spacing (z) was four times the jet hydraulic diameter. Detailed heat transfer contours have been presented for all the experimental cases. Globally averaged Nusselt numbers and normalized flow resistance values have been provided for the different hole shapes studied. V shaped holes have shown higher heat transfer compared to round and racetrack shaped holes. Also, shaped holes had higher flow resistance compared to round holes.

INTRODUCTION

Jet impingement has been widely used for applications demanding high heat removal rates from regions subjected to extreme thermal loads. Some of the typical usages of this method can be

found in the leading edge of modern gas turbine airfoils, in combustor liner cooling, cooling of electronic equipment, food processing industries etc. This method is often used as an array of impinging jets under different crossflow schemes, where round hole shapes have been widely used with different arrangements of jets and nozzle aspect ratios.

Prior studies on jet impingement have explored the effects of jet-to-target spacing, nozzle aspect ratio, spanwise and streamwise pitch of jets, crossflow schemes, target surface features, curvatures, etc. Sparrow and Wong [5.1] studied the mass transfer characteristics of single impinging jet on a smooth target surface and observed near constant mass transfer near impingement region for different jet discharge. The mass transfer decreased with the increase in jet-to-target plate spacing. Viskanta [5.2] distinguished between flow regions of a free jet and concluded that the boundary layer being very thin and highly turbulent near the stagnation region leads to significantly higher heat transfer augmentation. One way of characterizing heat transfer enhancement due to impinging jets is by the calculation of impingement effectiveness, based on adiabatic wall temperature, recovery temperature, jet temperature and the ambient temperature. Goldstein et al. [5.3] presented impingement effectiveness for a range of Reynolds number and different jet-to-target plate spacing and found that the effectiveness decreases with increase in jet-to-target plate spacing, supporting [5.1]. Detailed documentation of single jet impingement studies prior to 1992 can be found in Jambunathan et al. [5.4].

Impingement of multiple jets has been also studied extensively for different crossflow schemes. Crossflow leads to jet deflection and thus reduce the effective impingement effectiveness. Florschuetz et al. [5.5] investigated the effects of initial crossflow on heat transfer characteristics of array of impinging jets, with an intent to model the mid-chord region of turbine airfoils where some initial crossflow also exists. They found that the Nusselt numbers at the upstream rows were significantly reduced, even when the ratio of initial crossflow to total-jet-flow was small. Goldstein and Behbahani [5.6] studied heat transfer of an impinging jet for jet-to-target plate spacing of 6 and 12 jet diameters and found that the maximum Nusselt number decreases with increasing crossflow for 12 diameter spacing and inverse trend for the other configuration. Huang et al. [5.7] studied the effects of crossflow conditions on heat transfer enhancements, by carrying out experiments using transient liquid crystal technique for three configurations of exit schemes. They observed that the Nusselt numbers were lowest for the case in which entrance and

exit is in the same direction and highest for the case in which the crossflow was minimum. The current study is focused on exploring new hole shapes and calculating the resulting heat transfer enhancement under maximum crossflow condition. Some of the studies relevant to the present study, includes Gulati et al. [5.8], where the authors carried out detailed heat transfer measurements using infrared thermography technique and explored round, square and rectangular jet hole shapes for a range of jet-to-target plate spacing. They observed high Nusselt numbers for rectangular jets for z/d upto 6, however no significant effect was observed on the average stagnation Nusselt numbers for the different hole shapes. Harmon and Wright [5.9] recently studied racetrack and round shaped holes for the case of leading edge jet impingement under rotation.

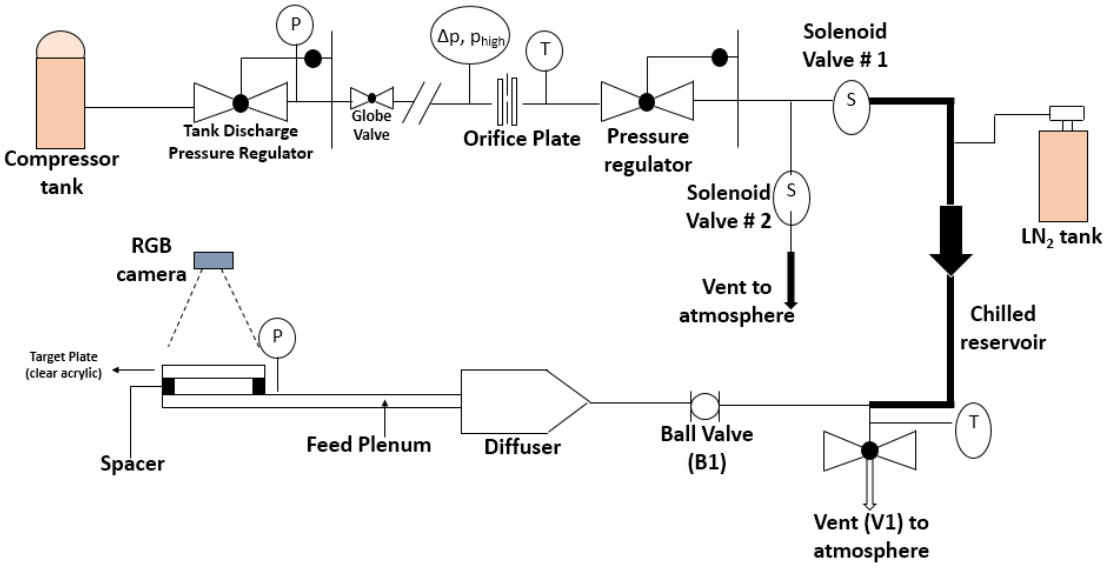

Figure 5.1 Description of experimental setup

For non-rotating case, the authors reported that racetrack shape holes result in slightly higher average heat transfer coefficient. Further details about jet impingement heat transfer are documented in [5.10]. The core belief of this study is to show that complex hole shapes can be designed and studied, which have the potential to perform better than the traditional round and race track holes. Very recently, Snyder et al. [5.11] reported the effects of build direction on heat transfer characteristics of additively manufactured channels. The authors concluded that with better machining tolerances, DMLS could be efficiently used in the future for the manufacturing of complex internal cooling concepts which have not been possible till now.

EXPERIMENTAL SETUP AND OPERATING PROCEDURE

The schematic of the experimental setup is shown in Fig. 5.1. The experimental setup is typical of transient heat transfer testing, where a step change in the temperature of working fluid is required to calculate the heat transfer coefficient. Working fluid in the experiments was air, which was discharged from the compressor at around 300 K and 7 atm and further regulated down to ~1-2 atm (by a pressure regulator downstream of the tank), depending on the mass flow rate requirements of a particular test. The fine tuning of the air flow rate was carried out by an inline globe valve. An orifice meter is located (~ 35 times the pipe diameter) downstream of the flow control valve, where the differential pressure (Dwyer 477-4-FM; 0 to 10 psi range) across the orifice was metered to calculate the mass flow rate. Also, the temperature (T-type thermocouple) of the air and the high pressure (Dwyer DPG – 103, range 0 to 30 psi) was metered at the orifice, to account for the variations in density of air during different runs. Downstream of the orifice plate, there was another pressure regulator to fine tune the airflow rate. A couple of solenoid valves were located downstream of the pressure regulator. These solenoid valves worked in pair and acted as a 3-way valve based on the command signal from LabVIEW. As mentioned earlier, a step change is required to accomplish a transient heat transfer experiment. In the present study, colder air has been chosen as working fluid because in the actual engine, the coolant is at a lower temperature than the wall. However, the specific study is independent of the fact whether the working fluid is at a temperature which is lower or higher than the target surface. Downstream of the Solenoid valve #1, a fitting was provided for liquid Nitrogen (LN2) intake. Air and Nitrogen mixture was used to chill the path between the solenoid valve (#1) and vent valve (V1). Once the thermal reservoir was suitably cooled, the nitrogen supply was cut off and all the remaining nitrogen in the reservoir line was purged into the atmosphere through the valve V1. The reservoir was chilled to a particular temperature depending upon the total mass flow rate to be passed during the testing e.g. for the testing of lower mass flow rates, the reservoir needed to be chilled to a much lower temperature in comparison to the higher mass flow rate testing. The reason behind this is that, higher heat transfer coefficients are associated with higher total mass flow rates. Thus in order to maintain uniform time duration of experiments across the complete range of mass flow rates tested, the minimum temperature of the chilled reservoir needed to be attenuated accordingly.

Further, the solenoid valve direction was switched towards the atmosphere and the combination of Ball valve (B1) and gate valve (V1) was used to open the line to test section. Now, the flow rate was set to the desired value and the test began once the solenoid valves were flipped towards the test section. Before the flow entered the test section, it passed through a diffuser and then into plenum feed chamber. The test section (with feed chamber) is shown is Fig. 5.2. The mass flow rate was continuously monitored during the experiments and it has been observed that the flow rate supply was uniform during the duration of test.

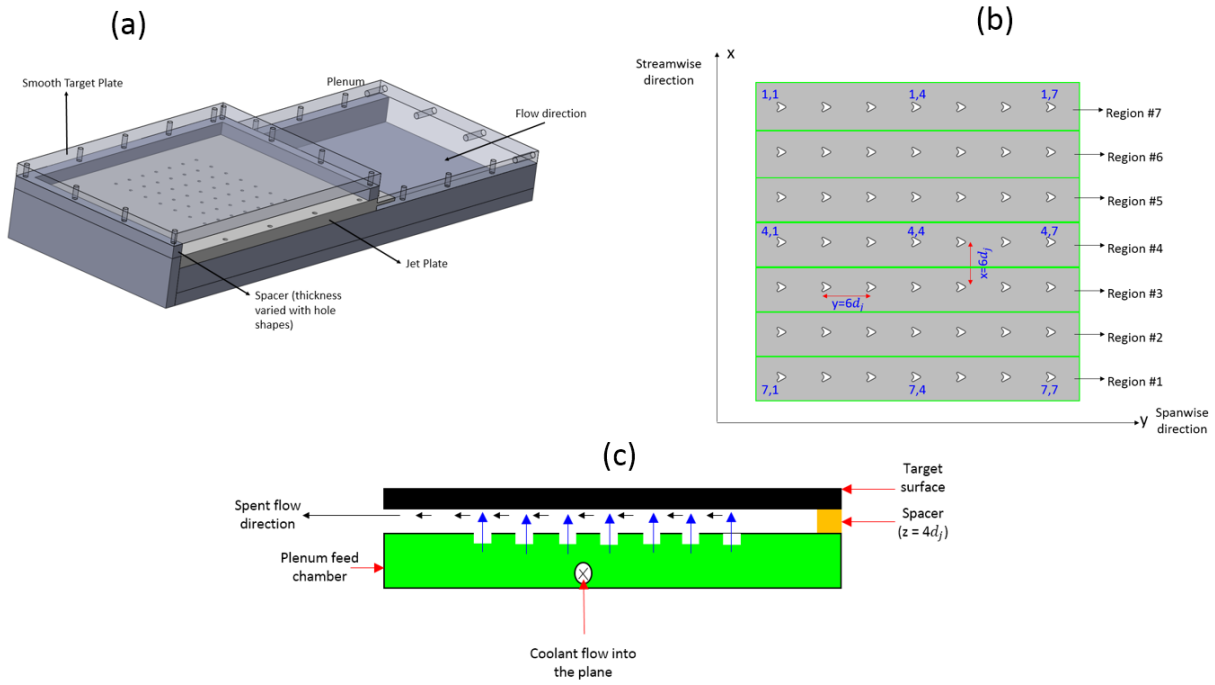

Figure 5.2 (a) Isometric view of impingement test section, (b) top view of the jet plate with jet nomenclature and region number, (c) side view of plenum feed chamber, spacer and spent flow direction

DESCRIPTION OF TEST SECTION AND EXPERIMENTAL CONDITIONS

The test section comprises of the plenum feed chamber, the jet plate, spacer and the target surface, for the study of jet impingement in maximum crossflow condition (Fig. 5.2). The plenum chamber used in this study is somewhat different from the ones used conventionally. This plenum is conceptualized for the study of impingement for double wall cooling channels in the mid-chord region of turbine airfoils. It will be later shown that a different type of crossflow has been observed during the heat transfer experiments, from the current arrangement of jet

impingement. The top view of the jet plate is shown in Fig. 5.2. The jet plate contained an array of 7 x 7 jets. Three different jet hole shapes have been studied – round, racetrack and V. The constraint in the design of these holes was to keep the physical area of all holes to be the same. This led to somewhat different hydraulic diameters for different jets. The geometrical parameter details are presented in Table 5.1. The isometric and top views of the holes are shown in Fig. 5.3. Heat transfer experiments were carried out at three different Reynolds number (based on jet Hydraulic diameter) – 2500, 5000 and 10000.

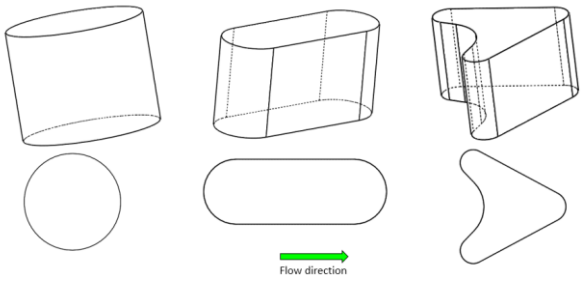

Figure 5.3 Jet hole shape designs and their orientation with respect to coolant flow in plenum

Table 5.1 Geometrical parameters

Hole shape	jet hydraulic diameter, d_h (m)	% diff in d_h from round	% diff in Physical Area from round	Spacer Thickness (z, in m)	Normalized parameters (x/d, y/d, z/d)
ROUND	0.003175	0.00	0	0.0127	6, 6, 4
RACETRACK	0.002678	15.65	0.0065	0.0107	6, 6, 4
V	0.002456	22.65	0.0054	0.0098	6, 6, 4

DATA REDUCTION PROCEDURE

NUSSELT NUMBER CALCULATION PROCEDURE

The target surface was designed such that it could be modeled as semi-infinite solid with convection boundary condition on the surface facing the jets. The 1-D transient heat conduction partial differential equation, when solved with convective boundary condition on one side and constant temperature wall condition on the other side, results in following equation,

$$\frac{T_w - T_i}{T_m - T_i} = 1 - exp\left(\frac{h^2 t}{\rho c k}\right) erfc\left(h\sqrt{\frac{t}{\rho c k}}\right) \quad Eq.(5.1)$$

The maximum permissible time for the transient liquid crystal experiment without violating the 1-D semi-infinite conduction model assumption was found from Eq. (2). The typical run time of experiments was well under t_{max}.

$$t_{max} = 0.1\frac{\rho c {t_{target}}^2}{k} \quad Eq.(5.2)$$

Equation 5.1 is valid for constant mainstream temperature (Tm). But since, the mainstream temperature (after the step change) keeps dropping (Fig. 5.4) as the test proceeds; Duhamel's superposition principle has been incorporated in the solution of 1-D semi-infinite solid conduction equation (Eq. 5.1). The time varying mainstream temperature was divided into small time steps.

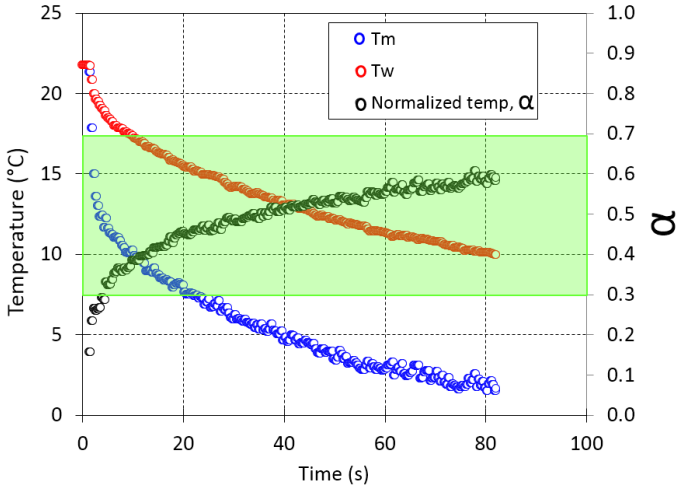

Figure 5.4 History of wall temperature and static temperature measured in plenum chamber, green region indicating $0.3 < \alpha < 0.7$

The mainstream temperature during such time step was taken to be constant. After applying Duhamel's superposition principle, the Eq. (1) can be written as,

$$T_w = T_i + \sum_{i=1}^{i=n_{max}} (T_{m,i} - T_{m,i-1}) \times \left[1 - \exp\left(\frac{h^2(t-t_i)}{\rho ck}\right) erfc\left(h\sqrt{\frac{(t-t_i)}{\rho ck}}\right)\right] \quad Eq.(5.3)$$

where, T_m represents the static temperature of air measured in the plenum chamber and 'i' indicates the summation index which goes upto the maximum number of time steps.

The coolant speed in the plenum chamber was very small such that the temperature measured by the thermocouple can be called as the static temperature of the air. Usually, in jet impingement studies, the reference temperature of the coolant is taken to be the jet total temperature at the hole exit. In the present study, isentropic expansion of the jets has been assumed, hence the static temperature measured in the plenum chamber was representative of the jet total temperature under this assumption. The static temperature of the coolant was measured by a fast response T-type thermocouple (bead diameter: 0.0762 mm) and the data acquisition was carried out using LabVIEW interface which linked the computer to a National Instrument chassis (cDAQ9174) housing thermocouple module (NI9214). Two T-type thermocouples were taped onto the target surface for in-situ calibration. Figure 5.4 shows the static temperature measured in the plenum and the wall temperature history with time. Ti is the initial temperature of the target surface, which was calculated by averaging the sampled wall temperature till the commencement of the transient test. Now, in Eq. (5.3), the only unknowns are Tw, t and h. These unknowns were determined by following procedure.

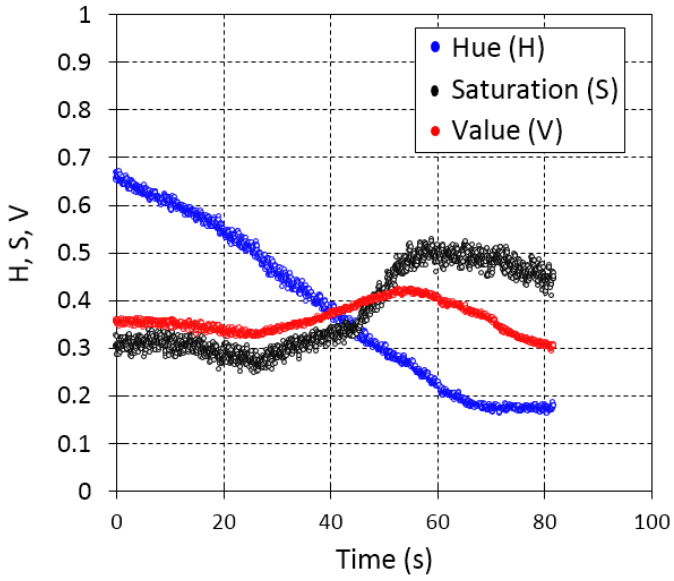

Figure 5.5 Time evolution of H, S, and V in the calibration region

Tw is the wall temperature corresponding to a particular Hue value (H_{ref}). In order to calculate H_{ref}, the hue history with time was calculated for a known 'calibration region', which was in the close vicinity of the wall thermocouple. A region of 25 pixels (5 x 5 pixels) was chosen as the 'calibration region'. It was ensured that the thermocouple had good contact with the wall, hence

eradicating possibilities where wall thermocouple might have the effects of mainstream flow. For redundancy, two such wall thermocouples were secured on the target surface. It was found that very similar calibrations curves were obtained for both the calibration regions. The color change data obtained from the recorded video (at 29.97 fps) was then converted to Red (R), Green (G) and Blue (B) values (8-bit scale, 0 to 2^8-1) for each pixel through standard function in MATLAB. The corresponding Hue (H), Saturation (S) and Value (V) was then calculated from the RGB information of each pixel. Figure 5 shows the Hue (H), Saturation (S) and Value (V) on a scale of 0 to 1 and averaged over 25 pixels representing the 'calibration region'. Also shown is the Hue versus wall temperature calibration plot (Fig. 5.6), which provides the linear relationship between Hue and wall temperature.

Once the linear relationship between the Hue and wall temperature was determined, a particular Hue (H_{ref}) was selected and the temperature (Tw) corresponding to that $H_{ref}$was calculated from the established linear relationship.

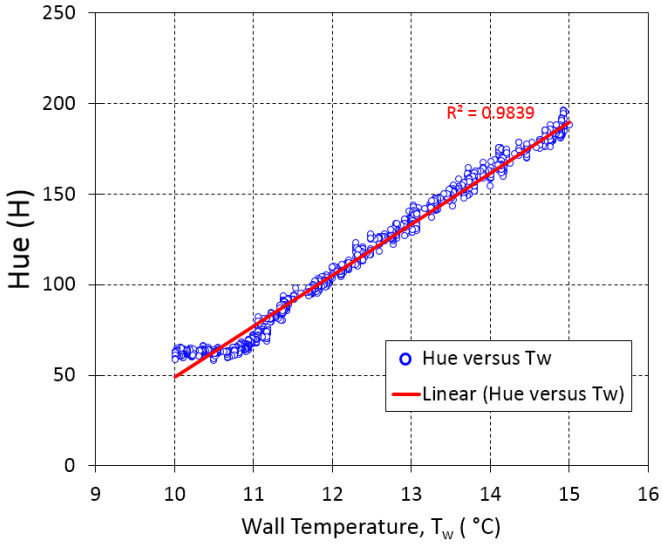

Figure 5.6 Typical Hue versus wall temperature relationship

Further, the time (t) matrix was built for each pixel. Each pixel was traversed one by one, and the Hue information was extracted according to the process mentioned earlier. For a particular pixel, each frame was then traversed to find the frame number which corresponded to H_{ref}. For data

quality check, a minimum normalized threshold of 0.25 was applied to the Saturation (S) and Value (V). It can be seen from Fig. 5 that both the S and V values are above 0.27. Once all of these criteria were met, the real time ((frame#) x fps^{-1}) corresponding to the particular frame number was calculated and stored at the specific pixel location in the time matrix.

At this stage, the only unknown left in Eq. 5.3 is the heat transfer coefficient (h). Heat transfer coefficient was then determined by a root finding algorithm (secant method). The tolerance specified for the convergence of root determination was 0.01 °C difference between T_w (calculated from H_{ref}) and T_w calculated from the substitution of calculated value of 'h' (through root finding algorithm) in Eq. 5.3. The Nusselt number (based on Jet diameter) was calculated using Eq. 5.4.

$$Nu_d = \frac{hd_j}{k_f} \quad Eq.(5.4)$$

where k_f is the thermal conductivity of air at the film temperature.

DISCHARGE COEFFICIENT (C_D) AND JET EXIT MACH NUMBER (M) CALCULATIONS

For the calculation of discharge coefficients of each hole shape for a range of plenum pressure ratios, ten static pressures were measured in the plenum feed chamber. The jet plate was assembled on top of the plenum feed chamber and the jet plate was exposed to ambient. Nine out of these measurements were arranged such that three measurements could be taken in one span and the three rows of pressure taps were aligned with 1st, 4th and 7th row of jets in the spanwise direction (spanwise & streamwise directions are indicated in Fig. 2). The 10th static pressure tap was at the inlet of the plenum feed chamber (right after the diffuser). All the ten pressures were more or less similar, thus implying uniform potential for air supply through the complete array of jets.

In order to calculate the discharge coefficients, firstly, the ideal mass flux (Eq. 5.5) was calculated assuming isentropic expansion. Ideal mass flux is given as:

$$G_{ideal} = \left[\frac{p_{m,abs}}{R_a T_m}\right]\sqrt{\gamma R_a T_m}\sqrt{\frac{2}{\gamma-1}\left[{p_{r,m}}^{*((\gamma-1)/\gamma)} - 1\right]} \quad Eq.(5.5)$$

The actual mass flux was determined from the pressure measurements made at the orifice plate and is given as,

$$G_{actual} = \frac{\dot{m}_{actual}}{A_{jet}N} \quad Eq.(5.6)$$

The discharge coefficient is given as,

$$C_d = \frac{G_{actual}}{G_{ideal}} \quad Eq.(5.7)$$

Figure 5.7 shows discharge coefficients for different hole shapes over a range of plenum pressure ratios. It can be seen that, for a particular hole shape, the discharge coefficients were more or less constant for a wide range of plenum pressure ratios.

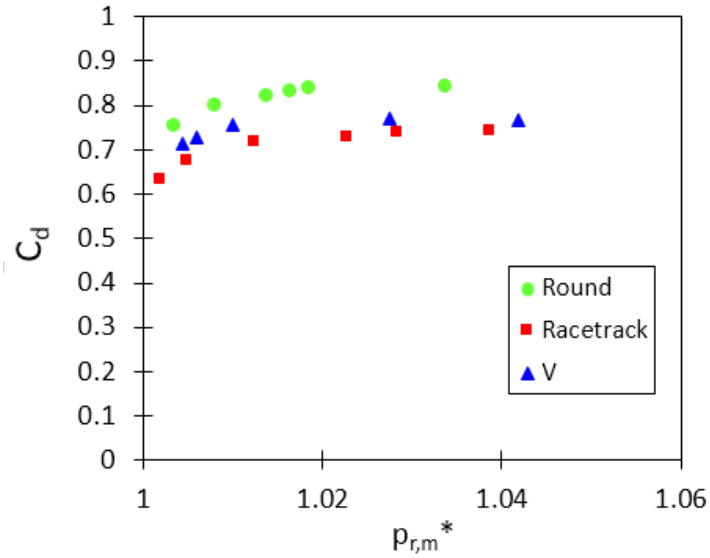

Figure 5.7 Variation of discharge coefficient of different hole shapes with plenum pressure ratio

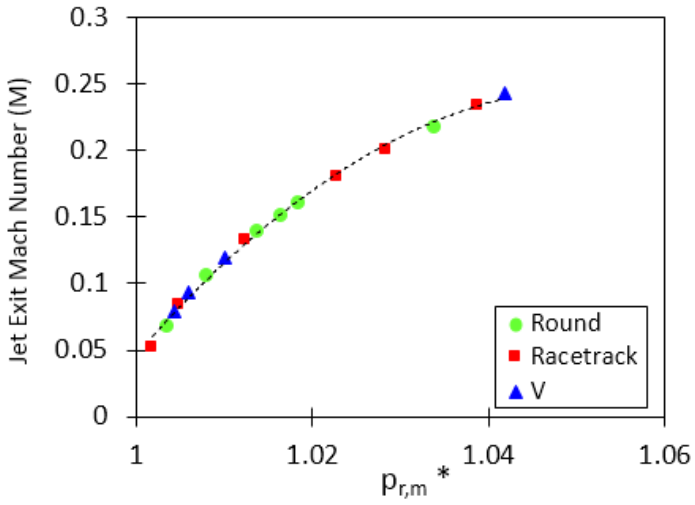

Figure 5.8 Jet exit Mach number variation for different jet hole shapes with plenum pressure ratio

So discharge coefficients can be considered as a fair parameter to characterize the flow properties of a particular hole shape. The C_d of racetrack and V shapes were similar and the C_d of round holes was greater by 10% when compared to round and racetrack shapes. Section 4 describes the uncertainties in the measurement of C_d. For a C_d of 0.82, the uncertainty was found to be 6%. Hence, it can be concluded that the C_d of round holes was greater than shaped holes.

Figure 5.8 shows the jet exit Mach number for different hole shapes for a range of plenum pressure ratios. Mach number for different jet hole shapes fall onto a single trajectory which has parabolic relation between Mach number and the plenum pressure ratio as expected.

UNCERTAINTY ANALYSIS

The uncertainty analysis in the measurement of Nusselt number, discharge coefficient, flow Reynolds number has been determined using sequential perturbation method described by Moffat [5.12]. In the calculation of Nusselt number, the measurements which contribute to uncertainty were Tw, Ti, Tm, t, $(\rho ck)^{-0.5}$. The contributions of Tw, Ti, Tm towards uncertainty was taken to be 0.5˚C. The contribution of time (t) was taken to be 0.033 seconds. The uncertainty for a typical Nusselt number of 10.36 was found to be 13.53%. Yan and Owen [5.13] carried out detailed study of uncertainties in transient liquid crystal experiments. They recommended that the experimenters should limit their normalized temperature (α) between 0.3 and 0.7 to achieve lower levels of uncertainty. From Fig. 5.4 it can be seen that α crosses the 0.3

value right at the initiation of the experiment. It was also seen that the usual time (t) taken for the wall to reach the calibration temperature (α) was typically around 10 to 60 seconds. This wide variation in the time t is due to the presence of stagnation region (leading to lower values of t) and crossflow dominated regions or regions of spent air interactions right after impingement (leading to higher values of t). However, a sensitivity analysis was carried out for the variables which affect the heat transfer coefficient, and it was found that the time (t) had the least effect on the uncertainty in the value of heat transfer coefficient.

The discharge coefficient calculation involved four pressure measurements – $p_{m,abs}$, $p_{in}{}^{*}$, differential pressure measured at the orifice plate and the static pressure measured at the inlet of orifice plate and one temperature measurement (Tm). The uncertainty in the measurement of C_D value of 0.84 was 6% and the corresponding uncertainty in the measurement of jet Reynolds number was 2.85%.

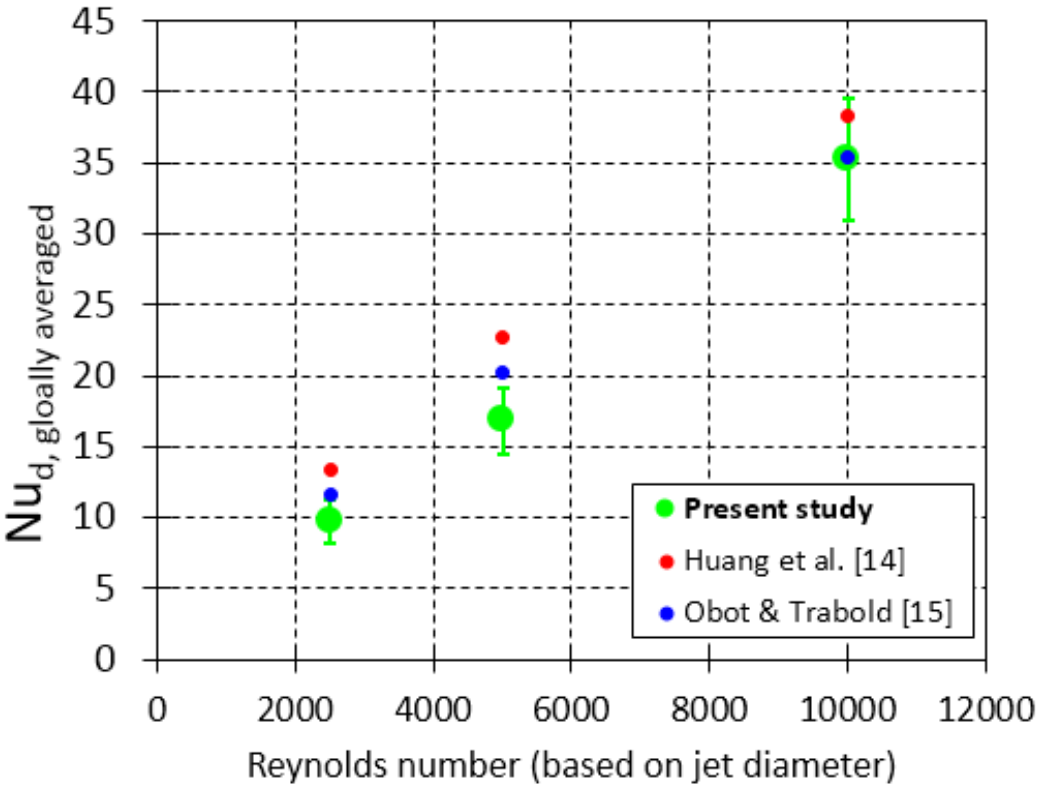

Figure 5.9 Validation of present experiment with established literature

RESULTS AND DISCUSSION

DETAILED HEAT TRANSFER COEFFICIENT CONTOURS

Figure 5.9 shows the comparison of the globally averaged Nusselt number for round shaped holes, with the correlations present in established literature on jet impingement heat transfer. It can be seen that the predictions from the correlations were very close to the experimentally obtained Nusselt number. This adds more credibility to the data presented in the present study and also to the claims made regarding the other hole shapes. Figure 5.10 shows the detailed Nusselt number contours for different jet Reynolds number and hole configurations. The inlet flow (plenum feed chamber) and outlet flow (channel) direction are shown by green arrows. Also shown is the speculated direction of crossflow based on a common trend observed in Heat Transfer Coefficient (HTC) contours in all nine experimental conditions.

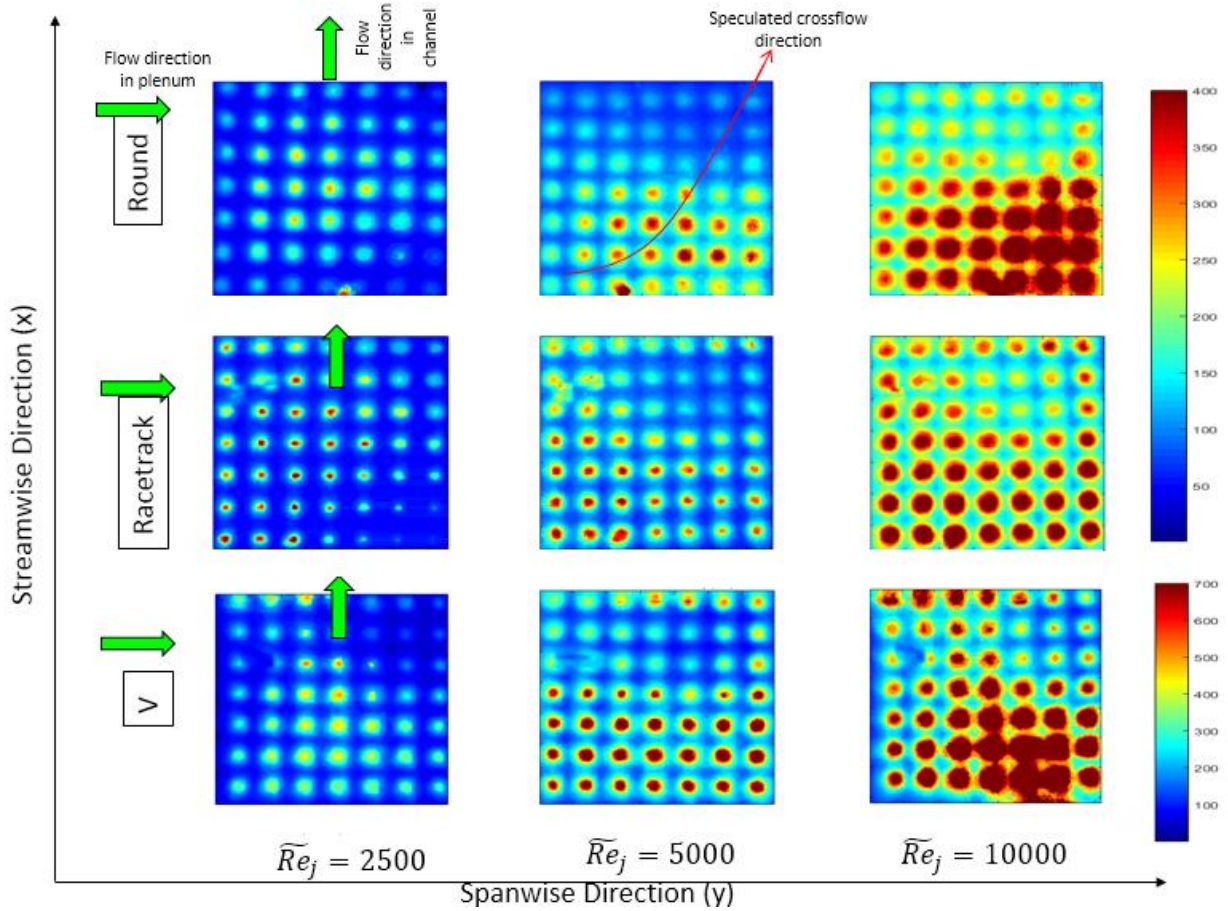

Figure 5.10 Detailed heat transfer coefficient (W/m2K) plots for three hole shapes studied

The jet number nomenclature is given in Fig. 5.2. The jet number (2,5), (2,6), (3,5) and (3,6), in particular, show clear effects of crossflow for all jet Reynolds number. The Row # 7 (closest to exit) experienced a steep fall in static pressure, which might lead to increased flow distribution through those jets, and thus seem to subjugate the effect of increasing crossflow strength as the spent air exits the impingement channel. It can be seen that the distribution of high heat transfer region shifts with varying jet Reynolds number. At the lowest $\widetilde{Re}_j$ (~2500), the central portion of the region of interest experienced relatively higher heat transfer as compared to the corners. This can possibly occur when the momentum flux of the coolant in the plenum chamber decayed at a faster rate than the net coolant extraction flux through the upstream rows of jets. However, as the average jet Reynolds number increased and so does the momentum in the feed chamber, the high heat transfer region prevailed throughout the span with an increasing trend towards the blocked end. Also, at lower Reynolds numbers, the effect of crossflow was not very dominant and with the doubling of Reynolds number, the crossflow affected region expanded and can be clearly seen in the top right corner of the contour plots.

Note that the heat transfer coefficient determined using the one-dimensional semi-infinite model (Eq. 5.3) assumes that the heat transfer coefficient is constant during the transient experiment. However, after analyzing the video of the liquid crystal color change, it was observed that the crossflow affected jets were showing some unsteady effects. So it should be noted that slight discrepancy can be expected in the calculation of heat transfer coefficient for the jets exhibiting unsteady effects. Similar observations were reported by Yang et al. [5.16] in a numerical study where jet impingement was simulated in a turbine leading edge setting. It was observed that the development of Kelvin-Helmholtz vortices cause temperature fluctuations, and the strength of these vortices depends on crossflow accumulation and non-uniformity, which might be the case in the present experimental study. However, in the present study, no comments have been made as to how will and how much will the unsteady effects change the heat transfer coefficient calculated from Eq. 5.3

SPANWISE AND STREAMWISE AVERAGED NUSSELT NUMBER

Figure 5.11 presents the spanwise averaged Nusselt number plotted in streamwise direction for round, racetrack and V hole shapes. At the lowest Reynolds number of 2500, the distribution of Nusselt number was more or less uniform in the streamwise direction for all three jet shapes. When the jet Reynolds number was doubled to 5000, the average Nusselt number was seen to increase by about 38%, 35% and 45%, for round, racetrack and V holes respectively. This increase in Nusselt number was despite the presence of strong crossflow effects near the exit area. It has been observed that the crossflow effect started to dominate at around 20 jet diameters downstream in the streamwise direction. The last row experienced a slight increase in heat transfer for both jet Reynolds numbers of 5000 and 10000. This might be because of the proximity of the last rows of jets from the exit (ambient), i.e. the steep pressure gradient between the channel pressure in the last row and the ambient might be the reason behind increased extraction of coolant air from the plenum feed chamber, and thus somewhat diminishing the crossflow effects. Figure 5.12 presents the streamwise averaged Nusselt number along the span. For the lowest Reynolds number, the central region experienced higher heat transfer than the other portions, and this trend was present for all jet shapes. As the Reynolds number was increased two and four folds, the distribution of high heat transfer shifted towards the blocked end.

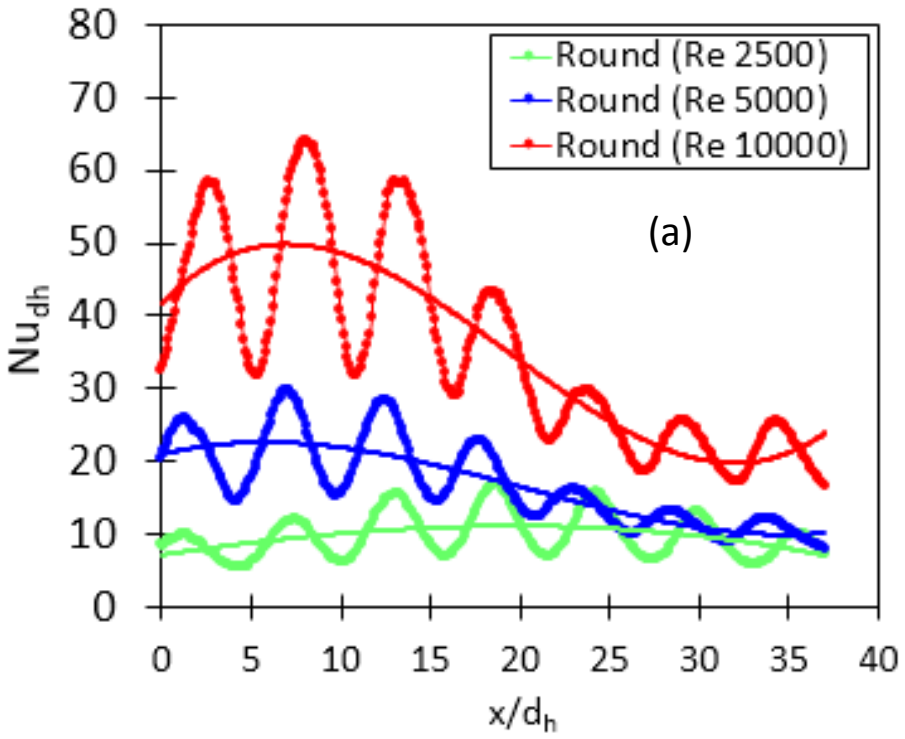

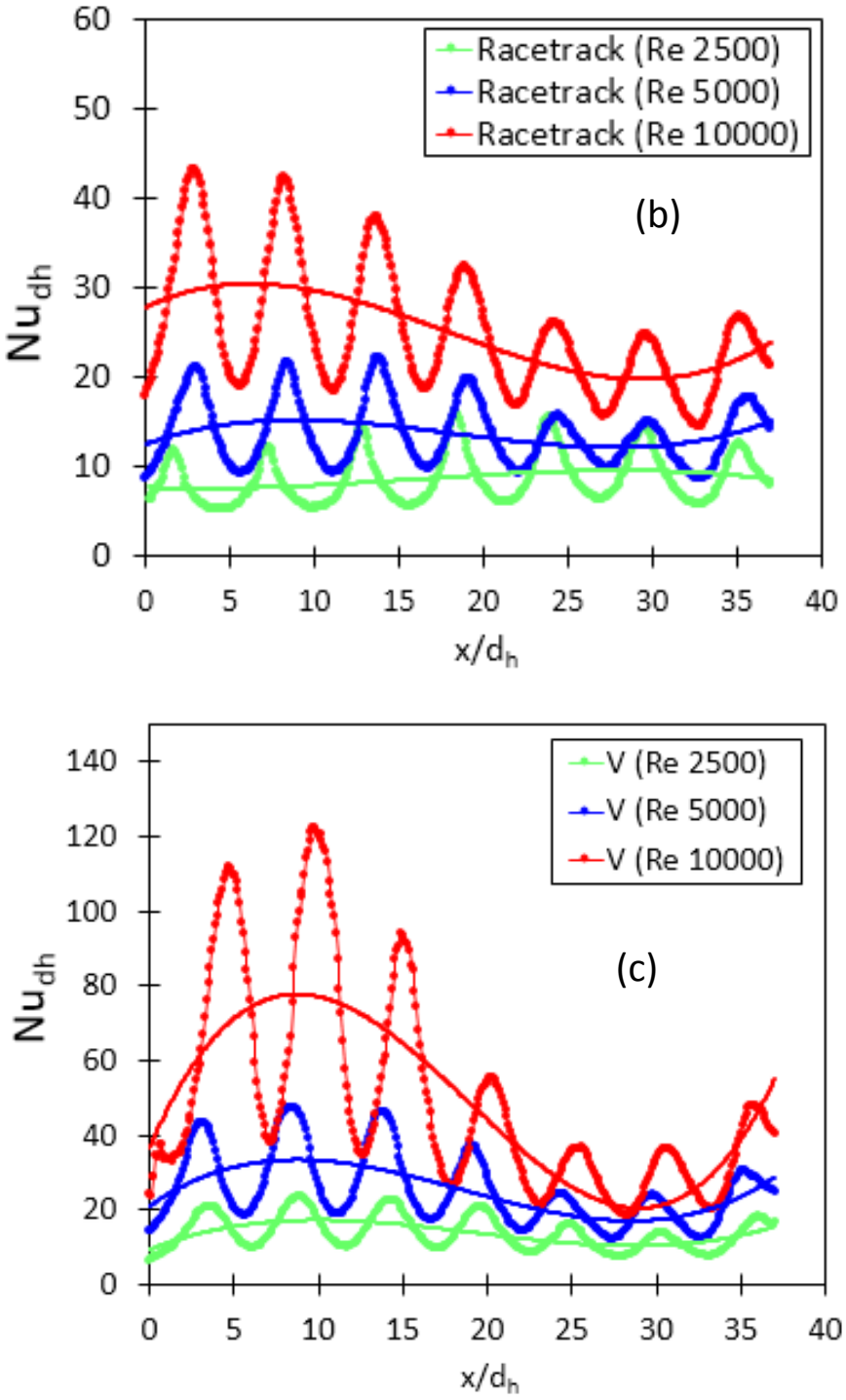

Figure 5.11 Spanwise averaged Nusselt number plotted in streamwise direction for (a) round, (b) racetrack, and (c) V jet hole shapes, respectively

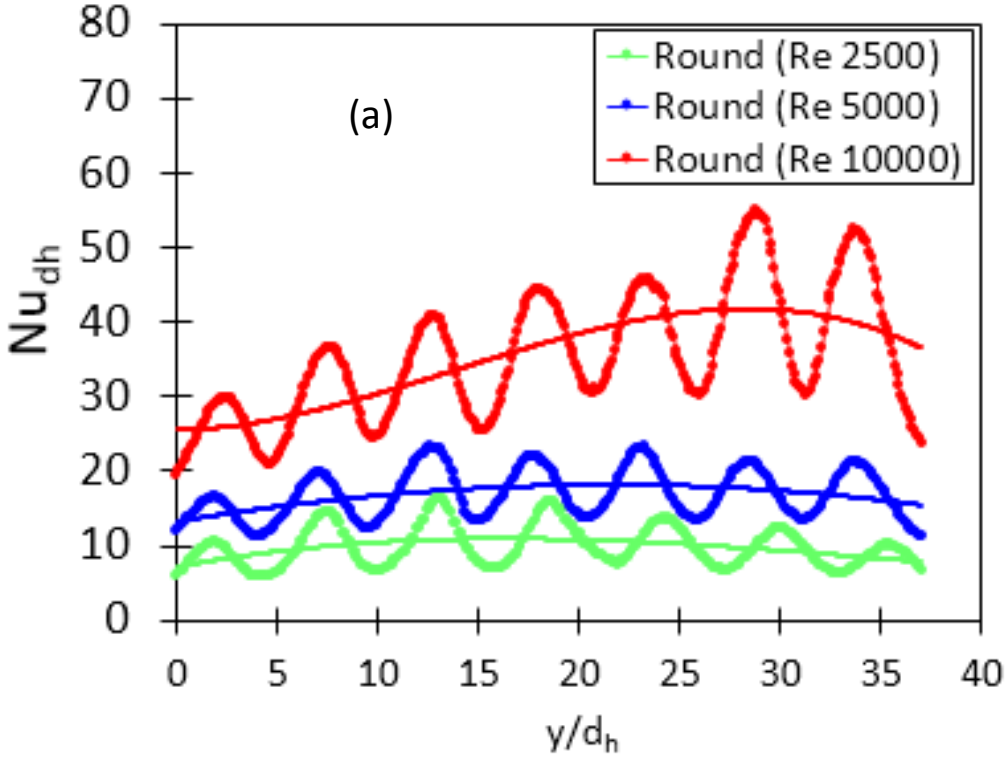
(a)
Round (Re 2500)
Round (Re 5000)
Round (Re 10000)
Nu_{dh}
y/d_h
0
10
20
30
40
50
60
70
80
0
5
10
15
20
25
30
35
40

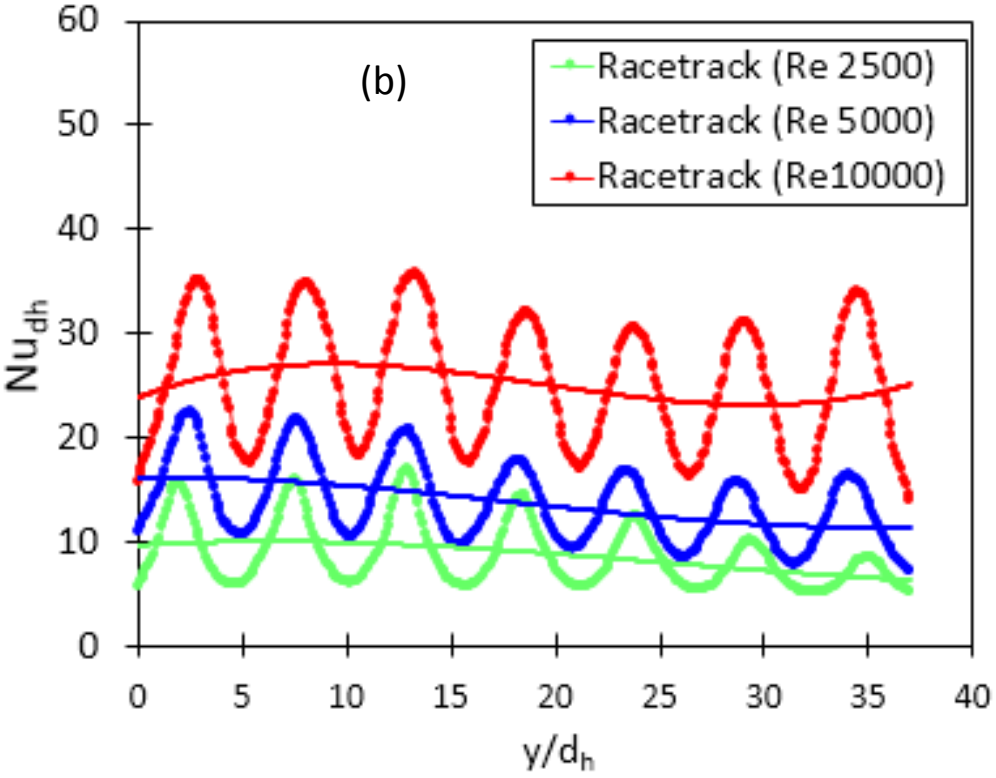
(b)
Racetrack (Re 2500)
Racetrack (Re 5000)
Racetrack (Re10000)
Nu_{dh}
y/d_h
0
10
20
30
40
50
60
0
5
10
15
20
25
30
35
40

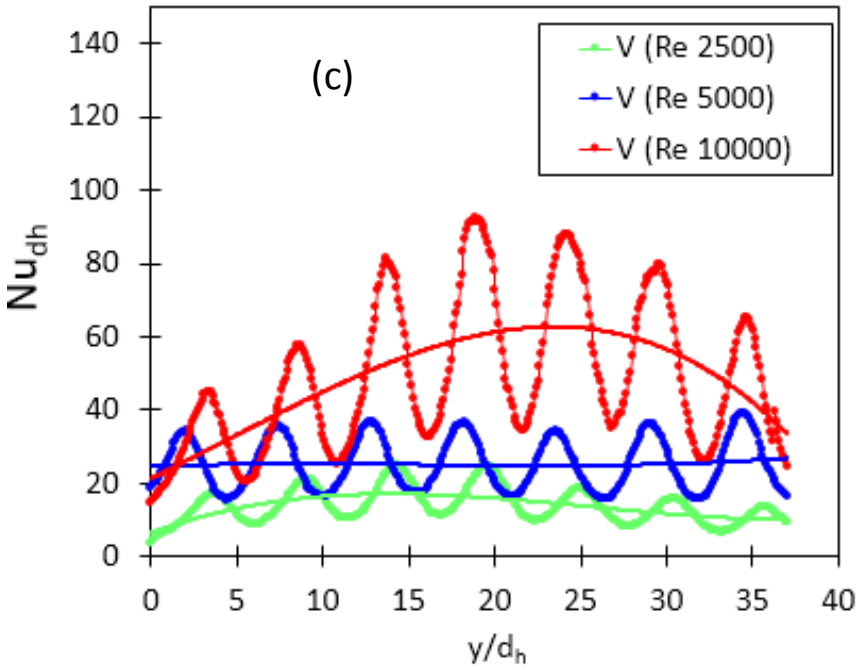

Figure 5.12 Streamwise averaged Nusselt number plotted in spanwise direction for (a) round, (b) racetrack, and (c) V jet hole shapes, respectively

STREAMWISE VARIATION OF AREA AVERAGED NUSSELT NUMBERS

Figure 5.13 presents the area averaged Nusselt numbers for three jet hole shapes and three Reynolds numbers. Each area is representative of one row of seven impinging jets where Region # 1 represents the row farthest from the exit and Region # 7 represents the row closest to the exit. Explanation of regions numbers can be found in Fig. 5.2(b). Region # 1 through 3 experienced high heat transfer compared to downstream regions. One reason for this trend might be the combined effect of crossflow and flow distribution (in Regions 4 through 7), leading to lower mass flux through the jets in these regions with added negative effects of spent air from Regions 1, 2 and 3. Figure 5.13 shows the region wise averaged Nusselt numbers for the nine experimental conditions. Crossflow effects were apparent for all hole shapes particularly at high Reynolds number. Region 2 experienced the highest heat transfer.

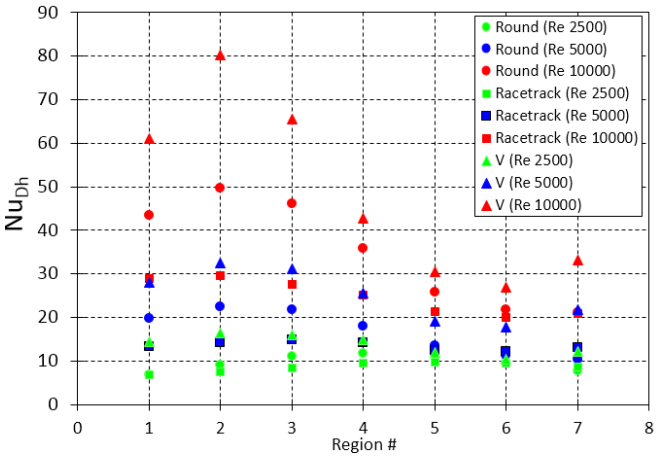

Figure 5.13 Streamwise variation of area averaged Nusselt number for different hole shapes

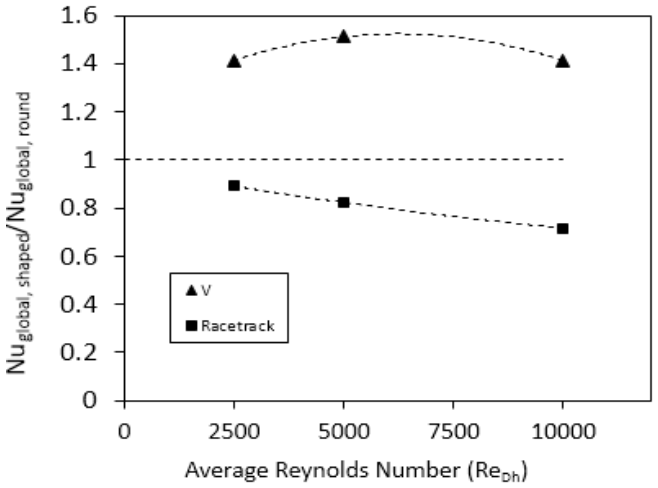

Figure 5.14 Globally averaged Nusselt numbers for racetrack and V hole shapes, normalized with round holes

GLOBALLY AVERAGED NUSSELT NUMBERS

Figure 5.14 presents the globally averaged Nusselt numbers for racetrack and V shaped holes normalized with the globally averaged Nusselt number of round jets. Racetrack holes have been found to have lower heat transfer as compared to round jets and the enhancement decayed with increase in Reynolds number. Whereas V shaped holes have been found to have more heat transfer enhancement when compared to round holes. It should be noted that the hydraulic diameters of the jets were different for each configuration, where racetrack hole hydraulic diameter was 15.65 % smaller than round holes, and V shaped hole hydraulic diameter was

22.65% smaller than round holes. However the design constraint for the shaped holes was to keep the physical area of the jets to be same. These lower hydraulic diameters imply higher mass flow rate through shaped holes (15.65% higher for racetrack and 22.65% higher for V), in order to keep the Reynolds number (based on Hydraulic diameter) to be same.

In this paper, heat transfer coefficients through different shape impinging jets have been compared with their Nusselt numbers (based on jet Hydraulic diameter). So the effect of pumping higher coolant mass on heat transfer is countered by normalizing the heat transfer coefficient with hydraulic diameter. In order to evaluate the thermal performance of a particular hole shape, the discharge coefficient or normalized flow resistance should be considered. The normalized flow resistance is defined as,

$$R = \frac{p_{in} - p_{out}}{\frac{1}{2}\rho \tilde{u}_j{}^2} = \frac{p_{in}}{p_{in}{}^*} \quad Eq.(5.8)$$

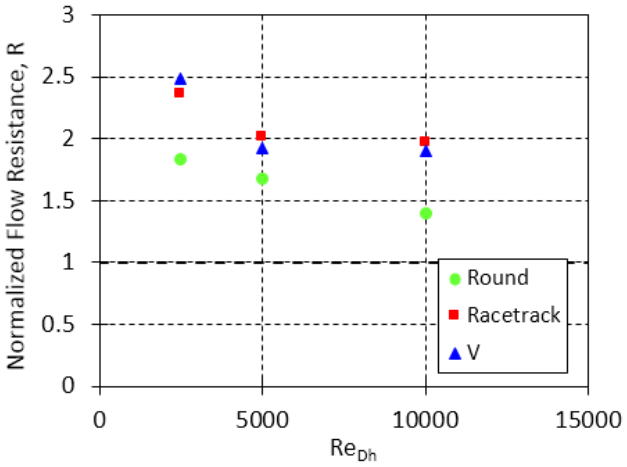

Figure 5.15 Normalized flow resistance (R) with Reynolds number for different jet hole shapes

p_{in} was measured with the target plate assembled and p_{out} was the ambient pressure at the exit of the test section. $p_{in}{}^*$ represents the dynamic pressure head available when a certain mass flow rate needs to be pumped through the jet plate when orifice plate is exposed directly to the ambient, i.e. without the target surface. Hence, normalized flow resistance (R) quantifies the resistance imposed by the target surface. The flow resistance for different hole shapes at different Reynolds number is presented in Fig. 15. As expected from the discharge coefficient trend, it

was easiest to pump coolant through round shaped holes and the flow resistance for Racetrack and V shaped holes were more or less similar. This information can be useful for designers in selection of a particular hole shape, based on the available coolant pumping potential.

CONCLUSIONS

Transient heat transfer experiments using liquid crystal thermography has been carried out to investigate heat transfer augmentation by different jet hole shapes. Three different jet hole shapes were investigated, viz. round, racetrack and V. Heat transfer experiments were carried out at three different Reynolds number (based on jet hydraulic diameter) – 2500, 5000 and 10000. The normalized spanwise and streamwise pitch of jets was 6 and the normalized jet-to-target plate spacing was 4. The plenum, jet plate and target plate were arranged such that the configuration was typical of double wall cooling arrangement for turbine airfoil mid-chord region. The spent air was allowed to exit in only one direction, thus imposing maximum crossflow.

Following conclusions can be drawn from the current study:

1. The overall heat transfer augmentation was maximum for V shaped holes, followed by round and racetrack shapes.
2. Crossflow effects were more dominant in the streamwise direction as compared to spanwise direction- which led to a unique direction of net spent air flow, and this direction was subject to change depending upon the crossflow mass flux and the jet mass flux.
3. The discharge coefficient of round holes (0.82) was highest, followed by V shaped hole (0.75) and racetrack (0.71).
4. Round shaped holes impose the least flow resistance as compared to V and racetrack, thus more pumping power is required to supply coolant in the case of shaped holes.

ACKNOWLEDGEMENTS

The authors are grateful to Dr. Sandip Dutta (GE Energy) for his suggestions and interesting discussions.

NOMENCLATURE

A area

c specific heat capacity of clear acrylic

c_p specific heat capacity at constant pressure

c_v specific heat capacity at constant volume

C_d discharge coefficient

d diameter

G mass flux

h heat transfer coefficient (W/m^2K)

H_{ref} hue value to be tracked

k_f thermal conductivity of air at film temperature

k thermal conductivity of clear acrylic

L thickness of jet plate

M jet exit Mach number

$\dot{m}$ mass flow rate

N number of holes

Nu_{d_h} Nusselt number (based on jet hydraulic diameter)

$p_{m,abs}$ absolute ambient pressure

p_{in} plenum static pressure (with target surface)

p_{out} ambient pressure

p_{in}^* plenum static pressure (without target surface)

$p_{r,m}*$ absolute plenum pressure to absolute ambient pressure ratio

R normalized flow resistance

R_a universal gas constant

$\widetilde{Re_j}$ average jet Reynolds number (based on hydraulic diameter of jet)

t time taken to reach T_{tlc}

t_{target} thickness of the target plate made of clear acrylic

T temperature

T_{tlc} temperature of target wall corresponding to H_{ref}

$\tilde{u}_j$ jet exit velocity (based on $\widetilde{Re_j}$)

x streamwise coordinate

y spanwise coordinate

z direction of impinging jets

Greek symbols

α normalized wall temperature, $(T_w(t) - T_i)/(T_m(t) - T_i)$

ρ density of clear acrylic

γ c_p/c_v

Subscripts

abs absolute

i initial

j jet

m mainstream

w wall

REFERENCES

[5.1] Sparrow, E.M., Wong, T.C., 1975, "Impingement Transfer Coefficients Due To Initially Laminar Slot Jets", Int. J. Heat Mass Transfer, 18, 597-605.

[5.2] Viskanta, R., 1993, "Heat Transfer To Impinging Isothermal Gas And Flame Jets", Experimental Thermal and Fluid Science, 6, 111-134.

[5.3] Goldstein, R.J., Sobolik, K.A., Seol, W.S., 1990, "Effect Of Entrainment on the Heat Transfer to a Heated Circular Air Jet Impinging On A Flat Surface", ASME J. Heat Transfer, 112, 608-611.

[5.4] Jambunathan, K., Lai, E., Moss, M.A., Button, B.L., 1992, "A Review Of Heat Transfer Data For Single Circular Jet Impingement", Int. J. Heat Fluid Flow, Vol 13(2), pp. 106-115.

[5.5] Florshcuetz, L. W., Metzger, D.E., Su, C.C., 1984, "Heat Transfer Characteristics for Jet Array Impingement with Initial Crossflow", ASME J. Heat Transfer, Vol. 106, pp. 34-41.

5. [6] Goldstein, R.J., and Behbahani, A.I., 1982, "Impingement of a Circular Jet with and Without Crossflow", Int. J. Heat Mass Transfer, Vol. 25, pp. 1377-1382.

[5.7] Huang, Y., Ekkad, S.V., Han, J.C., 1998, "Detailed Heat Transfer Distributions Under An Array Of Orthogonal Impinging Jets", AIAA Journal of Thermophysics and Heat Transfer, Vol. 12(1), pp. 73-79.

[5.8] Gulati, P., Katti, V., Prabhu, S.V., 2009, "Influence Of The Shape Of The Nozzle On Local Heat Transfer Distribution Between Smooth Flat Surface And Impinging Air Jet", Int. J. Thermal Sciences, Vol. 48 , pp. 602-617.

[5.9] Harmon, W.V., Elston, C.A, Wright, L.M., 2014, "Experimental Investigation Of Leading Edge Impingement Under High Rotation Numbers With Racetrack Shaped Jets," ASME Turbo Expo Paper No. GT2014-26181

[5.10] Han J.-C, Dutta S., Ekkad, S.V., 2013, "Gas Turbine Heat Transfer and Cooling Technology", Second Ed. CRC Press, Taylor & Francis.

[5.11] Snyder, J. C., Stimpson, C. K., Thole, K. A., & Mongillo, D., 2015, "Build Direction Effects on Additively Manufactured Channels" GT2015-43935, ASME IGTI TurboExpo 2015.

[5.12] Moffat, R. J., 1988, "Describing the uncertainties in experimental results", Experimental thermal and fluid science, 1(1), 3-17.

[5.13] Yan, Y., & Owen, J. M., 2002, "Uncertainties in transient heat transfer measurements with liquid crystal", International Journal of Heat and Fluid Flow, 23(1), 29-35.

[5.14] Huang, Y., Ekkad, S. V., & Han, J. C., 1998, "Detailed heat transfer distributions under an array of orthogonal impinging jets" Journal of Thermophysics and Heat Transfer, 12(1), 73-79.

[5.15] Obot, N. T., & Trabold, T. A.,1987, "Impingement heat transfer within arrays of circular jets: Part 1—Effects of minimum, intermediate, and complete crossflow for small and large spacings", Journal of Heat transfer, 109(4), 872-879.

[5.16] Yang L, Ligrani P, Ren J, Jiang H., 2015, "Unsteady Structure and Development of a Row of Impingement Jets, Including Kelvin–Helmholtz Vortex Development," ASME J. Fluids Eng. Vol. 137(5):051201-051201-12.

CHAPTER 6

Experimental and numerical investigation of heat transfer inside two-pass rib roughened duct (AR=1:2) under rotating and stationary conditions

Prashant Singh[1a], Weihong Li [a,b], Srinath V. Ekkad [a], Jing Ren [b]
[a] Advanced Propulsion and Power Laboratory, Virginia Tech, Blacksburg, VA US 24061
[b] Department of Thermal Engineering, Gas Turbine Institute, Tsinghua University, Beijing, China 100086

Under review, Int. J. Mass Transfer

ABSTRACT

Heat transfer enhancement inside ribbed channels for turbine blades is a critical phenomenon that impacts overall performance and life of the gas turbine. Present study investigates heat and fluid flow in a rectangular duct with heat transfer enhancement features, under rotating and stationary conditions. The heat transfer data obtained experimentally has been explained using numerical prediction of flow features. Detailed heat transfer coefficients have been measured on the walls of two-pass rectangular duct (AR=1:2) featuring V-shaped rib turbulators, using transient liquid crystal thermography (TLCT). The first pass and second pass featured nine V-shaped ribs each and the bend featured a 90° rib connecting the blade tip underside and the two-pass divider wall. The flow in the first pass was developing in nature. The rib-pitch to rib-height ratio (p/e) was 9.625 and the rib-height to channel hydraulic diameter (e/d_h) was 0.125. The baseline case for the rib roughened duct was geometrically identical smooth duct (with no heat transfer enhancement features). Stationary experiments were carried out for Reynolds numbers ranging from 25000 to 75000. The rotation experiments were carried out at 400 RPM (Ro=0.036) and 700 RPM (Ro=0.063), at Reynolds number of 25000. Also, numerical simulations were performed for a similar test model under similar flow conditions, using realizable $k-\epsilon$ turbulence model. Detailed discussion on rib induced secondary flows and rotational effects on heat transfer in smooth and rib roughened duct are presented in this paper using results obtained from detailed heat transfer measurements from experiments and fluid dynamics predictions from numerical simulations.

[1] Corresponding author, email: psingh1@vt.edu, Address: 445 Goodwin Hall, 635 Prices Fork Rd, Blacksburg VA 24061

Keywords: Rib turbulators; Transient Liquid Crystal Thermography; Rotation; Heat transfer

INTRODUCTION

Higher turbine inlet temperatures (~1700°C) impose significantly increased heat loads on high pressure turbines (HPT) blades. The turbine inlet temperatures are much higher compared to blade material melting point (~1000°C). The temperature of relatively colder air bled from compressor is typically around 700°C [6.1]. Hence, detailed understanding of heat transfer and fluid dynamics of internal flow in turbine blades is imperative in order to design heat transfer enhancement concepts with high thermal hydraulic performance.

In order to increase heat transfer between the coolant and blade internal walls, rib turbulators are typically installed periodically in serpentine passages. The angled rib turbulators trip the boundary layer, induce secondary flows and help enhance mixing of fluid as it passes through the serpentine passages. Some of the earlier studies on orthogonal rib turbulators were carried out by [6.2, 6.3]. The authors concluded that angled ribs have higher heat transfer compared to orthogonal ribs [6.3]. Detailed analysis of heat transfer augmentation and associated friction factors for developed turbulent flow in rectangular duct featuring rib roughened duct on two opposite walls was carried out in [6.4]. Heat transfer measurements for parallel, crossed, V, inverted V, orthogonal rib turbulators were reported in [6.5]. It was concluded that 60° V shaped ribs were found to have better heat transfer compared to 45° V shaped ribs. Broken V shaped ribs (45° and 60°) were investigated by Han and Zhang [6.6]. The authors concluded that broken ribs had higher heat transfer compared to corresponding continuous ribs. Separate effects of e/d and p/e were investigated by Taslim and Spring [6.7] for staggered arrangement of orthogonal ribs on two opposite walls of rectangular duct. The optimum pitch for orthogonal ribs was found to be eight times the rib height. Ekkad and Han [6.8] presented detailed measurements of heat transfer coefficients in a two-pass channel featuring rib turbulators. This was the first study of its kind and gave important insight into rib induced secondary flows, bend heat transfer etc. More details on rib turbulator shapes, geometrical parameters, Reynolds number effects under stationary conditions can be found in [6.9].

Over the years, several studies have been carried out to investigate the effects of rotation on heat transfer in rib turbulated two-pass channels. One of the earlier studies on the effects of rotation on heat transfer in multi-pass channel featuring skewed ribs was carried out by Johnson

et. al [6.10]. The authors studied the effects of Coriolis force and buoyancy force on heat transfer. The main conclusion of this study was that the buoyancy effects were reduced for skewed ribs compared to orthogonal ribs, and for rotation numbers less than 0.25, the effects of density difference were minimal. Due to Coriolis force, the heat transfer rates for trailing side in the case of radially outward flow was higher than the corresponding leading side and vice versa was found for radially inward flow. The effect of model orientation on heat transfer in multi-pass rib turbulated channel was studied by Johnson et al. [6.11]. The authors concluded that heat transfer can be affected by as much as 20 to 50 percent when the model orientation is changed by an angle of 45°.

The effects of rotation on heat transfer in a single pass rectangular channel (AR=4:1) featuring angled ribs, V shaped ribs and W shaped ribs (along with their discrete versions) were studied by Wright et al. [6.12]. The channel orientation with respect to rotation was 135°. Increasing trends in heat transfer with increasing streamwise distance was observed in this study for all the rib shapes. The authors reported that W shaped ribs had higher heat transfer compared to other rib shapes. The authors also concluded that the heat transfer enhancement increases on both leading and trailing sides with rotation for narrow channels. Effects of rotation on 45° rib turbulated channel was investigated in [6.13, 6.14]. For 1:2 aspect ratio channel, an increasing trend in heat transfer in first pass was observed for 45° angled rib turbulators. The conclusions on the effect of rotation in [6.13, 6.14] were similar to [6.10, 6.11]. Several heat transfer studies have been carried out on the Rotating rig at Virginia Tech (VT) using transient liquid crystal thermography. Two-pass rib turbulator passages [6.15, 6.16], jet impingement on smooth [6.17] and rough target surfaces [6.18], crossflow induced swirl [6.19], have been studied on VT rotating rig in the past. This test rig is a unique facility which allows detailed measurements of heat transfer coefficient under rotating conditions. More details on the effects of rotation on heat transfer on leading and trailing walls can be found in [6.9].

On one hand, experiments provide heat transfer data which is useful for gas turbine designers – the information on fluid dynamics in the internal cooling passage still remains sparse. Hence, several researchers carried out numerical studies in order to better understand the complex fluid dynamics in rotating internal cooling passages.

Al-Qahtani et al. [6.20] carried out numerical investigation of flow and heat transfer in a rectangular duct (AR=1:4) featuring 45° rib turbulators using Reynolds stress turbulence model. The authors studied the effects of density ratio, rotation number, angle of channel with respect to coolant flow on heat transfer on leading and trailing walls. Su et al. [6.21] carried out numerical investigation of heat transfer and fluid dynamics in rectangular channels with aspect ratios of 1:1, 1:2 and 1:4 with 45° angled rib turbulators. The authors presented secondary flows induced due to rotation. An increasing trend in heat transfer was observed in the first pass and the bend had the highest heat transfer, and the second pass had a uniform heat transfer trend. The aspect ratio of 1:2 lead to highest heat transfer in the second pass as the bend induced secondary flows had maximum strength when the vortices were near circular and occupied the entire channel cross-sectional area. Murata and Mochizuki [6.22, 6.23] carried out LES to understand turbulent heat transfer and fluid dynamics in a two pass channel featuring 45° angled rib turbulators. The authors also simulated a 90° bend at the inlet and the outlet of the two pass channel – this provided a more realistic inlet condition as the flow passes over the first rib in the first pass. In multi-pass channels, the flow is not fully developed when it encounters the rib turbulators – hence it is important to simulate realistic inlet conditions in order to better evaluate the contribution of rib turbulators towards heat transfer enhancement. Lin et al. [6.24] carried out detailed numerical study of flow and heat transfer in a two pass channel featuring 45° angled rib turbulators and a U-shaped bend. The authors concluded that rotation resulted in the development of secondary flows, particularly in the bend region and hence resulted in modification of heat transfer in the second pass leading and trailing walls. Chen et al. [6.25] carried out experimental and numerical investigation of heat and fluid flow in a two-pass duct with U bend featuring turning vanes. The two-pass channel had 45° angled rib turbulators. The experiments were carried out using TLCT and three turbulence models were used for numerical simulations, viz. k-ε, SST and ORS. The authors found that numerical prediction of heat transfer enhancement (Nu/Nu_0) was higher compared to experiments and all the three turbulence model were able to capture the flow physics, however, the ORS turbulence model proved to be better than the other two turbulence models. Kan et al. [6.26] carried out experimental and numerical investigation on single pass channel featuring different types of V shaped rib turbulators. The effects of lateral coolant ejection on heat transfer was studied.

From the review of available literature on internal flows and heat transfer under rotating conditions, it is clear that this heat transfer problem is very critical to investigate in order to better design the gas turbine blades from internal cooling perspective. The present study reports detailed heat transfer measurements for a two-pass duct (AR1:2) featuring V-shape ribs. The aspect ratio of the two-pass channel is found typically in the mid-chord region. Detailed measurements of heat transfer also provides insight into secondary flows induced from ribs, local hot spots which might occur due to flow separation or corner recirculation and how rotation impact these critical phenomena.

EXPERIMENTAL SETUP FOR TRANSIENT LIQUID CYRSTAL THERMOGRAPHY UNDER ROTATION

The experimental setup of TLCT under rotation is shown by a schematic (Fig. 6.1). In order to match the direction of buoyancy forces similar to gas turbine blades, colder air was chosen for the transient experiments. The air was drawn from the main compressor at around 300 K and 0.27 MPa. The pressurized air was regulated to working pressures by a pressure regulator located downstream of the main compressor. Downstream of the pressure regulator, a flow control valve was provided. The mass flow rate was metered by an orifice plate located about 35 pipe diameter downstream of the flow control valve. The differential pressure at the orifice plate was measured by differential pressure transducer manufactured by Dwyer (477-4-FM, 69 kPa range). The high pressure at the orifice plate was measured by Dwyer DPG-103 (2017 kPa range). Also, the temperature of the air was measured at the orifice plate in order to account for the density change of the air across different experimental runs. The detailed operational procedure for the transient experiment can be found in [6.18].

DESCRIPTION OF THE TEST SECTION

Figure 2 shows the ribbed two-pass channel investigated in the present study. The rib pitch to rib height ratio (p/e) was 9.625 and rib height to channel hydraulic diameter (e/d_h) was 0.125. The first and second pass feature eight rib pitches and the 180° bend featured a 90° rib connecting the blade tip underside internal wall to the divider wall. The ribs were present on both leading and trailing walls. The mean rotating radius (R_m/d_h) was 17.7. The flow in the first pass was not fully developed as it travels a distance of only 5.25 times the channel hydraulic diameter before it encounters the first rib. The developing flow in the first pass affects the heat transfer.

This effect is different for the baseline case (smooth duct) and ribbed duct. More discussions on this subject has been provided in the results and discussion section.

Also shown in Fig. 6.2 is the assembly drawing for in-situ wall temperature and mainstream temperature measurements. The test section for rotation studies was designed such that one transient experiment can yield heat transfer data on leading side, trailing side and blade tip underside. This approach was proved to be very useful in terms of experimental consistency and data turn around time, which in turn provided increased number of repeatability runs.

Computational methodology, grid independence study and flow data validation

The turbulent flow field in the two–pass ribbed channel was modeled using realizable version of k-ε model with enhanced wall treatment. The computations were carried out using a commercial CFD software package, Fluent which is a finite-volume based solver and the fluid domain was meshed using ICEM meshing software. Fig. 6.3 shows the computational structured grid which was used for the study. Internal O-grid mesh was used to generate boundary layer mesh for all walls to ensure that the chosen turbulence model was able to accurately capture the flow physics hence correctly predicting heat transfer. The realizable version of the k-ε model was chosen for computations since it has been known to perform well for accurate prediction in channel flows, separated flow etc.. Second order discretization scheme has been used for the governing equations.

Boundary conditions for computations

A uniform velocity (calculated based on experimental Reynolds number) and uniform bulk fluid temperature (275K) was specified at the inlet. The turbulence intensity of 5% was specified at the inlet. The pressure at the outlet was set to zero (gauge). A constant temperature of 280K was specified on the bottom and up wall for all the cases. The other walls including the rib wall were specified to be adiabatic. No slip boundary condition was imposed on all the walls. The working fluid (air) was modeled as an incompressible fluid and the flow was considered to be steady and three dimensional in nature.

Validation of numerically predicted total pressure drop with experiments

Figure 6.4(a) shows the comparison of numerically predicted pressure ratios with experimental measurements. Note that the static pressure measurements were only carried out for

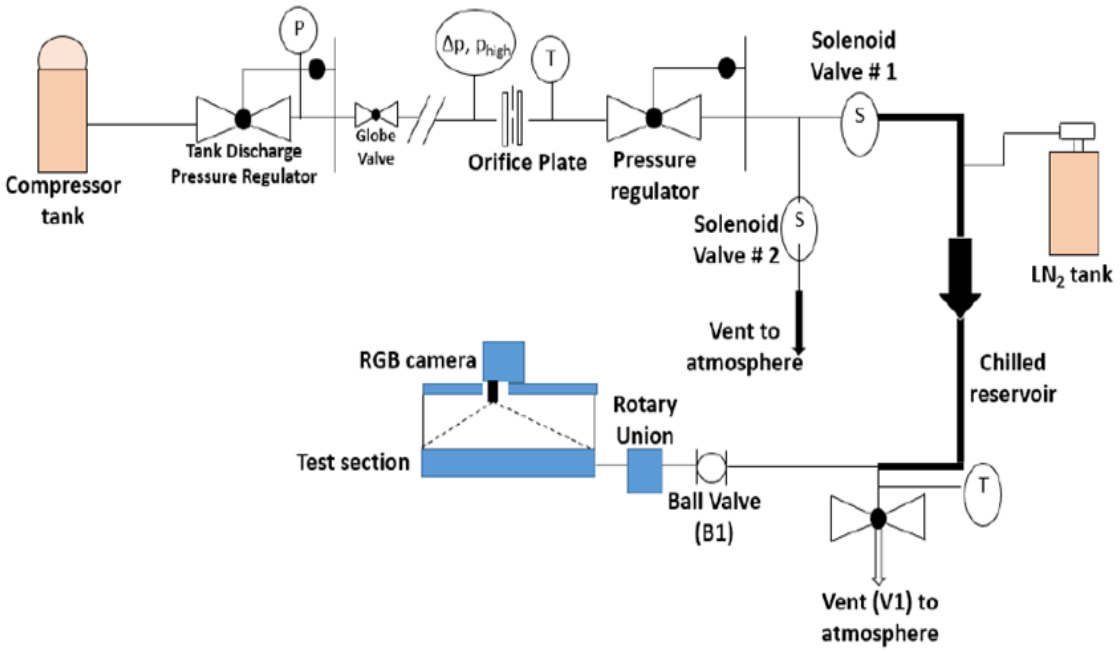

Fig. 6.1 Schematic of experimental setup

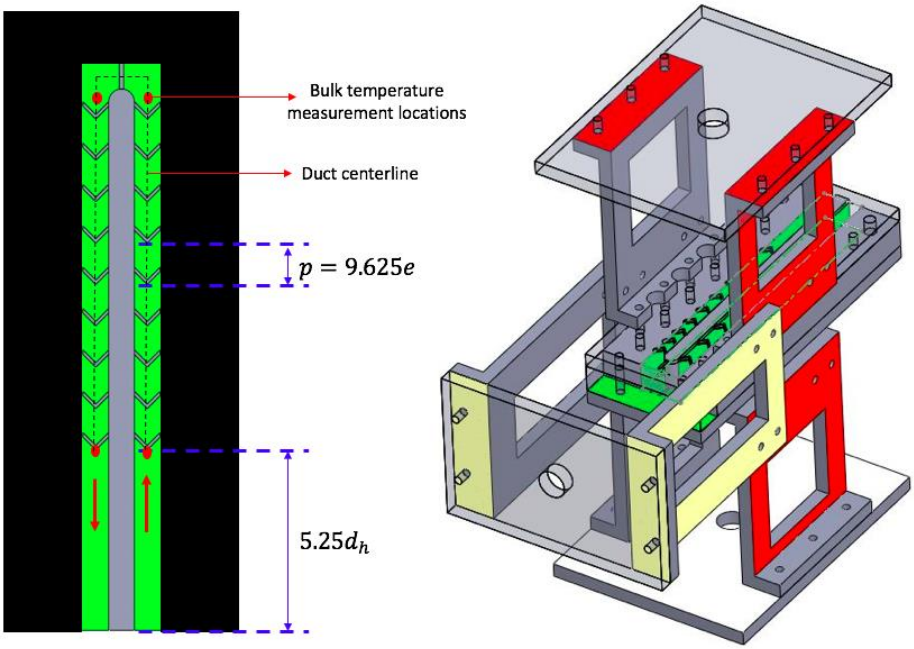

Fig. 6.2 Left figure: Two pass ribbed duct with bulk temperature measurement locations (red dots) in reference to channel centerline, green color indicates flow path. Right figure: assembly drawing for in-situ temperature measurements on leading side, trailing side and blade tip underside in one run

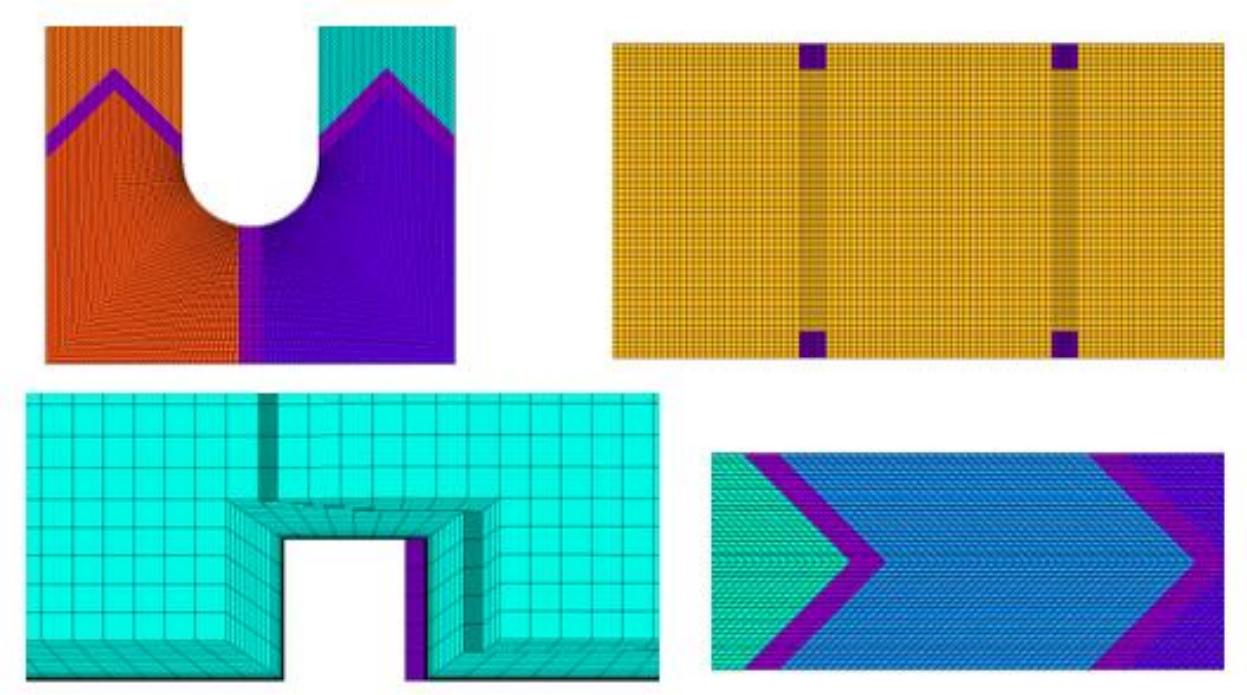

Fig. 6.3 Mesh generated using ICEM software

the stationary cases for Reynolds numbers ranging from 25000 to 75000. The definition of p^* is given as,

$$p^* = \frac{(\Delta p)_{ribbed}}{(\Delta p)_{smooth}}\Bigg]_{Ro=0} \quad (Eq.6.1)$$

The overall agreement between measurements and predictions for the stationary cases was reasonable. Good agreement between predictions and experiments for the stationary cases, allowed some analysis of changes in total pressure drop under rotating conditions when compared to stationary conditions. Since static pressure measurements under rotating conditions were out of scope of the present study, the numerical simulation results were used for analysis. Figure 6.4(b) shows the variation of normalized inlet static pressures ($p^* \; and \; p^{**}$). The definition of p^{**} is given as,

$$p^{**} = \frac{(\Delta p)_{Ro\neq 0}}{(\Delta p)_{Ro=0}} \quad (Eq.6.2)$$

The effects of rotation on p* shows a decreasing trend with increasing Rotation number, however p* shows an increasing trend with Reynolds number for the full range studied.

Normalized static pressure (p**) shows the effects of rotation alone on change in relative pressure drop and this number is exclusive for smooth and ribbed cases. It can be seen that p** values for ribbed cases remained less affected by rotation, however the smooth two-pass channel shows clear effects of change in p** with rotation. The comparison of numerically predicted heat transfer coefficient with experimental measurements has been shown in the results and discussion section.

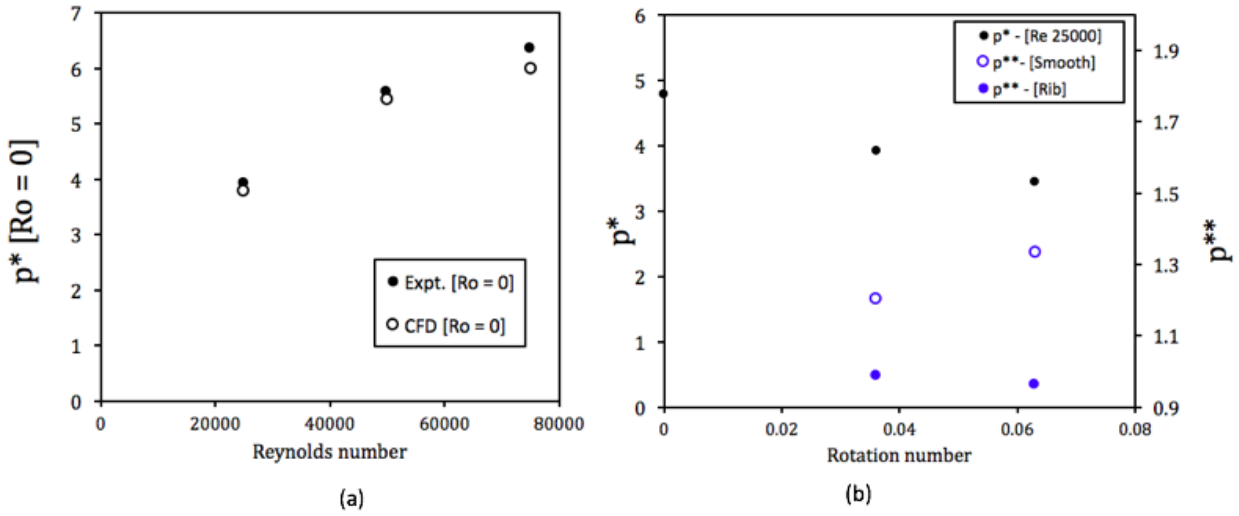

Fig. 6.4 (a) Variation of normalized pressure (p^*) with Reynolds number (Ro = 0), (b) variation of normalized pressures (p^* *and* p^{**}) with Rotation number (numerically predicted).

DATA REDUCTION PROCEDURE FOR TLCT UNDER ROTATION

The heat transfer coefficient was measured using 1-D semi infinite conduction model. For a time dependent mainstream temperature, Duhamel's superposition principle was incorporated in the wall temperature solution obtained from 1-D transient heat conduction equation using constant mainstream temperature. The resultant equation is given by,

$$T_w = T_i + \sum_{i=1}^{i=n_{max}} \left(T_{m,i} - T_{m,i-1}\right) \times \left[1 - exp\left(\frac{h^2(t-t_i)}{\rho c k_s}\right) erfc\left(h\sqrt{\frac{t-t_i}{\rho c k_s}}\right)\right] \quad (Eq.\,6.3)$$

More details about the derivation of above expression can be found in [6.27, 6.28]. In the present study, the bulk temperature has been taken to be the mainstream temperature or reference temperature for heat transfer coefficient calculations. The fluid temperature was measured by a fast response K-type thermocouple at the centerline of the duct. It was assumed that this temperature is representative of the bulk temperature of the coolant, given the turbulent nature of flow field. The mainstream temperature was measured at four locations in the two pass channel. The measurement locations are shown in Fig. 6.2 by red dots. Since, during the transient experiment, there was heat exchange between the coolant and the internal wall, the mainstream temperature was space dependent as well (Fig. 6.5). The spatial variation of mainstream temperature was considered only in the streamwise direction. In order to account for the variation of mainstream temperature in streamwise direction, the measured temperatures were linearly interpolated between the shown locations.

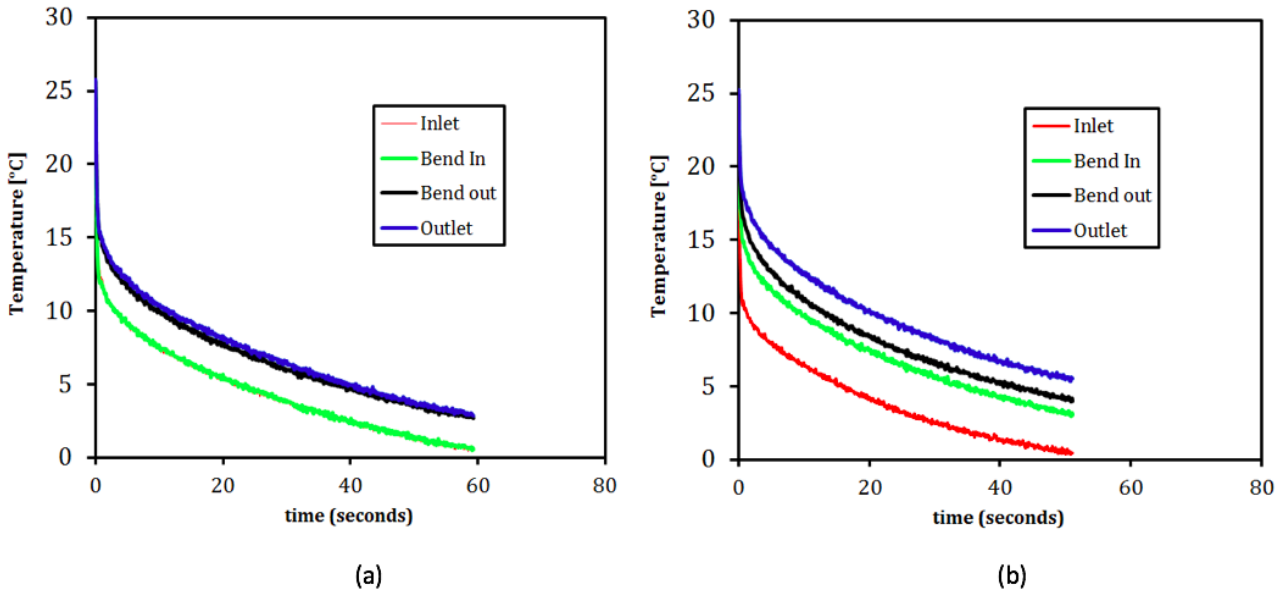

Fig. 6.5 Mainstream temperature variation with time, (a) smooth two pass channel, (b) ribbed two pass channel

The measurement locations near the bend region were chosen by taking into consideration, the complex fluid dynamics in the bend region. This is the reason why the mainstream temperature was not measured in the bend region, but slightly upstream and downstream where the flow was relatively well defined. The chosen locations proved to be satisfactory as the detailed

measurements replicated the raw color change observed during transient experiment. A sample response of mainstream temperature measurement at the four locations has been shown in Fig. 6.5. It can be seen from Fig. 6.5(a), that the streamwise variation in mainstream temperature in first pass was very low, while there was significant difference in temperature from bend inlet to bend outlet due to high rates of heat exchange between coolant and wall. In the case of ribbed channel, the difference in mainstream temperature from inlet to bend inlet is significant, because of heat transfer enhancements due to ribs. The complete data reduction procedure has been explained in detail in [6.29].

UNCERTAINTY ANALYSIS

The uncertainty in the measurement of heat transfer coefficient was calculated using sequential perturbation method prescribed by Moffat [6.30]. The contributing factors to the overall uncertainty in the measurement of heat transfer coefficient are $T_w, T_i, T_m, t, \sqrt{\rho c k_s}$. The contribution of T_w, T_i, T_m was taken to be 0.5°C. The contribution of t was taken to be time taken to record two frames (0.067 seconds). The contribution of $\sqrt{\rho c k_s}$ was taken to be 5% of the nominal value. For a typical heat transfer coefficient value of 236, an uncertainty of about 12% was obtained. The uncertainty in the calculation of Reynolds number of 25000 was 4%.

RESULTS AND DISCUSSION

This section reports measured and predicted Nusselt numbers under rotating and stationary conditions. Detailed discussion has been provided for the heat transfer and fluid dynamics peculiar to the configuration in particular and the effects of rotation on modification of heat transfer on leading wall, trailing wall and blade tip underside. Numerical results are used in conjunction with experiments in order to better explain the heat transfer in the two-pass duct and the effects of rotation on the same.

The detailed normalized Nusselt number (Nu/Nu_0) under stationary conditions have been shown in Fig. 6.6.

Consider the smooth two-pass channel (stationary cases) - the flow in the first pass was developing in nature and hence heat transfer decreased along the streamwise direction as the flow was developing. The effect of boundary layer growth along the sidewalls of the channel in first pass is apparent from relatively lower heat transfer near extremes of the channel span. Since

there was no obstruction towards coolant flow in the first pass, the coolant impinged on the blade tip underside before it made the 180° turn. The flow while making the 180° turn impinged on the outer wall of the second pass.

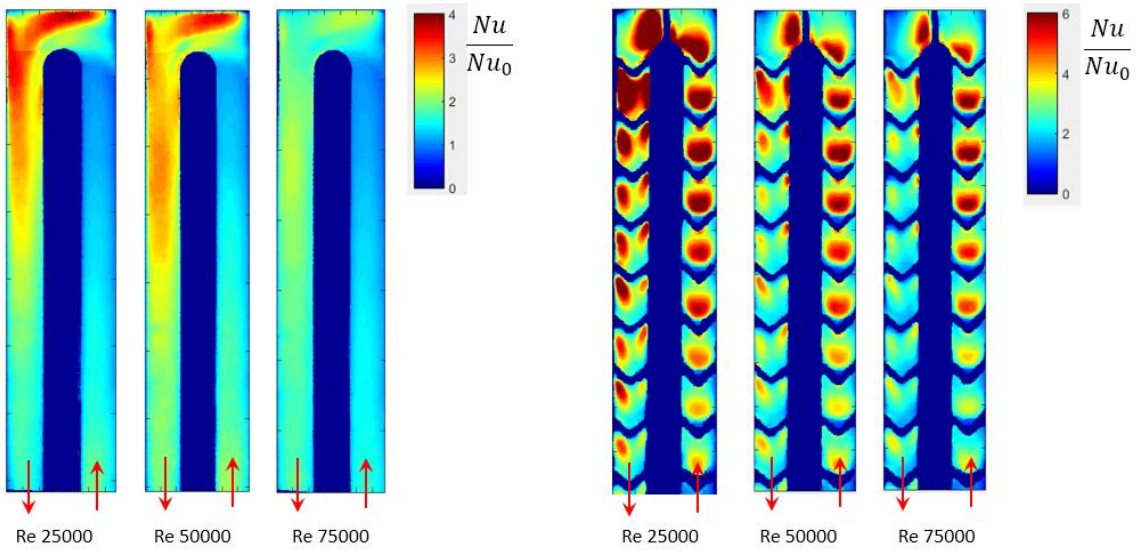

Fig. 6.6 Detailed Nusselt number enhancement contours under stationary conditions

Also, a small scale recirculation region has been identified near the top left corner of the contour. This recirculation region leads to lower heat transfer. The flow closer to divider wall undergoes acceleration while a portion of coolant separated from the bulk flow in the bend region. These regions of acceleration (vicinity of divider wall) and separation leads to high and low heat transfer regions. The heat transfer in the second pass was predominantly driven by bend induced flow disturbance and skewed momentum flux of coolant along the outer wall of the second pass. The coolant after making the 180° turn travelled along the outer wall and hence leading to higher heat transfer along that wall. As the streamwise distance increased in the second pass, these effects diminished and heat transfer became more uniform in the spanwise direction.

For the ribbed two-pass channel, in the first pass, the heat transfer enhancement was the result of the combined effects of rib induced secondary flows, developing flow, turbulent mixing. The interaction of rib induced secondary flows with the bottom wall enhances near wall shear and hence the heat transfer. The turbulent mixing provides a mean of transport of energy from

the endwalls through the fluid medium. The V shaped rib can be seen as two 45° angled ribs joined at the centerline of the channel. The angle of attack generates the secondary flows which increase near wall shear. Also, the flow diversion due to angle of attack hits the side walls and travels inwards, leading to turbulent mixing. As the flow progresses, the effect of turbulent mixing becomes dominant, hence leading to increased transport of energy from the wall, resulting in increasing heat transfer along the streamwise direction. The heat transfer in the bend region for the ribbed case is different compared to the smooth two pass channel. Due to presence of ribs, the flow in the first pass undergoes increase in turbulent mixing along streamwise direction, and hence a direct impingement of coolant on the blade tip underside was not seen for the ribbed case, as in the case of smooth duct. The presence of 90° rib in the bend region further mixes the flow while it makes the 180° turn and also trips the near wall fluid, hence creating a very complicated fluid dynamic scenario. The 90° rib trips the flow and results in higher heat transfer region in the near downstream region of the rib. The 90° rib was strategically placed in the bend region as it adds to the structural integrity of the blade since it connects the blade tip underside to the tip of the divider wall. In the second pass, the rib orientation with the coolant flow was different compared to the first pass. In this type of rib orientation, the secondary flows were induced from the corners (from sidewalls) and converged towards the centerline of the channel. This arrangement is not very useful for heat transfer enhancement compared to the orientation in the first pass. For detailed study of a different rib orientation in second pass, the reader is referred to [6.31].

Detailed Heat transfer measurements under rotation

Figure 7 shows the detailed Nusselt number enhancement (Nu/Nu_0) a Ro=0.063 (700 RPM). The data has been arranged as leading side, stationary and trailing side and contours have been shown for both smooth two-pass duct (baseline) and ribbed two-pass duct.

As mentioned earlier, rotation induces two types of forces on the fluid under rotation – Coriolis force and centrifugal force. The magnitude of both the forces is directly proportional to the rotation speed. The direction of centrifugal force is always radially outwards. The direction of Coriolis force depends on the relative angle between the bulk coolant flow and rotation. For radially outward flow, the boundary layer along the trailing wall was thinner compared to the leading wall and for radially inward flow, the boundary layer was thinner along the leading wall

as compared to trailing wall. This leads to higher heat transfer on the trailing wall for radially outward flow (1st pass) and vice versa for the leading wall. In the present study, the density difference between the near wall fluid and the core fluid was very small, hence the buoyancy effects were low even when they were coupled with rotational effects.

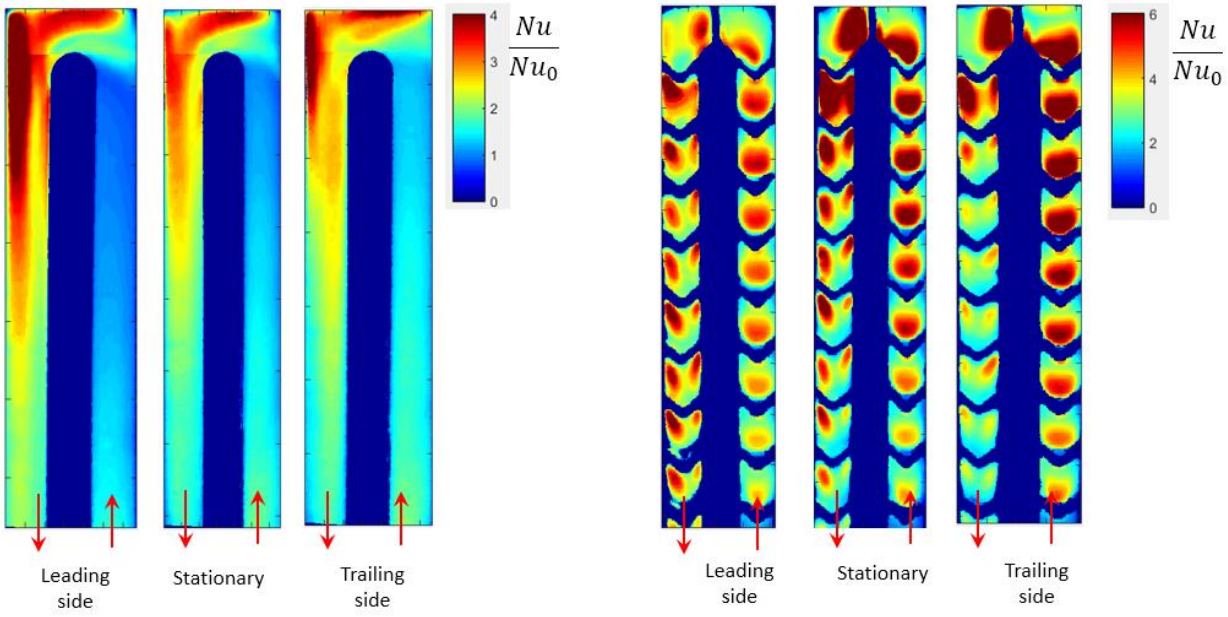

Fig. 6.7 Detailed Nusselt number enhancement (Nu/Nu_0) contour for smooth and ribbed two-pass duct at Re = 25000 and Ro = 0.063 (700 RPM).

Consider the smooth two-pass duct under rotation, the flow in the first pass was simpler compared to the second pass. The effect of Coriolis force was apparent in the first pass, where trailing side had higher heat transfer followed by no rotation case and leading wall. The effects of coolant impingement onto blade underside corresponding to first pass under rotating conditions can be seen from the contours shown in Fig. 6.7. Due to the centrifugal force, the radially outward flow of coolant further pumps the flow and hence impingement effects were more pronounced particularly for the trailing edge case. The impingement effect existed in the leading edge case as well since strength of centrifugal force was the same for both leading and trailing walls. However, the heat transfer in the bend region close to the blade tip underside is affected by Coriolis force as well. The impingement effect was slightly suppressed for the leading wall case as the Coriolis force still acted in a direction favorable for heat transfer on the trailing wall. One important distinction in the heat transfer contour in the bend region for rotation

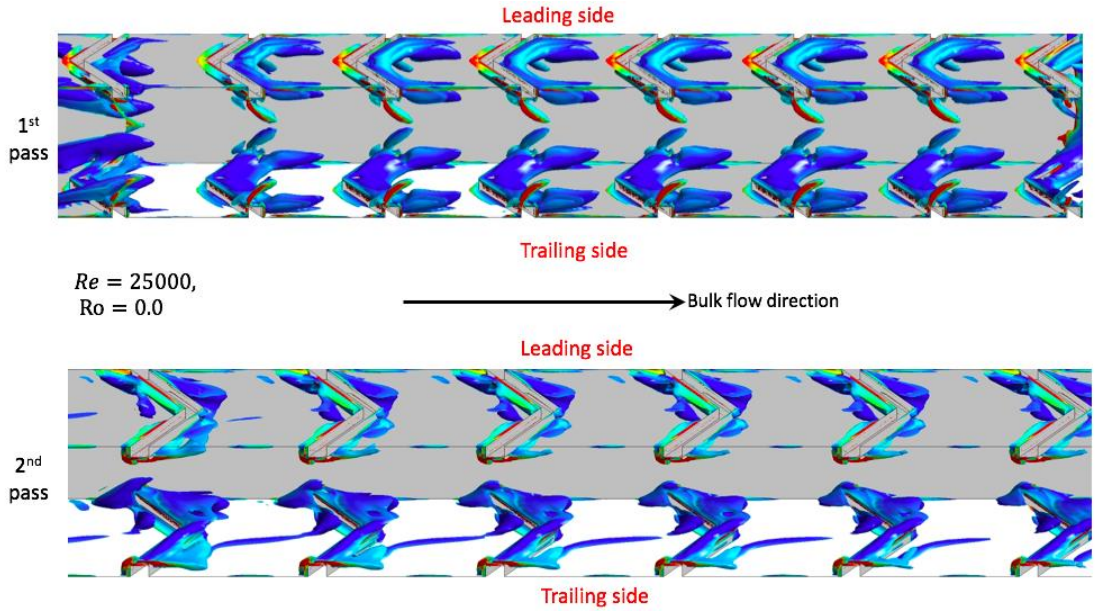

Fig. 6.8 Iso-surface of Q criterion colored by vorticity: Re= 25000 and Ro = 0 for the ribbed configuration

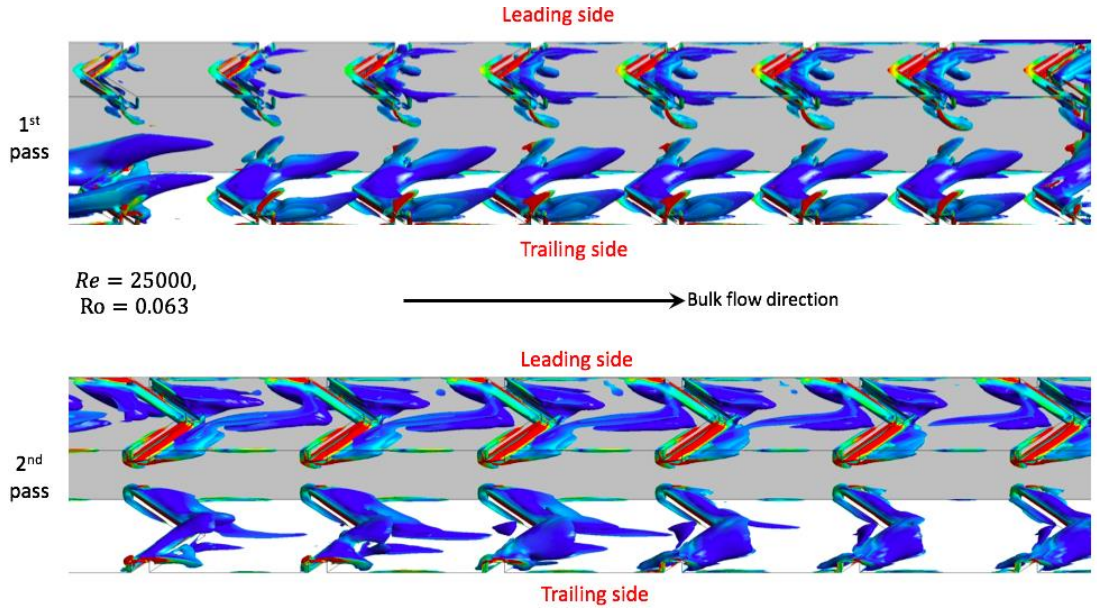

Fig. 6.9 Iso-surface of Q criterion colored by vorticity: Re= 25000 and Ro = 0.063 for the ribbed configuration

case and stationary case, was that the heat transfer along the outer wall of the second pass while the coolant made the 180° turn. The flow while turning hits the outer wall in the second pass due to skewed momentum flux towards that wall. This effect has been seen to further enhance for the rotation cases for both leading and trailing walls. Note that the buoyancy force will also act due to difference in density of fluid near the wall and the density of fluid in the core. However, since the temperature difference between the coolant and the wall is very small, this effect will be negligible compared to Coriolis and centrifugal forces. For the case of ribbed two pass channel under rotation, the trends of heat transfer in the first pass for leading and trailing walls were similar to that of the smooth two-pass channel under rotation. However, the magnitude of change in heat transfer (due to rotation) in the ribbed case compared to the smooth case were different because of the different fluid dynamics (turbulent mixing, secondary flow interaction with side walls etc.). This discussion has been presented in the next section which presents the regionally averaged Nusselt number enhancement.

Figures 6.8 and 6.9 show the iso-surface of the Q-criterion colored by vorticity. The iso-Q criterion indicates the vortex core where the flow structures with highest vorticity occurs. In the first pass, the vortex structures near the leading and trailing walls were similar to each other due to absence of rotational effects. The vortex structures were found to be mainly distributed just downstream of the ribs, where flow recirculation happens due to flow separation. In the second pass, the relative direction of flow and orientation of rib was reversed. The above mentioned fact combined with bend effects resulted in different nature of vortices in the second pass around the ribs. The flow recirculation zones were attenuated and the swirling flow moved towards the centerline of the passage.

When the rotation effects were introduced, the nature of vortices changed. In the first pass, the vortex structures near the ribs on the trailing wall were stronger than those at the leading walls due to the effect of Coriolis force. In the second pass, the rotation effects on vortical structures wasn't as apparent as in the first pass, because the flow in the second pass was mostly dominated by the bend induced secondary flows as well as the difference in the relative orientation of the ribs with respect to coolant flow. The strong mixing phenomena occurring in the bend region leads to comparably similar boundary layer distribution (turbulent) for leading and trailing sides.

Figure 6.10 shows the streamtraces superimposed with normalized turbulent kinetic energy. Streamtraces are representative of probable path taken by a massless particle if introduced in the flow without any initial energy. A total of seven planes have been drawn including first pass, bend region and the second pass. Planes P1 and P6 are drawn at the end of the rib, P2 and P7 are drawn at the beginning of the rib. The reason behind drawing planes, both at the beginning and at the end of the rib was to identify the changes in the fluid dynamics to introduction of rib turbulator. Planes P3, P4 and P5 were drawn to study the fluid dynamics in

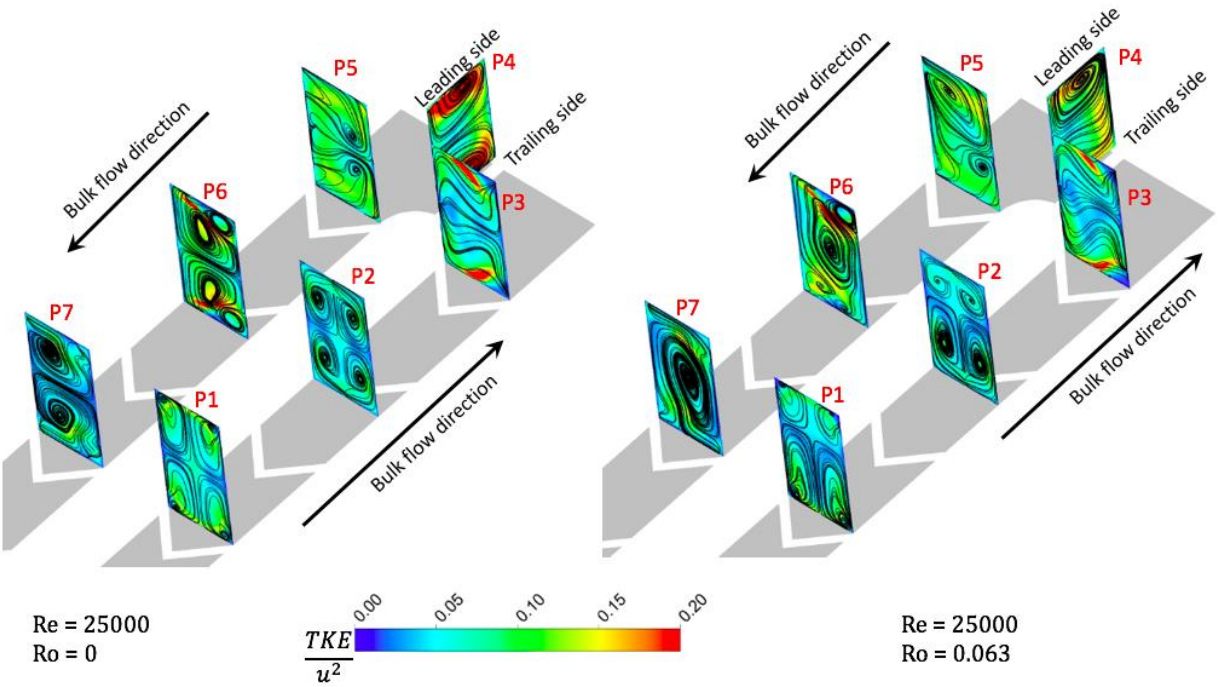

Fig. 6.10 Streamtraces superimposed with normalized TKE for Ro=0 and 0.063 cases.

the bend region. At plane P1, it can be seen that the streamtraces were symmetrical in nature as the flow became somewhat periodic while it reached P1. For Ro = 0 case, the symmetrical nature of streamtraces still remained as the flow reached plane P2. At P3 (in reference to P1), the bend downstream of the rib affected the symmetric nature of turbulent mixing. This is because of the fluid motion from outer to inner wall due to turning nature in the bend region, which suppresses

the effect of rib induced secondary flows on turbulent mixing at P3. However, the strength of turbulent kinetic energy (TKE) in the plane P3 was found to be higher than both P1 and P2. For the stationary case at Plane P4, Dean type vortices were found in the bend region. Dean type vortices are formed due to combined effect of curvature induced gradient in pressure and centrifugal force [32]. This trend in the bend region was also found in many other similar studies. The TKE near the leading and trailing walls was significantly higher at P4 compared to other planes in 1st and 2nd pass. The nature of turbulent mixing in 2nd pass was completely different from 1st pass due to difference in the orientation of ribs with bulk flow and the fact that 2nd pass ribs were downstream of the bend. At plane P6 (just downstream of the 2nd rib in 2nd pass), two big vortices were found near the outer wall with two small corner recirculation vortices.

From Fig. 6.10, it can be seen that the basic nature of turbulent mixing in the first pass (Planes P1 and P2) remained the same, since the rib induced secondary flows were similar in nature under rotating conditions as well. However, the turbulent mixing was affected by rotation. It can be seen that the transport of energy from trailing side endwall was faster than the transport from the leading side.

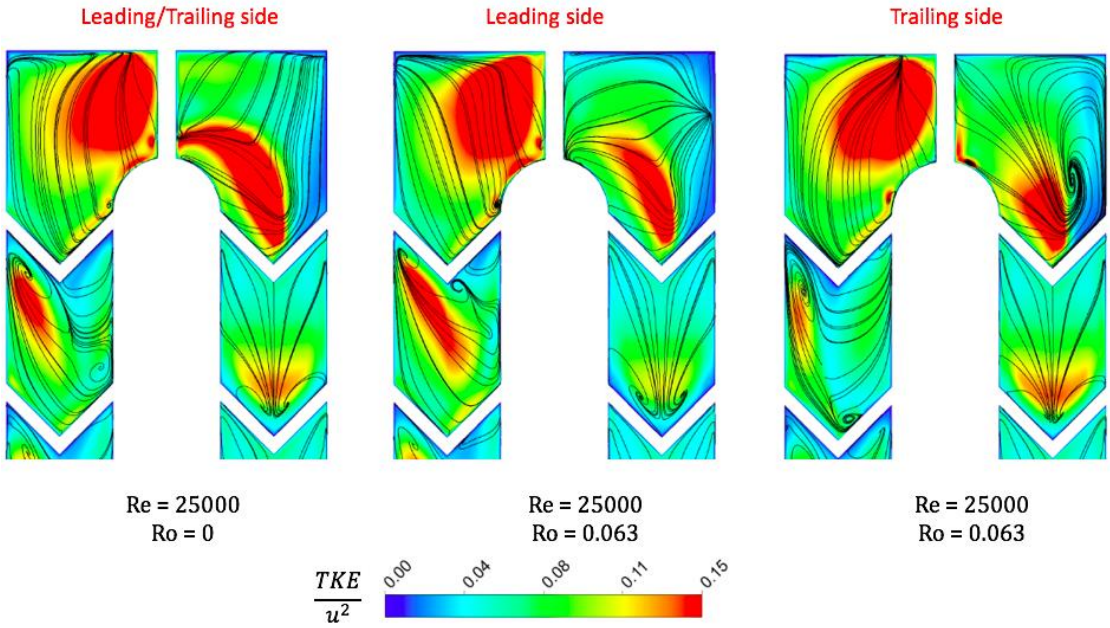

Fig. 6.11 Streamtraces superimposed with normalized TKE, plotted near endwall

This phenomenon is one of the reasons for higher heat transfer on the trailing side endwall compared to leading side endwall for radially outward flow (1st pass). At Plane P3, the

Dean type vortices were not observed in the rotating case. More discussion on bend heat transfer under rotating and non-rotating conditions will be provided in a separate sub-section. The size of large vortex in the second pass moved closer to leading side endwall and hence shifted the higher heat transfer region towards the leading side. As mentioned earlier, heat transfer on the endwall depends upon several factors – large vortex size is one such mechanism where the convective transport of energy is higher on one wall compared to other wall. However, the net heat transfer enhancement depends on combined effects of rib orientation with bulk flow, position of rib in two-pass channel, rotation number etc. Figure 11 shows the streamtraces superimposed with normalized turbulent kinetic energy plotted at a plane very close to the endwall (which is our region of interest for HTC calculations). Turbulent kinetic energy of fluid close to the endwall provides reasonable qualitative estimate of high and low heat transfer regions. Streamtraces indicate the direction of rib induced secondary flows near the wall. These secondary flows enhance the near wall shear and lead to enhanced heat transfer. As mentioned earlier, the secondary flow travel from channel centerline towards inner and outer walls in the first pass. In the second pass, the rib induced secondary flows travel from inner and outer walls towards channel centerline, however, this motion is also affected by skewed momentum flux due to turning flow exiting from the bend which leads to higher momentum flux along the outer wall in the second pass. The turbulent kinetic energy contour mimics very closely the heat transfer trends in the first and second pass and is consistent with experimental and numerical findings of heat transfer data.

Blade Tip Underside Heat transfer and Fluid Dynamics in Bend Region – numerical predictions

Figure 6.12 shows the iso-surface of Q-criterion colored with vorticity. Four contours are shown for ribbed and smooth cases at Ro = 0 and 0.063. For the stationary case, the fluid flow was symmetric in nature about the channel centerline for both smooth and ribbed configurations. Same color indicates that the local rotation is in similar direction. In all the iso-surface contours of Q-criterion, blue color indicates negative values and red color indicates positive values of vorticity. The presence of 90° rib disturbed the fluid flow in the turning region. In the ribbed configuration (Ro = 0), a small recirculation zone was observed just downstream of the rib leading to lower local heat transfer coefficient. On comparison of ribbed and smooth cases (Ro = 0), it can be seen that presence of ribs in 1st and 2nd pass along with the 90° rib affected the

impingement of flow and corner recirculation vortices at the outer wall of 2nd pass. For the smooth case, a strong impingement effect was seen on the outer wall and this effect was also reflected in the heat transfer on the leading/trailing walls (Fig. 6.13). However, for the ribbed case, the turning flow was tripped by the 90° rib and the impingement effect on the outer wall of the 2nd pass was suppressed. Also, for the ribbed configuration, a clear effect of last rib in the 1st pass was seen as the vortices induced by ribs on leading and trailing walls interacted with each other while turning, and hence creating complex fluid dynamics situation.

For the rotation case (Ro = 0.063) in contrast to the stationary case (Ro = 0), the vortex structures near the leading wall was stretched towards the trailing wall.

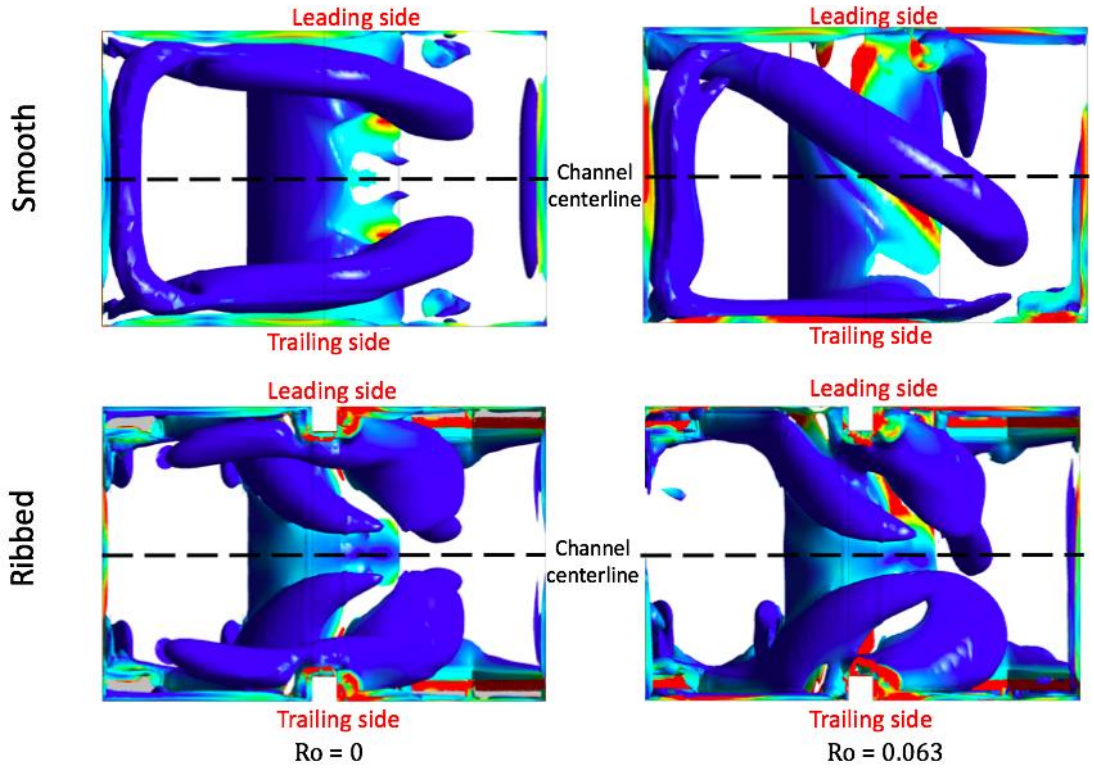

Fig. 6.12 Iso-surface of Q-criterion colored by vorticity

On comparison of smooth and ribbed cases (stationary cases), the vortex structure at the bend inlet disappeared in the case of ribbed channel. The vortex structure in the smooth case near the bend inlet region caused the increased heat transfer due to impingement effect. However, in the ribbed case, the vortex structure dissipated due to rib blockage upstream of the bend inlet. Hence,

the heat transfer in the bend inlet region was higher for the smooth case compared to the ribbed case due to dissipation effect caused by the rib turbulator. The presence of 90° rib in the bend region also had significant effects on heat transfer, as the vortex structure was broken into pieces. These broken vortex structures lead to increased number of venues for high heat transfer in the bend region due to higher turbulence intensity and small scale vortices.

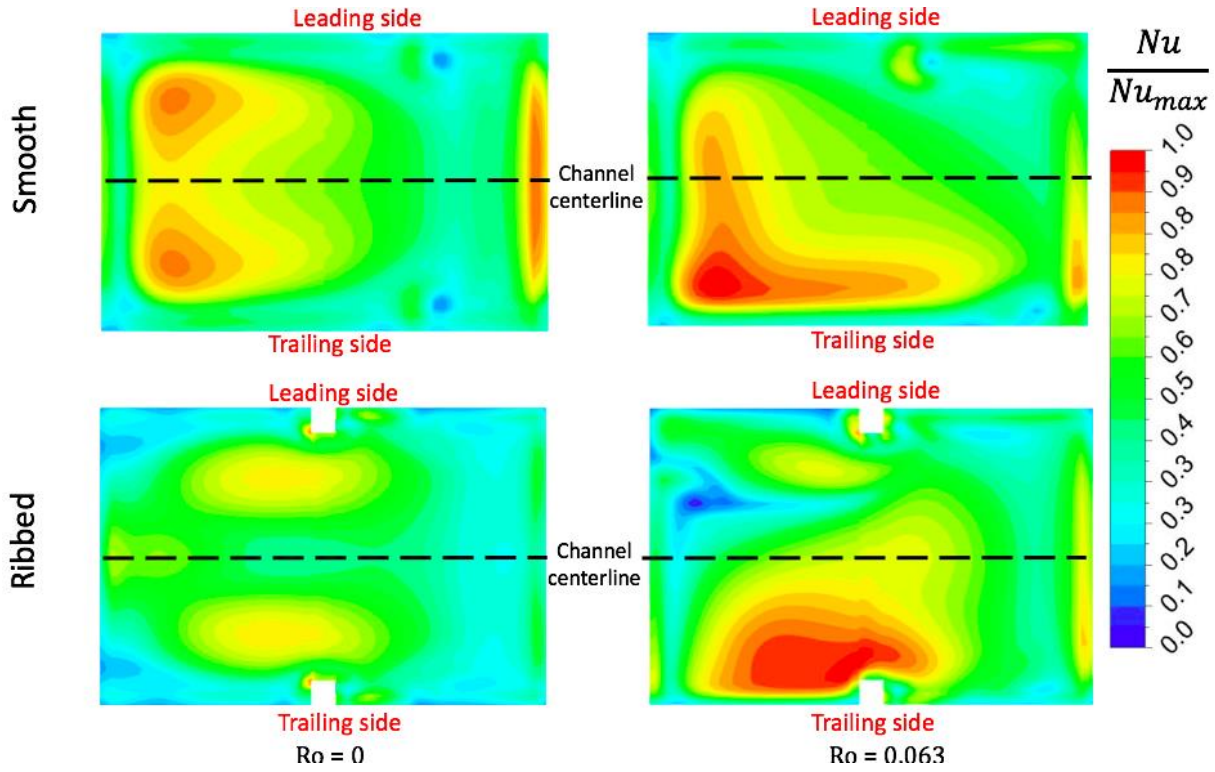

Fig. 6.13 Blade tip underside heat transfer – numerical predictions

On comparison of heat transfer in the bend region (blade tip underside corresponding to first pass, rotation case) between ribbed and smooth channel, it can be seen that the impingement effect was suppressed for the ribbed case for the rotation cases as well. On inter-comparison of heat transfer for the ribbed two-pass duct between the trailing and leading walls, the impingement effect was found to be more in the case of trailing side compared to the leading side. This trend was also observed for the smooth duct. Also, the bend heat transfer was highest for the trailing side followed by stationary case and leading side. The effects of rotation in the second pass heat transfer was not as apparent as in the case of first pass, because the flow in the second pass was extremely complicated and was the result of combined effects of bend induced

secondary flows, rib induced secondary flows, skewed momentum flux (higher towards the outer wall). However, the Coriolis force strength can still be seen in the second pass, as the heat transfer was highest for the leading side, followed by stationary case and trailing wall. The nature of secondary flows induced by ribs remained unaffected by the effects of centrifugal and Coriolis force.

Regionally Averaged Heat transfer Under Stationary Conditions:

Smooth and ribbed configurations under stationary condition– Experiments

Each rib pitch was considered as one region and the region numbers increased in the direction of increasing streamwise distance from the inlet. Regionally averaged data gives some understanding of heat transfer trends on a broader level as compared to detailed measurements. Figure 6.14 shows the regionally averaged normalized Nusselt number values (with Dittus-Boelter correlation for developed turbulent flow in circular duct) variation with increasing streamwise distance for the smooth two-pass channel (stationary case), where Reynolds number ranging from 25000 to 75000 were investigated. It can be seen that with the development of flow in the first pass, the Nusselt number enhancement decayed and eventually converged to a value close to unity. This signifies that the flow was just about developed prior to entering the bend region (Regions 9 and 10).

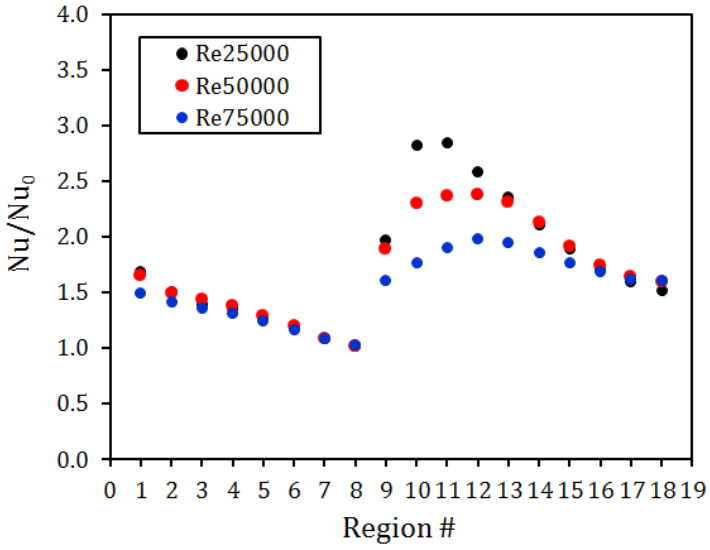

Fig. 6.14 Regionally averaged normalized Nusselt number for smooth two-pass channel under stationary conditions

The bend region heat transfer was about two times the Nusselt number at the inlet for Re 25000. The increase in heat transfer as coolant entered the bend was ~200%. Post the bend, the heat transfer decayed and converged to 1.5 times the Nusselt number through D-B correlation. Also, the heat transfer enhancements decreased with increasing Reynolds number. Increase in heat transfer scales differently as compared to frictional increments in the two-pass channel due to increase in Reynolds number.

Figure 6.15 shows the regionally averaged normalized Nusselt number (Nu/Nu_0) for the ribbed two-pass duct. The Nusselt number enhancement values decrease with increasing Reynolds number and this trend in heat transfer enhancement was similar to that of the smooth two-pass duct. An increasing trend in heat transfer has been observed as the flow progressed in the first pass. This might be the result of turbulent mixing which becomes more dominant in the downstream part of the first pass. This trend is further investigated through Fig. 6.16.

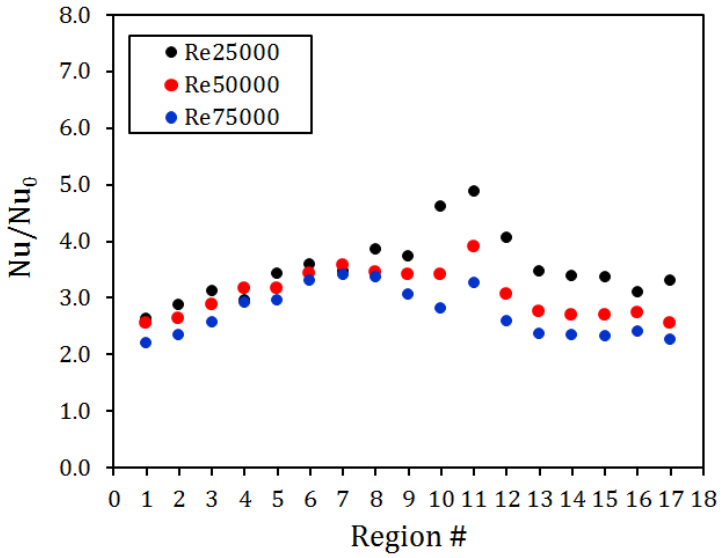

Fig. 6.15 Regionally averaged normalized Nusselt number for ribbed two-pass channel under stationary conditions

Figure 6.16 shows the streamlines downstream of the first rib and third rib of the first pass. It can be seen that the strength of the secondary flow near the bottom wall was higher for the 3rd rib compared to the first rib. Also shown is the normalized turbulent kinetic energy plotted in a plane orthogonal to the bulk fluid direction, and just downstream of the 1st and 3rd rib of the first

pass. It is evident that the turbulent mixing was stronger in the case of 3rd rib as the strength of vortices generated due to combined guidance of rib and side wall, increases with increasing streamwise distance.

Similar to smooth channel, the bend region had higher heat transfer compared to other locations in the two-pass channel. The highest heat transfer region in the two-pass ribbed duct occurred at the first pitch of the second pass. This was because of the combined effects of bend induced secondary flows, rib induced secondary flows and skewed momentum flux towards the outer wall. Downstream of the first pitch in the second pass, the heat transfer decayed. It should be noted that the orientation of rib with the bulk fluid flow was different in the second pass as compared to first pass. The reason of decreasing heat transfer in the second pass can be due to the combined effects of the nature of secondary flows induced by the ribs and relatively reduced turbulent mixing due to different rib-coolant orientation compared to that found in the first pass.

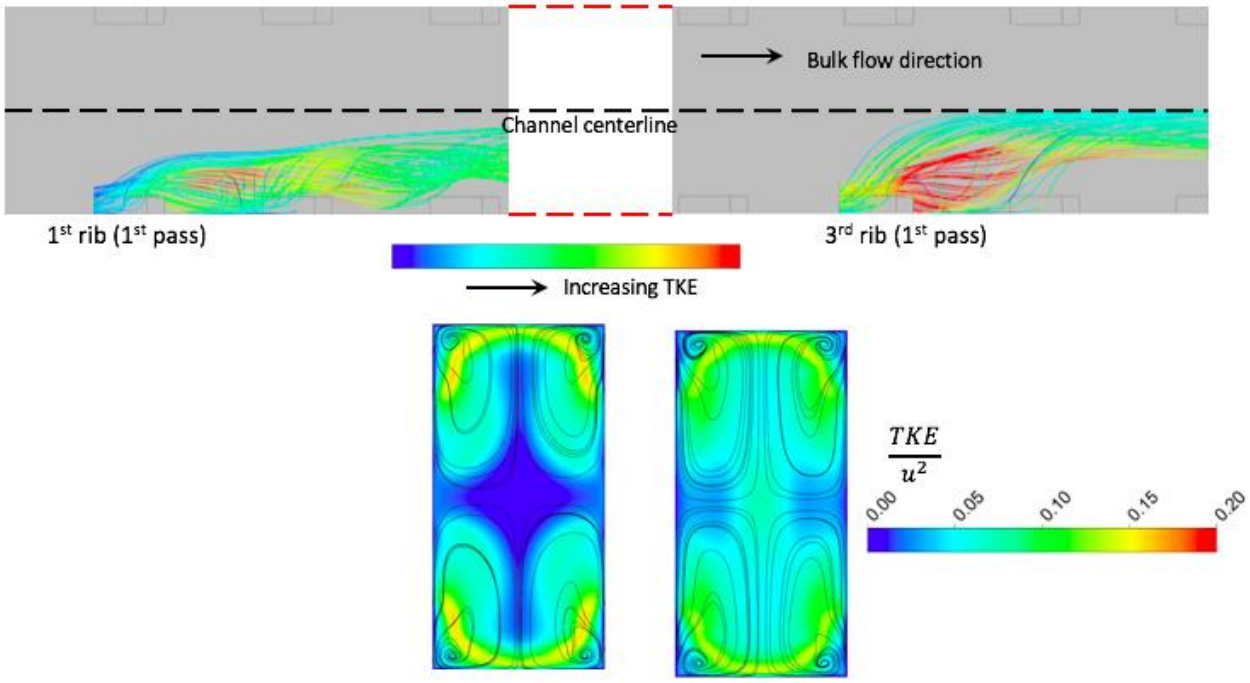

Fig. 6.16 Streamlines showing turbulent kinetic energy in the flow near the rib, also shown is the normalized TKE contour with streamtraces in a plane orthogonal to bulk flow direction. (The planes were drawn just downstream of the rib, left plane corresponds to first rib and right plane corresponds to third rib of the first pass): Re = 25000, Ro = 0

(Nu/Nu_s) and $(Nu/Nu_{0\ RPM})$: comparison between experiments and numerical predictions

Figure 6.17 shows the comparison of Nusselt number (normalized with corresponding regionally averaged data obtained for smooth channel) measured experimentally and predicted numerically. Figure 6.17(a) shows the regionally averaged Nusselt number enhancement plotted with increasing streamwise distance. The agreement between experiment and CFD for heat transfer results for stationary case has been found to be satisfactory. One difference between experiment and CFD is that the numerically predicted heat transfer becomes uniform more rapidly compared to experiments. One reason behind this phenomena, is the inlet conditions of flow is different for experiment and CFD. In numerical simulations, a uniform inlet velocity is provided based on the Reynolds number – this leads to faster development of flow in the first pass in CFD when compared with experiments. However, in the experiments, as has been mentioned in an earlier section, the flow keeps developing as it progresses in the first pass. One way to cancel the effects of inlet conditions between experiment and CFD is to compare the Nusselt numbers normalized with corresponding smooth channel results obtained separately in experiments and in CFD [6.31].

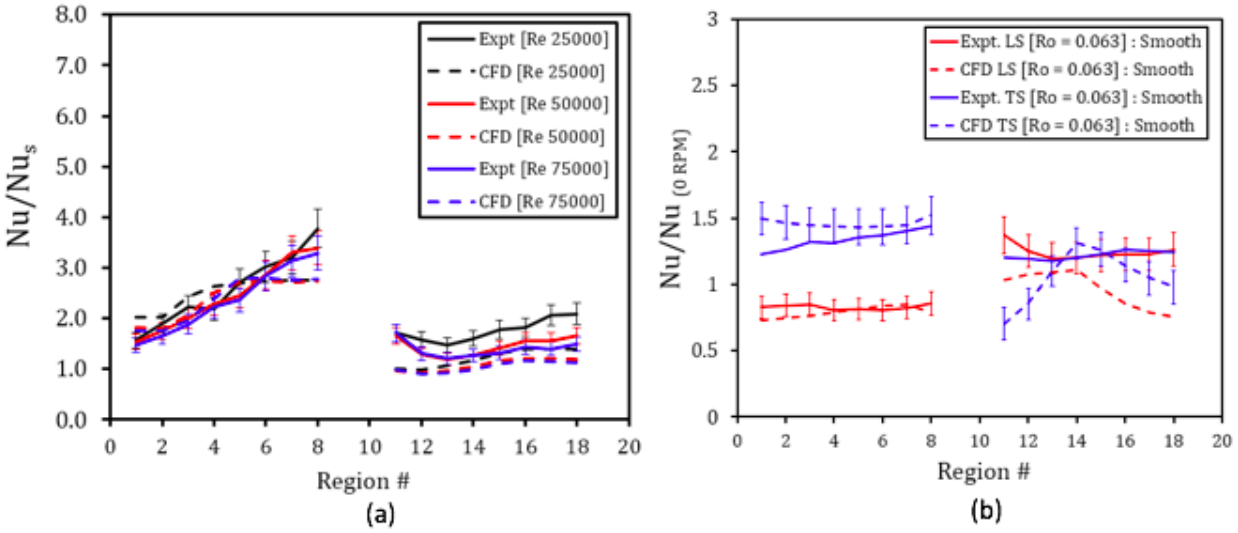

Fig. 6.17 (a) Regionally averaged Nusselt number enhancement (Nu/Nu_s) at Ro = 0 - experiment versus CFD, (b) regionally averaged Nusselt number $(Nu/Nu_{stationary})$ at Re = 25000, Ro = 0.063 – experiment versus CFD.

An increasing trend in heat transfer enhancement has been observed in both experimental and numerical results. This trend was expected as the heat transfer decreased in the first pass of the smooth channel and heat transfer increased in the first pass of the ribbed channel, resulting in increasing trend in heat transfer for Nu/Nu_s data. The reason behind decreasing heat transfer in the first pass of the smooth channel is the development of flow with increasing streamwise distance. However, in the ribbed channel, the turbulent mixing caused by the interaction of rib induced secondary flows increases with increasing streamwise direction.

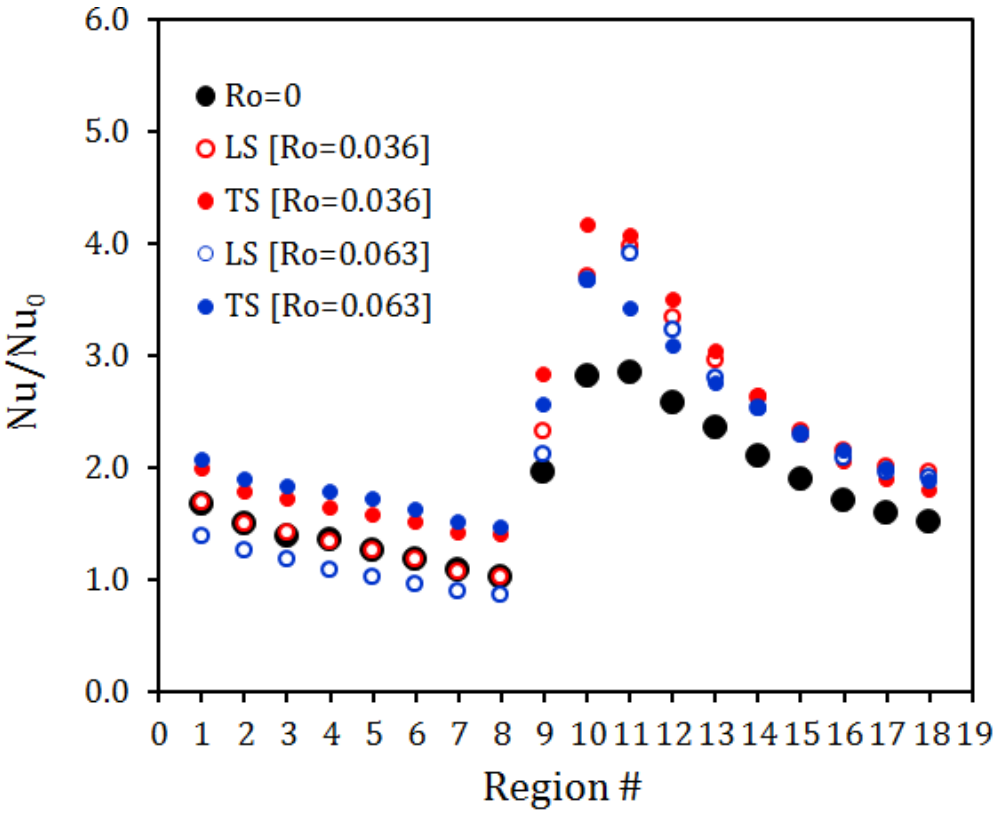

Fig. 6.18 Regionally averaged Nusselt number ($\mathrm{Nu}/\mathrm{Nu}_0$) for rotation and stationary cases (smooth): experimental results

Regionally averaged Nusselt number Enhancement (Nu/Nu_0) Under Rotating Conditions: Experiments

Figure 6.18 shows experimentally obtained regionally averaged Nusselt number for the smooth two-pass channel under stationary and rotating conditions. The rotating experiments were carried out at Rotation numbers of 0.036 and 0.063 while keeping the Reynolds number

fixed at 25000. Expected trends in heat transfer in the first pass were obtained where trailing side heat transfer was higher than the leading side. For all rotation cases and for both leading and trailing sides, the heat transfer in the bend region was higher compared to the stationary cases. Post the 180° turn, the flow underwent mixing and it had been observed that rotation helped in heat transfer in the second pass. The leading side and trailing had similar levels of heat transfer and were higher than the stationary cases.

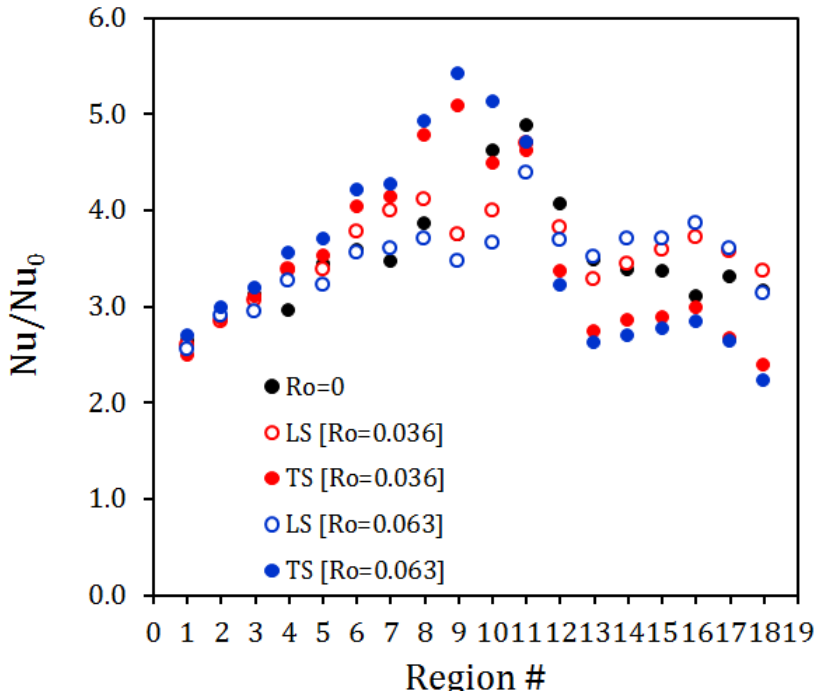

Fig. 6.19 Regionally averaged Nusselt number (Nu/Nu_0) for rotation and stationary cases (ribbed): experimental results

Figure 6.19 shows experimentally obtained regionally averaged Nusselt number for the ribbed two-pass channel under rotating and stationary conditions. The heat transfer enhancement in the first pass was found to be highest for the trailing side, followed by stationary and leading side. Also, this effect of rotation was proportional to rotation number. In the bend region, the trends were very distinct. In the first pass, trailing side enhancements were higher than the stationary case and the enhancements in heat transfer were lowest for the leading side. The heat transfer in the bend region is a result of several factors, such as bend induced secondary flows, Coriolis force, centrifugal force, the presence of 90° rib etc. More detailed numerical investigation with

high fidelity turbulence model which can take into account, the isotropic nature of fluid dynamics, is required for complete understanding of bend heat transfer. The heat transfer trends in the second pass remained the same for both stationary and rotation cases. The effects of Coriolis force favoring the leading side in the second pass was more apparent in the ribbed case compared to smooth channel. It can be seen that the heat transfer was highest for the leading side (Ro = 0.063) and minimum for trailing side (Ro = 0.063). This trend is consistent with earlier research findings.

CONCLUSIONS

Detailed heat transfer measurements are reported for ribbed (V-shape) and smooth two-pass duct (AR = 1:2) by transient liquid crystal thermography under rotating and non-rotating conditions. The configuration under consideration is typical of mid-chord region of high pressure turbine (HPT) blades. Under stationary condition, measurements of heat transfer were carried out for Reynolds numbers ranging from 25000 to 75000 for both the configurations. Under rotating conditions, two rotation numbers 0.036 (400 RPM) and 0.063 (700 RPM) were investigated at Reynolds number of 25000. Numerical predictions have been used in conjunction with experimental measurements, in order to better understand the flow physics in the two-pass channel featuring V-shaped rib turbulators. Some of the conclusions from the present study are:

(1) For stationary cases (smooth duct), Nusselt number enhancements levels reduce with increasing Reynolds number. For the first pass of smooth duct, the heat transfer enhancement reduces from 50% to about 5% (compared to D-B correlation) due to developing nature of the flow. The convergence of (Nu/Nu_0) values towards unity (in the first pass) for all the Reynolds number provides evidence of data consistency and strong validation by excellent agreement with well established Dittus-Boelter correlation.

(2) For stationary case of ribbed duct, the heat transfer enhancement in the first pass showed an increasing trend in the streamwise direction. Compared to the smooth duct, heat transfer levels increased from ~30% to ~200% in the first pass. The increased turbulent mixing is expected to be one of the reasons behind the increasing trend. The highest heat transfer was observed in the bend region, and the heat transfer decreased and showed an asymptotic nature in the second pass. The decreasing trend in heat transfer enhancement in the second

pass is because of the decrease in turbulent mixing due to difference in the rib-to-coolant orientation.

(3) For the rotation case in smooth duct, heat transfer in the first pass was highest on the trailing side followed by stationary and leading side. However, in the second pass, both leading and trailing sides had higher heat transfer compared to stationary case. The effect of Coriolis force in the first pass was apparent and resulted in observed and expected trends in heat transfer.

(4) For the rotation case of ribbed duct, the heat transfer in the first pass was highest on the trialing side followed by stationary and leading side. This trend was similar in the bend region as well. The heat transfer in the second pass was highest for the leading side followed by stationary case and trailing side. Numerical predictions shows the shifting of large scale vortices towards the wall where the Coriolis force acts relatively stronger, hence leading to increased mass flux as well as heat transfer along that wall.

Overall, the numerical predictions provided important insight into the complex fluid dynamics in a two-pass, rib roughened duct (with developing flow in 1st pass) under rotating conditions. Detailed experimental measurements of Nusselt number provided information about the role of secondary flows in enhancement of near wall shear. The effects of turbulent mixing on the heat transfer were explored using numerical results. The present study provides valuable information of heat transfer for a wide range of Reynolds number (25000 to 75000) under stationary conditions, and also the effects of rotation (at Ro = 0.036, 0.063) on heat transfer modification on leading and trailing walls, through comprehensive experimental and numerical investigation.

NOMENCLATURE

c	specific heat capacity of solid
d_h	channel hydraulic diameter
h	heat transfer coefficient
k_s	thermal conductivity of solid
k_f	thermal conductivity of air
p	static pressure
Re	Reynolds number, Vd_h/v
Ro	rotation number, $\Omega d_h/V$

R_m mean rotating radius

T_i initial wall temperature

t time

Nu Nusselt number

T_w wall temperature

T_m mainstream temperature

Greek symbols

ρ density

Subscripts

s smooth surface

0 Dittus-Boelter correlation

REFERENCES

[6.1] Han, J.C., 2013. Fundamental gas turbine heat transfer. Journal of thermal science and engineering applications, 5(2), p.021007.

[6.2] Webb, R.L., Eckert, E.R.G. and Goldstein, R.J., 1972. Generalized heat transfer and friction correlations for tubes with repeated-rib roughness. International Journal of Heat and Mass Transfer, 15(1), pp.180-184.

[6.3] Han, J.C., Glicksman, L.R. and Rohsenow, W.M., 1978. An investigation of heat transfer and friction for rib-roughened surfaces. International Journal of Heat and Mass Transfer, 21(8), pp.1143-1156.

[6.4] Han, J.C., 1984. Heat transfer and friction in channels with two opposite rib-roughened walls. Journal of heat transfer, 106(4), pp.774-781.

[6.5] Han, J.C., Zhang, Y.M. and Lee, C.P., 1991. Augmented heat transfer in square channels with parallel, crossed, and V-shaped angled ribs. Journal of Heat Transfer, 113(3), pp.590-596.

[6.6] Han, J.C. and Zhang, Y.M., 1992. High performance heat transfer ducts with parallel broken and V-shaped broken ribs. International Journal of Heat and Mass Transfer, 35(2), pp.513-523.

[6.7] Taslim, M.E. and Spring, S.D., 1994. Effects of turbulator profile and spacing on heat transfer and friction in a channel. Journal of Thermophysics and Heat Transfer, 8(3), pp.555-562.

[6.8] Ekkad, S.V. and Han, J.C., 1997. Detailed heat transfer distributions in two-pass square channels with rib turbulators. International Journal of Heat and Mass Transfer, 40(11), pp.2525-2537.

[6.9] Han, J.C., Dutta, S. and Ekkad, S., 2012. Gas turbine heat transfer and cooling technology. CRC Press.

[6.10] Johnson, B.V., Wagner, J.H., Steuber, G.D. and Yeh, F.C., 1994. Heat transfer in rotating serpentine passages with trips skewed to the flow. Journal of Turbomachinery, 116(1), pp.113-123.

[6.11] Johnson, B.V., Wagner, J.H., Steuber, G.D. and Yeh, F.C., 1994. Heat transfer in rotating serpentine passages with selected model orientations for smooth or skewed trip walls. Journal of turbomachinery, 116(4), pp.738-744.

[6.12] Wright, L.M., Fu, W.L. and Han, J.C., 2004, January. Thermal performance of angled, V-shaped, and W-shaped rib turbulators in rotating rectangular cooling channels (AR= 4: 1). In ASME Turbo Expo 2004: Power for Land, Sea, and Air (pp. 885-894). American Society of Mechanical Engineers.

[6.13] Al-Hadhrami, L. and Han, J.C., 2003. Effect of rotation on heat transfer in two-pass square channels with five different orientations of 45 angled rib turbulators. International Journal of Heat and Mass Transfer, 46(4), pp.653-669.

[6.14] Fu, W.L., Wright, L.M. and Han, J.C., 2004, January. Heat Transfer in Two-Pass Rotating Rectangular Channels (AR= 1: 2 and AR= 1: 4) With 45 Angled Rib Turbulators. In ASME Turbo Expo 2004: Power for Land, Sea, and Air (pp. 305-315). American Society of Mechanical Engineers.

[6.15] Lamont, J.A., Ekkad, S.V. and Alvin, M.A., 2012. Detailed Heat Transfer Measurements Inside Rotating Ribbed Channels Using the Transient Liquid Crystal Technique. Journal of Thermal Science and Engineering Applications, 4(1), p.011002.

[6.16] Lamont, J.A., Ekkad, S.V. and Alvin, M.A., 2014. Effect of Rotation on Detailed Heat Transfer Distribution for Various Rib Geometries in Developing Channel Flow. Journal of Heat Transfer, 136(1), p.011901.

[6.17] Lamont, J.A., Ekkad, S.V. and Alvin, M.A., 2012. Effects of Rotation on Heat Transfer for a Single Row Jet Impingement Array With Crossflow. Journal of Heat Transfer, 134(8), p.082202.

[6.18] Singh, P. and Ekkad, S., 2016, June. Effects of Rotation on Heat Transfer due to Jet Impingement on Cylindrical Dimpled Target Surface. In ASME Turbo Expo 2016: Turbomachinery Technical Conference and Exposition (pp. V05BT16A010-V05BT16A010). American Society of Mechanical Engineers.

[6.19] Yang, L., Tyagi, K., Ekkad, S. and Ren, J., 2015, June. Influence of Rotation on Heat Transfer in a Two-Pass Channel With Impingement Under High Reynolds Number. In ASME Turbo Expo 2015: Turbine Technical Conference and Exposition (pp. V05AT11A021-V05AT11A021). American Society of Mechanical Engineers.

[6.20] Al-Qahtani, M., Chen, H.C. and Han, J.C., 2002, January. A numerical study of flow and heat transfer in rotating rectangular channels (AR= 4) with 45 rib turbulators by Reynolds stress turbulence model. In ASME Turbo Expo 2002: Power for Land, Sea, and Air (pp. 533-542). American Society of Mechanical Engineers.

[6.21] Su, G., Chen, H.C., Han, J.C. and Heidmann, J.D., 2004, January. Computation of Flow and Heat Transfer in Two-Pass Rotating Rectangular Channels (AR= 1: 1, AR= 1: 2, AR= 1: 4) With 45-deg. Angled Ribs by Reynolds Stress Turbulence Model. In ASME Turbo Expo 2004: Power for Land, Sea, and Air (pp. 603-612). American Society of Mechanical Engineers.

[6.22] Murata, A. and Mochizuki, S., 2004. Effect of rib orientation and channel rotation on turbulent heat transfer in a two-pass square channel with sharp 180° turns investigated by using large eddy simulation. International Journal of Heat and Mass Transfer, 47(12), pp.2599-2618.

[6.23] Murata, A. and Mochizuki, S., 2000. Large eddy simulation with a dynamic subgrid-scale model of turbulent heat transfer in an orthogonally rotating rectangular duct with transverse rib turbulators. International Journal of Heat and Mass Transfer, 43(7), pp.1243-1259.

[6.24] Lin, Y.L., Shih, T.P., Stephens, M.A. and Chyu, M.K., 2001. A numerical study of flow and heat transfer in a smooth and ribbed U-duct with and without rotation. Journal of Heat Transfer, 123(2), pp.219-232.

[6.25] Chen, W., Ren, J. and Jiang, H., 2011. Effect of turning vane configurations on heat transfer and pressure drop in a ribbed internal cooling system. Journal of Turbomachinery, 133(4), p.041012.

[6.26] Kan, R., Yang, L., Ren, J. and Jiang, H., 2013, June. Effect of rib configuration and lateral ejection on a high aspect ratio trailing edge channel. In ASME Turbo Expo 2013: Turbine Technical Conference and Exposition (pp. V03AT12A018-V03AT12A018). American Society of Mechanical Engineers.

[6.27] Bergman, T.L. and Incropera, F.P., 2011. Introduction to heat transfer. John Wiley & Sons.

[6.28] Ekkad, S.V. and Han, J.C., 2000. A transient liquid crystal thermography technique for gas turbine heat transfer measurements. Measurement Science and Technology, 11(7), p.957.

[6.29] Singh, P., Pandit, J. and Ekkad, S.V., 2017. Characterization of heat transfer enhancement and frictional losses in a two-pass square duct featuring unique combinations of rib turbulators and cylindrical dimples. *International Journal of Heat and Mass Transfer, 106*, pp.629-647.

[6.30] Moffat, R.J., 1988. Describing the uncertainties in experimental results. Experimental thermal and fluid science, 1(1), pp.3-17.

[6.31] Singh, P., Ravi, B.V. and Ekkad, S.V., 2016. Experimental and numerical study of heat transfer due to developing flow in a two-pass rib roughened square duct. International Journal of Heat and Mass Transfer, 102, pp.1245-1256.

[6.32] Ravi, B.V., Singh, P. and Ekkad, S.V., 2017. Numerical investigation of turbulent flow and heat transfer in two-pass ribbed channels. International Journal of Thermal Sciences, 112, pp.31-43.

CHAPTER 7

EXPERIMENTAL INVESTIGATION OF ROTATING RIB ROUGHENED TWO-PASS SQUARE DUCT WITH TWO DIFFERENT CHANNEL ORIENTATIONS

Prashant Singh and Srinath V. Ekkad
Department of Mechanical Engineering, Virginia Tech
Blacksburg, VA USA 24061

Accepted for publication in conference proceedings of ASME – IGTI TurboExpo,
GT2017-64225

ABSTRACT

Effects of rotation on heat transfer on leading and trailing sides of gas turbine blades has been extensively studied in the past. It has been established for typical two-pass channel that radially outward flow (first pass) has higher heat transfer on trailing side and lower heat transfer on leading side and vice versa for radially inward flow (second pass). Rotation induces three forces on the coolant flow – Coriolis, Centrifugal and Buoyancy forces. The direction of Coriolis force depends on the relative angle between the coolant flow and the rotation direction, because of which the direction of Coriolis force is different in individual passes – which in turn results in non-uniform distribution of high heat transfer regions on leading and trailing walls. The present study is focused on utilizing the Coriolis force favorably in both the passes by rotating the typical arrangement of two-pass channels by 90°. Firstly, smooth two pass duct (Model A-smooth) having typical arrangement of coolant flow and rotation direction is studied. The second configuration is the corresponding ribbed channel (Model A-ribbed) featuring V-shaped ribs on both leading and trailing walls. The rib-height-to-channel hydraulic diameter ratio was 0.125, rib pitch-to- rib height ratio was 8, and channel aspect ratio was unity. Model B was obtained by rotating the Model A by 90° and changing the coolant inlet port as well. Model B had three configurations- (a) smooth duct, (b) single sided ribbed duct, and (c) double sided ribbed duct. Detailed heat transfer coefficients were measured by transient liquid crystal thermography under rotating conditions. In order to match the direction of Buoyancy force as it exists in actual engines, colder air was passed during the transient experiment. The heat transfer experiments were carried out at a Reynolds number of 20000 and Rotation numbers of 0, 0.05 and 0.1. The Nusselt numbers have been reported in two forms, (a) normalized with respect to Dittus-Boelter

correlation for developed turbulent flow in circular duct, (b) normalized with corresponding Nusselt number obtained from smooth channel experiments. The effects of Coriolis force and centrifugal force on heat transfer has been discussed in detail. A new model has been proposed based on the understanding and findings of the present study, which has positive effects of rotation on both leading and trailing walls.

INTRODUCTION

Higher turbine inlet temperatures are required in order to achieve higher turbine thermal efficiency. This leads to high heat loads on high pressure turbine (HPT) stage components. Highly complicated film cooling and internal cooling concepts are employed in HPT airfoils in order to protect them from hot gases exiting the combustor. Several factors affect the heat transfer from hot gases to airfoil surface, e.g., airfoil surface temperature, free-stream turbulence, surface roughness, injection location of film cooled air, Reynolds number etc. [7.1]. Gas turbine designers take into account the above mentioned factors while designing internal cooling concepts and pumping power requirements to maintain the airfoil operating temperatures within the safe limits. Internal cooling concepts enhance the heat transfer between the coolant and the internal walls of the airfoils. Existing literature consists of detailed investigation of different concepts which enhance heat transfer coefficient in the internal cooling passages, e.g. rib turbulators, jet impingement, pin fin array etc. Detailed documentation of these heat transfer enhancement features can be found in [7.2]. While it is important to test cooling features under stationary conditions to evaluate their capabilities in terms of heat transfer enhancement for a given pumping power, evaluation of these concepts under rotating conditions is imperative, as rotation modifies the heat transfer on leading and trailing walls. Rotation induces two forces on fluid (at same temperature as that of wall) – Coriolis force and centrifugal force, on the coolant flowing through internal cooling passages. Since, the coolant temperature and internal wall temperatures are different, it leads to buoyancy forces which is directly proportional to square of Rotation number, mean rotating radius and density ratio. Several researchers have investigated the effects of Coriolis force, centrifugal force and buoyancy force.

One of the earlier studies on the effects of rotation on heat transfer in multi-pass channel featuring skewed ribs was carried out by Johnson et al. [7.3]. The authors studied the effects of Coriolis force and buoyancy force on heat transfer. The main conclusions of this study was that

the buoyancy effects were reduced for skewed ribs compared to orthogonal ribs, and for rotation numbers less than 0.25, the effects of density difference were minimal. Due to Coriolis force, the heat transfer rates for trailing side in the case of radially outward flow was higher than the corresponding leading side and vice versa was found for radially inward flow. The effect of model orientation on heat transfer in multi-pass rib turbulated channel was studied by Johnson et al. [7.4]. The authors concluded that heat transfer can be affected by as much as 20 to 50 percent when the model orientation is changed by an angle of 45°. One other study on the effects of model orientation on heat transfer in rib roughened two-pass channel was carried out by [7.5]. It has been observed that the rotation induced secondary flows change its nature with the orientation of coolant with respect to the direction of rotation, and hence effect the heat transfer on leading and trailing walls in different ways. Dutta et al. [7.6] studied the effects of model orientations on triangular two-pass channel with rib turbulators.

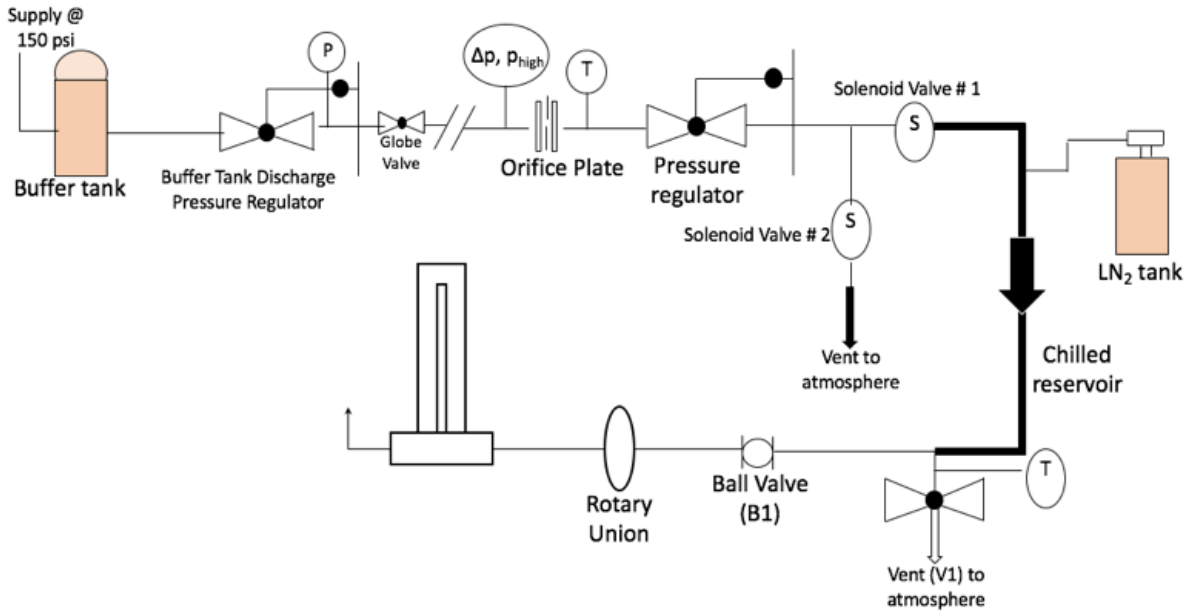

Fig, 7.1 Schematic of experimental setup

Dutta and Han [7.7] investigated a unique model orientation for a two-pass rib roughened duct featuring broken rib turbulators. This study investigated three model orientations where Model B is an interesting design for gas turbine blades where rotation can have positive effects on both leading and trailing walls. This particular concept of two-pass channel has been explored in

detail in the present study and a new design for high thermal-hydraulic performance two-pass channel design is proposed. Detailed heat transfer measurements under rotating conditions have been a challenge. In the past five years or so, there has been an increase in these type of studies [7.8-7.16]. Our group has carried out several studies on rib turbulated two-pass channel, crossflow induced swirl, jet impingement on dimpled target surface under rotating conditions with detailed heat transfer measurements [7.12-7.16].

In the present study, an attempt has been made to develop a two-pass channel configuration with high thermal hydraulic performance and where rotation can be used in favor of heat transfer on both the leading and trailing walls. The authors of the present study believe that, with the advent of advanced manufacturing technologies, these innovative designs have lot of potential as their implementation in real gas turbine engines has become more realizable and opportunities to optimize cooling designs have become endless.

EXPERIMENTAL SETUP

The experimental setup of transient liquid crystal thermography (TLCT) under rotation is shown by a schematic (Fig. 7.1). In order to match the direction of buoyancy forces similar to gas turbine blades, colder air was chosen for the transient experiments. The air was drawn from the main compressor at around 300 K and 1 MPa. The pressurized air fed the buffer tank. A pressure regulator was provided downstream of the buffer tank in order to control the pressure of buffer tank. The mass flow rate was metered by an orifice plate located about 35 pipe diameter downstream of the flow control valve. The differential pressure at the orifice plate was measured by differential pressure transducer of 70 kPa range.

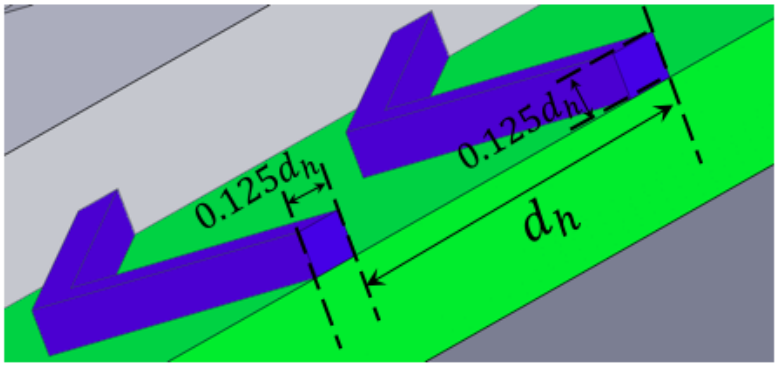

Fig. 7.2 Rib details

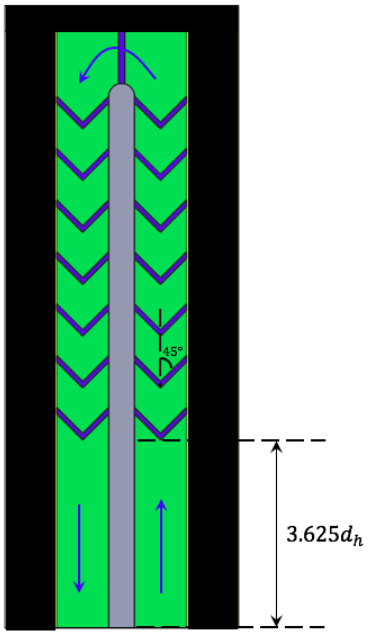

Fig. 7.3 Two-pass channel inlet conditions, rib angle of attack (Model A)

The high pressure at the orifice plate was measured by a pressure transducer of 200 kPa range. Also, the temperature of the air was measured at the orifice plate in order to account for the density change of the air across different experimental runs. The transient experiment in the present study was carried out using air at relatively lower temperature than the initial temperature of the solid featuring heat transfer enhancement features. A cold reservoir was created prior to every transient test in order to achieve reduced air temperatures during the transient test. Fig. 7.1 shows the location of Liquid Nitrogen intake. The solid black line shows the thermal reservoir. A k-type thermocouple was installed to measure the wall temperature near the vent (V1), in order to make sure that nearly similar thermal conditions were maintained across different transient runs in order to keep the Buoyancy number same. A mixture of air and Liquid nitrogen was used to chill the reservoir. Usually it took about 10 minutes to create the desired reservoir. The reservoir was considered to be chilled when the thermocouple reading at the wall near the vent V1 was close to -23°C (250K). Once the reservoir was cooled suitably, the supply of Liquid nitrogen was cut off and the full air flow was allowed to pass through the reservoir and through the vent in order to purge any remnants of nitrogen or moisture in the reservoir line.

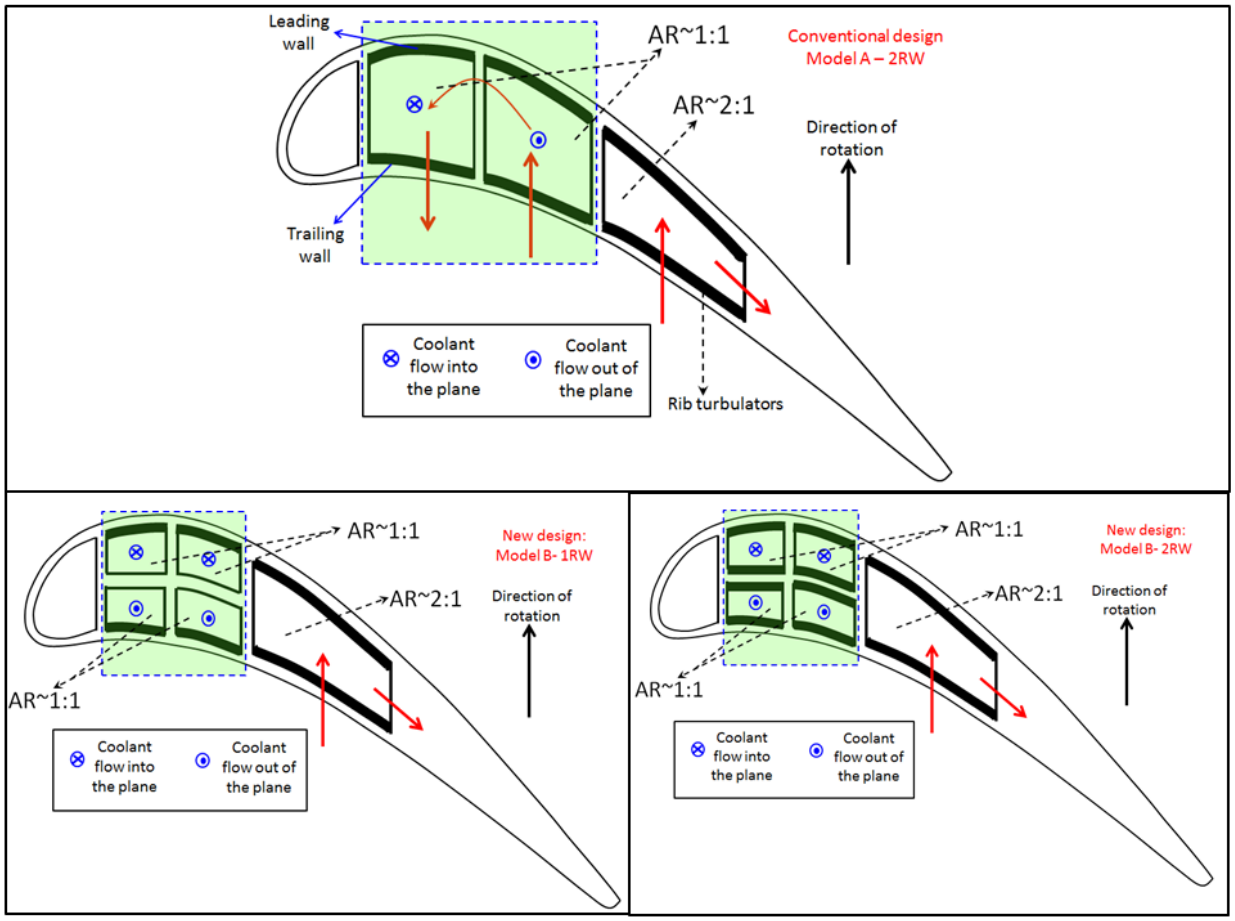

Fig. 7.4 Model orientations with respect to direction of rotation and their locations in mid-chord region in turbine blade

At this stage, the experimental setup was deemed ready for the transient experiment. The air flow was routed to the laboratory ambient and the valves were flipped towards the test section. A LabVIEW code was written to execute the transient experiment through a single-click system. Before the start of the transient test, the test section was set to desired rotational speed. Once the rotation speed was achieved, the single-click system was initiated. Based on one-click, the cold air was allowed to pass through the reservoir and then through the test section via a rotary union. The single-click also started the data acquisition for mainstream and wall temperature measurements.

Also, the Go Pro camera mounted on the test section was started prior to the beginning of the transient test. A light bulb was installed in the test space, which was also controlled via the

single-click system. This light bulb used to turn OFF with the commencement of the transient test. The video recording and temperature data acquisition was synced by the LabVIEW binary command output (0 or 1) based on the solenoid valve condition (1: flow through vent into the atmosphere, 0: flow towards the test section). This system proved to be very reliable in terms of error associated with the start of the transient experiment. Over years of iterations towards improvement of TLC experiments under rotation, our group has currently reached to this stage where consistent transient experiments can be executed with minimal errors from various external factors which have direct effect on heat transfer coefficient.

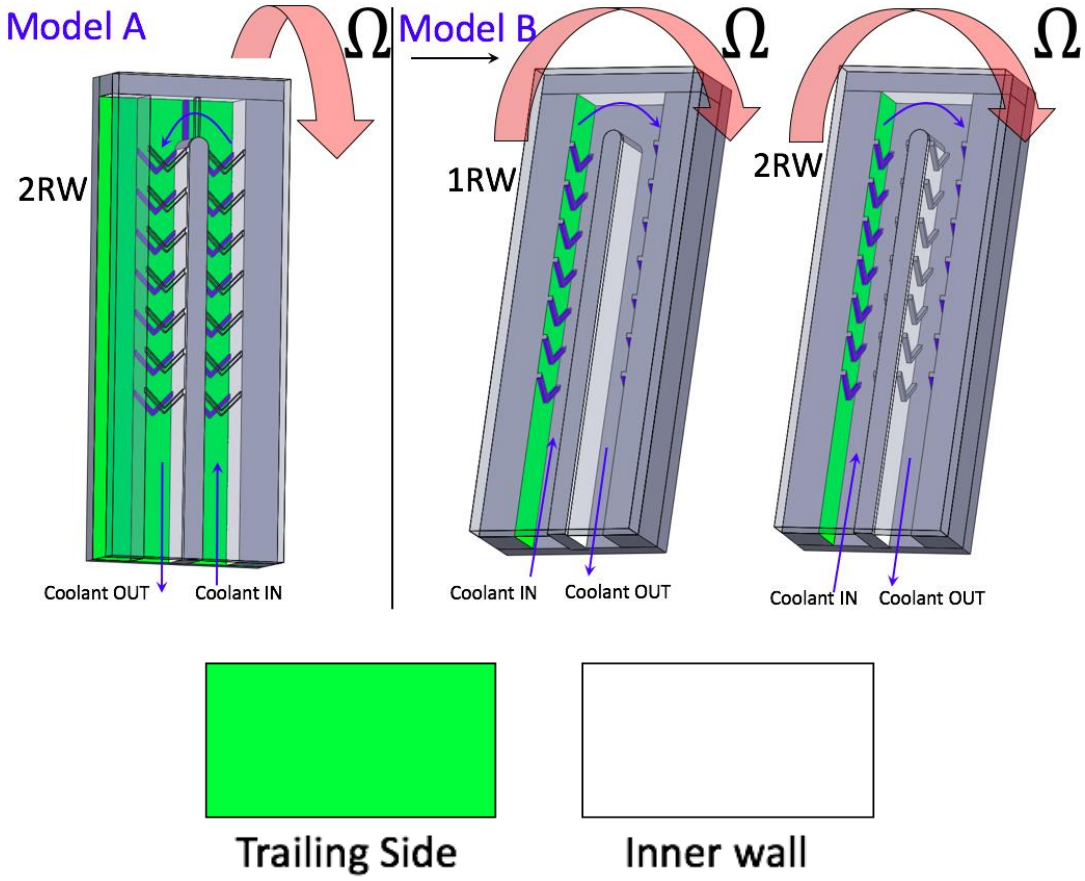

Fig. 7.5 Demonstration of channel orientation with respect to direction of rotation, and rib arrangement

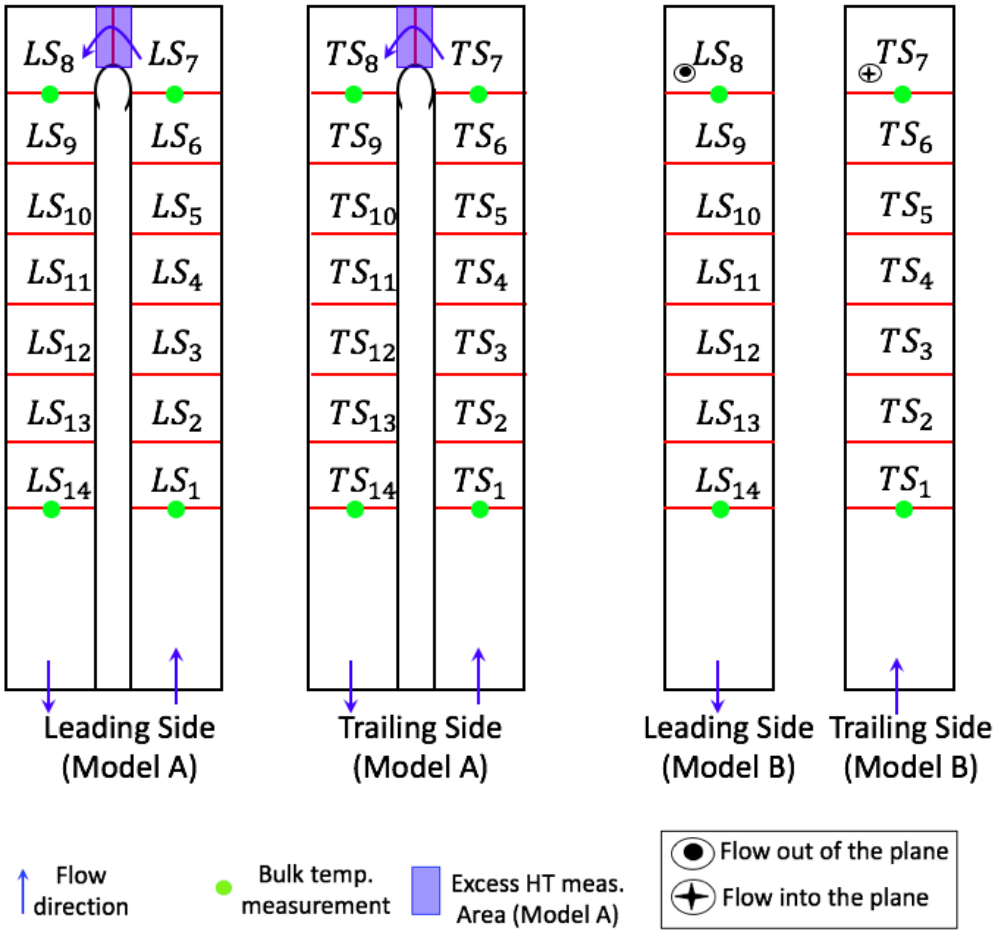

Fig. 7.6 Heat transfer measurement regions, bulk temperature measurement locations

DESCRIPTION OF TEST CONFIGURATIONS

The rib pitch to rib height (p/e) was 8 and rib height to channel hydraulic diameter (e/d_h) was 0.125. The blade tip underside and the divider wall of two-pass channel was connected with a 90° rib $(e/d_h = 0.125)$ for Model A. The details of rib geometry have been shown in Fig. 7.2. The channel inlet conditions have been shown in Fig. 7.3. An entrance length of $3.625d_h$ existed before the start of the rib turbulators. As a result of which, the flow in the first pass wasn't fully developed. Its effect on heat transfer has been discussed in the Results and discussion section.

The configurations in the present study have been divided in two categories – Model A and B. The arrangement of the two configurations in a typical blade has been shown in Fig. 7.4. Here, Model A is the traditional two-pass channel with aspect ratio of unity. Model B was obtained by changing the two-pass channel orientation by 90°.

In Model A, two configurations have been tested – smooth two-pass channel and ribbed two-pass channel (smooth serving as baseline case). The ribbed configuration (ModelA-2RW) has V-shaped rib turbulators on both leading and trailing walls (2RW). Model B had a total of three configurations, viz. smooth, one-ribbed wall (ModelB-1RW) and two-ribbed wall (ModelB-2RW). The ModelB-1RW had ribs only on the leading and trailing walls and but not on the divider wall. The ribbed configurations of Model B did not feature the 90° rib at the bend region. The reason behind the arrangement of 90° rib in the bend region of Model B has been discussed at a later stage in this paper. Fig. 7.5 shows the cooling channel orientation with the direction of rotation for both the Models.

The region numbers have been shown in Fig. 7.6 for all the configurations. Each region has a surface area nearly equal to one rib pitch. As can be seen in Fig. 7.6, the total heat transfer region of Model A was about two times that of Model B. For direct comparisons of heat transfer results obtained for Models A and B, an averaging method has been employed and is discussed later in the Results and discussion section. Also shown in Fig. 7.6 is the excess area of heat transfer in Model A compared to Model B. The location of mainstream temperature measurement has been shown by green dots in Fig. 7.6.

EXPERIMENTAL CONDITIONS

The experiments were carried out at a Reynolds number of 20000 and Rotation numbers of 0, 0.05 and 0.1. The present study primarily aims at exploring the effects of rotation for two different model orientations. The normalized mean rotating radius R_m/d_h was 17. As mentioned earlier, colder air was chosen as the working fluid in order to match the direction of buoyancy forces as they exist in actual blades. However, the temperature difference between coolant and wall was not significant, and hence the effects of buoyancy forces in the present experiments were minimal.

Separate study is recommended to study the effects of buoyancy parameter on the heat transfer. The present study accurately models the Coriolis force and Centrifugal force acting on fluid flowing through the two-pass channel.

DATA REDUCTION PROCEDURE

Detailed measurement of heat transfer coefficient was carried out by transient liquid crystal thermography. A 1-D semi-infinite conduction model has been employed for the calculation of heat transfer coefficient at the boundary with forced convection condition. The evolution of wall temperature exposed to a constant mainstream temperature with a time-independent heat transfer coefficient is given by Eq. 1 [7.17].

$$\frac{T_w(t) - T_i}{T_m - T_i} = 1 - exp\left(\frac{h^2 t}{\rho c k_s}\right) erfc\left(h\sqrt{\frac{t}{\rho c k_s}}\right) \quad (Eq. 7.1)$$

Here, T_m represents the reference mainstream temperature. In the present study, the mainstream temperature was measured at the channel centerline and has been assumed to be the bulk fluid temperature. During the transient experiment, the mainstream temperature was not constant with time. In order to incorporate the time-varying mainstream temperature, Duhamel's superposition principle was employed in Eq. 7.1, where the mainstream temperature was discretized in small time steps. During each time step, the mainstream temperature can be assumed to be constant. The modified equation for wall temperature evolution is given by Eq. 2 [7.18].

Due to heat exchange between the coolant and the wall, the coolant temperature rises as it flows through the two-pass channel. In order to account for the streamwise variation of mainstream temperature, the mainstream temperature was linearly interpolated across the measurement locations.

$$T_w = T_i + \sum_{i=1}^{i=n_{max}} \left(T_{m,i} - T_{m,i-1}\right) \times \left[1 - exp\left(\frac{h^2(t - t_i)}{\rho c k_s}\right) erfc\left(h\sqrt{\frac{t - t_i}{\rho c k_s}}\right)\right] \quad (Eq. 7.2)$$

The mainstream temperature for the bend region was taken to be the average of the temperatures measured at bend inlet and bend outlet. Hence, the interpolation scheme for the 1st pass was from inlet to the averaged value of bend inlet and bend outlet temperatures. For the

second pass, the temperatures were interpolated from the averaged value of bend inlet and bend outlet values and the temperature measured at the channel outlet. The variation of mainstream temperature in the spanwise direction was very minimal and has been neglected in the heat transfer coefficient calculations. The measurement locations of the mainstream temperature in the two-pass channel has been shown in Fig. 7.6. The temperature measurements were carried out by a fast response T-type thermocouple with bead diameter of 0.0762 mm. The transient experiment carried out in the present study has a relatively slower rate of change of mainstream temperature compared to typical mesh heater experiments. The time constant of these thermocouples were very low and were sufficient to capture the rate at which the temperature was changing with time. Figure 7.7 shows the evolution of mainstream temperature with time. At this stage, the unknowns in Eq. 7.2 are $T_w, t \; and \; h$.

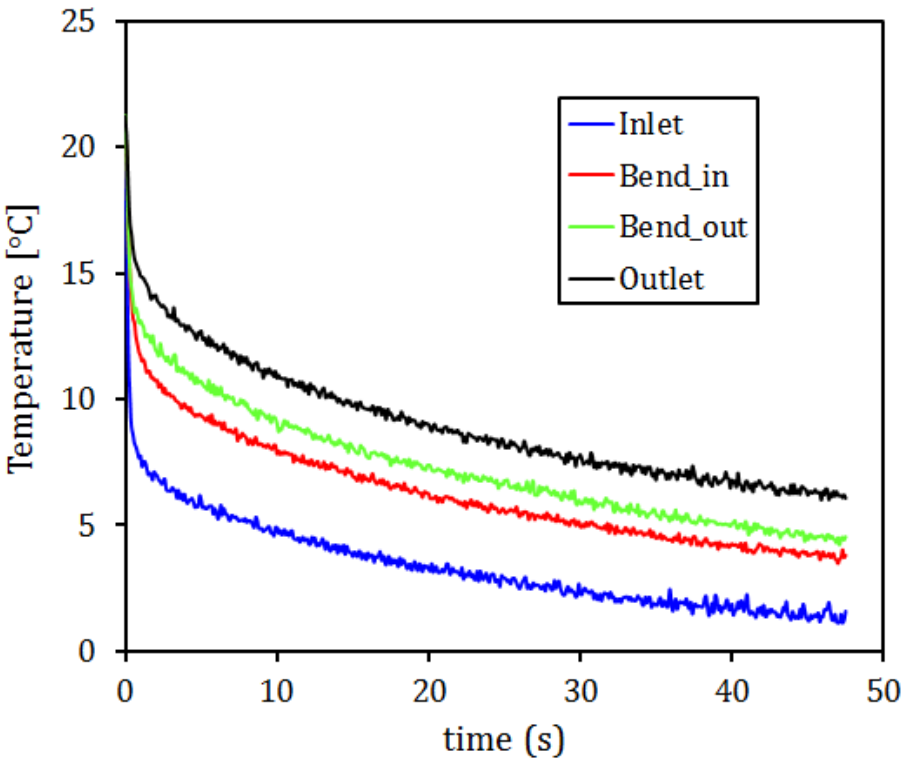

Fig. 7.7 Mainstream temperature evolution with time, measurements carried out at four locations in the two pass channel

Determination of T_w

T_w is the wall temperature which was tracked in order to calculate the heat transfer rate required to reach that particular temperature in a given time. In our calculations, same wall temperature (12.5°C) was tracked for each pixel and for all the experimental conditions. The first step in the determination of T_w is the calibration of liquid crystal color change with wall temperature measured by a thermocouple.

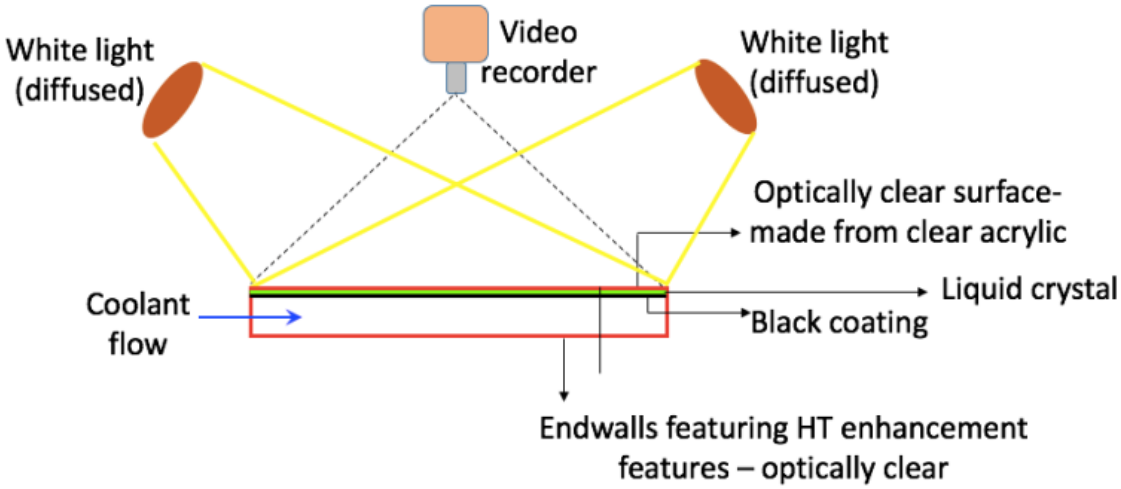

Fig. 7.8 Camera orientation, lighting conditions, liquid crystal and black coating locations

The liquid crystal used in the present study had a color play between 10°C to 15°C. The arrangement of camera and lighting conditions, in reference to coolant flow and the wall where heat transfer coefficient was measured has been shown in Fig. 7.8. A Hue based calibration technique was used in order to relate the LC color change with measured wall temperature. Two T-type thermocouples were used in order to calibrate the LC in the first pass and second pass. Although the Hue-based technique has been proven to be very robust with lighting conditions, camera inclination angles [7.**19**], it was still made sure that the calibration curves of the LC color change were very similar to each other. A sample calibration curve has been shown in Fig. 7.**9**. The aim of calibration of LC color change is to establish a relationship between wall temperature and Hue. Also, the calibration was carried out in-situ under both rotating and non-rotating

conditions to make sure that there were minimal effects of changes in lighting conditions, LC degradation in different runs on heat transfer coefficient determination.

In the close vicinity of the thermocouple, a 5 x 5 pixel region was chosen to be the 'calibration region'. Two such calibration regions were considered – (a) located $2d_h$ downstream of the inlet, (b) $2d_h$ upstream of the outlet. The Hue was calculated at each of the 25 pixels and averaged to one value. This averaged value of Hue has been obtained for each frame of the video which was recorded at 30 frames per second. In order to make sure that the lighting conditions were diffused and uniform across the region of interest, a minimum threshold of 0.3 for saturation and intensity was applied to each pixel, for that pixel to qualify for heat transfer data reduction procedure.

Once the relationship between Hue and measured wall temperature was established, each pixel was traversed frame by frame in order to check for the reference Hue value (corresponding to a particular wall temperature), saturation and intensity values. For each pixel and for each frame, saturation and intensity values were also calculated along with Hue. The frame at which all the criterions on Hue, saturation and intensity were satisfied, that particular frame number was stored in a frame matrix, which was eventually converted to time matrix since the frame capture rate was known. At this stage, the only unknown in Eq. 7.2 is the heat transfer coefficient.

The heat transfer coefficient was then determined by an error minimization routine (secant method). The Nusselt number is given by Eq. 7.3.

$$Nu = \frac{hd_h}{k_f} \quad (Eq. 7.3)$$

The thermal conductivity for air was obtained at the film temperature.

UNCERTAINTY ANALYSIS

The uncertainty in the measurement of Nusselt number and Reynolds number has been carried out using sequential perturbation method described by Moffat [7.20]. The factors contributing to uncertainty in Nusselt number are $T_w, T_i, T_m, t, \sqrt{\rho c k_s}$. The contribution of temperature measurements was taken to be 0.5°C. The contribution of time (t) was taken to be

0.033 seconds. The uncertainty for a typical Nusselt number of 100 was found to be to around 12%. The uncertainty in the measurement of Reynolds number was about 2.85%.

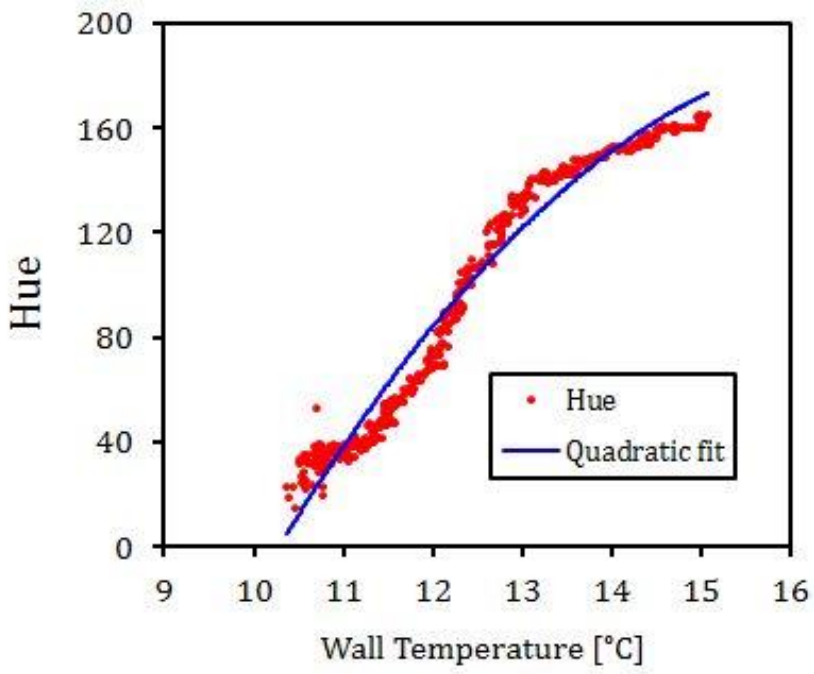

Fig. 7.9 Calibration of wall temperature with Hue [LC part # R10C5W]

RESULTS AND DISCUSSION

Experimental results on above mentioned configurations and conditions have been reported and analyzed in this section. Detailed Nusselt number enhancement contours have been presented for one representative Rotation number of 0.1 and a Reynolds number of 20000. The detailed heat transfer contours are followed by regionally averaged Nusselt number enhancement which provides further insight into heat transfer behavior at a broader scale.

Detailed Nusselt number enhancement (Nu/Nu_0) contours: Model A

Figure 7.10 shows the detailed measurements of Nusselt number enhancement in the two-pass channel for the Model A smooth configuration. The analysis of heat transfer in a smooth two-pass channel is very important in the development of cooling concepts involving turbulence promotors. The direction of the bulk flow of coolant is shown by red arrows at the bottom of the contour. For the stationary case (Ro = 0), the flow in the first pass was developing in nature and

it can be seen that the heat transfer was fairly uniform in the spanwise direction with a decreasing trend in the streamwise direction. The heat transfer near the sidewalls was lower than that of the channel centerline because of the boundary layer growth along the sidewalls. As the flow approached the 180° turn, a part of it impinged on the blade tip underside corresponding to the first pass due to the inertia effect. While the flow made the 180° turn, a part of it impinged on the outer sidewall of the second pass and traveled along the same wall while moving downstream in the second pass- this phenomena resulted in higher heat transfer in the above mentioned regions. In the discussion, outer sidewall is referred to the sidewall to the right when looking in the direction of bulk coolant flow.

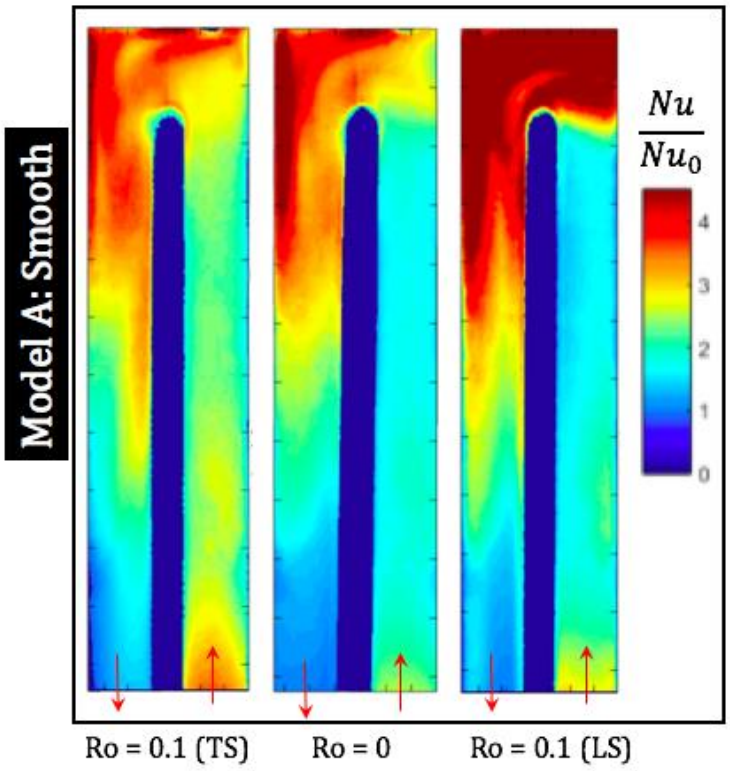

Fig. 7.10 Detailed map of normalized Nusselt number (Nu/Nu_0), Model A- Smooth configuration

From an earlier numerical study carried out by this group [7.21] on a similar two-pass channel, it was found that upstream of the bend region, there was a strong motion of fluid from the outer wall to the inner wall. In the bend region, Dean type vortices were formed due to a combination of centrifugal force and curvature induced pressure gradient. The Dean type vortices have direct effect on heat transfer as it transports fluid near the blade tip underside to the core, hence improving mixing – one method of enhancing net heat exchange.

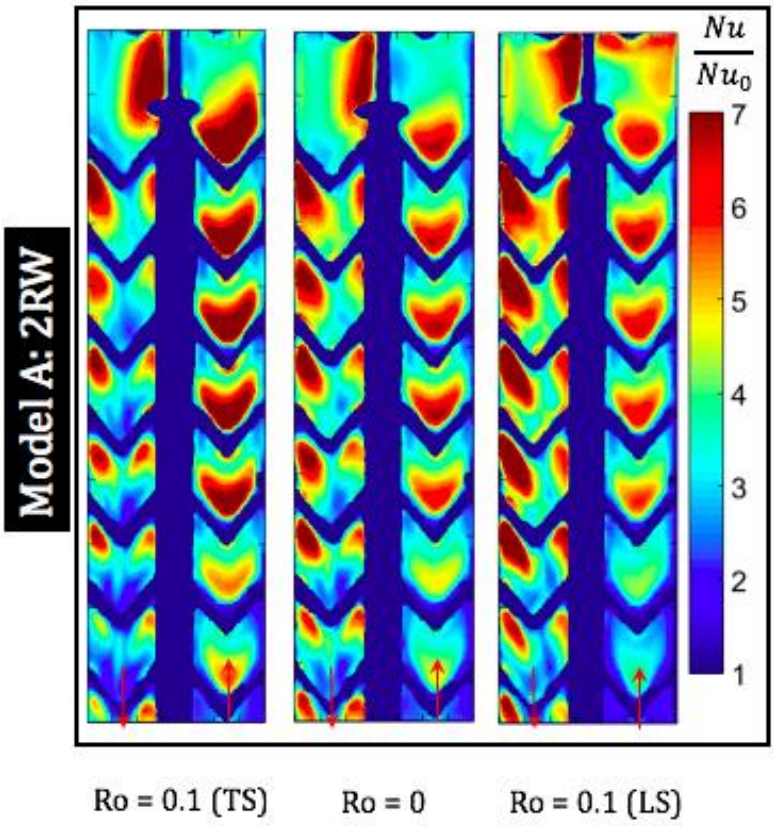

Fig. 7.11 Detailed map of normalized Nusselt number (Nu/Nu_0), Model A- 2RW

As the flow progressed in the second pass, the heat transfer decreased in the streamwise direction, with higher heat transfer towards the outer sidewall due to higher momentum flux along that wall. The contours for the leading and trailing sides show that the heat transfer in the first pass (radially outward) was higher for trailing side and lower for the leading side (radially inward). In the second pass, higher heat transfer was observed on the leading wall and lower heat transfer was observed on the trailing wall. The effect of the Coriolis force was apparent in both

the passes and is consistent with many other similar findings in the past. However, the effects of rotation on heat transfer behavior in the bend region is not trivial to understand from just the heat transfer measurements alone. A more detailed and high fidelity numerical simulation and/or PIV experiments are required in order better understand the complex fluid dynamics in the bend region under rotating conditions. For detailed discussion on bend fluid dynamics, the reader is referred to some of the best numerical work carried out on this problem for more understanding on bend fluid dynamics [7.22-7.26].

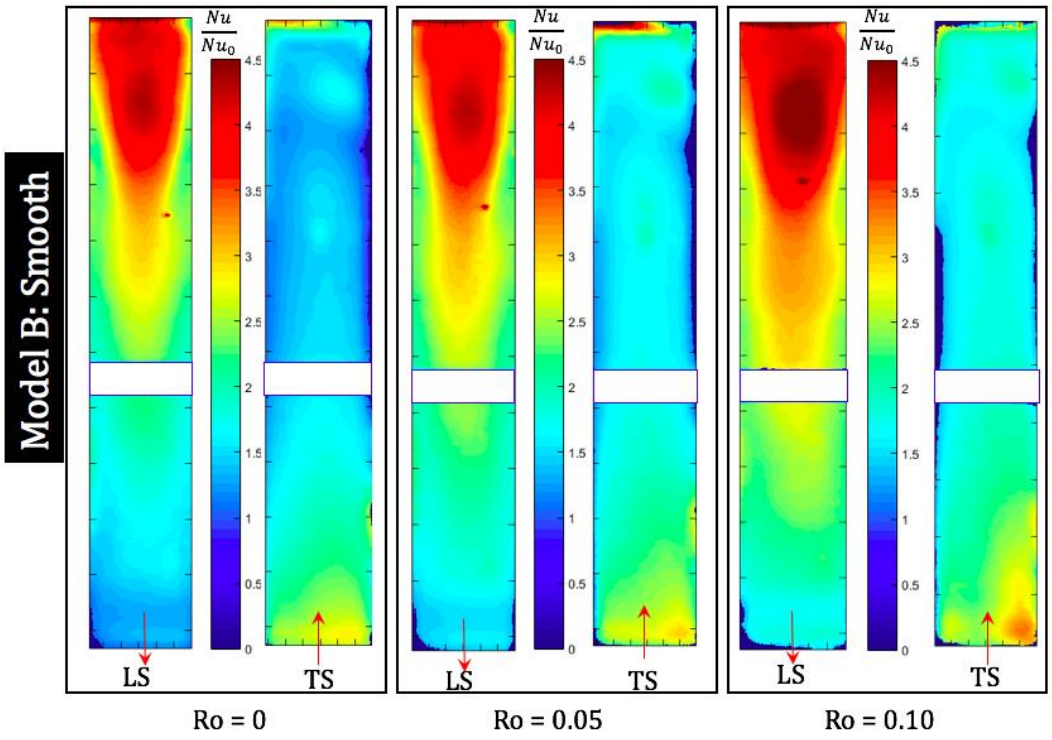

Fig. 7.12 Detailed map of normalized Nusselt number (Nu/Nu_0), Model B- Smooth [White stripe : NO data]

Figure 7.11 shows the detailed map of normalized Nusselt number at Re 20000 at stationary and rotating condition (Ro = 0.1) for Model A - 2RW configuration. As the flow enters the 1st pass, it interacts with the V-shaped rib turbulators. The mechanism of heat transfer enhancement by V-shaped rib turbulators is through increase in near-wall shear due to rib induced secondary flow interaction with bottom wall, increase in turbulent mixing due to interaction between rib induced secondary flows (travelling at an angle) with the side walls. The V-shaped rib can also be viewed as two 45° ribs joined together at the channel centerline. When the bulk fluid passed over the

turbulators, secondary flows were induced at an angle of about 45° starting at the channel centerline. Also, just downstream of the rib, a recirculation zone was present which led to low heat transfer region. The contour shows the high heat transfer regimes in the shape of the V rib. This shape of high heat transfer regime has been found in several earlier investigations on similar V-shaped ribs [7.21, 7.27-7.31]. It has also been found that heat transfer increased as the flow progressed in the first pass due to increase in turbulent mixing due to interaction of rib-induced secondary flows and channel sidewalls. At the end of the first pass, the impingement effect on blade tip underside wasn't observed as it was found in the smooth channel.

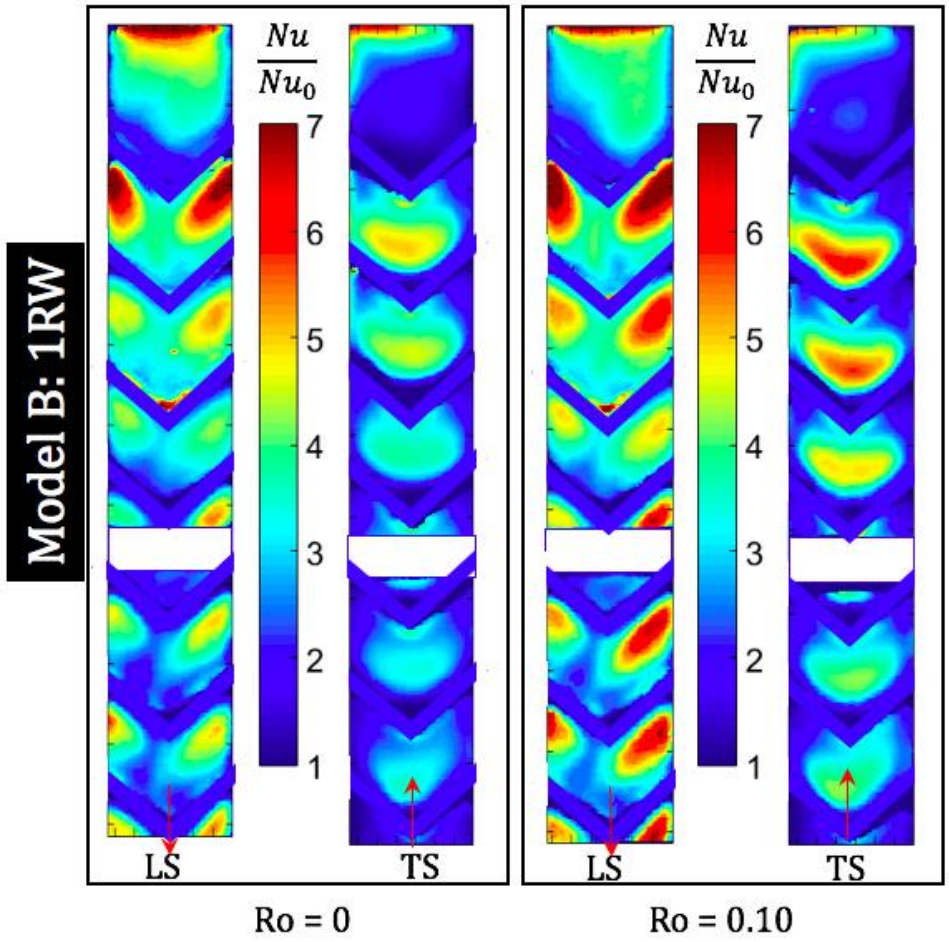

Fig. 7.13 Detailed map of normalized Nusselt number (Nu/Nu_0), Model B - 1RW [White stripe : NO data]

This was because of the effect of upstream rib and the presence of 90° rib at the bend region. The 90° rib was provided in Model A configuration to establish a baseline case which is typical of

many other studies on two-pass rib turbulators. The rib at the bend further trips the turning flow and enhances heat transfer just downstream of that rib. As the flow entered the second pass, the orientation of the rib turbulator with respect to the bulk flow changed. The rib induced secondary flow now originated at the corner where the rib and the side wall was connected. Since, the momentum flux was higher towards the outer sidewall due to flow turning by 180°, the high heat transfer region due to rib turbulators was towards the outer sidewall. Here inner sidewall refer the wall defined by the divider of the two-pass channel. The turbulent mixing phenomena in the second pass is different when compared to that in the first pass due to different orientation with rib and bulk flow. The mixing in the second pass would be weaker since the rib-induced secondary flows were guided towards the channel centerline, and this would be carried away by the bulk flow. This phenomenon can be seen more clearly in the downstream ribs in the second pass where a high heat transfer streak could be seen at the centerline of the rib. This change in the nature of turbulent mixing caused by rib induced secondary flows in the second pass led to decreasing trend in heat transfer as the bulk fluid moved towards the exit.

Detailed Nusselt number enhancement (Nu/Nu_0) contours: Model B

Figure 7.12 shows the detailed Nusselt number enhancement contour for Smooth two-pass channel with Model B orientation. The orientation of coolant with the axis of rotation is different from Model B and is explained in Figs. 7.4 and 7.5. The flow in the first pass of Model B is similar to Model A, except the bend region. Also, the coolant while making a 180° turn, impinges on the second pass wall and then travels along the second pass outer wall as it exits the two-pass channel. The concept behind such a design is that the Coriolis force will act in directions, which will lead to enhanced heat transfer on both trailing wall (radially outward flow) and leading wall (radially inward flow). Also, note that the total heat transfer measurement area for Model B is approximately half of that of the Model A (Fig. 7.6). Further details about total heat transfer area will be provided in a later section. The contour shown in Fig. 7.12 includes all the rotation numbers studied. For the stationary case, the flow in the first pass was developing in nature and hence a decreasing trend in heat transfer was observed. As the coolant approached the bend region, the flow started to separate from the trailing side wall while making the 180° turn. This led to lower heat transfer in the end region of the first pass (trailing side). However, the coolant showed an impingement effect at the beginning of the second pass, resulting in relatively

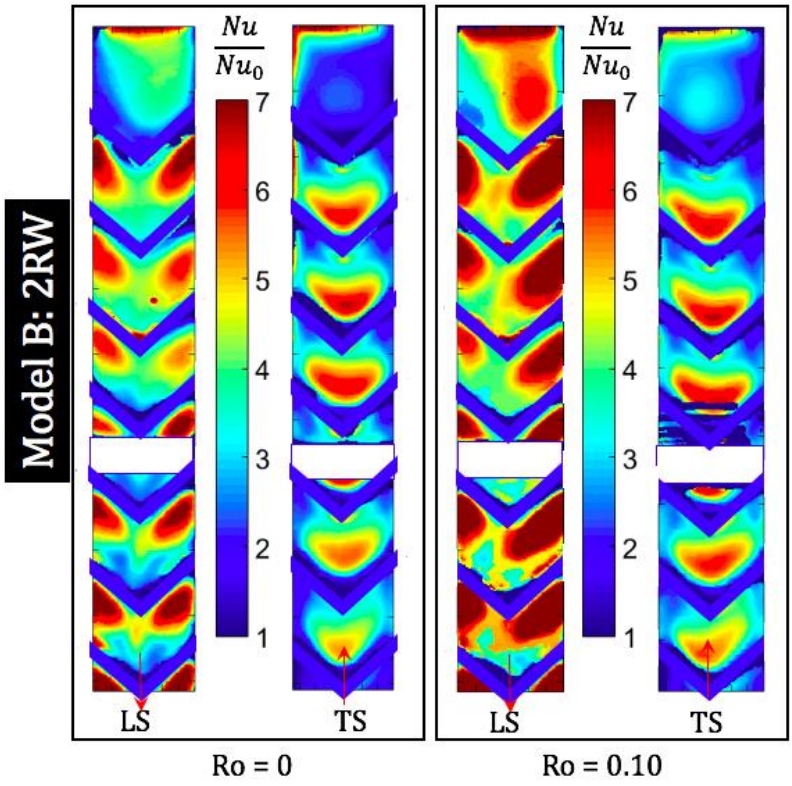

Fig. 7.14 Detailed map of normalized Nusselt number (Nu/Nu_0), Model B - 2RW [White stripe : NO data]

higher heat transfer on the leading wall. The high heat transfer was also due to the bend induced secondary flows. As the flow moved towards the exit of the two-pass channel, the bend induced secondary flows and the impingement effect diminished, which resulted in decreasing trend in heat transfer. The positive effects of rotation on both leading and trailing walls can be seen for Model B smooth configuration. The first pass of model B (trailing side) had radially outward flow, hence the Coriolis force led to thinner thermal boundary layer on the outer wall (trailing side). Note that the heat transfer measurements on the smooth side (inner wall) was not carried out in the present study, as those measurements are not helpful in the design of cooling features since they are not subjected to direct heat loads from the hot gas path. Similarly, the flow in the second pass (leading side) was radially inward and the Coriolis force led to thinner thermal boundary layer on the outer wall. Model B configuration is just a slight adjustment of Model A and low and high heat transfer surfaces still exist in Model B, the only difference being the low

heat transfer surfaces are moved inwards and are not affected by direct heat loads. The strength of Coriolis force increases as the rotation number increases and this effect can be seen by increasing heat transfer trends in the second pass. The smooth channel results for the Model B provided much needed confidence in the new design as all the design intents were needed to be fulfilled for the baseline case, and only then the complex turbulated passages could have been designed from the knowledge database developed thus far.

As mentioned earlier, two configurations of ribbed channels were investigated for the Model B configuration. The configurations were named as – Model B - 1RW and Model B - 2RW. Model B - 1RW is referred to the ribbed two-pass channel with only one wall ribbed and the inner wall was kept smooth (Fig. 7.5). The configuration named Model B 2RW had ribs on both the outer wall and the divider wall (Fig. 7.5). Both the configurations in Model B didn't feature the 90° rib in the bend region, which was present in Model A 2RW configuration. The reason for such a choice in the design of the bend region was the observed direct impingement effect of the coolant in the second pass of Model B smooth channel. Presence of a 90° rib at the blade tip underside would have tripped the bulk of coolant and reduced the impingement effect on the leading wall. However, the presence of a rib at the blade tip underside would have resulted in enhanced heat transfer at the blade tip underside, but present study is not focused on heat transfer enhancement in that region. Blade tip underside heat transfer has been investigated by Ledezema and Bunker [7.32] and the authors have proposed designs where the bend could accommodate micro pin fins for a Model A type configuration. Such design could also be implemented in the present study's Model B configuration.

Figure 7.13 shows the detailed Nusselt number enhancement (Nu/Nu_0) contour for Model B - 1RW configuration. The heat transfer pattern in the first pass was similar to Model A – 2RW configuration with reduced levels of Nusselt number enhancement due to absence of ribs on the inner walls of the channel (Fig. 7.5). This led to reduced turbulent mixing as the flow progressed through the first pass. However, the nature of heat transfer enhancement due to rib induced secondary flows remained the same. As observed for the smooth configuration of Model B, the heat transfer towards the bend region was lower as the coolant separated from the outer wall (corresponding to 1st pass) due to skewed momentum flux towards the divider wall because of the presence of 180° bend. Post the 180° turn, the coolant impinged on the second pass outer

wall and resulted in enhanced heat transfer. In the second pass, the highest heat transfer was observed at the first rib pitch because of the combined effects of bend induced secondary flows and rib induced secondary flows. Due to the absence of ribs on the divider wall and the difference in the nature of the rib and coolant orientation, the turbulent mixing also weakened as the flow exits the second pass. This configuration was studied as it contains heat transfer enhancement features on the walls which are exposed to hot main gases. The inner wall, however, is protected from direct effects of hot main gases and hence didn't feature rib turbulators. The concept behind such design was to reduce the pressure drop penalty and potentially increase the thermal-hydraulic performance. More discussion has been provided on this in later section where regionally averaged and globally averaged heat transfer enhancement data have been compared.

Figure 7.14 shows the detailed Nusselt number enhancement for Model B - 2RW configuration. This configuration had two ribbed walls and the bend didn't feature any rib turbulator (Fig. 7.5). The first pass of this configuration witnessed similar heat transfer trends as that of Model A - 2RW. The increasing strength of turbulent mixing combined with enhanced near wall shear due to rib induced secondary flow resulted in overall increasing heat transfer trend and higher heat transfer was observed when compared with Model B – 1RW configuration. The heat transfer trend near the bend region was similar to that observed in Model B 1RW and witnessed lower heat transfer as the flow started making the 180° turn. The real benefit of this configuration was found in the second pass (leading side: radially inward flow) where heat transfer trend was decreasing and then increasing with overall levels higher than any other configuration for the second pass in the present study.

Regionally averaged Nusselt number enhancement: Model A and Model B

Figure 7.15 shows the variation of normalized Nusselt number (Nu/Nu_0) with increasing streamwise locations for the smooth configuration (Model A). The region numbers have been identified as the area of the bottom wall between two consecutive ribs. Region 1 to 6 indicates the rib pitches in the first pass, and regions 9 through 14 represent the second pass. The bend regions 7 and 8 have been excluded in the plots of current sub-section and will be analyzed separately as the definition of bend for Model A and B are different due to asymmetrical nature of coolant flow in two model orientations. Refer Fig. 7.6 for region nomenclature.

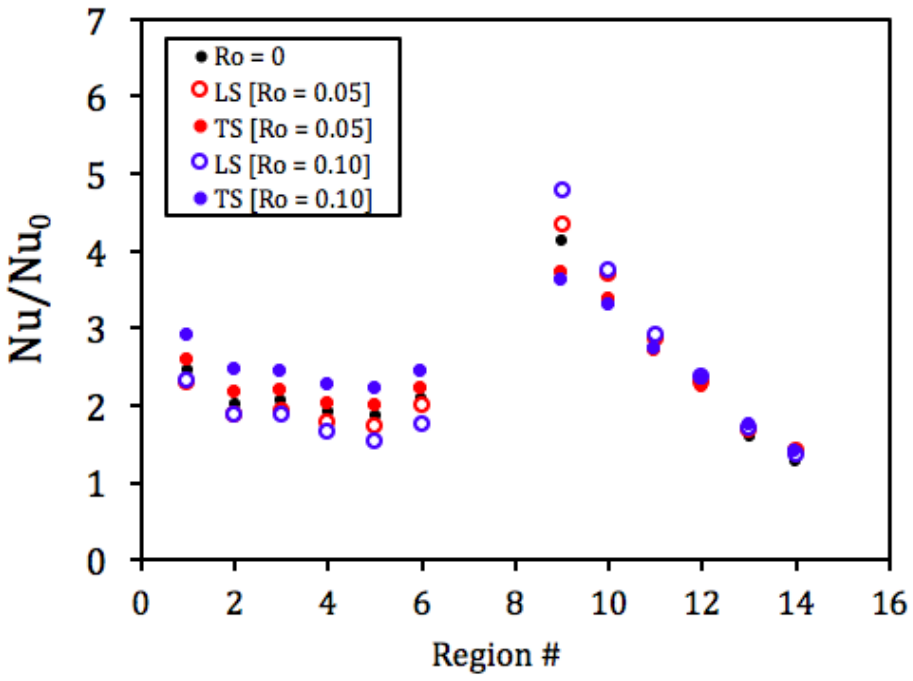

Fig. 7.15 Regionally averaged normalized Nusselt number variation with increasing streamwise distance from inlet [Model A - Smooth]

The flow in the first pass was developing in nature and hence led to higher heat transfer, which decreased with increasing streamwise distance. From the smooth channel results (Fig. 7.15), it can be seen that the Nusselt number for the stationary condition at region 1 (first rib pitch) was about 100% higher than the Nusselt number obtained from the Dittus-Boelter correlation for developed turbulent flow in a circular duct. Since the channel length was not long enough to allow the complete development of flow, the Nusselt number enhancement in the first pass could only reach to a lowest value of about 1.8. The precursor effects of bend was found in the upstream region of bend as the (Nu/Nu_0) trend started to flatten out, a trend which was expected to decrease as the flow becomes more developed with increasing streamwise distance. The effects of rotation on heat transfer on leading and trailing walls can be clearly seen in the first pass. The Coriolis force acting on the radially outward flow in the first pass resulted in higher heat transfer on the trailing side and lower heat transfer on the leading side. This trend in heat transfer has been observed by many other prior studies [e.g. 7.3-7.5, 7.9, 7.33, 7.34]. The coolant flowing radially outward has higher momentum flux towards the trailing walls and lower towards the leading walls [7.35]. The fluid dynamics in the bend region, however, is more

complicated in the first pass, even for a smooth channel. For the stationary condition, the bend region had higher heat transfer compared to the upstream regions in the first pass. This trend in heat transfer was sustained for first three rib pitches in the second pass (regions 9, 10 and 11). The Coriolis force acting on a fluid flowing radially inwards, helped enhance the heat transfer on the leading wall and reduced the heat transfer on the trailing wall. However, for the smooth channel, the rotation effects were found to diminish for low values of local normalized rotating radius R_x/d_h (in the second pass).

Figure 7.16 shows the variation of normalized Nusselt number with increasing streamwise distance for the ribbed configuration of Model A – 2RW. Compared to the smooth case of Model A, the ribbed case had higher heat transfer due to rib induced secondary flows, enhanced turbulent mixing etc.

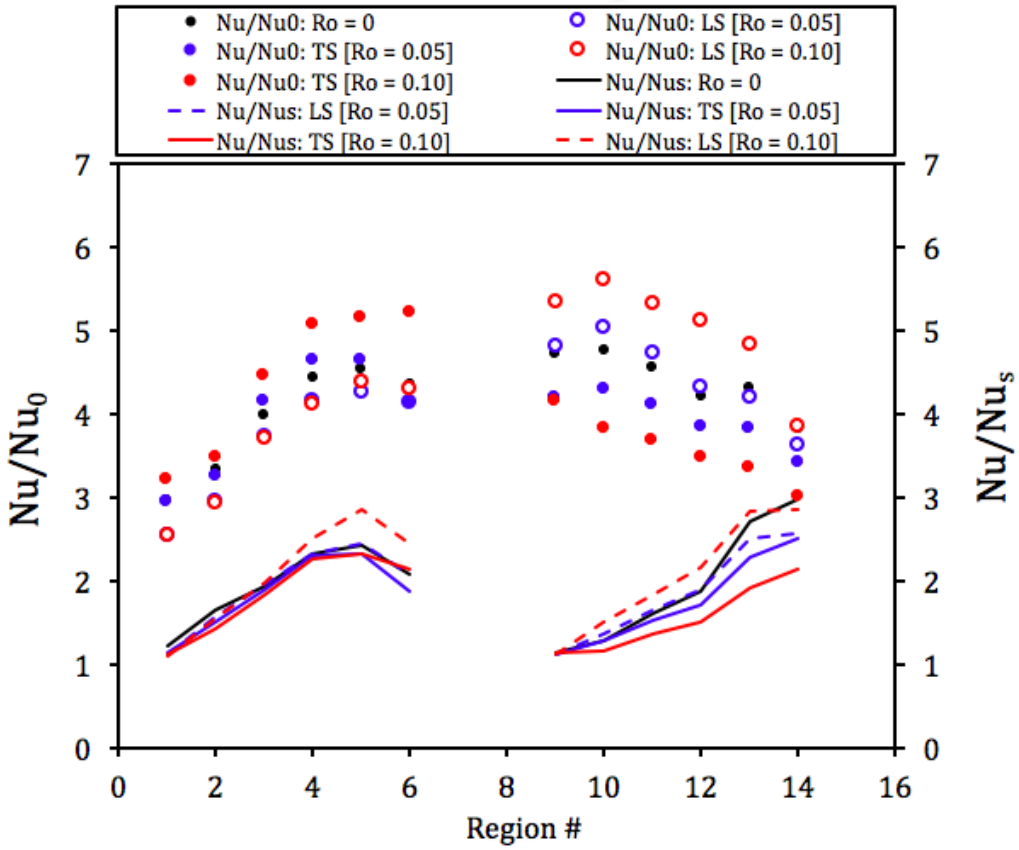

Fig. 7.16 Regionally averaged normalized Nusselt number (Nu/Nu_0 and Nu/Nu_s) variation with increasing streamwise distance from inlet [Model A - 2RW]

An increasing trend in heat transfer has been observed in the first pass due to increase in strength of turbulent mixing as the flow moves in the first pass. The Coriolis force led to enhancement in heat transfer on trailing walls (radially outward) and leading walls (radially inward) and reduction in heat transfer on leading walls (radially outward) and trailing walls (radially inward). This trend is consistent with the findings of many other similar studies [7.3-7.7, 7.10-7.14]. Also, shown is the enhancement in heat transfer compared to corresponding regions of smooth channel of Model A. The ribs were not very effective in the beginning of the first pass and second pass and the heat transfer was found to increase with increasing streamwise distance in both first and second pass. An interesting trend was observed for the heat transfer under rotating conditions. When compared to smooth channel, leading side heat transfer enhancement was higher compared to trailing side for radially inward flow (2^{nd} pass), however, for the radially outward flow (1^{st} pass), the heat transfer enhancement gain was similar for both leading and trailing sides, with leading side on the higher end. Comparison of heat transfer enhancement with respect to geometrically similar smooth channel provides realistic evaluation of heat transfer performance of cooling technologies.

Figure 7.17 shows the comparison of normalized Nusselt number (Nu/Nu_s) with the results of Dutta and Han [7.7]. The streamwise distance has been adjusted according to the present study configurations. The reason why (Nu/Nu_s) ratio has been compared is because the inlet conditions (development length etc.) were different in both studies. Normalized Nusselt numbers with similar smooth channel can be compared across different studies [7.21, 7.30, 7.31]. There were several differences with the present study and that of Dutta and Han [7]. Dutta and Han studied 60° broken V shaped ribs, whereas in the present study, the rib turbulators were continuous V. Earlier studies by Han and Zhang [7.36] has shown that broken V shaped ribs have higher heat transfer compared to continuous V shaped ribs. This is one reason why the stationary case Nusselt number ratio was slightly higher for Dutta and Han [7.7] compared to the present study. The other factor is the difference in Reynolds number. It has been seen in most of the studies focused on heat transfer enhancement features, that the Nusselt number ratio decreases with increasing Reynolds number. Taking into account these factors, the agreement between the two experimental studies is very satisfactory.

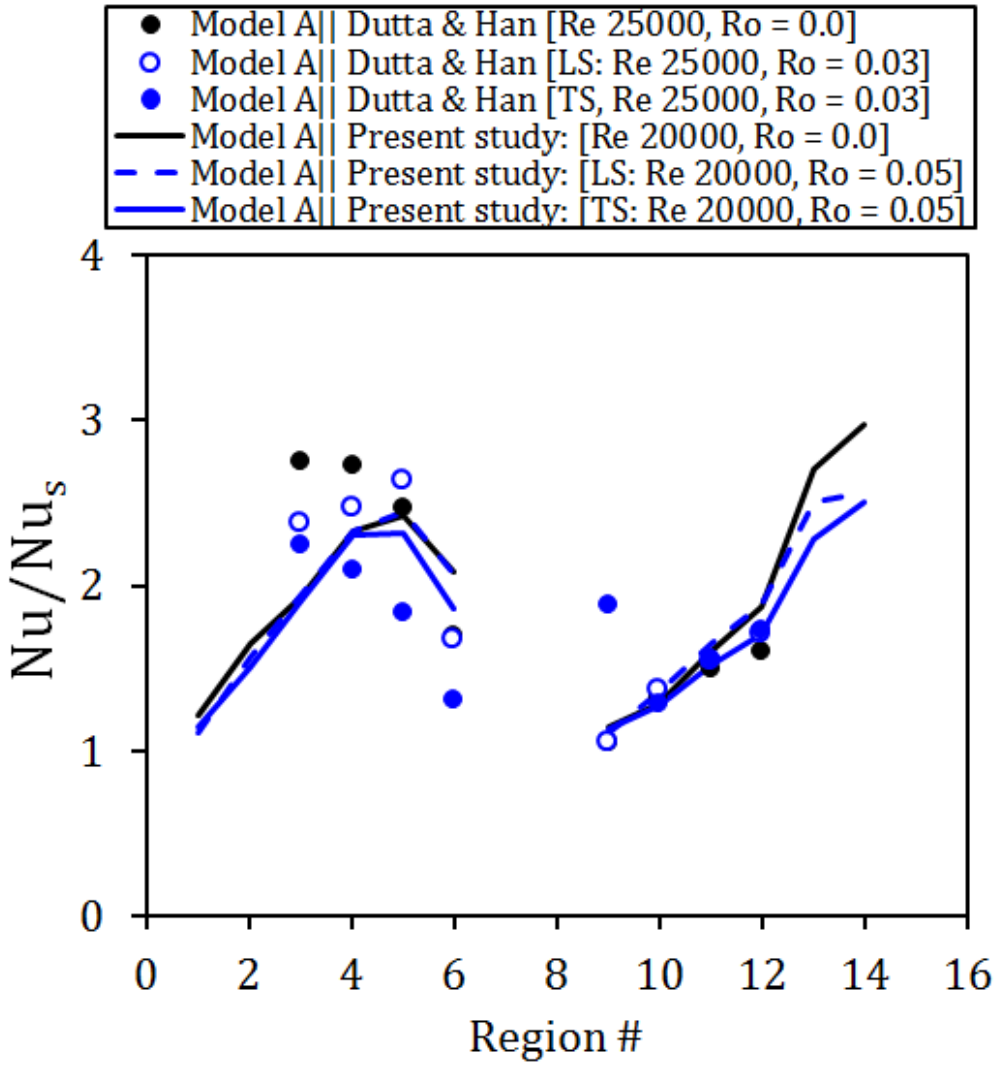

Fig. 7.17 Regionally averaged normalized Nusselt number (Nu/Nu_s) with corresponding smooth channel configuration

For the Model B smooth channel configuration, the heat transfer regions were different when compared to Model A. These differences have been identified in Fig. 7.6. The heat transfer enhancement (normalized with D-B) has been shown in Fig. 7.18. The decreasing trend of heat transfer in both first and second pass was similar to Model A because of flow development in 1st pass and reduction of the strength of bend induced secondary flows (2nd pass).

Also shown is the heat transfer enhancement of Model A smooth channel since the heat transfer of leading and trailing walls of smooth channel under stationary conditions were very similar, as expected. In the first pass, Model A and B heat transfer were similar, however, as the

flow approached the bend region, Model A had higher enhancement in heat transfer compared to Model B. The reason behind this trend has been discussed in detail in a previous section. For the stationary case, the rate of decrease of heat transfer enhancement was higher for Model A compared to Model B. The effects of rotation on heat transfer characteristics of Model B smooth channel was different compared to Model A. The design intent of Model B was to have positive effects of rotation on both leading and trailing walls. It can be seen that Coriolis force led to higher heat transfer enhancement on both trailing (radially outward) and leading (radially inward) walls. The enhancement factor increased with increase in rotation number as expected, since the effect of Coriolis force also increased with increase in rotation speed.

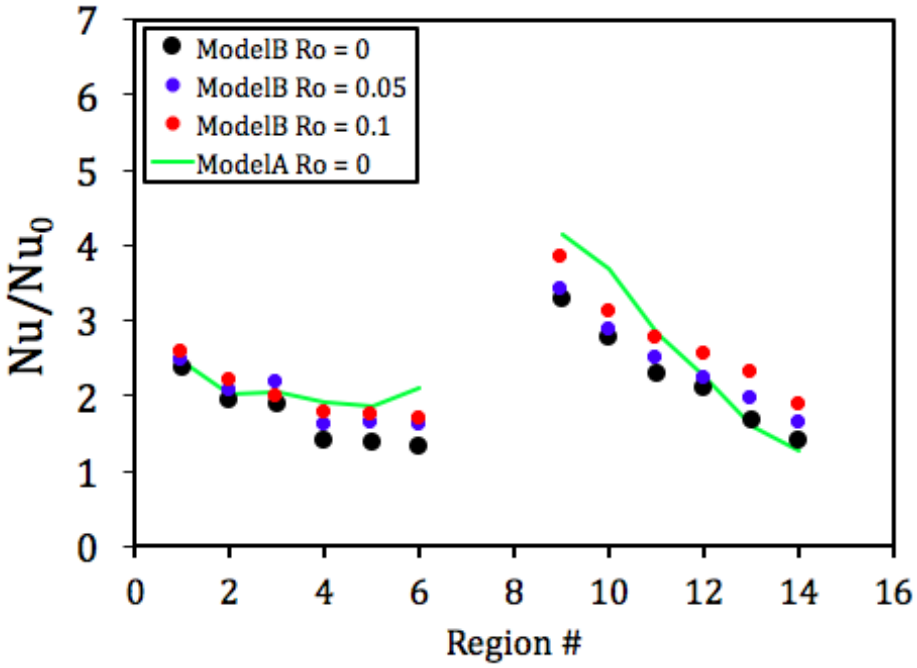

Fig. 7.18 Regionally averaged normalized Nusselt number (Nu/Nu_0) variation with increasing streamwise distance from inlet [Model B - Smooth]

The second configuration in Model B category was single ribbed wall configuration (1RW). The heat transfer enhancement for Model B - 1RW has been shown in Fig. 7.19. The trends of heat transfer enhancement for radially outward flow was similar to Model A - 2RW configuration and was monotonically increasing till region 5.

Due to different nature of bend flow, there was a deviation of heat transfer enhancement trend in Model A and B. A decrease in heat transfer was observed in region 6 due to presence of bend downstream. Further, in second pass, a combined impingement and rib induced secondary flow effect was observed which led to high heat transfer in region 9. The heat transfer enhancement then decreased till region 11 and then again increased till the end of the two-pass channel. Compared to the smooth configuration of Model B, the effects of rotation on heat transfer enhancement was more apparent for the Model B - 1RW configuration. An increase in heat transfer was observed for both leading and trailing walls, with higher heat transfer enhancement at higher rotation numbers.

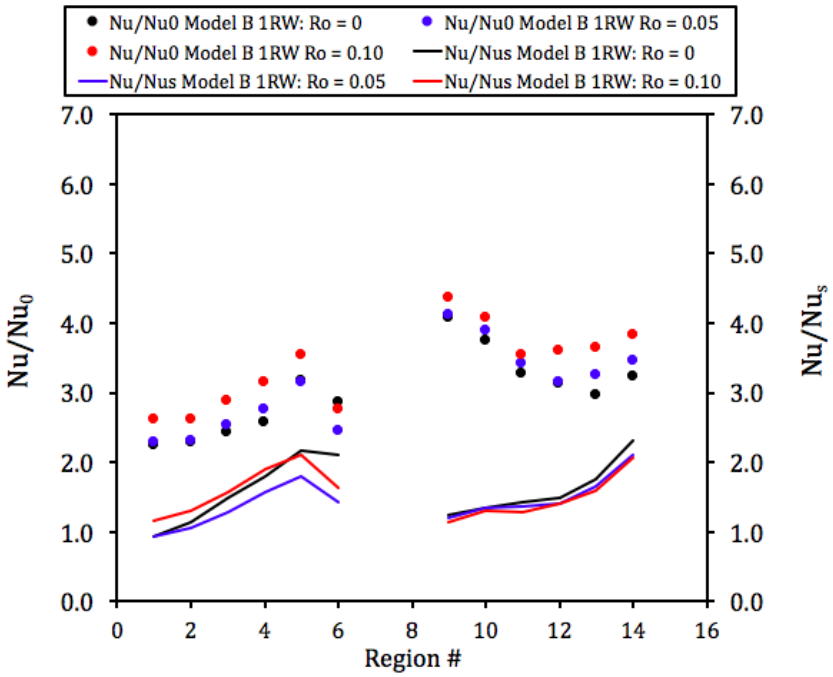

Fig. 7.19 Regionally averaged normalized Nusselt number (Nu/Nu_0 *and* Nu/Nu_s) variation with increasing streamwise distance from inlet [Model B 1RW]

This configuration was promising since there are fewer ribs compared to 2RW configurations of Models A and B. However, 1RW configuration heat transfer was lower compared to 2RW configurations due to reduced turbulent mixing. Also shown in Fig. 7.19 is the enhancement in heat transfer compared to corresponding regions in smooth configuration of Model B. The ribs were ineffective at regions 1 and 9, and heat transfer enhancement was about 100% more than

the smooth channel towards the end of first pass and second pass. This trend was similar to Model A - 2RW configuration. Compared to the leading side of Model B - 1RW, trailing side showed increased effects of rotation, however, the heat transfer enhancement due to rib turbulator alone was higher for stationary case in comparison to rotation cases.

The last configuration in Model B category was double sided ribbed wall (Model B - 2RW). The heat transfer enhancement for different regions has been shown in Fig. 7.20. The trends for both Nu/Nu_0 and Nu/Nu_s were similar to Model B - 1RW, with elevated levels due to increase in turbulent mixing because of the presence of ribs on both opposite walls (outer and inner, Fig. 7.5). This configuration was very effective in terms of heat transfer enhancement, particularly in the second pass. Rotation had positive effects on heat transfer in both passes, which was the design intent.

The heat transfer in the bend region has been shown in Fig. 7.21. For Model A, the heat transfer regions have been shown in Fig. 7.6. For direct comparison of Models A and B, the model A heat transfer regions have been combined together for radially outward flow and radially inward flow by following equation, in order to arrive at an average heat transfer value.

$$\left(\frac{Nu}{Nu_0}\right)_{Model\ A,i} = mean\ (LS_i, TS_i) \qquad Eq.7.4$$

As shown in Fig. 7.6, region 7 corresponds to bend region in first pass and region 8 corresponds to bend region in the 2nd pass. Overall, the heat transfer enhancement was found to have weak dependence upon Rotation number (upto 0.1) for all the configurations studied. Model B - 1RW configuration's region 7 had the lowest heat transfer however Model B - 2RW region 8 had highest heat transfer enhancement among all configurations.

Regionally averaged Nusselt number enhancement: Model A and Model B comparisons

Figure 7.22 shows the comparison between smooth configurations of Model A and B. The averaging of heat transfer enhancement for Model A has been carried out using Eq. 7.4 in order to have direct comparisons with Model B. In the first pass, Model A had higher heat transfer enhancement compared to Model B. However, in the 2nd pass, Model B smooth channel had higher heat transfer towards the end of the two-pass channel for high rotation numbers.

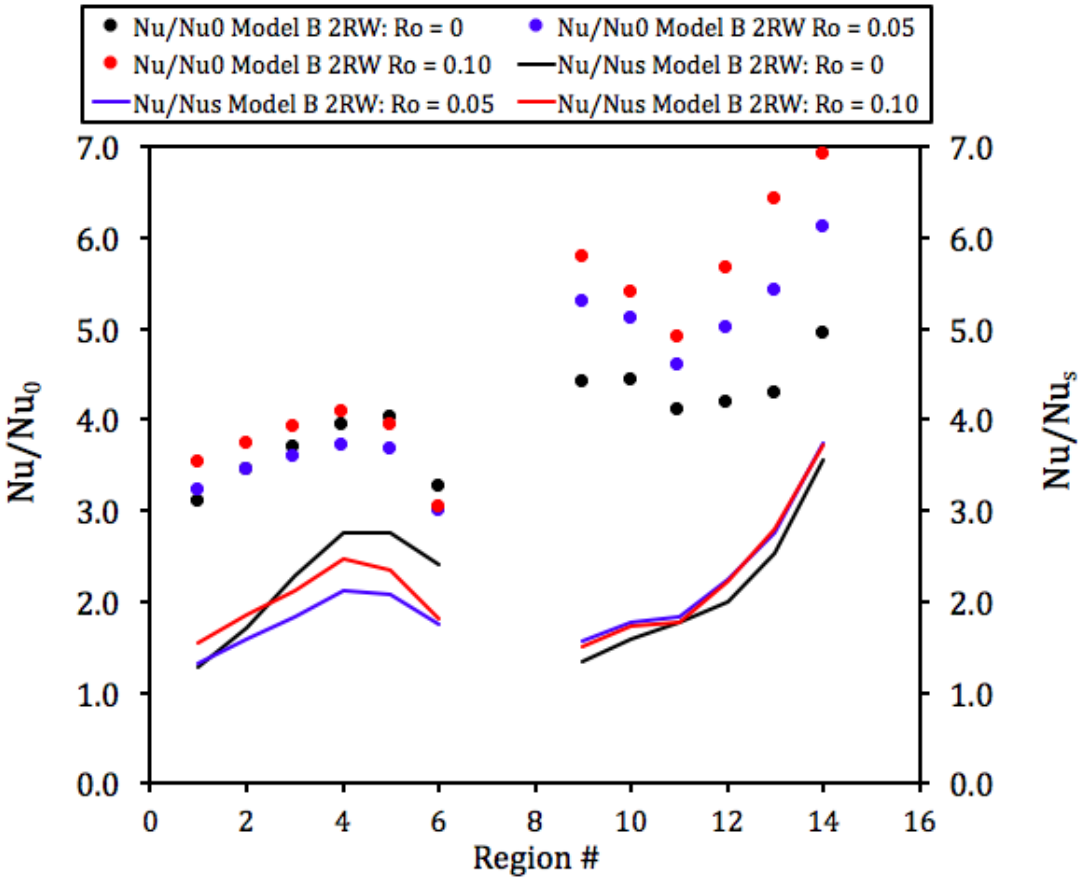

Fig. 7.20 Regionally averaged normalized Nusselt number (Nu/Nu_0 *and* Nu/Nu_s) variation with increasing streamwise distance from inlet [Model B: 2RW]

Figure 7.23 shows the comparison of heat transfer enhancement by all the ribbed configurations of Models A and B. Model B - 1RW had lowest heat transfer compared to other two Models with double ribbed walls (2RW).

This trend was found in both first and second pass and the reason behind this phenomenon was the reduced turbulent mixing due to absence of ribs on the divider wall of Model B – 1RW configuration. Model A - 2RW configuration showed higher heat transfer in the last half of the first pass compared to Model B - 2RW configuration. Also, the stationary cases of Model A and B 2RW had similar heat transfer enhancement in the first half of the first pass. The second half of the first pass showed different heat transfer characteristics for Model A and B (2RW) since the flow started to separate from the ribbed wall of Model B - 2RW while a

flattening trend in heat transfer was observed for the Model A - 2RW case. In the second pass, the stationary cases of Models A and B (2RW) had similar heat transfer.

Model B - 2RW showed distinctively higher heat transfer for the rotation cases when compared to Model A 2RW configuration. This effect was more dominant as the flow progressed in the second pass.

Globally averaged Nusselt number enhancement and Imposed Pumping Power Requirements

Figure 7.24 shows the globally averaged Nusselt number enhancements (Nu/Nu_0 and Nu/Nu_s) for all the configurations. The Model B - 2RW configuration had the highest heat transfer enhancement followed by Model A - 2RW and Model B - 1RW configurations. For all the ribbed configurations, the heat transfer showed an overall increment with increasing rotation number when normalized with D-B correlation.

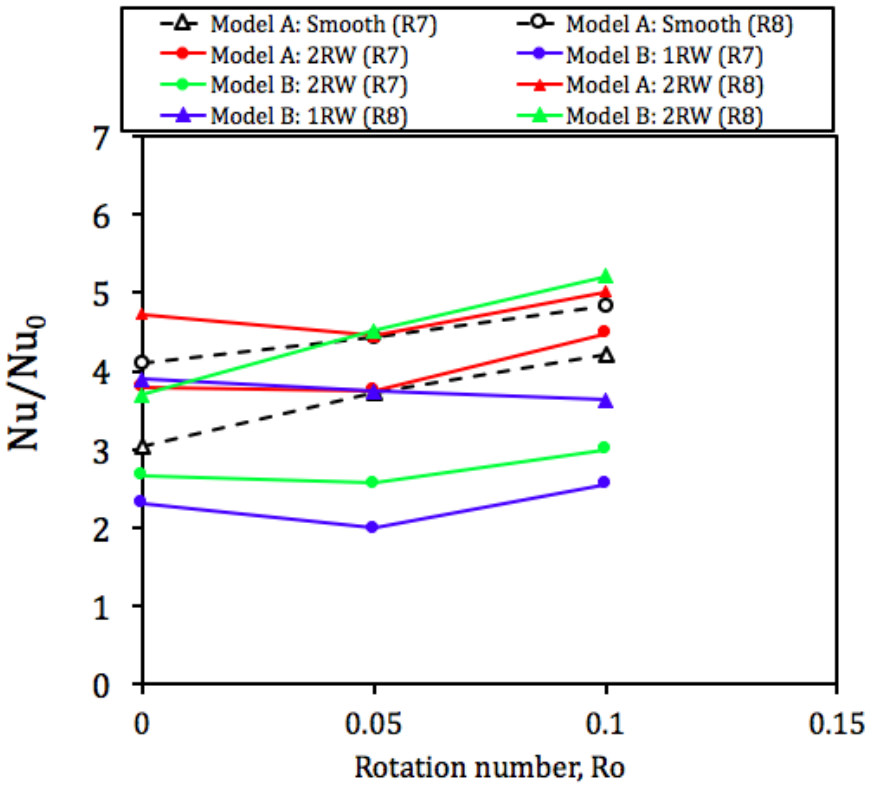

Fig. 7.21 Nusselt number enhancement (Nu/Nu_0) in bend region (# 7 and # 8) for all configurations: variation with Rotation number

However, normalized globally averaged Nusselt number with corresponding smooth configurations showed weak dependence over Rotation number. The trends of heat transfer enhancement were same for both types of normalizations.

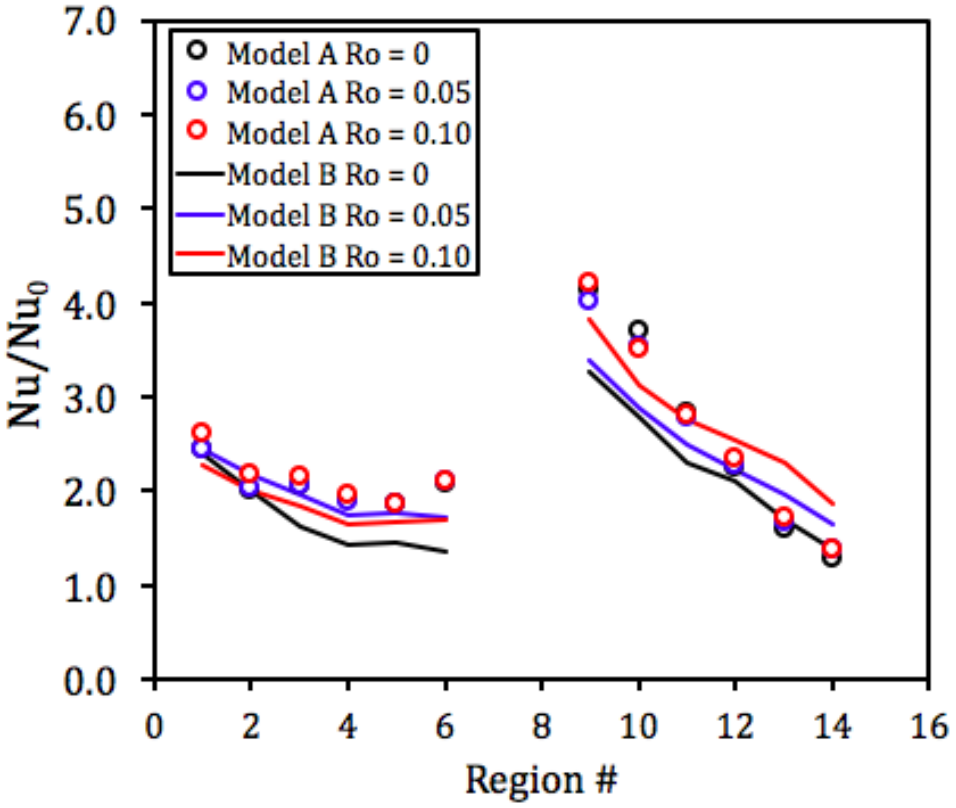

Fig. 7.22 Nusselt number enhancement (Nu/Nu_0) comparison between Model A and B smooth configurations

The heat transfer enhancement for Model A 2RW configuration was ~60% higher, Model B 1RW was ~40% higher and Model B 2RW was ~85% higher, with respect to corresponding smooth channel.

In order to develop cooling technologies which have high thermal-hydraulic performance, it is imperative to evaluate the net heat transfer enhancement with respect to imposed pumping power requirements. The pumping power was calculated using Eq. 7.5.

$$Pumping\ Power, P\ [Watt] = Re d_h \nu \Delta p_{total} \quad Eq. 7.5$$

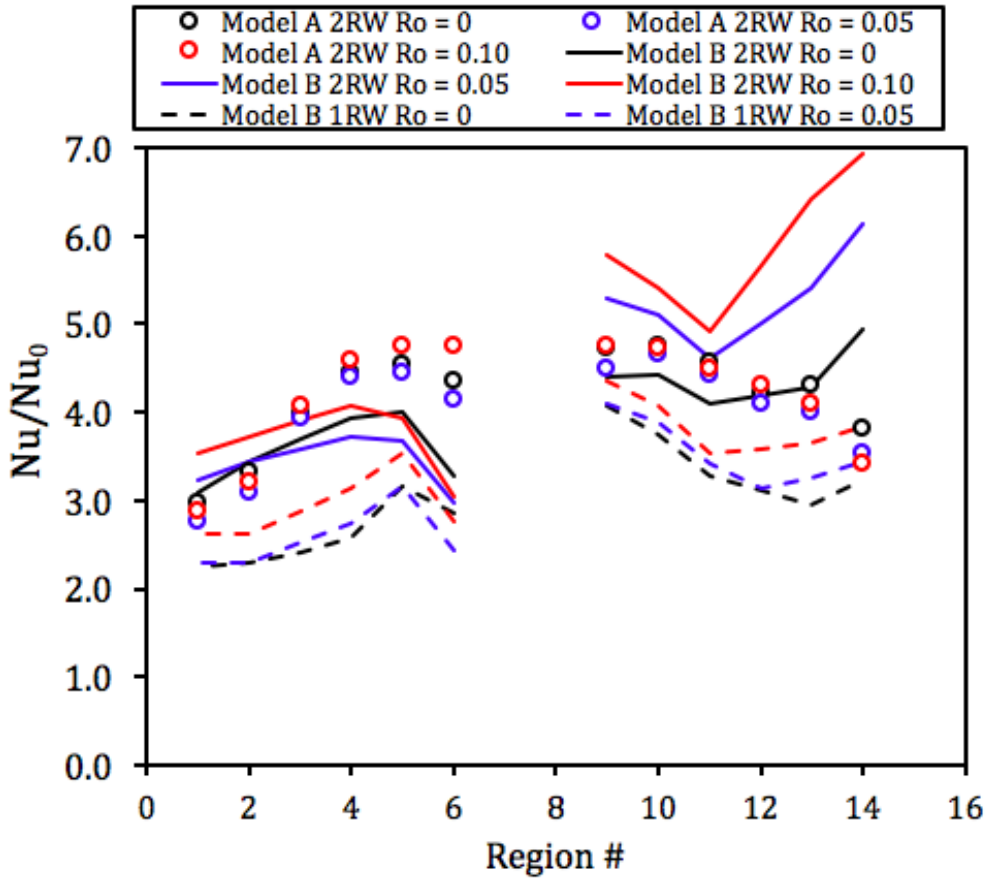

Fig. 7.23 Nusselt number enhancement (Nu/Nu_0) comparison between Model A and B ribbed configurations

Figure 7.25 shows the globally averaged heat transfer enhancement with the pumping power requirements of the configurations. The Models have been shown by colored bands. The bands indicate globally averaged Nusselt number variation with rotation number. Since, the pumping power requirements were not expected to change dramatically under rotating conditions, the total pressure drop measurements which were taken under stationary conditions were used for this analysis. Note that the static pressure measurements were not carried out under rotating conditions.

The smooth channels of Models A and B had lower enhancement in heat transfer as well as low pumping power requirements, as expected. The Model B - 1RW had higher heat transfer and pumping power requirements compared to the smooth configurations. An interesting conclusion comes out of Fig. 7.25 on comparing Model A and B 2RW configurations. Model B

showed more response towards increase in Rotation number (hence more spread in color band) compared to Model A while the pumping power requirements for Model B were on the lower side. One reason behind this trend is the absence of rib turbulators on the bend region of Model B and the fluid dynamic changes in the two-pass due to difference in orientation of coolant flow in two-pass channel with the rotation direction. Model B - 2RW configuration showed greater benefits at higher Rotation numbers at relatively lower pumping power requirements compared to corresponding ribbed configuration of Model A.

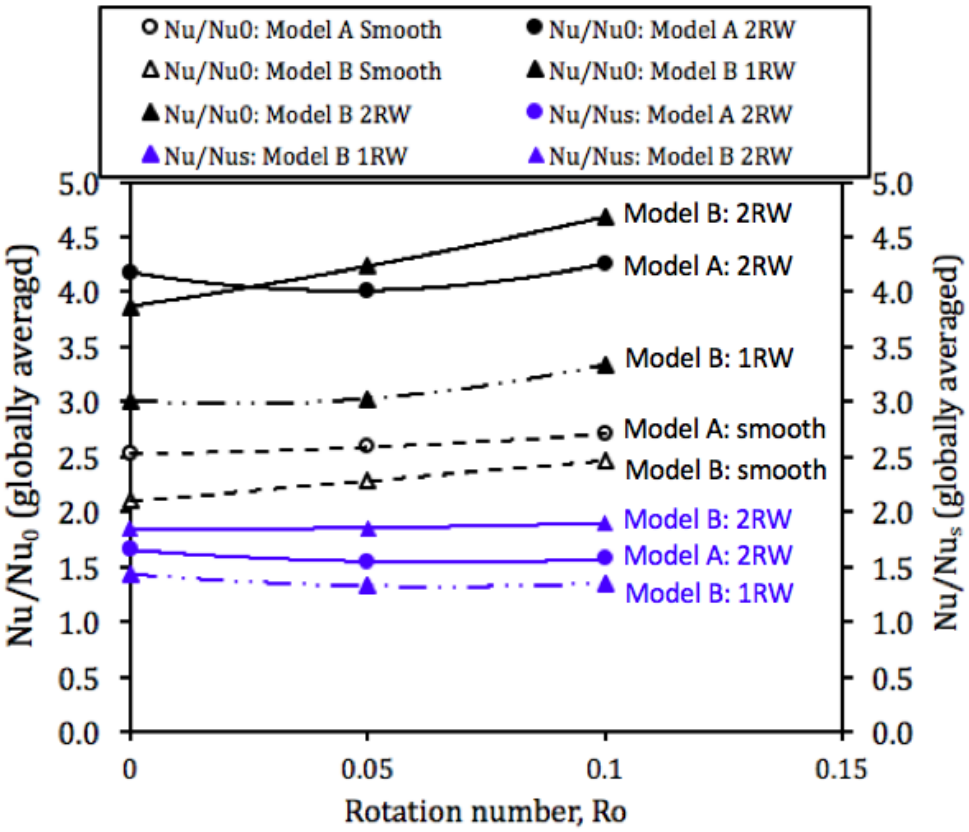

Fig. 7.24 Globally averaged Nusselt number enhancement (Nu/Nu_0 *and* Nu/Nu_s) with Rotation number

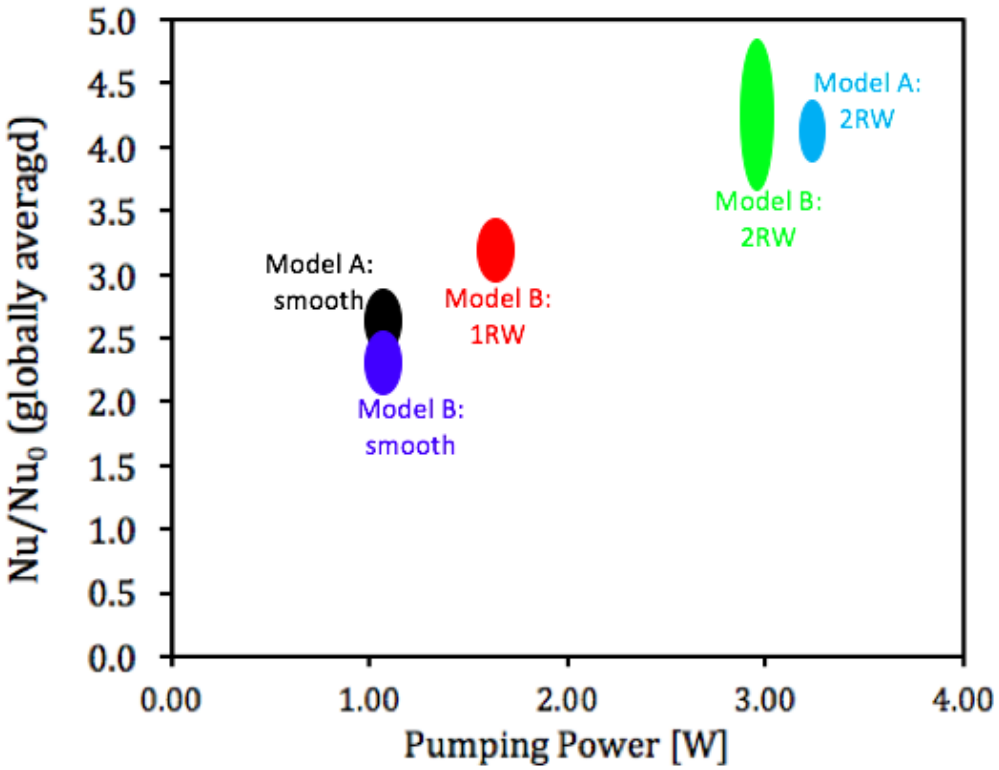

Fig. 7.25 Globally averaged Nusselt number enhancement (Nu/Nu_0) with total Pumping power [Watts] requirements

CONCLUSIONS AND RECOMMENDATIONS

Experiments have been carried out on rib turbulated two-pass channel under stationary and rotating conditions using transient liquid crystal thermography. Detailed measurements of Nusselt number have been reported for Reynolds number of 20000 and Rotation numbers of 0, 0.05 and 0.1. A total of five configurations were tested and studied. The configurations were divided in two categories – Model A and Model B. Model A was the traditional two-pass channel with rib turbulators on both leading and trailing walls. Model B had a different coolant to rotation orientation and had two ribbed configurations, single ribbed wall and double ribbed wall. The baseline case for both Models A and B were the smooth channels. Heat transfer enhancement has been evaluated from two perspectives – with respect to D-B correlation and with respect to corresponding smooth channel heat transfer results. Also, total pressure drop was

measured in order to calculate the pumping power requirements for each configuration. Following conclusions have been drawn from the current study:

(1) Model A smooth channel showed higher heat transfer compared to Model B smooth channel in the 1st pass (radially outward flow). However, at higher streamwise locations in the second pass, Model B heat transfer was higher than Model A and this difference tend to increase with increasing Rotation numbers.
(2) Model A configuration had higher heat transfer in the first pass (radially outward) compared to Model B. A clear contrast in heat transfer enhancement was observed near the bend region, where Model A heat transfer became periodic while Model B heat transfer tend to decrease near the bend region due to difference in the flow in the bend region.
(3) Model B - 1RW had lower heat transfer compared to Model B - 2RW configuration due to reduction in turbulent mixing because of absence of rib turbulators on inner (divider) wall.
(4) Model B - 2RW showed higher heat transfer in the second pass due to combined effects of coolant impingement in the first pitch of second pass, rib induced secondary flows and turbulent mixing.
(5) For higher streamwise distance, Model B heat transfer showed a contrasting trend (increasing) compared to Model A (decreasing). Also, Model B configuration had increasing heat transfer on both leading and trailing walls, which was the design intent.
(6) Overall, double ribbed wall (2RW) configurations had higher heat transfer compared to single ribbed wall (1RW) configuration.
(7) Model B - 2RW had the highest heat transfer enhancement followed by Model A - 2RW configuration. When compared to heat transfer in corresponding smooth configurations, the heat transfer enhancement of all ribbed configurations showed weak dependence on Rotation number.
(8) Model B - 2RW showed more response towards increase in Rotation number. Also, the thermal-hydraulic performance of Model B - 2RW was higher than Model A - 2RW, and this difference in thermal hydraulic performance is expected to increase with increase in Rotation numbers.

More experiments need to be carried out at higher Rotation number to quantify the benefit in heat transfer for Model B, which is expected to be more compared to Model A since the Coriolis force strength is directly proportional to rotational speed.

NOMENCLATURE

c	specific heat capacity of solid
d_h	channel hydraulic diameter
h	heat transfer coefficient
k_s	thermal conductivity of solid
k_f	thermal conductivity of air
Nu	Nusselt number
P	pumping power
Δp	pressure drop across two-pass channel
Re	Reynolds number, Vd_h/υ
Ro	rotation number, $\Omega d_h/V$
R_m	mean rotating radius
R_x	local radial location
T_i	initial wall temperature
t	time
T_w	wall temperature
T_m	mainstream temperature

Greek symbols

ρ	density
ν	kinematic viscosity
Ω	rotational speed

Subscripts

s	smooth surface
0	Dittus-Boelter correlation

Abbreviations

D-B	Dittus-Boelter correlation
HT	heat transfer
LC	liquid crystal

LS leading side

RW ribbed wall

TS trailing side

TLCT transient liquid crystal thermography

1RW single ribbed configuration

2RW double ribbed configuration

REFERENCES

[7.1] Han, J.C., 2013. Fundamental gas turbine heat transfer. Journal of thermal science and engineering applications, 5(2), p.021007.

[7.2] Han, J.C., Dutta, S. and Ekkad, S., 2012. Gas turbine heat transfer and cooling technology. CRC Press.

[7.3] Johnson, B.V., Wagner, J.H., Steuber, G.D. and Yeh, F.C., 1994. Heat transfer in rotating serpentine passages with trips skewed to the flow. Journal of Turbomachinery, 116(1), pp.113-123.

[7.4] Johnson, B.V., Wagner, J.H., Steuber, G.D. and Yeh, F.C., 1994. Heat transfer in rotating serpentine passages with selected model orientations for smooth or skewed trip walls. Journal of turbomachinery, 116(4), pp.738-744.

[7.5] Al-Hadhrami, L. and Han, J.C., 2003. Effect of rotation on heat transfer in two-pass square channels with five different orientations of 45 angled rib turbulators. International Journal of Heat and Mass Transfer, 46(4), pp.653-669.

[7.6] Dutta, S., Han, J.C. and Lee, C.P., 1996. Local heat transfer in a rotating two-pass ribbed triangular duct with two model orientations. International Journal of Heat and Mass Transfer, 39(4), pp.707-715.

[7.7] Dutta, S. and Han, J.C., 1996. Local heat transfer in rotating smooth and ribbed two-pass square channels with three channel orientations. Journal of heat transfer, 118(3), pp.578-584.

[7.8] Waidmann, C., Poser, R., Nieland, S. and von Wolfersdorf, J., 2016. Design of a Rotating Test Rig for Transient Thermochromic Liquid Crystal Heat Transfer Experiments.

[7.9] You, R., Li, H., Tao, Z. and Wei, K., 2016, June. Heat Transfer Investigation in a Smooth Rotating Channel With Thermography Liquid Crystal. In ASME Turbo Expo 2016: Turbomachinery Technical Conference and Exposition (pp. V05BT16A006-V05BT16A006). American Society of Mechanical Engineers.

[7.10] Pagnacco, F., Furlani, L., Armellini, A., Casarsa, L. and Davis, A., 2016. Rotating Heat Transfer Measurements on Realistic Multi-pass Geometry. Energy Procedia, 101, pp.758-765.

[7.11] Pagnacco, F., Furlani, L., Armellini, A., Casarsa, L. and Davis, A., 2016, June. Rotating Heat Transfer Measurements on a Multi-Pass Internal Cooling Channel: II—Experimental Tests. In ASME Turbo Expo 2016: Turbomachinery Technical Conference and Exposition (pp. V05BT16A004-V05BT16A004). American Society of Mechanical Engineers.

[7.12] Lamont, J.A., Ekkad, S.V. and Alvin, M.A., 2012. Effects of Rotation on Heat Transfer for a Single Row Jet Impingement Array With Crossflow. Journal of Heat Transfer, 134(8), p.082202.

[7.13] Lamont, J.A., Ekkad, S.V. and Alvin, M.A., 2012. Detailed Heat Transfer Measurements Inside Rotating Ribbed Channels Using the Transient Liquid Crystal Technique. Journal of Thermal Science and Engineering Applications, 4(1), p.011002.

[7.14] Lamont, J.A., Ekkad, S.V. and Alvin, M.A., 2014. Effect of Rotation on Detailed Heat Transfer Distribution for Various Rib Geometries in Developing Channel Flow. Journal of Heat Transfer, 136(1), p.011901.

[7.15] Yang, L., Tyagi, K., Ekkad, S. and Ren, J., 2015, June. Influence of Rotation on Heat Transfer in a Two-Pass Channel With Impingement Under High Reynolds Number. In ASME Turbo Expo 2015: Turbine Technical Conference and Exposition (pp. V05AT11A021-V05AT11A021). American Society of Mechanical Engineers.

[7.16] Singh, P. and Ekkad, S., 2016, June. Effects of Rotation on Heat Transfer due to Jet Impingement on Cylindrical Dimpled Target Surface. In ASME Turbo Expo 2016: Turbomachinery Technical Conference and Exposition (pp. V05BT16A010-V05BT16A010). American Society of Mechanical Engineers.

[7.17] Incropera, F.P. and De Witt, D.P., 1985. Fundamentals of heat and mass transfer.

[7.18] Ekkad, S.V. and Han, J.C., 2000. A transient liquid crystal thermography technique for gas turbine heat transfer measurements. Measurement Science and Technology, 11(7), p.957.

[7.19] Camci, C., Kim, K. and Hippensteele, S.A., 1992. A new hue capturing technique for the quantitative interpretation of liquid crystal images used in convective heat transfer studies. Journal of Turbomachinery, 114(4), pp.765-775.

[7.20] Moffat, R.J., 1988. Describing the uncertainties in experimental results. Experimental thermal and fluid science, 1(1), pp.3-17.

[7.21] Ravi, B.V., Singh, P. and Ekkad, S.V., 2017. Numerical investigation of turbulent flow and heat transfer in two-pass ribbed channels. International Journal of Thermal Sciences, 112, pp.31-43.

[7.22] Al-Qahtani, M., Chen, H.C. and Han, J.C., 2002, January. A numerical study of flow and heat transfer in rotating rectangular channels (AR= 4) with 45 rib turbulators by Reynolds stress turbulence model. In ASME Turbo Expo 2002: Power for Land, Sea, and Air (pp. 533-542). American Society of Mechanical Engineers.

[7.23] Su, G., Chen, H.C., Han, J.C. and Heidmann, J.D., 2004, January. Computation of Flow and Heat Transfer in Two-Pass Rotating Rectangular Channels (AR= 1: 1, AR= 1: 2, AR= 1: 4) With 45-deg. Angled Ribs by Reynolds Stress Turbulence Model. In ASME Turbo Expo 2004: Power for Land, Sea, and Air (pp. 603-612). American Society of Mechanical Engineers.

[7.24] Murata, A. and Mochizuki, S., 2004. Effect of rib orientation and channel rotation on turbulent heat transfer in a two-pass square channel with sharp 180° turns investigated by using large eddy simulation. International Journal of Heat and Mass Transfer, 47(12), pp.2599-2618.

[7.25] Murata, A. and Mochizuki, S., 2000. Large eddy simulation with a dynamic subgrid-scale model of turbulent heat transfer in an orthogonally rotating rectangular duct with transverse rib turbulators. International Journal of Heat and Mass Transfer, 43(7), pp.1243-1259.

[7.26] Lin, Y.L., Shih, T.P., Stephens, M.A. and Chyu, M.K., 2001. A numerical study of flow and heat transfer in a smooth and ribbed U-duct with and without rotation. Journal of Heat Transfer, 123(2), pp.219-232.

[7.27] Tanda, G., 2004. Heat transfer in rectangular channels with transverse and V-shaped broken ribs. International Journal of Heat and Mass Transfer, 47(2), pp.229-243.

[7.28] Ekkad, S.V. and Han, J.C., 1997. Detailed heat transfer distributions in two-pass square channels with rib turbulators. International Journal of Heat and Mass Transfer, 40(11), pp.2525-2537.

[7.29] Sundén, B., 2011. Convective heat transfer and fluid flow physics in some ribbed ducts using liquid crystal thermography and PIV measuring techniques. Heat and mass transfer, 47(8), pp.899-910.

[7.30] Singh, P., Ravi, B.V. and Ekkad, S.V., 2016. Experimental and numerical study of heat transfer due to developing flow in a two-pass rib roughened square duct. International Journal of Heat and Mass Transfer, 102, pp.1245-1256.

[7.31] Singh, P., Pandit, J. and Ekkad, S.V., 2017. Characterization of heat transfer enhancement and frictional losses in a two-pass square duct featuring unique combinations of rib turbulators and cylindrical dimples. International Journal of Heat and Mass Transfer, 106, pp.629-647.

[7.32] Ledezma, G.A. and Bunker, R.S., 2015. The Optimal Distribution of Pin Fins for Blade Tip Cap Underside Cooling. Journal of Turbomachinery, 137(1), p.011002.

[7.33] Wright, L.M., Fu, W.L. and Han, J.C., 2004, January. Thermal performance of angled, V-shaped, and W-shaped rib turbulators in rotating rectangular cooling channels (AR= 4: 1). In ASME Turbo Expo 2004: Power for Land, Sea, and Air (pp. 885-894). American Society of Mechanical Engineers.

[7.34] Fu, W.L., Wright, L.M. and Han, J.C., 2004, January. Heat Transfer in Two-Pass Rotating Rectangular Channels (AR= 1: 2 and AR= 1: 4) With 45 Angled Rib Turbulators. In ASME Turbo Expo 2004: Power for Land, Sea, and Air (pp. 305-315). American Society of Mechanical Engineers.

[7.35] Han, J.C. and Wright, L.M., 2006. Enhanced internal cooling of turbine blades and vanes. The Gas Turbine Handbook, 4, pp.1-5.

[7.36] Han, J.C. and Zhang, Y.M., 1992. High performance heat transfer ducts with parallel broken and V-shaped broken ribs. International Journal of Heat and Mass Transfer, 35(2), pp.513-523.

CHAPTER 8

Conclusions and Recommendations for Future Work

Driven by the need to develop intelligent cooling concepts which require minimal modification and can be easily implemented in existing cooling designs of gas turbine blades, the present study investigates new cooling concepts for gas turbine airfoils under both stationary and rotating conditions. Several cooling concepts were investigated under stationary conditions which includes rib turbulators, dimples, rib-dimpled compound channels, criss-cross rib patters, jet impingement hole shapes, internal side heat transfer enhancement by changing the cross scheme in an impingement-effusion system and many more. It has been observed that the heat transfer enhancement levels (Nu/Nu_0) by rib turbulators is typically around 2 to 3 over a range of Reynolds numbers from 20000 to 80000. Dimples have been shown to provide heat transfer enhancement levels (Nu/Nu_0) of around 2 to 2.5 over the same range of Reynolds numbers. However, their combinations arranged in a particular way yields enhancement levels in heat transfer ranging from 3 to 4.5 with minimal increase in pumping power requirements. This provides an encouraging result and it is recommended that different rib shapes should be tested with different shapes of dimples and a detailed parametric study is recommended in order to develop highly efficient cooling concepts. Flow Reynold number upto 500,000 can be investigated for the newly developed cooling designs in order to determine the applicability for land based gas turbines as well. For the impingement-effusion system, it has been found that simply changing the crossflow scheme can significantly affect the thermal-hydraulic performance of the thermal system. All the possible crossflow schemes were investigated in the present study for a jet-to-target plate spacing of 1 and for jet Reynolds numbers ranging from 3500 to 9000. It has been recommended that a parametric study should be carried out to explore different jet-to-target plate spacings for a more wider range of Reynolds numbers (upto 20000) in order to develop an impingement-effusion system which has high thermal hydraulic performance and accordingly its location in gas turbine airfoils can be decided.

The second part of this work was focused on assessing the effects of rotation on heat transfer enhancement and reduction on leading and trailing side internal walls depending upon radially outward and inward flows. Detailed heat transfer measurements were carried out using transient liquid crystal thermography in order to evaluate the effects of Coriolis force on heat transfer

distributions. It has been found that the heat transfer gets enhanced on the trailing side internal walls for the 1st pass (radially outward flow) and the heat transfer gets reduced on the leading side of the 1st pass. A reverse trend was observed in terms of heat transfer enhancement in the 2nd pass. This problem of non-uniform cooling at near similar pumping power costs as stationary cases, needed to be addressed. A new cooling concept has been provided where the rotational energy was used in favor of heat transfer enhancement on both leading and trailing side internal walls by simply rotating the two-pass channel configuration by 90°. Also, the traditionally used 90° rib was dropped in the new design in order to preserve the impingement effect found in the 2nd pass. It has been experimentally found that the new design has 11% higher heat transfer enhancement (Nu/Nu_s) at 8% lower pumping power(P/P_s) requirement when compared to the (Nu/Nu_s) and (P/P_s) of the traditional two-pass channel. The new design also resulted in more uniform cooling which is one of the design intents in gas turbine cooling. The new design was tested for rotation numbers of 0.05 and 0.1. It is expected that the rotational effects will be more pronounced at higher rotation numbers and increased heat transfer can be expected. However a detailed study on rotation numbers upto 0.3 is recommended that the additional effects of centrifugal buoyancy should also be studied in order to validate the new design intent at full range of operating rotation numbers.